# Final Report

## Project: DTFH61-11-C-00025

## The Impact of Wide-Base Tires on Pavement – A National Study

## VOL I

## Submitted to the

### FEDERAL HIGHWAY ADMINISTRATION
### (FHWA)

## August 2015

## Submitted by

**University of Illinois at Urbana-Champaign**
**1207 Newmark Lab, 205 N. Mathews, M/C 250**
**Urbana, IL 61801**

**Participants: UC-Davis, FLDOT, Delft, CSIR**

# ACKNOWLEDGMENT AND DISCLAIMER

# EXECUTIVE SUMMARY

Researchers have been studying wide-base tires for over two decades, but no evidence has been provided regarding the net benefit of this tire technology. The present study reflects a relevant step forward, where a comprehensive approach is used to compare new-generation wide-base tires (NG-WBT) with the dual-tire assembly (DTA). Numerical modeling, prediction methods, experimental measurements, and environmental impact assessment were combined to provide recommendations about the use of NG-WBT.

Numerical modeling allows the calculation of pavement responses for an ample combination of variables, which would be expensive, time-consuming, and impractical if performed as part of any experimental program. A finite element approach, considering variables usually omitted in the conventional analysis of flexible pavement, such as dynamic analysis, continuously moving load, linear viscoelastic asphalt materials, nonlinear anisotropic granular materials, interaction between pavement layers, and three-dimensional contact stresses/loads, was utilized for modeling. Five hundred seventy-six cases combining layer thickness, material properties, tire load, tire inflation pressure, and pavement type (thick and thin) were analyzed to obtained critical pavement responses. The numerical model comprised an experimental measurement of three-dimensional contact stresses, material properties from nation-wide databases, and pavement structures as part of the road infrastructure. Based on the pavement responses, current transfer functions used in the Mechanistic-Empirical Pavement Design Guide (MEPDG) were proven to be inappropriate for comparing the damage resulting from NG-WBT with that from DTA. Consequently, a new procedure based introduced.

The experimental program aimed to validate the results of the numerical model. It could also be used to experimentally verify the trends inferred from the finite element model for the scenarios of the testing program. Stress, strain, and temperature were measured at various locations in the pavement structure in sections subjected to accelerated pavement testing (Florida and California) and controlled truck loading (Ohio). In addition, measurements from previous projects were used by the research team (California, Florida, Illinois, Ohio, and Virginia). The information was compiled in a database that users could access to retrieve experimental results.

Even though the numerical and experimental testing program was broad and robust, it did not cover all possible scenarios. Consequently, a prediction tool based on artificial neural networks was developed to obtain critical pavement responses in cases outside the finite element analysis matrix. The tool, known as ICT-Wide, can promptly predict critical pavement responses without performing finite element calculations.

The environmental impacts were determined using life cycle assessment. Based on the bottom-up fatigue cracking, permanent deformation, and international roughness index, the life cycle energy consumption, cost, and green-house gas (GHG) emissions were estimated. Three scenarios were established with different levels of market penetration of NG-WBT: i) NG-WBT and dual tires demonstrating equivalent fatigue and international roughness index (IRI) performance; ii) design life determined by fatigue performance; and iii) design life determined by IRI performance.

Finally, to make the outcome of this research effort useful for state departments of transportation and practitioners, a modification to AASHTOWare is proposed to account for NG-WBT. The revision is based on two adjustment factors, one accounting for the discrepancy between the

AASHTOware approach and the finite element model of this study, and the other addressing the impact of NG-WBT.

# TABLE OF CONTENTS

# LIST OF TABLES

# LIST OF FIGURES

xi

# 1  INTRODUCTION

## 1.1  BACKGROUND

After more than two decades of research by the tire industry and pavement researchers, a new generation of wide-base tires (NG-WBT) (445/50R22.5 and 455/55R22.5) was introduced to improve safety, reduce the impact on the environment, and provide cost savings. The introduced NG-WBT is wider, has improved structure and design, and offers a rolling tread width increase of 15 to 36% compared with the first generation wide-base tires (FG-WBT). In addition, the new tires adhere to the "inch-width" rule applicable all over the U.S. for 5-axle, 79.8 kip gross-vehicle-weight trucks.

In Europe, wide-base tires (having a different design than the ones introduced in the U.S.) have been used successfully on trucks since the early 1980s. In 1997, around 65% of trailers and semi-trailer tires in Germany used wide-base tires (COST 334, 2001). In April 2008, Canada increased the allowable weight limit on axles with wide-base tires. Per the new guidelines, axle loads may not exceed 17 kip for single axles and 34 kip for tandem axles when an axle is fitted with two single tires (each 445 mm wide or greater), compared with 20.2 and 37.4 kip, respectively, for dual-tire assemblies (DTA).

The impact NG-WBT on trucking operations has also been evaluated. Fuel economy improved when NG-WBT was used. NG-WBT reduced the rolling resistance coefficient to 0.005, which is translated in fuel efficiency of 10% higher than that of DTA, according to a fuel consumption model (Muster, 2000). In addition, in combination of aerodynamic devices, WBT improved fuel economy by 18% for a truck traveling on a highway at 65 mph according to field testing (Bachman et al., 2005). Moreover, based on data collected from hauling companies, the use of WBT translated into fuel savings ranging between 3.5 and 12% (Genivar, 2005). In 2010, the improvement of fuel economy resulting from the use of NG-WBT was reported at approximately 10% (Franzese et al., 2010).

Other benefits of using WBT have been reported. Since a WBT is lighter than DTA, the hauling capacities of trucks equipped with WBT increases (Markstaller et al., 2000). WBT is easier to inspect, repair, and maintain (Genivar, 2005), uses less rubber material, and decreases the amount of disposable materials (Environmental Protection Agency 2004). Furthermore, WBT has similar or slightly better performance than DTA with regard to safety and comfort (Markstaller et al., 2000).

WBT is more environmentally friendly than DTA; using WBT leads to lower consumption of gas, which also leads to a reduction in gas-emission. Moreover, since the amount of materials needed to produce a WBT is less than that for DTA, the material disposed at the end of the life cycle of the tire is relatively less (Genivar, 2005). In addition, it is worth mentioning that WBT produces slightly less noise (Markstaller et al., 2000).

## 1.2  OBJECTIVE AND SCOPE

The objective of this study was to quantify the impact of vehicle-tire interaction on pavement damage for various pavement structures using advanced theoretical modeling and to validate this impact by performing full-scale pavement testing based on available data. In addition, the study aimed to further assess the economic, safety, and environmental effects of using NG-WBT as related to pavement performance. Finally, to allow for the use and implementation of NG-WBT by state departments of transportation, a simple user-friendly tool was introduced developed to assess the impact of NG-WBT on pavement networks and to facilitate decision-making.

The main objectives of this project include:

- Develop a tool and methodology that allow state departments of transportation and practitioners to assess the impact of NG-WBT on the pavement network.
- Perform an analysis of the economic and environmental effects of using NG-WBT relative to their impact on pavement performance.
- Quantify the impact of NG-WBT compared with DTA using validated finite element model. The comparison was performed not only to investigate critical pavement responses, but also the corresponding distresses and environmental and economic impacts. Appropriate and accurate input for the three-dimensional finite element model was determined including contact stresses/loads and material properties.

NG-WBT Michelin X One® 445/50 R22.5 (tread design XDN®2) and DTA 275/80 R22.5 (tread design XDN®2) tires were considered. The three-dimensional contact stresses/loads were measured for a wide range of loads and tire inflation pressures, and a subset of the testing matrix was used in the finite element analysis. Material selection was made using extensive databases of material test results and material characteristics. The finite element model, which was validated using the experimental measurements, provided critical pavement responses for comparing NG-WBT with DTA. In addition, the outcome of numerical modeling was used to develop a prediction tool based on artificial neural networks. Life cycle cost analysis (LCCA) and life cycle assessment (LCA) were performed to complement the mechanistic comparison between the two investigated tires for a holistic evaluation. Finally, a methodology based on two adjustment factors, considering the finite element analyses and the relative effect of wide-base tires, was proposed to account for the effect of NG-WBT using the current pavement design guide (AASHTOware).

## 1.3    OVERVIEW OF THE REPORT

The body of the report consists of eleven chapters and eight appendices. Chapter 2 presents a concise background on WBT and their applications and impact. Chapter 3 expands on the measurement of the three-dimensional tire-pavement contact stresses/loads, where the measuring equipment and data processing and analysis are detailed. Details of the developed finite element model are discussed in Chapter 4, which also includes the definition of input parameters. The effect of tire configuration on critical pavement responses is presented in Chapter 5, which is the foundation for developing the prediction tool introduced in Chapter 6. Chapter 7 explains the development of two adjustment factors that would allow using AASHTOWare for NG-WBT loading. Chapters 8 and 9 present the experimental pavement sections (pavement structure, instrumentation, and testing matrix), and the quantification of pavement damage, respectively. Finally, the LCA is introduced in Chapter 10, and conclusions and recommendations are provided in Chapter 11.

The eight appendices provide detailed three-dimensional (3-D) tire contact stresses/loads, modeling results of thin and thick pavements, and a user guide of the prediction tool. In addition, the design and material characteristics of the pavement sections built and tested in Florida and California are presented in the appendices, which also include details about the data processing of pavement instrument responses of the experimental pavement sections and database management.

# 2 LITERATURE REVIEW

Research conducted to date on WBT can be divided into two time periods. The first period focused on the first generation of wide-base tires (FG-WBT) and spanned from early 1980s to 2000. The second period started in early 2000 with the introduction of the NG-WBT after it became evident that FG-WBT was more damaging to the pavement infrastructure than the conventional DTA.

Studies of WBT may be divided into four impact categories: impact on road infrastructure, dynamic tire loading, trucking operations, and the environment. To investigate the effect of WBT on road infrastructure, researchers followed three main approaches: accelerated pavement testing, numerical modeling and analytical methods, and evaluation of in-service field data.

Accelerated pavement testing was used in Finland to study the effect of tire type and axle configurations (Huhtala, 1986; Huhtala et al., 1989). Flexible pavements with thicknesses of 2, 3, and 6 in were instrumented and subjected to various axle configurations and tire types. The study concluded that FG-WBT was more damaging than DTA; the amount of damage caused by these two types of tires decreased as the thickness of the asphalt concrete (AC) layer increased (Huhtala, 1986). Furthermore, FG-WBT was reported to cause between 1.2 and 4 times more damage than DTA (Huhtala et al., 1989).

In 1992, studies conducted in Virginia and Pennsylvania reported several findings related to FG-WBT. In Virginia, FHWA compared DTA and FG-WBT through performance and response analysis (Bonaquist, 1992). Twelve pavement sections were tested at various environmental conditions, axle loads, and tire inflation pressures. FG-WBT was found to be more damaging than DTA as it demonstrated two times more permanent deformation and 25% less fatigue life than DTA. On the other hand, a study led by Pennsylvania State University test track used trucks traveling at 40 mph with various tire inflation pressures, tire types, axle loads, and axle configurations. The study showed that the damage caused by FG-WBT was 50-70% greater than the damage caused by DTA (Sebaaly and Tabatabaee, 1992).

FG-WBT was also evaluated in overlay systems. A study in California compared the performance of dense-graded AC and asphalt-rubber hot-mix gap-graded (ARHM-GG). The accelerated pavement testing was carried out at high temperature, including aircraft tires. The number of repetitions to failure (excessive rutting) of FG-WBT ranged between 10 and 60% of DTA (Harvey and Popescu, 2000).

Several different countries in Europe also studied WBT at the beginning of the previous decade (COST 334, 2001). The study included WBT 495/45R22.5, which was referenced as the new generation of WBT. In the United Kingdom, a comparison between WBT-385 and WBT-495 concluded that WBT-385 produced 70 and 50% more rutting in medium-thick and thin flexible pavements, respectively. Thick pavements were tested in Germany, and the ratio between the rutting generated by WBT-495 and DTA (315/80R22.5) was around 1.3. Very thick and stiff pavement structures were built and tested in France. No significant difference was found between measurements of both tires at the bottom of the AC. Finally, the difference in dynamic loading between various types of tires was investigated in Finland. Measurements were taken of a truck traveled at 50 mph. The WBT-495 originated a greater response (COST 334, 2001).

Twelve different pavement sections were built, heavily instrumented, and tested in Virginia in the past decade. The testing program included various tire types, loading configurations, and speeds (Al-Qadi et al., 2004; Al-Qadi et al., 2005a; Al-Qadi et al., 2005b; Elseifi et al., 2005). Transfer functions were used to link pavement response to damage. The comparison between the combined damage ratio of NG-WBT and DTA showed that NG-WBT is, in general, less damaging.

Research on WBT has also been conducted in Canada (Pierre et al., 2003). Strains near the surface of a flexible pavement with 4 in AC layer were measured and compared considering different tire types, speeds, loads, and tire inflation pressures. The damage of NG-WBT and DTA was found to be dependent on environmental conditions and location. For instance, strains at the base resulting from NG-WBT and DTA loading during summer were close in magnitude. However, NG-WBT produced higher strains in the spring (Pierre et al., 2003). National Center for Asphalt Technology (NCAT) also reported that the horizontal strains at the bottom of the AC and the stresses on top of the subgrade produced by NG-WBT and DTA are comparable (Priest and Timm, 2006).

The effect of DTA, FG-WBT, and NG-WBT on full-depth pavements was compared in a study at the University of Illinois at Urbana-Champaign (Al-Qadi and Wang, 2009a; Al-Qadi and Wang, 2009b). The thickness of the flexible pavements varied between 6 and 16.5 in After testing at various tire inflation pressures, axle loads, and temperatures, it was observed that WBT-425 (FG-WBT) is more damaging than WBT-455 (NG-WBT). Similar tests carried out on low-volume road test sections showed that NG-WBT is more damaging to this type of pavement (Al-Qadi and Wang, 2009c).

Finally, a study performed in Florida that focused on permanent deformation compared WBT-445, WBT-455, WBT-425, and DTA. Foil strain gauges close to the surface were installed, and the pavement was tested at high temperatures (Greene et al., 2009). DTA had the highest number of passes to reach 0.5 in rutting, and WBT-425 needed the least number of passes. A summary of field and accelerated pavement testing for quantifying the impact of WBT is presented in Table 2-1 and Table 2-2.

Numerical models have also been used to evaluate the effect of WBT. Radial, bias ply, and FG-WBT in thin (2 in.) and thick (8 in.) flexible pavements (Sebaaly and Tabatabaee, 1989) were compared using BISAR. The study concluded that FG-WBT (15R22.5 and 18R22.5) generated the greatest strain at the bottom of the AC and stress on top of the subgrade, respectively. VESYS-DYN was used to assess fatigue damage and rutting. It was reported that FG-WBT caused wider and shallower rut depth than DTA (Gillespie et al., 1992). In addition, no influence of the tire inflation pressure on rutting was observed. FG-WBT produced 15-40% greater critical strain when using CIRCLY, software that considers shear contact stresses and friction between layers (Perdomo and Nokes, 1993). The relevance of the shear contact stresses was highlighted in the study.

A continuum-based finite-layer method was used to show that for FG-WBT traveling at high speed, the transverse tensile strain was more critical when predicting fatigue life (Siddharthan et al., 1998). The study also mentioned the importance of nonuniform 3-D contact stresses. ABAQUS was used to conclude that the contact stresses between the tire and the pavement were independent from the material of the layer in contact with the tire (Myers et al., 1999). Also, BISAR was used to highlight the importance of lateral contact stresses and their influence on surface cracking and near-surface rutting. Finally, the software 3D-MOVE was used to evaluate the shape of the contact area for different types of tires on pavement response (Siddharthan et al., 2002). FG-WBT with circular contact area provided the highest longitudinal strain at the bottom of AC and vertical strain on top of the subgrade. The study also found that lateral contact stresses were relevant only close to the surface.

The general-purpose software ABAQUS has been continuously improved to address details in the modeling of flexible pavements response. The software was used to include viscoelastic material characteristics (Elseifi et al., 2006), dynamic analysis (Yoo and Al-Qadi, 2007), 3-D contact stresses (Al-Qadi and Yoo, 2007), continuous moving loading and layer interaction (Yoo et al., 2006), and nonlinear granular material (Al-Qadi et al., 2010; Kim et al., 2009). All these effects have proven relevant when evaluating the response of flexible pavements. Table 2-2 presents a summary of the modeling conducted to date on this topic.

Available literature clearly suggests that FG-WBT causes more pavement damage. On the other hand, the impact of NG-WBT on pavement is inconsistent according to the findings in the literature. Hence, it is evident that a gap exists in the current state of knowledge; specifically with regard to pavement responses to loaded by NG-WBT. In addition, results have shown significant variations caused by the inconsistency in load modeling (including tire configuration, axle loading, and contact stresses) and use of material models. Therefore, accurate models of pavement responses to tire loading are needed and must be validated with in-situ measured data.

**Table 2-1. Summary of Field and Accelerated Pavement Testing**

| Source | Pavement Structure | Instrumentation | Tire Type | Load (kip) | Tire Pressure (psi) | Outcome |
|---|---|---|---|---|---|---|
| Finland (Huntala, 1986; Huntala et al. 1989) | AC: 2, 3, and 6 in.; base: 22 in.; subgrade: fine sand | Strain gauges at bottom of AC and pressure cells on top of subgrade | 12R22.5, 265/70R19.5, 445/65R22.5, 385/65R22.5, and 350/75R22.5 | 8.8, 11, and 13.2 | 69.6 to 156.5 | • WBT caused 1.2-4 times more damage<br>• The wider the WBT, the less the damage |
| Virginia (Bonaquist, 1992) | 12 sections. AC: 3.5 and 7 in; base: 12 in; subgrade: silty fine sand | Strain gauges at bottom of AC, and LVDT at different depths | 425/65R22.5 and 11R22.5 | 9.2, 12.1, 14.4, and 16.6 | 75.4, 103, and 140 | • WBT produced two times more permanent deformation and 25% less fatigue life than DTA |
| Texas (Akram, 1992) | 2 sections: i) AC: 1.5 in.; base: 10 in.; ii) AC: 7 in.; base: 14 in.; subbase: 6 in stabilized w/ lime; Subgrade: sandy clay | Multi-depth deflectometers | 425/65R22/5 and 11R22.5 | 16.5 and 18.5 | 130 and 120 | • Maximum shear at edge of WBT<br>• WBT produced higher deflections<br>• WBR caused 2.8 more damage for thin and 2.5 for thick AC pavements |
| Pennsylvania (Sebaaly and Tabatabaee, 1992) | Thin section: AC: 6 in.; base: 8 in<br>Thick section: AC: 10 in.; base: 10 in. | Strain gauges at bottom of AC (instrumented core); geophones | 11R22.5, 245/75R22.5, 385/65R22.5, and 385/65R22.5 | 7.3, 8.6, 8.8, and 10.8 | 75, 90, 100, 105, 120, and 130 | • WBT resulted in 0.5 and 2.8 times more fatigue damage<br>• WBT caused 30 to 60% more rutting |
| California (Harvey and Popescu, 2000) | Overlays: 1.5 and 2.5 in DGAC, and 2.5 and 3 in ARGM-GG. Preexisting: AC: 6 in.; base: 10.8 in., subbase: 9 in 3-in. ATPB under AC in some sections | Thermocouples | Bias ply 10.00-20, 11R22.5, 425/65R22.5, and Aircraft 46x16 | 9 and 22.5 | 90, 105, 110, and 150 | • Aircraft tire showed the worst rutting performance followed by WBT. WBT required 10-60% the number of repetitions to failure (0.5 in rutting) |
| Europe (COST 334, 2001)<br>England | Two AC thicknesses: 4 and 8 in.; subbase: 9 in.; subgrade: 3-4% CBR | LVDTs and strain gauges | 295/60R22.5, 295/80R22.5, 315/70R22.5, 315/80R22.5, 385/65R22.5, and 495/40R22.5 | 6.7, 9.69, and 12.7 | 72-145 | • Ratio of rutting between 385/65R22.5 and 495/45R22.5 was 1.7 for 8 in pavement and 1.5 for 4 in pavement |

| Source | Pavement Structure | Instrumentation | Tire Type | Load (kip) | Tire Pressure (psi) | Outcome |
|---|---|---|---|---|---|---|
| Europe (COST 334, 2001) Germany | Four sections with: AC: 10.6 in.; base: 10 in.; subgrade: clay/peat | N/A | 385/65R22.5, 315/80R22.5, 495/45R22.5, and 295/60R22.5 | 10.1 and 12.9 | 101.5 and 130.5 | • Ratio of rutting between WBT-385 and DTA-315: 1.94 to 2.73<br>• Ratio of rutting between WBT-495 and DTA-315: 1.32 to 1.34 |
| Europe (COST 334, 2001) France | AC: 3.2 in.; AC base: 16 in.; base: 16 in.; subbase: 12 in.; subgrade: sandy clay | Strain gauges and thermocouples at different depths | 385/65R22.5, 495/45R22.5, 315/80R22.5, and 295/60R22.5 | 10.1 and 12.9 | 116, 145, 166, and 87-167 | • Similar vertical and longitudinal strains for WBT-495 and WBT-385 |
| Europe (COST 334, 2001) Finland | AC: 6 in.; base: 6 in.; and subbase: 16 in. | 7 long strain gauges at bottom of AC and three pressure cells at various depths | 315/70R22.5 495/45R22.3 | 12.8 | 110 130 | • At 50 mph, WBT-495 induced 17% more strain at bottom of AC than DTA-315<br>• 21 and 14% greater stress on top of the base and subbase, respectively. Almost the same on top of subgrade |
| Canada (Pierre et al., 2003) | AC: 4 in.; base: 8 in.; subbase: 19 in.; subgrade: silty | Distortion gauges, multi-depth deflectometer; slab built and instrumented in laboratory | 11R22.5, 12R22.5, 385/65R22.5, and 445/55R22.5 | 6.6, 8.8, 11, 13.2, and 15.4 | 81.2, 105.9, and 130.5 | • WBT-385 was more damaging than the other tires<br>• Similar strain at base for WBT-455 and DTA during summer<br>• WBT performed better in rutting<br>• Less deflection for DTA |
| Virginia (Al-Qadi et al., 2004; Al-Qadi et al., 2005a; Al-Qadi et al., 2005b; and Elseifi et al., 2005) | 12 pavement structures | Strain gauges and pressure cells at different depths. Thermocouples and TDRs | 275/8R22.5 445/50R22.5 | 17.0 and 8.5 | 90/90, 90/60 and 90/30 105 | • Combined pavement damage for WBT-445 was less than that for DTA-275 |
| Alabama (Priest and Timm, 2006) | AC: 6.7 in.; base: 6 in.; 17 in compacted subgrade | Long and transverse strain gauges at bottom of AC and pressure cells on top of subgrade | 275/80R22.5 445/50R22.5 | 9.25 and 7.8 | 100 120 | • Insignificant difference at the instrumented location between both tires |

| Source | Pavement Structure | Instrumentation | Tire Type | Load (kip) | Tire Pressure (psi) | Outcome |
|---|---|---|---|---|---|---|
| Illinois (Al-Qadi and Wang, 2009a; Al-Qadi and Wang, 2009b) | AC: 16.5, 10, and 6 in.; lime modified subgrade | Two long and one transverse strain gauge at bottom of AC | 425/65R22.5, and 455/55R22.5 11R22.5 | 6, 8, 10, 12 and 14 6, 10, and 14 | 80, 100, and 110 110./30, 110/50, 110/70, 110/90, and 110/110, | • WBT-425 showed higher response than WBT-455 • Difference between WBT and DTA was relevant close to surface • WBT-425 was more damaging for fatigue cracking |
| Illinois (Al-Qadi et al., 2006; and Al-Qadi and Wang 2009c) | AC: 3 and 5; base: 8, 12, and 18 in.; subgrade silty sand @4%. geogrid in 5 sections | Strain gauge at bottom of AC; LVDTs in 3directions. Pressure cells; TDR, thermocouples | 11R22.5 and 455/55R22.5 | 6, 8, and 10 | 80, 100, and 110 and differential tire pressure | • WBT-455 caused more damage to low-volume roads than DTA |
| Florida (Greene et al., 2009) | AC: 5.1 in dense-graded and open-graded; base: 10.5 in.; subbase: 12 in.; subgrade: A-3 | Foil gauges at the wheel path and 2 and 5 in from the edge of the tire | 11R22.5 425/65R22.5 445/50R22.5 455/55R22.5 | 9 | 100 115 | • DTA showed the best and WBT-425 the worst performance with respect to rutting. • WBT-425 generated the highest transverse strain at the surface • WBT-455 generated the lowest shear strain at edge of the tire; WBT-445 and DTA generated similar values |
| Ohio (Xue and Weaver, 2011) | AC: 4 and 8 in.; base: 6 in DGAB | Strain gauges rosettes and longitudinal and transverse strain gauges at the bottom of AC and close to the surface | 275/80R22.5 295/75R22.5 425/65R22.5 495/45R22.5 | 5.05 4.2 5 5 | 70, 100, and 120 | • WBT-425 produced higher response (shear strain) than the other tires |

**Table 2-2. Summary of Numerical Modeling and Analytical Methods**

| Study | Pavement Structure | Tire | Load Configuration | Tire pressure (psi) | Material Characterization | Outcome |
|---|---|---|---|---|---|---|
| Hallin et al. (1983) | AC: 3, 6, and 9.5 in.; base: 8 in. | Dual and single (width between 10 and 18 in) | Circular contact area: constant radius-variable pressure, double circle constant pressure, and single circle constant pressure | 80 | Resilient modulus test. Effect of temperature considered | • The difference in equivalent loading factor decreased as the tire width increased |
| Sebaaly and Tabatabaee (1989) | AC: 2, 4, 6, and 8 in.; base: 8 in. | 11R22.5, 11-22.5, and 385/65R22.5 | Measured contact stresses inputted as concentric circles with different pressures | DTA: 80-130; WBT: 105-145 | Linear elastic | • Inflation pressure affected thin pavement, mainly for WBT-385<br>• WBT-385 generated the greatest strain at the bottom of AC and compressive stress on top of subgrade |
| Gillespie et al. (1992) | AC: 2 - 6.5 in.; base: 4 - 11 in. | 215/75R17.5, 245/75R19.5; 11R22.5, 10.0-20, 11R24.5, 295/75R22.5; 15R22.5, 18R22.5, 385/65R22.5, and 445/65R22.5 | Circular area with uniform pressure | 75-120 | Linear elastic | • WBT was more damaging than DTA for typical highway pavement<br>• WBT caused wider but shallower rut profile than DTA; WBT 15R22.5 produced nine times more fatigue damage after changing tire inflation pressure from 75 to 120 psi |
| Perdomo and Nokes (1993) | AC: 6.6 in.; base: 3 in. | WBT and DTA (specific models not provided) | Circular contact area. Shear and nonuniform vertical contact stresses were considered | Maximum contact stress: WBT: 220; DTA: 160 | Linear elastic | • WBT resulted in 15-40% higher critical strains, and 30-115% higher strain energy of distortion<br>• Shear contact stresses had a high impact on tensile strain and strain energy |

| Siddhartan et al. (1998) and Siddhartan and Sebaaly (1999) | AC: 6 and 10 in.; base: 8 and 10 in. | 425/65R22.5 and DTA | Moving load with any shape of contact area. 3D contact stresses | 123-130 | Elastic and viscoelastic AC layer | • 16 and 33% higher strain at the bottom of AC for thin and thick pavement, respectively<br>• When using WBT, transverse normal strain should be used |
|---|---|---|---|---|---|---|
| Myers et al. (1999) | AC: 8 in.; base: 12 in. | Bias ply, Radial, and WBT | Measured 3D contact stresses incorporated in BISAR | 90-140 | Linear elastic | • WBT at high values of load and inflation pressure were considerably more damaging than DTA (surface rutting and cracking)<br>• Surface cracking and near-surface rutting were mainly influenced by lateral stresses |
| Siddharthan et al. (2002) | AC: 6 and 10; base: 8 and 10 | 425/65R22.5 | Circular, elliptical, and rectangular contact area. Uniform and nonuniform pressure. 3D contact stresses | 125 | Elastic and viscoelastic AC layer | • For WBT, greater long strain at the bottom of AC and vertical strain on top of subgrade<br>• Response at a depth of 2 in was greater for WBT with circular contact area<br>• Shear contact stresses were relevant and close to the surface only |
| Al-Qadi et al. (2005a), Elseifi et al. (2005) | AC: 7.4 in.; OGDL: 3 in.; base: 6 in.; subbase: 7 in. | 11R22.5, 445/50R22.5 and 455/55R22.5 | Exact contact area and 3D contact stresses | 104.4 | Viscoelastic AC (creep test) | • WBT-445 was more damaging than DTA for subgrade and surface rutting<br>• WBT-455 caused as much damage as DTA<br>• Both WBTs were less damaging than DTA and might cause more fatigue cracking |

| | | | | | | |
|---|---|---|---|---|---|---|
| Kim et al. (2005) | AC: 6 in.; base: 6.7 in. | 425/65R22.5 and conventional 5R17.5DTA | Rectangular contact area. Uniform contact stress and equal to maximum vertical contact stress | 125 | Subgrade: Druvker-Prager model. Linear elastic AC | • WBT produced the highest vertical stress on top of subgrade<br>• WBT produced four times more permanent strain |
| Yoo et al. (2006) | AC: 7.4 in.; OGDL: 3 in.; base: 6 in.; subbase: 7 in. | 445/50R22.5 and DTA | Continuous moving load. Measured 3D contact stresses | 104.4 | Viscoelastic AC, linear granular | • Continuous moving load, interface friction, and 3-D contact stresses improve accuracy of modeling |
| Priest and Timm (2006) | AC: 6.7 in.; base: 6 in. | 445/50R22.5 and 275/80R22.5 | Comparison between experimental results at NCAT and mechanistic calculation using WESLEA (properties backcalculated by EVERCALC 5.0 | 120 | Linear elastic (backcalculation from FWD) | • Measurement showed similar stresses and strain for WBT and DTA; based on analytical result, WBT response was higher<br>• Based on WESLEA: WBT created 69% less fatigue life |
| Al-Qadi et al. (2008), Al-Qadi and Wang (2009a, 2009b, and 2009c) | Thin and thick | 455/55R22.5, 445/50R22.5, and 425/65R22.5, | Dynamic analysis, continuous moving load, and measured 3D contact stresses | 80-110 | Viscoelastic AC, and nonlinear granular material | • WBT produced higher long strain at bottom of AC and higher vertical stress on top of subgrade, and less compressive and vertical shear strains close to surface<br>• WBT-445 created less damage on highway pavements, but more on low-volume roads |

# 3 MEASURED TIRE-PAVEMENT CONTACT STRESSES/LOADS

The contact stresses/forces of the tires were measured by the Council for Scientific and Industrial Research (CSIR) in South Africa. A representative DTA, set of two new Michelin 275/80 R22.5 (Tread design XDN®2) tires, and WBT, single NG-WBT Michelin X One® tire of size 445/50 R22.5 (Tread design XDN®2), selected by the Rubber Manufacturer Association, were used in this study. This chapter describes the measuring equipment and testing program and provides an analysis of contact stresses.

## 3.1 STRESS-IN-MOTION EQUIPMENT

The dual Stress-In-Motion (SIM) Mk IV system used in this study for contact stress measurement consists of two SIM pad assemblies, each $33 \times 18.5$ in in nominal area. The single SIM pad assembly of the SIM Mk IV tire contact load/stress measurement system consists of an array of 21 instrumented installed across the center portion of the SIM pad assembly. In addition to the instrumented pin assemblies, supporting pins bore the test tire on both sides of the instrumented pins (approximately 1020 for each SIM pad) during SIM testing. These conical-shaped pins of an approximate height of 1.97 in were fixed to a 1.77-in-thick rigid steel base plate. Figure 3-1 shows the SIM system and sign convention.
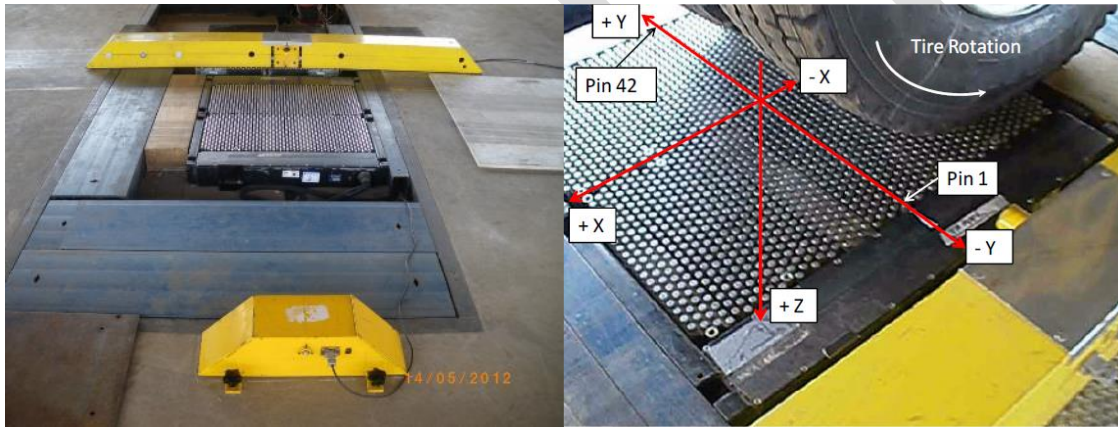


**Figure 3-1. Dual SIM Mk IV pad assembly and sign convention of contact stresses.**

In the current study, the test tires were fixed to the axle on the hydraulic loading test carriage of the Heavy Vehicle Simulator (HVS Mk III). The test tires were also fixed in the lateral position over the dual SIM pads for all measurements in the test series. Therefore, no lateral shifts were allowed during SIM testing. The vertical contact stresses were assumed positive in the vertical downward direction, while positive longitudinal contact stresses pointed in the traffic direction. The direction of positive transverse contact stresses can be inferred from the right-hand rule (Figure 3-1). The average tire speed was 0.75 mph and sampling frequency was 1001 Hz.

Static tire ink imprints were made using black roof paint on white paper under the HVS Mk III (Figure 3-2) to obtain prints for the target loads indicated in the test matrix. Photos were then taken of each case (per the test matrix) and scaled in Excel spreadsheets. To calculate the contact area, tire footprints were imported and properly scaled in AutoCAD.

## 3.2 TEST TIRES AND TEST MATRIX

Three-dimensional (3-D) tire-pavement contact stresses/loads were measured for the NG-WBT (445/50R22.5) and DTA (275/80R22.5). Four values of tire inflation pressure ($\sigma_o$) at 80, 100, 110, and 125 psi, and five tire loadings ($P$) at 6, 8, 10, 14, and 18 kip, were applied to the tires to measure the 3-D contact

12

stresses. In addition, differential inflation pressure was applied to DTA; one tire of the assembly was kept at 110 psi while two values, 60 and 80 psi, were applied to the other. Figure 3-3 presents the test tires, and Table 3-1 summarizes the test matrix.
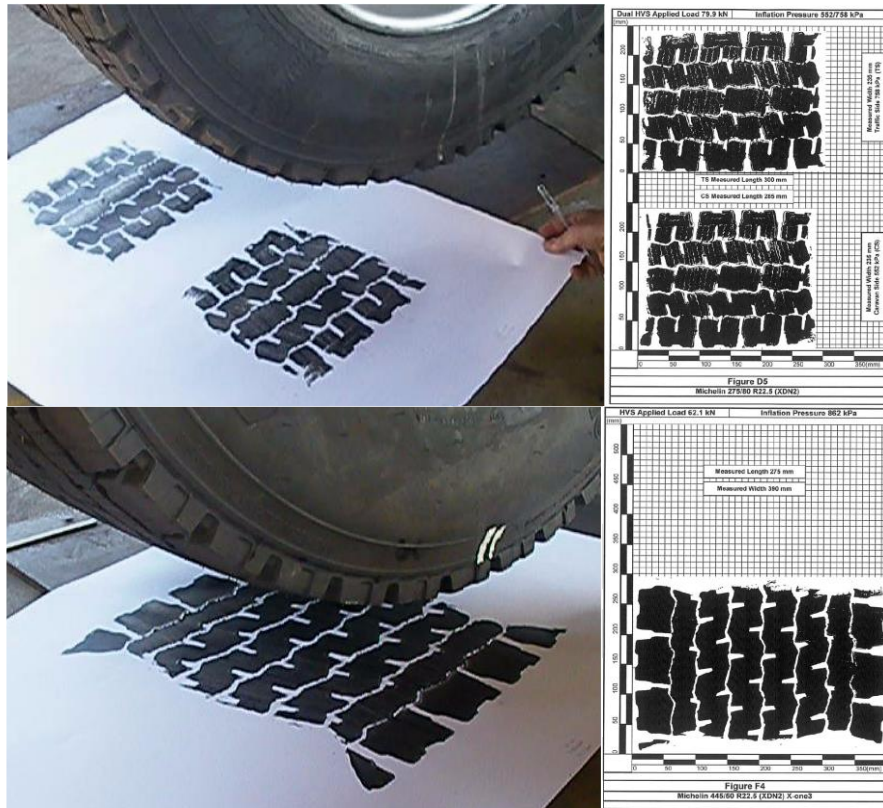


**Figure 3-2. Typical tire footprint for WBT and DTA.**



**Figure 3-3. Test tires: WBT and DTA.**

**Table 3-1. Test Matrix for WBT and DTA**

| Tire Type | Tire Inflation Pressure (kPa) | Tire Loading (kN) | | | | |
|---|---|---|---|---|---|---|
| WBT and Dual | 552.0 | 26.6 | 35.5 | 44.4 | 62.1 | 79.9 |
| WBT and Dual | 690.0 | 26.6 | 35.5 | 44.4 | 62.1 | 79.9 |
| WBT and Dual | 758.0 | 26.6 | 35.5 | 44.4 | 62.1 | 79.9 |
| WBT and Dual | 862.0 | 26.6 | 35.5 | 44.4 | 62.1 | 79.9 |
| Dual Only | 414.0/758.0* | 26.6 | 35.5 | 44.4 | 62.1 | 79.9 |
| Dual Only | 512.0/758.0* | 26.6 | 35.5 | 44.4 | 62.1 | 79.9 |

*Indicates differential inflation pressure. 1 kPa=0.145 psi, 1 kN=224.8 lb

## 3.3 THREE-DIMENSIONAL CONTACT STRESSES/LOADS

The SIM measurements were reported in .txt format. Each file included the readings of the 42 instrumented pins in one of the three directions and its own measuring test speed and applied SIM total load (in kN). Three repetitions of each loading case were reported. SIM load distribution measurements were reported in load units (N). Load values were converted to "effective contact stress" values by applying the "effective area" geometrical conversion factor of 0.388 in$^2$ to the load data. The conversion factor assumed full contact between the tire and the measuring pins (no treads) (De Beer et al., 1997).

The three repetitions of the experimental readings were filtered using the moving average method with a window size of 20 measurements. The same value was used for all data files, and it was selected based on the final smoothness and small shift of the data. After each repetition was filtered, average measurements were calculated. The distance along the tire contact patch was obtained using the sampling frequency and the speed of tire in each case. The filtered data and the three repetitions are given in Figure 3-4 along with a zoomed view showing the effect of the filter.
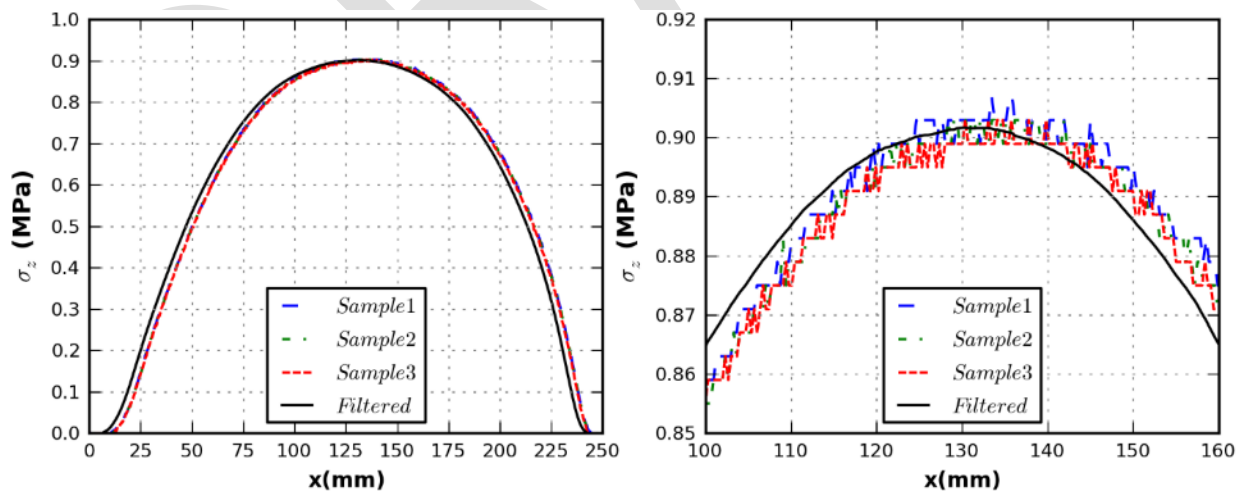


**Figure 3-4. Three repetitions and filtered output.**

In general, the shape of distribution of the vertical and transverse contact stresses ($\sigma_z$ and $\sigma_y$, respectively) was very similar, even though their magnitudes were different. $\sigma_z$ and $\sigma_y$ were zero at the beginning and end of the contact length and had a maximum value around the center of the tire. The location of the maximum of the vertical contact stresses were consistently close to the center. In some cases, $\sigma_y$ showed a

negative peak at the end of the contact length, whose magnitude was small when compared with the positive peak.

The variation of the longitudinal contact stresses ($\sigma_x$) varied according to the rib's location. When the rib was at the edge of the tire, the distribution had three peaks, two negative and one positive. The first negative peak was located at the tire's front part and its magnitude was comparable to the positive peak. The second negative peak was greater than the other two extreme values, and it was located at the end of the contact length. For non-edge ribs, the negative peak at the tire's end vanished and the distribution of $\sigma_x$ had two peaks only, one positive and one negative. In this case, the magnitude of the positive peak (rear part of the tire) was significantly higher than that of the negative peak. The value and location of the described peaks for each entry of the test matrix were extracted from every measuring pin. A graphical representation of typical distribution of 3-D contact stresses is shown in Figure 3-5. The contact length used in the analysis was determined based on $\sigma_z$, and it was defined as the distance at which $\sigma_z$ is not equal to zero in each measurement. For each loading case, the maximum value of contact length was selected.
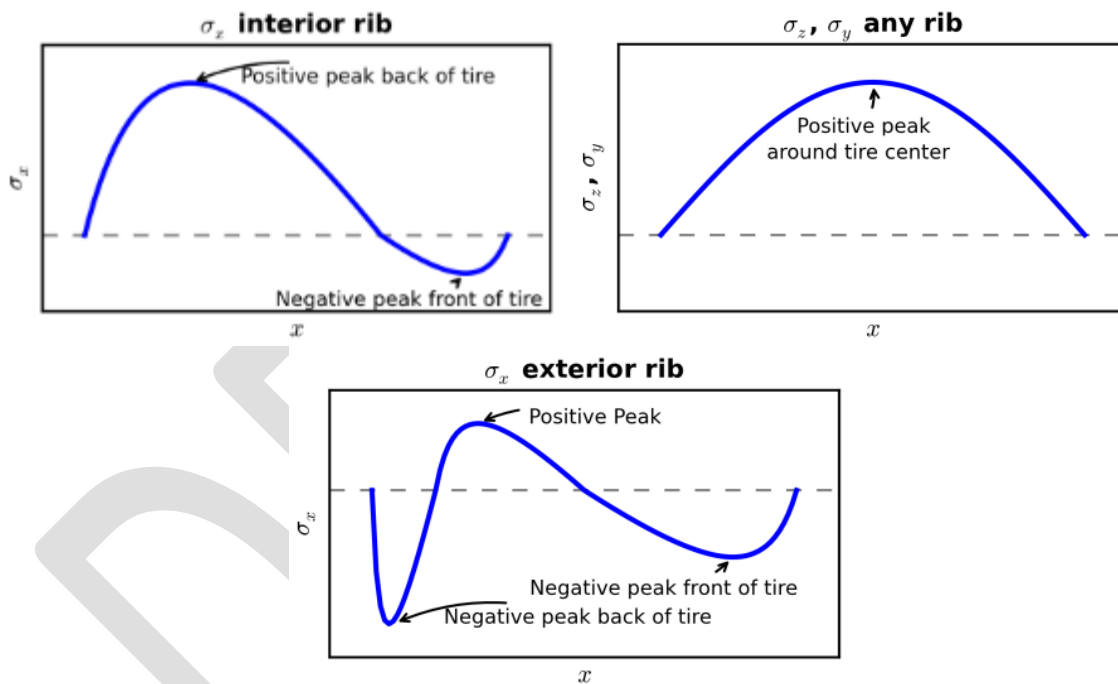


**Figure 3-5. Typical distribution of 3-D contact stresses.**

Once the measurements of each pin were filtered, a summary plot was created for each loading case. These plots included the variation of the 3-D contact stresses in every rib of WBT and DTA. It is important to notice the presence of more than one pin in one rib. A calculated contact patch is also included. Based on the contact area from AutoCAD and the contact length from the vertical contact stresses, the width of each rib was obtained. This width was divided by the number of pins in the corresponding rib to determine the influence width of a pin. A sample of the mentioned summary plots is presented in Appendix A. A total of 50 graphics was elaborated corresponding to 20 loading cases (four tire inflation pressure cases and five applied load cases) per tire (WBT and DTA) plus ten cases of differential tire inflation pressure.

In converting forces to stresses, the use of 0.388 in$^2$ as the influence area assumes that the tire is smooth (no ribs) and in full contact (tire rubber covers pin's influence area). However, these assumptions are invalid for the tires under analysis. Each tire comprises a number of ribs (8 and 10 ribs for WBT and DTA,

respectively). Moreover, each tread pattern is nonuniform. For instance, if a pin is located at a rib edge with partial contact, the area in contact between the pin and tire could potentially be half that of a pin at the middle of the rib, resulting in stress values double the ones computed with 0.388 in$^2$ as the contact area. To overcome the issue, the measurements were converted to nonuniform force per unit length variations along the length of the tire $x$ in the longitudinal $q_x(x)$, transverse $q_y(x)$, and vertical $q_z(x)$ directions. It is important to note that the shape of $q_x(x)$, $q_y(x)$, and $q_z(x)$ is the same as the contact stresses; however, the unit is force over distance.

The ratio of the load carried by each rib $P_i$ ($i$=1 to 8 for WBT and 1 to 10 for DTA) with respect to the applied load $P$ is presented in Figure 3-6 for three $P$ values (6, 10, and 18 kip) and four $S$ values (80, 100, 110, and 125 psi). For both tires, the shape of the distribution across the tire width changed as $P$ increased. when $P$ was low, the center ribs carried more load than the ones at the edges of the tire (*n* shape distribution across the patch). On the other hand, when $P$ was high, the center ribs carried less load than the ones at the edges of the tire (*m* shape distribution across the patch). The patterns were observed for all tire inflation pressure values considered. As the load increased, the percentage of load carried by the edge ribs became significantly higher for WBT than for DTA. This was due to the higher number of sidewalls of DTA compared with WBT (4 vs. 2). Furthermore, the variations of $P_i/P$ across all the ribs with various $S$ values for WBT were relatively close to each other for a given $P$ value. This finding indicates that the percentage of $P$ carried by each rib was not significantly affected by $S$. For DTA, however, the observation is valid only if the tire inflation pressure was less than or equal to 100 psi. Finally, it was noted that $P_i/P$ was generally higher for WBT than for DTA because of the lower number of ribs.

The magnitudes of the measured forces in three directions were also compared. Ratios of the maximum transverse $q_{y,max}$ and longitudinal $q_{x,max}$ forces per unit length with respect to vertical force $q_{z,max}$ for each rib are illustrated in Figure 3-7. The horizontal axis represents the combination of the number of ribs with various $S$ (e.g., WBT: 8 ribs by 4 $S$ equates to 32 case indicators). Even though a distinct relationship between the aforementioned ratios, tire type, $P$, and $S$ was not identified, two observations can be made regarding the relative magnitude of $q_{x,max}$ and $q_{y,max}$ with respect to $q_{z,max}$. On one hand, 85% of the data points fall in the range of $0.05 < q_{x,max}/q_{z,max} < 0.32$ for WBT, whereas the range changes to $0.05 < q_{x,max}/q_{z,max} < 0.26$ in the case of DTA. On the other hand, the variation range for $q_{y,max}/q_{z,max}$ becomes narrower in comparison with $q_{x,max}/q_{z,max}$. The tighter band enables a greater number of data points to be considered. For WBT, 90% of the data varies between 0.16 and 0.35, while the lower and upper limits change to 0.10 and 0.28 for DTA.

Based on these remarks, it can be concluded that the peak transverse and longitudinal forces per unit length (or contact stresses) are relatively higher for WBT than DTA. Additionally, regardless of the tire type, the magnitude of the tangential contact stresses are considerably high, thereby highly influencing pavement responses. Previous research has indicated the importance of considering transverse contact stresses, which have been linked to near-surface cracking and shear flow (Yoo and Al-Qadi, 2008). Since ratios $q_{x,max}/q_{z,max}$ and $q_{y,max}/q_{z,max}$ are different for both tires, same effect on pavement responses and performance may not be assumed, although both tires have the same applied load and tire inflation pressure.

## 3.4 CONTACT AREA AND CONTACT LENGTH

Characterization of the 3-D tire-pavement contact stresses was completed by accurate contact area and length. The contact area was obtained from static imprints, whereas the contact length was determined based on the variation of vertical contact stresses/loads. Figure 3-8 compares the change of the contact area $Ac$ and the average contact length $l$ of both tires. As expected, the contact area increased as $P$ reached 18 kip. In addition, $Ac$ was greater for DTA than WBT for all loading cases, and the contact area ratio between DTA and WBT was as high as 1.3. Regarding the average contact length, a strong linear relationship was

found when comparing $l$ of both tires. The average contact length for DTA was approximately 8% shorter than the contact length for WBT.

## 3.5    SUMMARY

Tire-pavement contact stresses/loads possess two important characteristics that significantly affect pavement responses: non-uniformity and three dimensionality. Experimental data for two truck tires, WBT and DTA, were measured and analyzed to emphasize the importance of considering realistic contact loads. The ratio of transverse and longitudinal contact forces with respect to the vertical contact force was found to be higher for NG-WBT than DTA. The results also indicated considerably high magnitudes of the transverse contact load, regardless of the tire type, which asserts its relevance in pavement analysis. Finally, the contact area of the DTA was as much as 30% higher than NG-WBT. The transfer-load mechanism of each tire is very different, and it is expected not to be constant across various geometries of WBT.
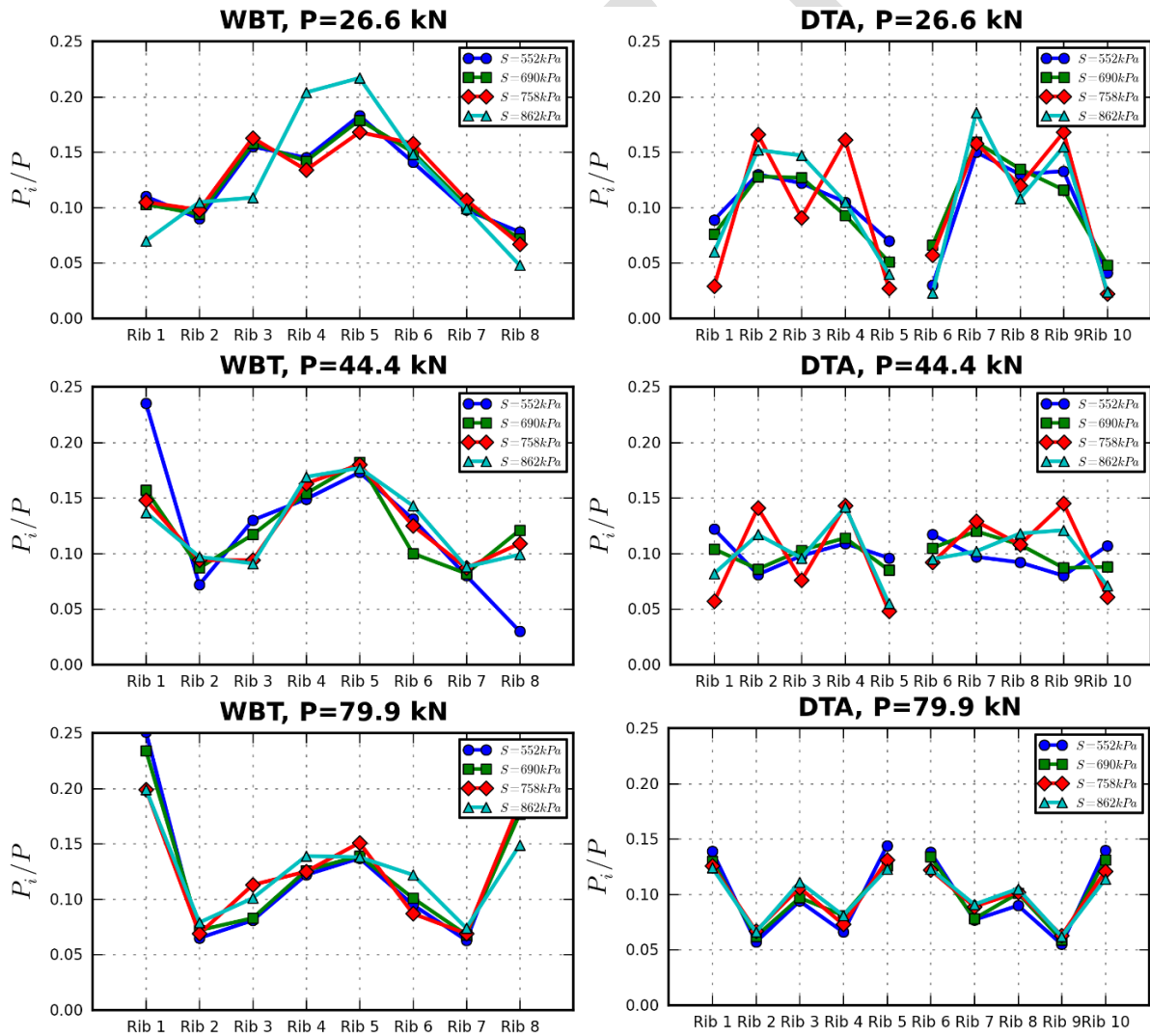


**Figure 3-6. Percentage of load carried by each rib.**

17
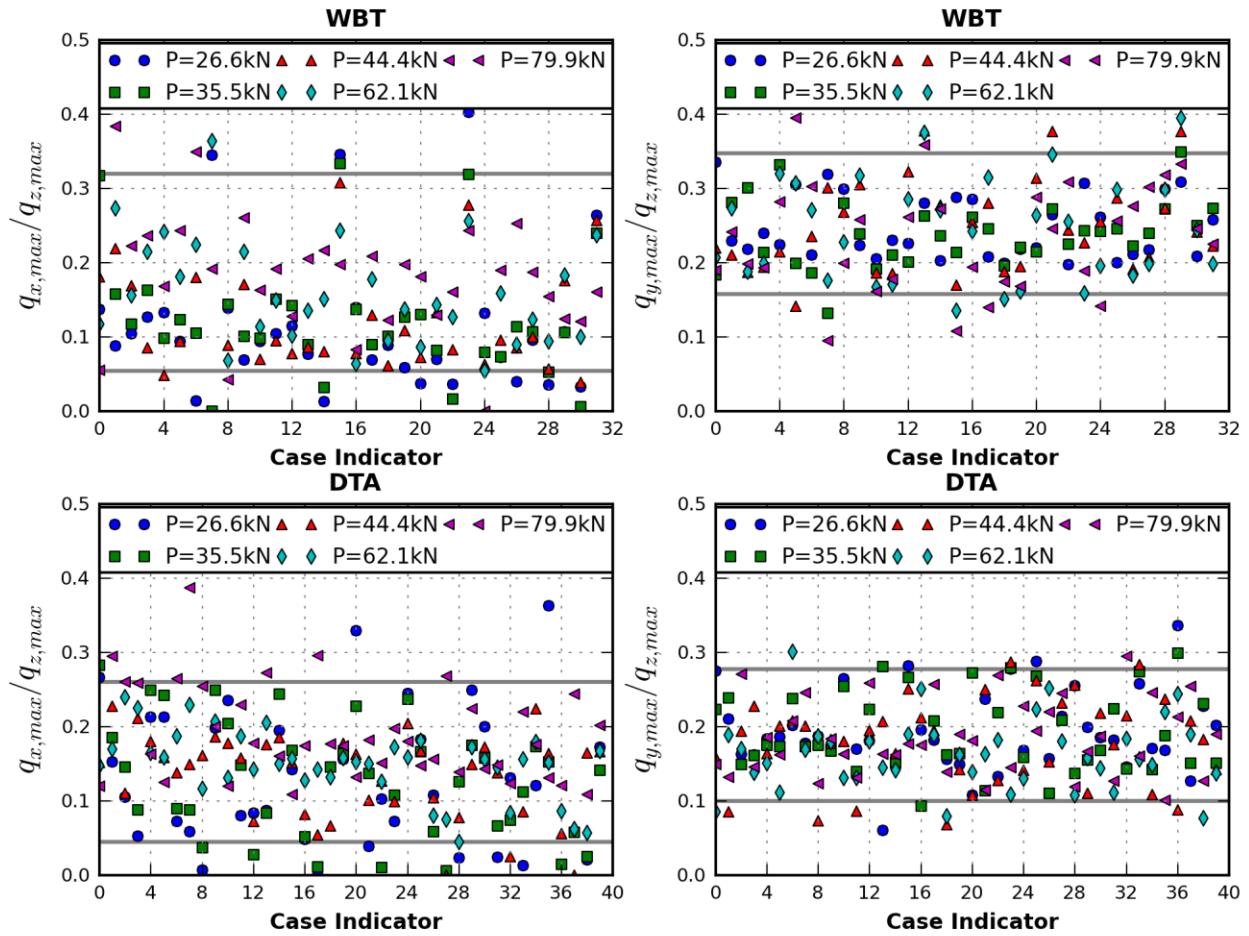
**Figure 3-7. Ratio of maximum contact forces.**
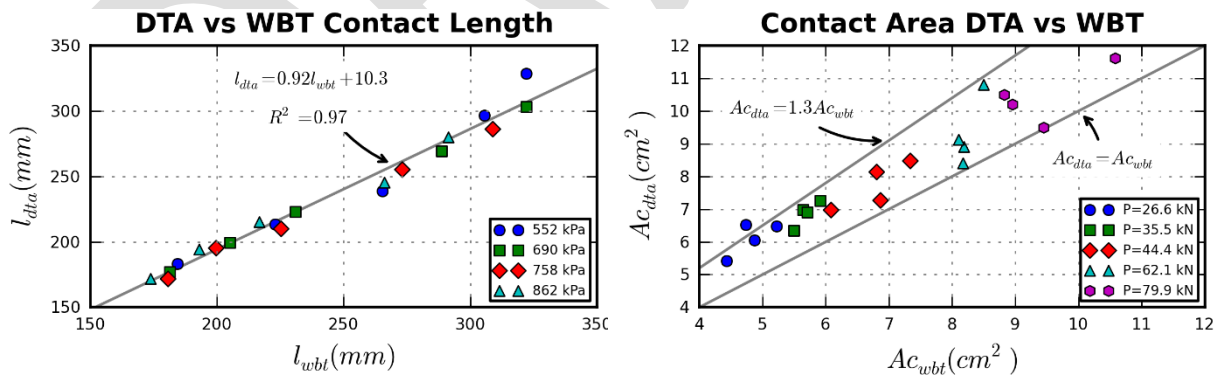


**Figure 3-8. Average contact length and contact area.**

# 4 NUMERICAL MODELING OF PAVEMENT STRUCTURES

The current design method for flexible pavements is based on the structural response that uses inappropriate assumptions. Static analysis of multilayer elastic systems simulates the tire load as a uniformly distributed vertical load on a circular contact area with the contact pressure equal to the tire inflation pressure, which does not accurately represent the actual phenomenon of a flexible pavement subjected to truck loading. Therefore, a numerical model was generated to mend the gap between reality and the current representation of a flexible pavement loading. This enabled a more robust analysis of pavement responses under various combinations of tire load and tire inflation pressure, pavement structure, and pavement material properties.

## 4.1 DEVELOPMENT OF THREE-DIMENSIONAL FINITE ELEMENT MODEL

One of the key aspects of the loading configuration highlighted in the analysis below is the three-dimensionality and non-uniformity of contact stresses, which is the main excitation for pavement responses. Other important factors considered in the simulations include linear viscoelastic material characterization of AC, nonlinear anisotropic behavior of the granular base (thin pavement only), dynamic analysis, contact stress measurements, continuous moving load, layer interaction, temperature profile in the AC layer, and an optimized mesh discretization with infinite elements.

### 4.1.1 Viscoelastic Asphalt Materials

The U.S. Federal Highway Administration (FHWA) Long-Term Pavement Performance (LTPP) Standard Release 26.0 provides material characterization of the AC layers. The group of tables used for this project are named, 'TST_ESTAR,' indicating the dynamic modulus, $|E^*|$, data of AC mixtures.

Dynamic modulus is a fundamental material property that defines AC stiffness as a function of temperature and loading time. The test data collected at different temperatures were shifted relative to the time of loading or loading frequency to align various curves to form a single master curve (FHWA, 2012). Using a sigmoidal fitting function solves shift factors simultaneously with the coefficients of the fitting function. It also eliminates irrational modulus value predictions when extrapolating outside the range of data, which occurs when a single polynomial model is used at high and low temperatures. Below is the sigmoidal function that the MEPDG uses to fit the dynamic modulus test data.

$$log(|E^*|) = \delta + \frac{\alpha}{e^{\beta - \gamma \log(\xi)}} \tag{3.1}$$

where: $|E^*|$ = dynamic modulus
$\xi$ = reduced angular frequency in Hertz
$\delta$ = minimum modulus value
$\alpha$ = span of modulus values
$\beta, \gamma$ = shape parameters

Additionally, the 'TST_ESTAR_MODULUS_COEFF' table contains the coefficients for the time-temperature shift factor function for $|E^*|$ as indicated in the following equation:

$$log(a_T) = \alpha_1 T^2 + \alpha_2 T + \alpha_3 \tag{3.2}$$

where: $a_T$ = AC time-temperature shift factor
$T$ = temperature of interest
$\alpha_1, \alpha_2, \alpha_3$ = regression coefficients

For initial filtration of the data provided, a 'MASTERCURVE_QUALITY' check was included in the 'TST_ESTAR_MODULUS_COEFF' table to differentiate between passing and failing data. A pass was

assigned whenever the confidence level was greater than 0.99 and ratio of standard error to standard deviation was less than 0.05. Data were further filtered to appropriately choose material properties through statistical analysis, wherein the minimum modulus value became the controlling factor as it represents the behavior of the material under slow loading condition and/or high temperature.

The remaining data, approximately 1000 data sets, was sorted in an increasing order according to the minimum modulus value. Using normal distribution, three tolerance intervals were considered 95.4%, 97.5%, and 99.8%, respectively. The chosen intervals denoted the percentage of values lying within their respective standard deviations. The three tolerance intervals determined the minimum and maximum modulus values for the wearing surface, intermediate, and base layers, respectively. Another parameter, the nominal maximum aggregate size (NMAS), was used to further refine the data. For the wearing surface, typical NMAS had to be 0.37 in or 0.5 in to be acceptable; whereas, typical NMAS had to be 1 in or 0.77 in for the intermediate layer and 1 in or 1.5 in for the base layer.

With the combination of the statistical tolerance level and typical layer NMAS, the data were refined to the most appropriate material properties. Based on the remaining data passing the multiple criteria, graphical comparison of the master curves led to the determination of appropriate material properties for the three AC layers to represent the 'weak' and 'strong' sets that will be used for numerical analysis. Additionally, based on visual inspection, an intersection and/or overlap between the data sets was prevented. Six appropriate data sets were finalized, wherein the top three master curves were chosen for the 'strong' set and the bottom three represented the 'weak' set (Figure 4-1). The corresponding sigmoidal function coefficients are presented in Table 4-1.
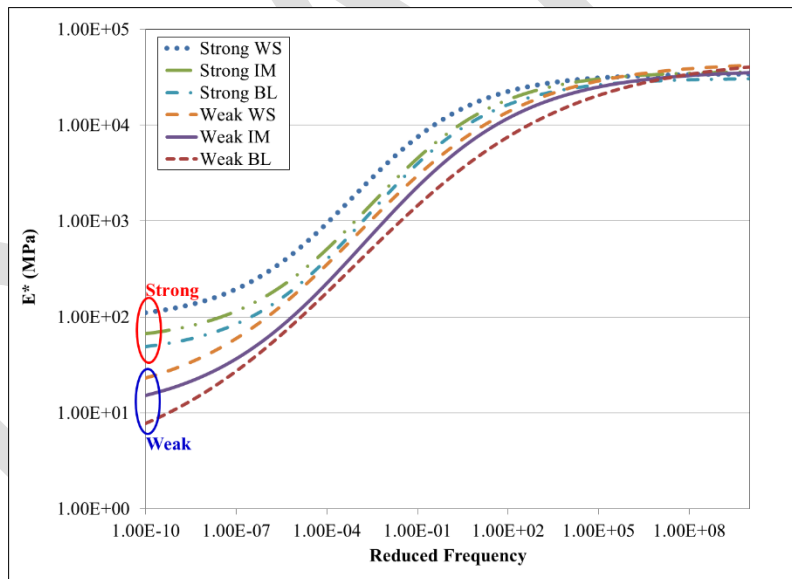


**Figure 4-1. AC linear viscoelastic material characterization.**

20

**Table 4-1. Sigmoidal Function Coefficients Representing AC Material Properties**

| Mix Type | Layer | $\delta$ | $\alpha$ | $\beta$ | $\gamma$ | $\alpha_1$ | $\alpha_2$ | $\alpha_3$ |
|---|---|---|---|---|---|---|---|---|
| Strong | WS* | 1.9654 | 2.5711 | -1.5622 | 0.4982 | 0.0002 | -0.1053 | 6.3104 |
| Strong | IM* | 1.7370 | 2.8245 | -1.2149 | 0.4656 | 0.0002 | -0.1053 | 6.3104 |
| Strong | BL* | 1.6067 | 2.8820 | -1.2840 | 0.4812 | 0.0004 | -0.1533 | 8.6010 |
| Weak | WS | 1.0967 | 3.5621 | -1.0530 | 0.3572 | 0.0002 | -0.1169 | 6.9827 |
| Weak | IM | 0.9694 | 3.6050 | -1.0560 | 0.3825 | 0.0001 | -0.0962 | 6.1900 |
| Weak | BL | 0.3505 | 4.3576 | -0.8800 | 0.2829 | 0.0009 | -0.2285 | 11.6836 |

*Note: WS = Wearing Surface, IM = Intermediate Layer and BL = Base Layer*

### 4.1.2 Granular Material

For the simulated interstate highway, the base and subgrade materials were considered linear elastic. The assumed behavior was considered appropriate as thickness of the AC layer reduces the stress-dependency of the granular layers. On the other hand, for the low-volume pavement cases, the base layer materials were considered nonlinear anisotropic, and the subgrade was assumed to be linear elastic.

To select appropriate strong and weak base layers, a database of 114 materials with appropriate nonlinear cross-anisotropic laboratory characterization was considered (Tutumluer, 2008). Pulse load was applied in the vertical and radial directions. Hence, cross-anisotropic characterization was possible. As part of the database, $k$-values were reported based on the Uzan model:

$$M_{rv} = k_1 \left(\frac{\theta}{p_o}\right)^{k_2} \left(\frac{\sigma_d}{p_o}\right)^{k_3} \tag{3.3}$$

where: $M_{rv}$ = resilient modulus in the vertical direction
$k_1, k_2, k_3$ = regression coefficients
$\theta = \sigma_1 + \sigma_2 + \sigma_3$ = bulk stresses
$\sigma_d$ = deviator stress
$p_o$ = unit reference pressure

It is known that the resilient modulus of granular materials depends on the stress level. To select appropriate weak and strong base materials, two stress levels (Table 4-2) were defined based on the field condition of base materials (Xiao et al., 2011).

**Table 4-2. Stress Level for Low and High Base Material Resilient Moduli**

| | Low (kPa) | Low (psi) | Low (kPa) | Low (psi) |
|---|---|---|---|---|
| $\sigma_3$ | 34.9 | 5.0 | 104.8 | 15.0 |
| $\sigma_d$ | 104.8 | 15.0 | 209.5 | 30.0 |
| $\sigma_1$ | 139.7 | 20.0 | 314.3 | 45.0 |
| $\sigma_2$ | 34.9 | 5.0 | 104.8 | 15.0 |
| $\theta$ | 209.5 | 30.0 | 523.9 | 75.0 |

Using the aforementioned stress levels and the $k$-values from the database, the resilient modulus for each material was calculated. The resilient moduli obtained for both stress states are presented in Figure 4-2. Assuming a normal distribution, the weak base material was selected as the one corresponding to the

21

average, minus two standard deviations ($\mu - 2\sigma = 9.8$ ksi) of the set of resilient modulus corresponding to low-stress level. Similarly, the strong base material corresponded to the closer value of the vertical resilient modulus of $\mu + 2\sigma = 47.3$ ksi. After materials selection, the laboratory data were used to determine the $k$-values based on the MEPDG model used in AASHTOWare.
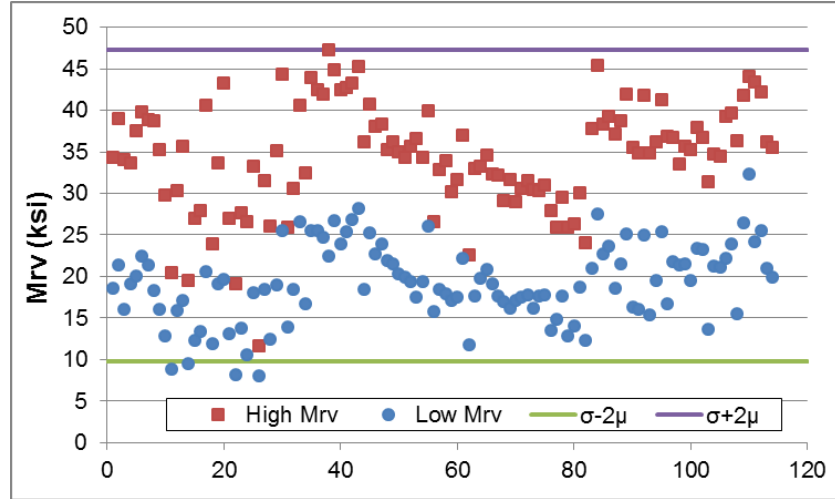


**Figure 4-2. Resilient modulus for low and high granular base stress levels.**

Pulse loading was not applied in the shear direction during laboratory testing; hence, a simplified procedure proposed by Tutumluer and Thompson (1998) was used to determine the $k$-values in the shear direction. The procedure is summarized as follows:

- In case of cross-anisotropy, the Uzan model becomes:

$$M_{rv} = k_1 \left(\frac{\theta}{p_o}\right)^{k_2} \left(\frac{\sigma_d}{p_o}\right)^{k_3} \tag{3.4}$$

$$M_{rh} = k_4 \left(\frac{\theta}{p_o}\right)^{k_5} \left(\frac{\sigma_d}{p_o}\right)^{k_6} \tag{3.5}$$

$$M_{rs} = k_7 \left(\frac{\theta}{p_o}\right)^{k_8} \left(\frac{\sigma_d}{p_o}\right)^{k_9} \tag{3.6}$$

Note that the database provides values for $k_1$ through $k_6$.

- Using a simplified method proposed by Tutumluer and Thompson (1998), the shear $k$-values for the shear direction are calculated as follows:

$$\begin{aligned}
k_7 &= -90.92 + 0.27k_1 + 305.34k_2 + 158.22k_3 \ (psi) \\
k_8 &= 0.2 + k_2 \\
k_9 &= -0.2 + k_3
\end{aligned} \tag{3.7}$$

- Using $k_7$, $k_8$, and $k_9$ and the stress levels of the vertical resilient modulus, the shear resilient modulus data can be computed.
- Regression parameters of the MEPDG model are obtained from the resilient moduli in the vertical, horizontal, and shear directions. The MEPDG version of the nonlinear cross-anisotropic model is as follows:

$$M_{rv} = k_1 p_a \left(\frac{\theta}{p_a}\right)^{k_2} \left(\frac{\tau_{oct}}{p_a} + 1\right)^{k_3}$$

$$M_{rh} = k_4 p_a \left(\frac{\theta}{p_a}\right)^{k_5} \left(\frac{\tau_{oct}}{p_a} + 1\right)^{k_6} \quad \text{(3.8)}$$

$$M_{rs} = k_7 p_a \left(\frac{\theta}{p_a}\right)^{k_8} \left(\frac{\tau_{oct}}{p_a} + 1\right)^{k_9}$$

The regression parameters for the selected materials are summarized in Table 4-3. In addition, Table 4-4 details calculation of the resilient modulus for both stress levels and materials, while Figure 4-3 compares the measured and calculated resilient moduli of the selected materials. The resilient modulus was 42.7 ksi in the vertical direction for the strong material at high stress level and 9.9 ksi for the weak material at low stress level. For thick pavements, the resilient modulus for weak and strong granular base was 20.0 ksi and 60.0 ksi, respectively.

**Table 4-3. Regression Parameters of the MEPDG Model for Weak and Strong Granular Materials**

| Direction | Weak | Weak | Weak | Strong | Strong | Strong |
|---|---|---|---|---|---|---|
| Vertical | $k_1$=453.3 | $k_2$=0.8858 | $k_3$=-0.5713 | $k_1$=869.6 | $k_2$=0.9785 | $k_3$=-0.5673 |
| Horizontal | $k_4$=282.4 | $k_5$=0.6701 | $k_6$=-1.1341 | $k_4$=596.6 | $k_5$=1.1419 | $k_6$=-1.3464 |
| Shear | $k_7$=310.3 | $k_8$=1.0297 | $k_9$=-1.1036 | $k_7$=389.1 | $k_8$=0.9083 | $k_9$=-0.2409 |

**Table 4-4. Summary Results of Resilient Moduli in the Vertical, Horizontal, and Shear Directions at Two Stress Levels**

| | Weak Low (MPa) | Weak High (MPa) | Weak Low (psi) | Weak High (psi) | Strong Low (MPa) | Strong High (MPa) | Strong Low (psi) | Strong High (psi) |
|---|---|---|---|---|---|---|---|---|
| $\sigma_3$ | 0.0349 | 0.1048 | 5.0 | 15.0 | 0.0349 | 0.1048 | 5.0 | 15.0 |
| $\sigma_d$ | 0.1048 | 0.2095 | 15.0 | 30.0 | 0.1048 | 0.2095 | 15.0 | 30.0 |
| $\sigma_1$ | 0.1397 | 0.3143 | 20.0 | 45.0 | 0.1397 | 0.3143 | 20.0 | 45.0 |
| $\sigma_2$ | 0.0349 | 0.1048 | 5.0 | 15.0 | 0.0349 | 0.1048 | 5.0 | 15.0 |
| $\theta$ | 0.2095 | 0.5239 | 30.0 | 75.0 | 0.2095 | 0.5239 | 30.0 | 75.0 |
| $p_a$ | 0.1000 | 0.1000 | 14.3 | 14.3 | 0.1000 | 0.1000 | 14.3 | 14.3 |
| $t_{oct}$ | 0.0494 | 0.0988 | 7.1 | 14.1 | 0.0494 | 0.0988 | 7.1 | 14.1 |
| $M_{rv}$ | 69.41 | 132.75 | 9937.2 | 19006.3 | 142.8 | 297.7 | 20447.4 | 42624.8 |
| $M_{rh}$ | 29.41 | 39.30 | 4210.0 | 5626.9 | 80.88 | 156.75 | 11579.9 | 22442.3 |
| $M_{rs}$ | 42.68 | 80.00 | 6110.7 | 11453.4 | 69.16 | 148.40 | 9901.9 | 21246.4 |
| $M_{rh}/M_{rv}$ | 0.42 | 0.30 | 0.42 | 0.30 | 0.57 | 0.53 | 0.57 | 0.53 |
| $M_{rs}/M_{rv}$ | 0.61 | 0.60 | 0.61 | 0.60 | 0.48 | 0.50 | 0.48 | 0.50 |
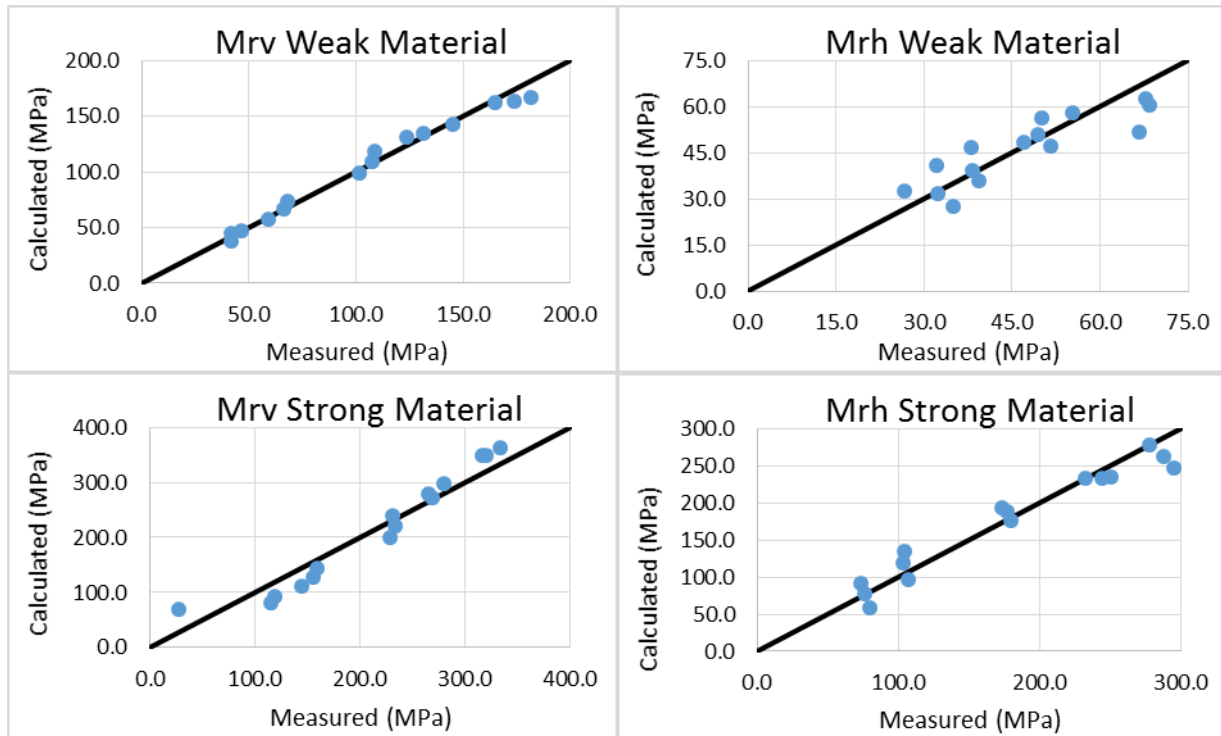
**Figure 4-3. Comparison between measured and calculated resilient moduli.**

### 4.1.3 Implicit Dynamic Analysis

In pavement analysis, three approaches are used to consider truck loading: i) static, ii) quasi-static, and iii) dynamic transient analysis. Conventionally, static loading is considered in multilayer elastic analysis. The quasi-static approach, on the other hand, incorporates the moving load concept at subsequent positions along the pavement at a given time step, wherein each load step is assumed to be one position. However, neither the inertial or damping effect nor the frequency-dependence of the material properties are considered in this approach. Therefore, the most suitable approach is the dynamic transient analysis, which takes into account the aforementioned factors.

When considering dynamic transient loading on a pavement system, a structural dynamic problem, rather than a wave propagation problem, arises as the wave propagation speed in a flexible pavement structure is significantly less than vehicle speed (OECD, 1992). This calls for a dynamic equilibrium equation, which can be solved using either an implicit or explicit direct integration method. For the frequencies given in this study, an implicit method would be more effective (Bathe, 1996).

For a dynamic analysis, the energy dissipation mechanisms dictate that a damping factor, friction factor, or viscoelastic material behavior be implemented. Hence, the AC layers do not require a damping factor due to the given linear viscoelastic material characterization. On the contrary, Rayleigh damping is used for the granular materials, where the mass proportional damping, $\alpha$, and stiffness proportional damping, $\beta$, are assumed to be 3.1416 and $7.95 \times 10^{-4}$, respectively (Wang, 2011).

### 4.1.4 Three-Dimensional Contact Stresses

Measured contact loads/stresses were used in the pavement model to represent the three-dimensionality and non-uniformity of tire loading. In conventional pavement analysis, only vertical pressure is considered and is made equal to the tire inflation pressure. Traditionally, the contact area is also assumed to be circular,

which leads to poor correspondence to the reality of pavement loading. A detailed analysis and description of the contact stresses are provided in the following chapter.

### 4.1.5  Continuous Moving Load

In order to simulate a continuous tire movement over the pavement structure at a specified speed, the tire loading was gradually shifted over the total loading area in the longitudinal direction (simulated traffic direction) until a single pass was completed. As indicated in Figure 4-4, the initial step included the span of the varying contact stresses over the tire imprint area, which then shifted over onto the next set of elements, while maintaining the same number of elements governed by the load.

Based on Yoo et al. (2008), the moving wheel load length in the longitudinal direction needs to be approximately 39.4 in to appropriately observe the continuous moving load effect on the pavement structure. To define the length of the loading area, the element size in the loading area was determined to be 0.79 in and the number of element steps was determined to be 16, moving three elements in every step. Additionally, the length of the tire was considered in the total length of the loading area.
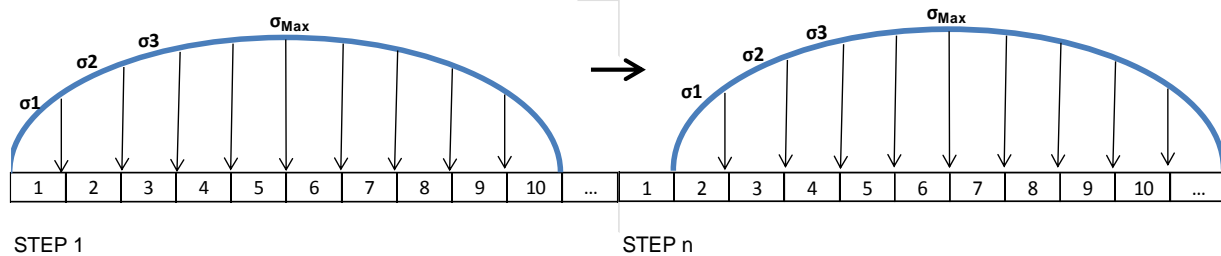


**Figure 4-4. Step loading of the tire imprint over 3D-FE model.**

Initially, tire loading was shifted one element at a time. However, it was necessary to evaluate the effect of load shifting over a larger span of elements to reduce computational time. Six cases were considered: 1, 2, 3, 4, 6 and 12 elements span. Moving the load one element at a time captured the most detailed and least incremental step; therefore, it was considered as a reference case. Table 4-5 indicates the results of an example analysis including the 'wall time' and percentage of error between the critical strains. Although the percentage of error between the cases did not exceed 5%, it was necessary to capture the utmost accuracy of the critical responses. The critical strain responses are presented in Figure 4-5. With the balance of low computational time and accuracy, the number of loading steps chosen for the 3-D FEM model was 16, wherein each step spans over three elements.

**Table 4-5. Effect Step Element Span for a Continuous Moving Load on the Critical Strains**

| Steps | No. of Elements | Wall Time | Error (%) | Error (%) | Error (%) | Error (%) | Error (%) | Error (%) |
|---|---|---|---|---|---|---|---|---|
| | | (hr.) | $\varepsilon_{11botAC}^{+}$ | $\varepsilon_{33botAC}$ | $\varepsilon_{11topAC}$ | $\varepsilon_{33topAC}$ | $\varepsilon_{23midAC}$ | $\varepsilon_{22topSG}$ |
| 4 | 12 | 2.79 | 0.353 | -0.101 | 0.135 | -1.383 | -0.878 | -0.233 |
| 8 | 6 | 5.01 | 0.583 | 1.764 | 0.599 | 0.352 | 0.169 | 4.345 |
| 12 | 4 | 7.16 | 0.474 | 1.719 | 0.741 | 0.464 | 0.455 | 3.179 |
| **16** | **3** | **9.09** | **0.416** | **1.653** | **0.857** | **0.499** | **0.686** | **3.021** |
| 24 | 2 | 13.23 | 0.381 | 1.228 | 0.962 | 0.366 | 0.816 | 2.411 |
| 48 | 1* | 21.27 | -- | -- | -- | -- | -- | -- |

*Assumed Reference*
+*Parameters defined in Chapter 5*

### 4.1.6 Layer Interaction

Defining the interaction between pavement layers is critically important as it affects pavement response to load excitation. The interface reflected a tied interaction between the AC layers. A Coulomb friction model was implemented for the AC to base and base to subgrade interfaces. The model assumes that the resistance of movement is proportional to the normal stress at the interface. A tolerance level was set for the shear strength, and when the two bodies passed the tolerance level, they slid relative to each other. For this scenario, the frictional stress was assumed to be constant. The proportionality of the friction coefficient to the allowed maximum shear stress (strength) and normal stress is defined by the following equation:

$$\mu = \frac{\tau_{max}}{\sigma} \tag{3.9}$$

where: $\tau_{max}$ = the allowed maximum shear stress prior to relative sliding of layers

$\sigma$ = the normal stress at the interface
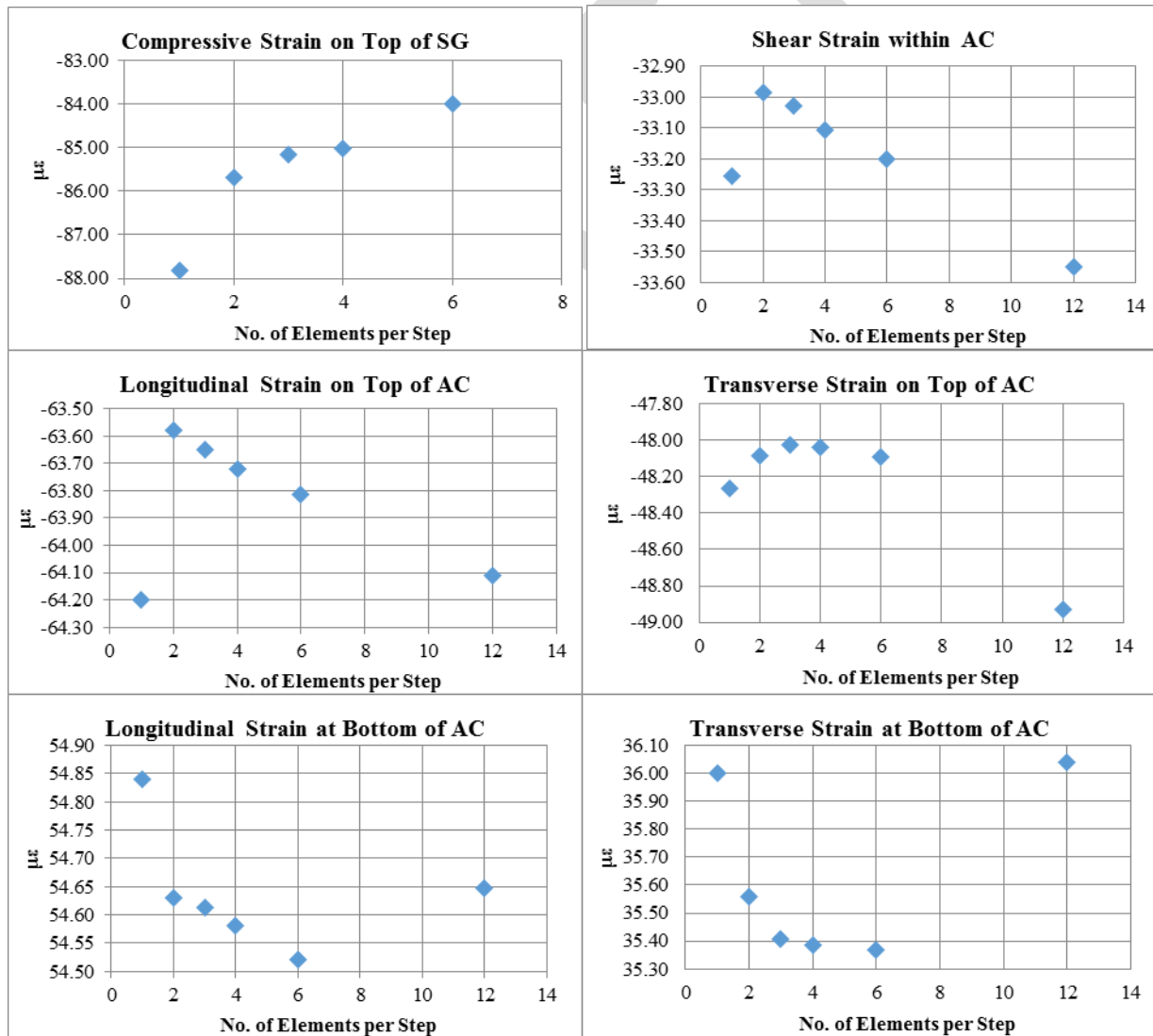


**Figure 4-5. Effect of the number of elements per step on critical strains.**

### 4.1.7 Temperature Profile

The viscoelastic material characterization of AC invokes the importance of temperature in this study. Depending on the environmental conditions, pavement responses vary significantly in the asphalt layer. At low temperature, AC stiffness tends to increase, whereas it decreases at high temperature. Hence, temperature directly affects pavement responses.

However, imposing a constant temperature throughout the AC layers inaccurately bounds the problem and can lead to erroneous results. Aside from capturing sensitivity to temperature, it is also pertinent to consider the temperature gradient within the AC layer. In addition, the time of the day significantly impacts pavement temperature. Based on a two-layer system analysis, consisting of AC and granular base, a temperature profile was derived. An initial temperature was defined on the surface of the AC layer as the reference temperature. The resulting temperature distribution is a function of the AC layer thickness, initial temperature, thermal conductivity and diffusivity of the AC and granular material, and discrete pavement depths.

## 4.2 SIMULATED PAVEMENT STRUCTURES

The pavement structure factorial consists of two conventional roadway types, low-volume road and interstate highway. The thicknesses vary between two extreme conditions, as the artificial neural network (discussed later) has a robust capability to accurately interpolate within the problem domain. Thickness variations for the two structures are summarized in Table 4-6.

**Table 4-6. Pavement Structure Factorial**

|  | Low-Volume | Interstate Highway |
|---|---|---|
| Wearing Surface | 75 and 125 mm* | 25 and 62.5 mm |
| Intermediate | 75 and 125 mm* | 37.5 and 100 mm |
| Binder | 75 and 125 mm* | 62.5 and 250 mm |
| Granular Base | 150 and 600 mm | 150 and 600 mm |

*Note: Low-volume road cases consider only one AC layer*

## 4.3 MESH VERIFICATION

To achieve an acceptable level of accuracy, the three-dimensional finite element (3-D FE) solution must converge into a continuum model solution and the stress transition across element must be adequately continuous. One measure that may help meet the aforementioned criteria is mesh refinement. Selection of the element thickness at the interface between layers of a pavement system affects the continuity of stresses. Therefore, a robust sensitivity analysis must be carried out.

The first task in the mesh sensitivity analysis is to determine the element size in the tire loading area. It is worth noting that the element size can be analogous to the computational time in the sense that a decrease in element size will generate an increase in computational time. In addition, infinite boundary must be used around the sides and bottom of the 3-D FE model to simulate the stresses and strains dissipating to nearly zero at the boundary.

### 4.3.1 Vertical Mesh Refinement

It was previously determined that the mesh thickness of the first element, from the top surface of the AC layer, should be 0.4 in or smaller, and that the top element of the subgrade layer must range between 30 and 1.97 in (Al-Qadi et al., 2008).

Although most critical strain results indicate that decrease of the element size leads to more accurate results, throughout the iterations, a plateau value was reached wherein the difference in the strain value from BISAR and FEM model became negligible. Therefore, it was decided that the range of the element size on top of

the subgrade should be reduced to 2 in or less for higher accuracy. It was also decided that appropriate transitions between the elements throughout the remaining layers should be considered; the element thickness from one layer to another should be almost equal. Iterations consist of altering the number of elements and bias until the desired convergence is reached for the "coarsest" mesh. A relatively coarse mesh would limit computational time while maintaining accuracy within acceptable limits.

### 4.3.2 Longitudinal and Lateral Mesh

Tire-pavement contact area, which initially defined the longitudinal and lateral mesh properties, was extended using mesh sensitivity analysis to ensure that the responses tended to zero on the model boundaries. Based on previous studies, the element length of 0.79 in along the 39.4 in wheel path is adequate for the critical strain values to become nil (Yoo et al., 2008). However, the selected wheel path length of 39.4 in was inadequate for capturing a full pulse duration. Two models were generated to investigate the impact of wheel path length on pavement responses, wherein the length varied between 39.4 and 78.7 mm. Specifically, the pavement structure was held constant with an AC thickness of 16.2 in and a base of 5.9 in The load and tire inflation pressure applied were 18 kip and 125 psi, respectively.

The results revealed a shift in the vertical stress as the wheel path increased from 39.4 to 78.7 in The model with 78.7 in wheel path failed to capture the full pulse duration as the tail of the corresponding curve in Figure 4-6 did not reach zero, thereby implying that a larger wheel path is needed for this purpose. It is worth noting that the spike near time, $t$=0, for the vertical compressive stress is induced by the initial impact of loading the model.
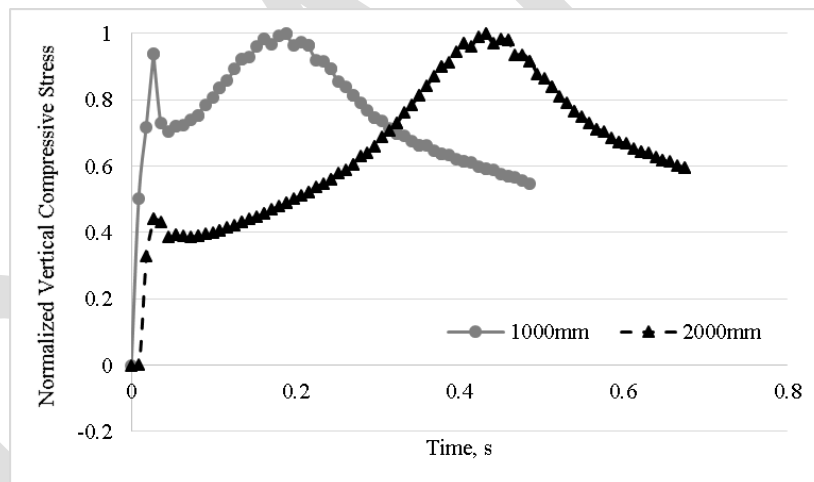


**Figure 4-6. Pulse duration results for the two varied wheel paths.**

However, to simulate full pulse duration, starting from zero and tending back to zero after a peak, significant computational effort was required. For this criteria, increasing the wheel path further than 78.7 in was not feasible for all simulation cases considered in this study. In addition, because the maximum pavement response values were not significantly affected by the assumed wheel path length of 39.4 in., the FE model was reasonably accurate as the remainder of the analysis would be based on critical/maximum point responses.

As shown in Figure 4-7, the critical responses were generally low, except for the shear strain in the base layer, which differed up to 12.6%. Therefore, a wheel path length of 39.4 in was appropriate as it did not adversely impact critical pavement responses, which are required inputs for pavement damage quantification.

In terms of pulse duration, the truncated version was used wherein the ascending part only fits the revised haversine equation, and data were extrapolated to a normalized vertical compressive stress of 0.1. Duration of the half pulse was then multiplied by two under the assumed pulse symmetry (Fakhri et al., 2013).

The lateral meshing was controlled by the width of the rib and groove partition of the specified tire pressure and loading condition. Longitudinal and lateral meshing was further refined by altering the dimensions of the biased elements surrounding the loading area and narrowing the thickness of the element across the depth of the pavement structure.
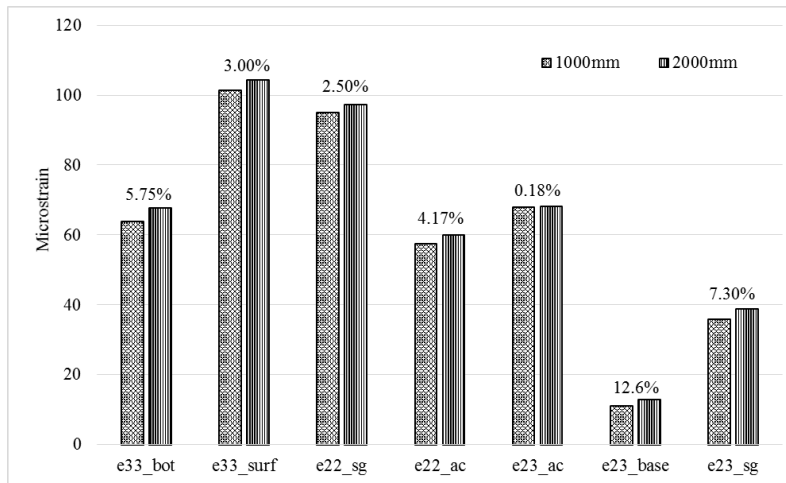


**Figure 4-7. Pavement response comparison for varying wheel path lengths.**

To simulate the characteristics of perpetual interstate roadways, a finite element model with a significantly large domain must be created, but it is computationally inefficient. Therefore, infinite elements, which simulate far-field boundary conditions, were placed on the vertical external sections and the bottom of the subgrade. Proper transitions from the finite section of the model to the infinite elements were also implemented.

Following a multitude of iterations, it was determined that reduction of the elements with bias in both longitudinal and lateral directions would be appropriate to create a smooth transition to the infinite boundary, while still maintaining accuracy and reducing computational time (Figure 4-8). There were two transition zones from the loading area. The first transition included biased elements in the longitudinal and transverse directions, with lengths $L1$ and $B1$, respectively. The second transition area consisted of a single finite element around the model in the longitudinal and transverse directions, which were defined as $L2$ and $B2$ lengths, respectively, and were placed adjacent to the infinite boundary. The transitional area reduced the required finite elements as the bias imposed larger sized elements towards the infinite boundary.
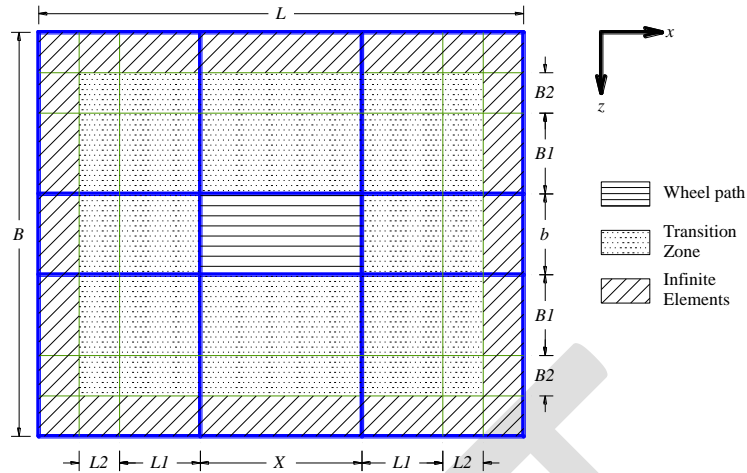
**Figure 4-8. Mesh definition in plan view.**

### 4.3.3 Verification of the Constructed Mesh Combination

Based on the continuum model theory, vertical stresses should be continuous between pavement layers. Computational time and data storage space requirements should be considered, provided that the results stay within acceptable bounds of accuracy. As the element size within the domain decreased, computational time and data storage space increased. To evaluate accuracy of the results, the FE model with varying mesh element thicknesses throughout different pavement layers was compared with the results obtained from BISAR, which is based on the multilayer elastic theory that uses an axisymmetric model. The two approaches followed the same vehicular loading, material properties, and pavement structure.

The comparison was simplified with a static and uniform load over a circular contact patch and linearly elastic material to minimize possible computational errors. In order for the FE model to be directly comparable to BISAR, layer interactions were 'tied' to preserve continuity between layers for convergence purposes. The results of the statically linear elastic case showed negligible errors, thus indicating that the constructed meshing combination is appropriate.

BISAR is considered inadequate for simulating the cross-anisotropic behavior of granular layers, continuous moving load, and realistic interfacial friction properties between pavement layers. In BISAR, the response locations must be determined a priori to running the analysis, whereas the FE model is capable of simulating the analysis and responses throughout the entire model without being pre-defined.

The goal was to reach a level of accuracy of 5% or better. Using BISAR solution as reference, the pavement responses of the two methods were compared at the same location. Being the main inputs in the transfer functions for pavement damage evaluation, critical strains were investigated. The vertical and longitudinal mesh parameters were altered at each iteration until the relative comparison of strain values met the defined level of accuracy.

To compare the results obtained from the FE software, ABAQUS, and BISAR, an axisymmetric model was implemented in ABAQUS. The final mesh was then transformed into the 3-D domain and a similar check was done. The results are presented in Table 4-7 and Table 4-10. Generally, the percentage of difference was less than 5%. The final mesh configuration (i.e., layer thickness, number of elements, and bias) for the interstate and low-volume pavement structures are presented in Table 4-11 and Table 4-12.

30

**Table 4-7. Comparison of Results from BISAR and ABAQUS Simulations for Interstate Highway Pavements and AC=5 in.**

|  | ABAQUS B=6 in. | BISAR B=6 in. | Diff. (%) B=6 in. | ABAQUS B=24 in. | BISAR B=24 in. | Diff. (%) B=24 in. |
|---|---|---|---|---|---|---|
| **Tensile strain bottom of AC** | 65.6 | 68.1 | 3.7 | 61.1 | 63.8 | 4.2 |
| **Vertical strain top of subgrade** | 300.0 | 295.5 | 1.5 | 157.4 | 159.7 | 1.4 |
| **Shear AC** | 19.4 | 19.2 | 1.0 | 19.8 | 19.4 | 1.8 |
| **Shear base** | 73.3 | 70.0 | 4.7 | 74.9 | 74.7 | 0.3 |
| **Shear subgrade** | 83.2 | 88.2 | 5.7 | 53.7 | 56.6 | 5.1 |

Note: 25.4 mm=1 in.

**Table 4-8. Comparison of Results from BISAR and ABAQUS Simulations for Interstate Highway Pavements and AC=16.2 in.**

|  | ABAQUS B=6 in. | BISAR B=6 in. | Diff. (%) B=6 in. | ABAQUS B=24 in. | BISAR B=24 in. | Diff. (%) B=24 in. |
|---|---|---|---|---|---|---|
| **Tensile strain bottom of AC** | 9.9 | 9.4 | 5.2 | 9.1 | 9.7 | 6.3 |
| **Vertical strain top of subgrade** | 36.0 | 36.1 | 0.3 | 27.9 | 27.8 | 0.3 |
| **Shear AC** | 7.3 | 7.6 | 4.0 | 7.6 | 7.3 | 4.2 |
| **Shear base** | 6.8 | 6.6 | 3.3 | 7.9 | 8.0 | 1.3 |
| **Shear Subgrade** | 8.5 | 8.1 | 5.0 | 7.8 | 8.2 | 4.8 |

Note: 25.4 mm=1 in.

**Table 4-9. Comparison of Results from BISAR and ABAQUS Simulations for Low-Volume Roads and AC=3 in.**

|  | ABAQUS B=6 in. | BISAR B=6 in. | Diff. (%) B=6 in. | ABAQUS B=24 in. | BISAR B=24 in. | Diff. (%) B=24 in. |
|---|---|---|---|---|---|---|
| **Tensile strain bottom of AC** | 126.5 | 133.8 | 5.5 | 105.4 | 111.3 | 5.3 |
| **Vertical strain top of subgrade** | 817.9 | 836.8 | 2.3 | 354.6 | 364.4 | 2.7 |
| **Shear AC** | 27.0 | 27.4 | 1.4 | 25.5 | 26.1 | 2.3 |
| **Shear base** | 193.0 | 190.4 | 1.4 | 179.1 | 170.7 | 4.9 |
| **Shear Subgrade** | 269.9 | 276.6 | 2.4 | 128.7 | 135.1 | 4.8 |

Note: 25.4 mm=1 in.

**Table 4-10. Comparison of Results from BISAR and ABAQUS Simulations for Low-Volume Roads and AC=5 in.**

|  | B=6 in. | | | B=24 in. | | |
|---|---|---|---|---|---|---|
|  | ABAQUS | BISAR | Diff. (%) | ABAQUS | BISAR | Diff. (%) |
| Tensile strain bottom of AC | 63.9 | 67.2 | 4.9 | 56.6 | 59.5 | 4.9 |
| Vertical strain top of subgrade | 341.0 | 348.9 | 2.3 | 206.5 | 212.6 | 2.9 |
| Shear AC | 17.0 | 17.0 | 0.2 | 16.4 | 16.5 | 0.7 |
| Shear Base | 68.4 | 67.9 | 0.8 | 75.2 | 73.0 | 3.0 |
| Shear Subgrade | 101.6 | 103.9 | 2.2 | 70.6 | 75.8 | 6.9 |

Note: 25.4 mm=1 in.

**Table 4-11. Interstate Highway Mesh Configuration**

|  | AC=5 in., B=6 in. | AC=5 in., B=24 in. | AC=16.2 in., B=6 in. | AC=16.2 in., B=24 in. |
|---|---|---|---|---|
| Wearing course | 25.0 | 25.0 | 62.5 | 62.5 |
| Intermediate course | 37.5 | 37.5 | 100.0 | 100.0 |
| Binder course | 62.5 | 62.5 | 250.0 | 250.0 |
| Base | 150.0 | 600.0 | 150.0 | 600.0 |
| Subgrade | 4225.0 | 3775.0 | 3937.5 | 3487.5 |
| Wearing course | 4 @ 1 | 4 @ 1.1 | 5 @ 1.2 | 5 @ 1.2 |
| Intermediate course | 5 @ 1.2 | 5 @ 1.0 | 6 @ 1.4 | 6 @ 1.4 |
| Binder course | 7 @ 1.15 | 7 @ 1.2 | 12 @ 1.0 | 9 @ 1.0 |
| Base | 12 @ 1.5 | 25 @ 1.0 | 7 @ 1.0 | 22 @ 1.0 |
| Subgrade | 15 @ 75.0 | 15 @ 30.0 | 15 @ 30.0 | 15 @ 25.0 |

Note: 25.4 mm=1 in.

**Table 4-12. Low-Volume Road Mesh Configuration**

| Low-Volume Pavement Structure | Thickness (mm) | | | |
|---|---|---|---|---|
|  | AC75_B150 | AC75_B600 | AC125_B150 | AC125_B600 |
| Surface | 75.0 | 75.0 | 125.0 | 125.0 |
| Base | 150.0 | 600.0 | 150.0 | 600.0 |
| Subgrade | 4275.0 | 3825.0 | 4225.0 | 3775.0 |
|  | Number of Elements @ Bias | | | |
|  | AC75_B150 | AC75_B600 | AC125_B150 | AC125_B600 |
| Surface | 12 @ 1.0 | 12 @ 1.0 | 15 @ 1.2 | 15 @ 1.2 |
| Base | 12 @ 1.7 | 25 @ 1.3 | 12 @ 1.7 | 25 @ 1.0 |
| Subgrade | 15 @ 70.0 | 15 @ 30.0 | 15 @ 50.0 | 15 @ 30.0 |

Note: 25.4 mm=1 in.

## 4.4 PAVEMENT RESPONSE

The numerical model produces a database of stresses and strains at any location within the problem domain. However, the essential output values were the maximum and minimum strains at each layer, vertical compressive pressure at every layer, and von Mises stress within the AC layer. Within this subdomain, the critical responses include the following:
- Tensile strain at the surface of AC for near-surface cracking
- Tensile strain at the bottom of the AC for bottom-up cracking
- Compressive strain for rutting (AC and granular layers)
- Shear strain within the AC layer

### 4.4.1 Thick Pavement Damping

After simulations for the thick pavement were completed, it was determined that appropriate damping parameters were not adequately applied to the thick pavement model. This section explains the correction process.

To account for damping and mass inertia effect, damping properties must be defined for all pavement layers in the finite element model. The sources of damping could be an arbitrary damping factor, friction factor, or viscoelastic material behavior. Given that the asphalt layers are characterized by viscoelasticity, the structural damping is appropriately accounted for. However, the granular layers are defined with elastic moduli values, which does not consider dissipation.

Using the Rayleigh damping model in ABAQUS, energy dissipation can be considered for the elastic granular base and subgrade layers. Two damping coefficients are required for the Rayleigh model, $\alpha$ and $\beta$, which are dependent on a proper damping ratio. Based on Wang (2011), the critical damping ratio for soils range from 2% to 5%. For this study, 5% is used. In addition, the typical natural frequency of 62.8 rad/sec (10Hz) is assumed.

Given the aforementioned parameters, $\alpha$=3.1416 and $\beta$=7.95×10$^{-4}$ were selected. However, the thick pavement cases were run using 0.02 and 0.06. For the same damping ratio of 5%, this corresponds to 0.695 rad/sec, a significantly low natural frequency. The difference in Rayleigh damping coefficients result in inaccurate material property representation. In addition, these parameters are not held constant for thin and thick pavements, so a direct comparison between the two cannot be conducted appropriately. Due to the fact that the relationship between damping influence and pavement layer thickness is inversely proportional, the simulation case selected as an initial check includes a combination of lowest pavement layer thicknesses, highest applied load, tire inflation pressure, and *weak* material properties from the thick pavement matrix.

The load case considered the applied load of 18 kip and the tire inflation pressure of 125 psi. The selected structure had layer thicknesses of 5 in and 6 in, for the total AC and granular base layers, respectively. Material characterizations were assumed weak for both AC and base layers. Table 4-13 shows that the difference between the baseline and corrected values ranged from 2.2% to 8.6%, wherein the maximum stemmed from the shear strain values of the granular base layers. It was also considered that 5% variation for the horizontal strain in the AC layers, connected to fatigue distresses, can have a significant impact, especially when taking the number of loading repetitions into account.

**Table 4-13. Difference in Responses Using Correct Damping Parameters**

| Pavement Response | Corrected | Base | Diff (%) |
|---|---|---|---|
| Long strain, surface of AC | 372.7 | 352.9 | 5.3 |
| Trans strain, surface of AC | 332.4 | 320.8 | 3.5 |
| Long strain, bottom of AC | 321.5 | 305.4 | 5.0 |

| | | | |
|---|---|---|---|
| Trans strain, bottom of AC | 318.1 | 307.8 | 3.2 |
| Vertical strain, AC | 324.2 | 311.4 | 3.9 |
| Vertical strain, base | 795.9 | 778.4 | 2.2 |
| Vertical strain, subgrade | 975.4 | 949.9 | 2.6 |
| Shear strain, AC | 145.9 | 142.5 | 2.3 |
| Shear strain, Base | 242.1 | 221.4 | 8.6 |
| Shear strain, subgrade | 288.7 | 277.7 | 3.8 |
| Mises stress, AC | 4.1 | 4.0 | 2.4 |

However, due to the fact that the impact of damping decreases as pavement thickness increases, it was deemed appropriate to perform a repetition of the extreme cases to adequately cover the scope of the thick simulation matrix. From this approach, 24 cases were rerun. The factorial included:
- Two pavement structures: AC=5 in and B=6 in.; and AC=16.2 in and B=24 in.
- Two material properties: weak and strong for both AC and base layers
- Six loading conditions: L1, L5, L4, L9, L11, and L12 (Table 5-1)

Figure 4-9 through Figure 4-13 illustrate the relationship between the baseline and corrected cases for all critical pavement responses. The terms in the title of each figure are defined in Chapter 5.
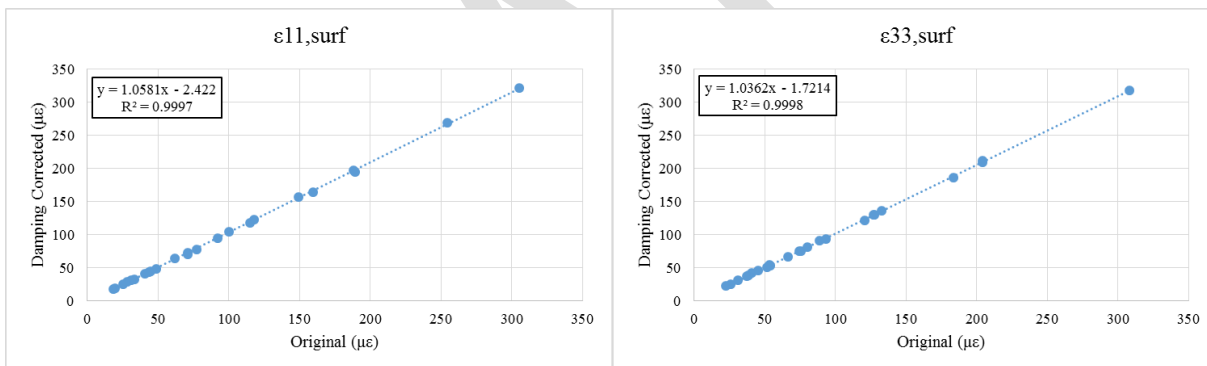


**Figure 4-9. Longitudinal and transverse strains at the AC surface.**
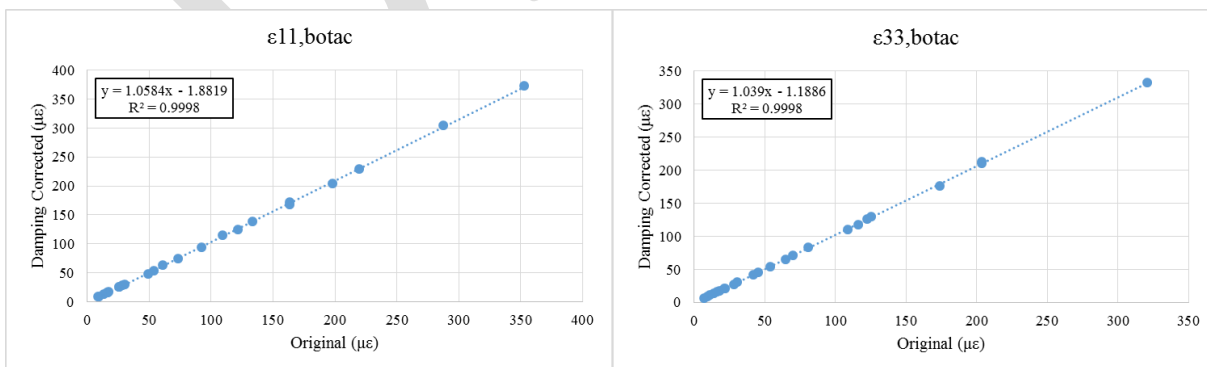


**Figure 4-10. Longitudinal and transverse strains at the bottom of the AC.**

34
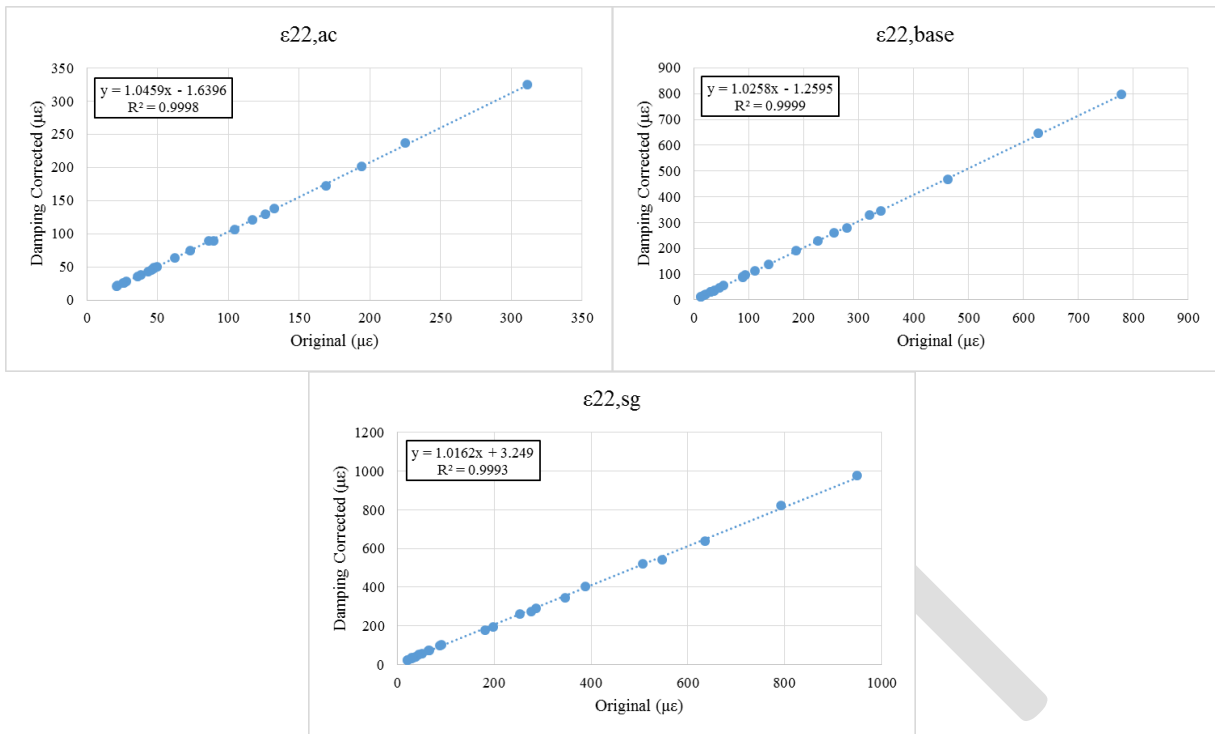
**Figure 4-11. Vertical compressive strain within the AC, base, and subgrade layers.**
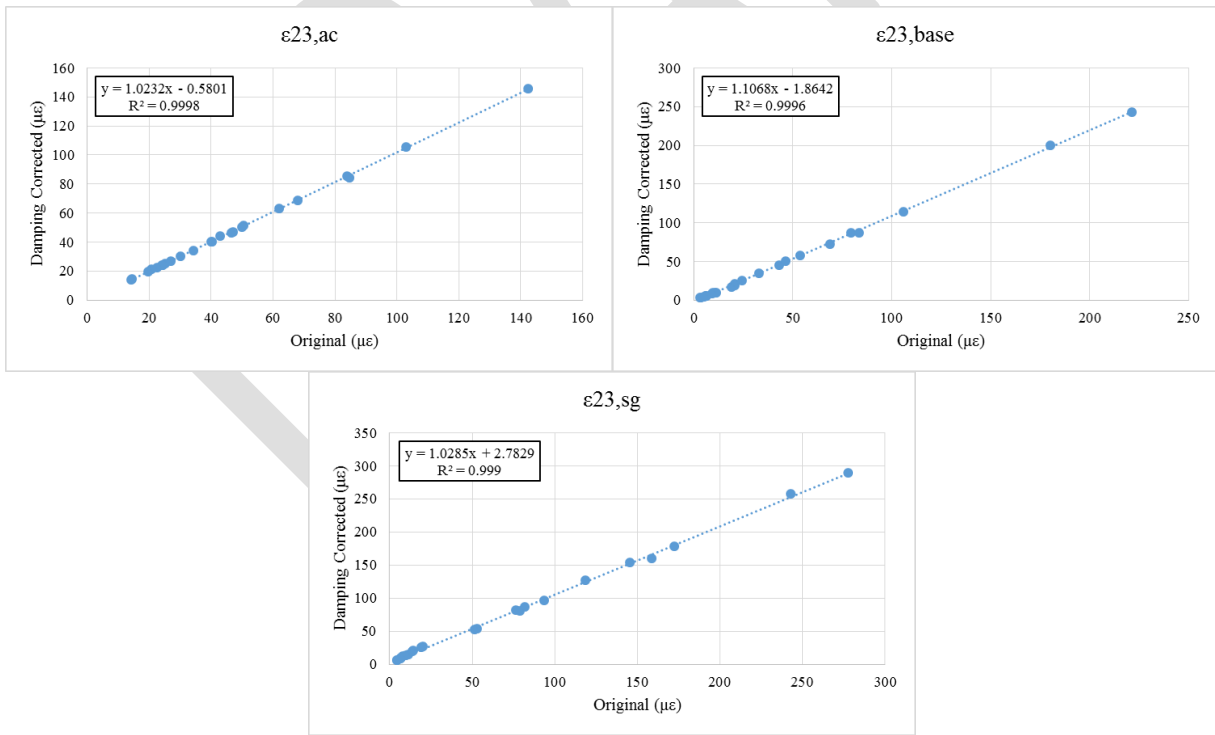


**Figure 4-12. Shear strain in the AC layer.**
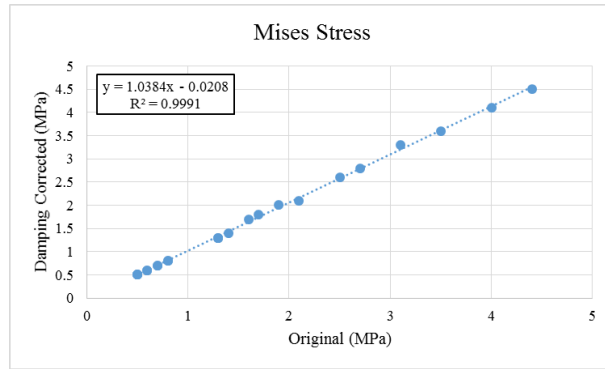
**Figure 4-13. Mises stress in the AC layer.**

Based on the plots comparing baseline values to the same cases with corrected damping parameters, a linear relationship can be observed. For the rerun cases, all pavement responses were underestimated ranging from 1.6% to 10.7%, as indicated in Table 4-14. Therefore, the slopes can be treated as damping adjustment factors for all critical responses. The finite element model represented the granular materials more accurately when these factors were applied on the remainder of the database, and a direct comparison between the thin and thick cases could thus be appropriately performed.

**Table 4-14. Damping Adjustment Factors (Slope and RMSE) for Critical Pavement Responses**

| Response | Slope | RMSE |
|---|---|---|
| Long strain, surface of AC | 1.058 | 2.737 |
| Trans strain, surface of AC | 1.036 | 2.038 |
| Long strain, bottom of AC | 1.058 | 2.378 |
| Trans strain, bottom of AC | 1.039 | 1.620 |
| Vertical strain, AC | 1.046 | 1.950 |
| Vertical strain, base | 1.026 | 2.473 |
| Vertical strain, subgrade | 1.016 | 7.874 |
| Shear strain, AC | 1.023 | 0.726 |
| Shear strain, base | 1.107 | 2.251 |
| Shear strain, subgrade | 1.028 | 3.784 |
| Mises stress, AC | 1.038 | 0.042 |

## 4.5 VALIDATION OF THE FINITE ELEMENT MODEL

After developing the 3-D FE pavement model, the model was validated against results of accelerated pavement testing that were conducted on a number of pavement sections built in participant states. Details about the sections and FE validations are given below.

### 4.5.1 Thin Section at Illinois Center for Transportation

FEM was validated for a thin section that was built at the Illinois Center for Transportation testing facility. Nine thin pavement sections were constructed and heavily instrumented. A section with 5 in of HMA layer and 12 in of base layer was used. Loading conditions were 8 kips tire load and 100 psi tire inflation pressure for DTA. Two pressure cells were installed at the bottom of the base. Data were collected for four runs. The eight pressure measurements are given in Table 4-15.

**Table 4-15. Field Pressure Measurements at the Bottom of the Base**

| | |
|--------|--------|
| 10.589 | 14.456 |
| 13.784 | 16.104 |
| 15.934 | 14.906 |
| 19.500 | 17.321 |

The mean of these eight field vertical pressure measurements was 2.2 psi with a standard deviation of 0.38 psi. On the other hand, the FEM model predicted the vertical pressure as 2.44 psi at the bottom of base. FEM provided accurate approximation for vertical pressure at the bottom of the base layer. The transverse strain at the bottom of AC was also used for validation. There were four strain measurements for this section because one strain gauge was installed (1x4 pass), as shown in Table 4-16.

**Table 4-16. Field Strain Measurements at the Bottom of the AC**

| Transverse Strain ($\mu\varepsilon$) |
|:-----------------------------------:|
| 68.581 |
| 59.406 |
| 76.288 |
| 79.323 |

The mean of the four field transverse strain measurements were calculated as 70.9 µε with 8.9 µε standard deviation. FEM resulted in 53.3 µε. This variation could be attributed to the bending of the strain gauge in the field as a result of loading thin AC layer and because the strain gauge was supported by a weak platform.

### 4.5.2 Thick Section at Smart Road

Section B of the Smart Road project was used to validate the finite element model of thick pavement. This section is considered as a "thick" section and has the input parameters in Table 4-17 (Al-Qadi et al., 2008).

**Table 4-17. Smart Road Pavement Input Parameters**

| Layer | Thickness (mm) | Instantaneous Modulus (MPa) | Poisson's Ratio | Density | Rayleigh Damping Parameters (α and β) | |
|----------|------|----------|------|-----------------------|-------|--------|
| SMA-9.5* | 38   | 4230.29  | 0.2  | $2.30\times10^{-6}$   | N/A   | N/A    |
| BM-25*   | 150  | 4750.49  | 0.2  | $2.30\times10^{-6}$   | N/A   | N/A    |
| OGDL*    | 75   | 2415.00  | 0.3  | $2.10\times10^{-6}$   | 0.107 | 0.015  |
| CTB*     | 150  | 10342.14 | 0.2  | $2.00\times10^{-6}$   | 0.024 | 0.0015 |
| Subbase  | 175  | 310.26   | 0.35 | $1.50\times10^{-6}$   | 0.02  | 0.06   |
| Subgrade | -    | 262.00   | 0.35 | $1.50\times10^{-6}$   | 0.02  | 0.06   |

*Note: SM-9.5: HMA Surface Mix with NMAS of 9.5mm, BM-25: HMA Base Mix with NMAS of 25mm, OGDL: Open-Graded Drainage Layer, and CTB: Cement-Treated Base*

The top two layers, SM-9.5 and BM-25, were characterized as viscoelastic and defined using the Prony series from Table 4-18. Al-Qadi et al. (2008) shifted the Prony series to 77 °F and therefore the William-Landel-Ferry coefficients were omitted. In this scenario, the two layers are assumed to be subjected to uniform temperature condition of 77 °F. In addition, the optimized mesh for the corresponding section resulted in the configuration presented in Table 4-19.

**Table 4-18. Viscoelastic Material Characterization of SM-9.5 and BM-25**

| $i$ | $G_i$ (SM-9.5) | $K_i$ (SM-9.5) | $\tau_i$ (SM-9.5) | $G_i$ (BM-25) | $K_i$ (BM-25) | $\tau_i$ (BM-25) |
|---|---|---|---|---|---|---|

| | | | | | | |
|---|---|---|---|---|---|---|
| 1 | $7.7465\times10^{-1}$ | $7.7471\times10^{-1}$ | $1.00\times10^{-2}$ | $6.49899\times10^{-1}$ | $6.49562\times10^{-1}$ | $1.00\times10^{-2}$ |
| 2 | $1.6498\times10^{-1}$ | $1.6493\times10^{-1}$ | $1.00\times10^{-1}$ | $2.24921\times10^{-1}$ | $2.25154\times10^{-1}$ | $1.00\times10^{-1}$ |
| 3 | $3.9793\times10^{-2}$ | $3.9752\times10^{-2}$ | $1.00$ | $8.51861\times10^{-2}$ | $8.53679\times10^{-2}$ | $1.00$ |
| 4 | $1.3829\times10^{-2}$ | $1.3822\times10^{-2}$ | $1.00\times10^{1}$ | $2.46542\times10^{-2}$ | $2.46481\times10^{-2}$ | $1.00\times10^{1}$ |
| 5 | $2.7364\times10^{-3}$ | $2.7285\times10^{-3}$ | $1.00\times10^{2}$ | $1.07095\times10^{-2}$ | $1.07301\times10^{-2}$ | $1.00\times10^{2}$ |
| 6 | $1.7106\times10^{-3}$ | $1.7133\times10^{-3}$ | $1.00\times10^{3}$ | $1.79179\times10^{-3}$ | $1.79305\times10^{-3}$ | $1.00\times10^{3}$ |
| 7 | $2.0405\times10^{-3}$ | $2.0364\times10^{-3}$ | $1.00\times10^{4}$ | $7.27802\times10^{-4}$ | $7.27326\times10^{-4}$ | $1.00\times10^{4}$ |
| 8 | $1.6524\times10^{-5}$ | $1.6487\times10^{-5}$ | $1.00\times10^{5}$ | - | - | - |
| 9 | $6.8306\times10^{-6}$ | $6.9430\times10^{-6}$ | $1.00\times10^{6}$ | - | - | - |

**Table 4-19. Section B Mesh Details**

| | | |
|---|---|---|
| | Length (mm) | 6420.0 |
| | Width (mm) | 5571.5 |
| | Depth (mm) | 4500.0 |
| | L1=B1 (mm) | 1800.0 |
| | L2=B2 (mm) | 300.0 |
| SM-9.5 | No. of Elements | 4 |
| | Bias | 1.20 |
| BM-25 | No. of Elements | 12 |
| | Bias | 1.20 |
| OGDL | No. of Elements | 5 |
| | Bias | 1.00 |
| CTB | No. of Elements | 10 |
| | Bias | 1.00 |
| Subbase | No. of Elements | 10 |
| | Bias | 1.30 |
| Subgrade | No. of Elements | 18 |
| | Bias | 35.00 |
| L1=B1 | No. of Elements | 18 |
| | Bias | 18.0 |
| L2=B2 | No. of Elements | 1 |
| | Bias | 1.0 |

Moreover, the loading condition was defined with a half-axle load of 7.8 kip and 105 psi for the DTA 275/80R22.5. The contact stresses used in the model were based on previous experimental measurements and the same input definition (details in Chapter 4) was applied. Given the input parameters, three critical responses were extracted from the FE model and compared with field data, as shown in Table 4-20. Based on the resulting difference, the vertical pressure on top of the subgrade and the transversal and longitudinal strain underneath the AC layers varied by 2.36%, 12.06%, and 2.14 %, respectively. This exercise ensures that the models used in this study to evaluate the impact of NG-WBT are representative of field conditions and are suitable for completing the selected analysis matrix.

**Table 4-20. Comparison of Simulation Results and Field Measurements**

| Depth (mm) | Location Definition | Pavement Response | Simulation Results | Field Measurement | Difference (%) |
|---|---|---|---|---|---|
| 588 | Top of subgrade | Vertical Pressure (MPa) | 0.04 | 0.04 | 2.36 |
| 188 | Bottom of AC (BM-25) | Transversal Strain (με) | 103.79 | 92.62 | 12.06 |

| 188 | Bottom of AC (BM-25) | Longitudinal Strain (με) | 116.11 | 118.65 | 2.14 |
|---|---|---|---|---|---|

### 4.5.3 Thin Section at Florida

Results of the Accelerated Pavement Test conducted at the Florida Department of Transportation (FDOT) were used to validate FEM pavement model. A "Test Pit" section with 3 in of AC, 10.5 in of limerock base and 12 in of subbase was selected for the validation. The load condition was 80 psi tire inflation pressure with 6 kips axle load for DTA.

Four pressure cells were installed in this section, two of which are located at the bottom of AC and the other two at the bottom of the base layer. While the average pressure was measured as 24.5 psi at the bottom of AC, it was 4.5 psi at the bottom of the base layer. FEM computed those stresses as 24.2 psi and 3.8 psi. Six strain gauges were installed at the bottom of the AC layer, three in the traffic direction and three of in the transverse direction. The average tensile strain was measured as 21.1 and 98.0 με for transverse and traffic directions, respectively. On the other hand, FEM predicted these strains at 18.5 and 43.0 με.

FEM resulted are in quite accurate approximation for the vertical pressures and tensile strains in the transverse direction. However, the prediction of the strain in traffic direction was off by a factor of 2. The base material is characterized as stress-dependent nonlinear material to simulate the behavior of the However, since the resilient modulus test was only conducted using vertical load, it was not possible to obtain nonlinear material characterization parameters for all three dimensions. Therefore, the base material was assumed isotropic leading to underestimation of the tensile strains in the traffic direction.

### 4.5.4 Thin Section at UC-Davis

Another section used for FEM validation was built at the University of California Pavement Research Center facility in Davis, California. Section "671HC" was selected for FEM validation. This section has two AC layers, each with 2.4 in layer thickness. While the top layer is warm-mix asphalt, the bottom later is HMA. Underneath the two AC layers are recycled base and subbase layers with 9.8 and 10.6 in layer thicknesses, respectively.

Four pressure cells were installed in this section, two of them are located at the top of the recycled base layer and the other two at the bottom of the recycled base layer. While the average pressure was measured as 12.3 psi at the top of the base layer, it was 5.8 psi at the bottom of base layer. FEM computed those stresses as 8.6 psi and 4.5 psi. There was a total of eight strain gauges installed in this section. Four of them were placed at the bottom of the top AC layer as two strain gauges are oriented for each direction (traffic and transverse direction). The other four strain gauges are located at the bottom AC layer in a same way. The transverse strains at the bottom of top and bottom AC layer measured 59.2 and 11.57 με, respectively. On the other hand, FEM predicts those strains as 4.3 and 16.9 με.

FEM prediction for vertical pressure at the top and bottom of the base layer was much lower than field responses. The base material was characterized as linear elastic material due to the lack of resilient modulus data. As reported in the literature (Kim et al., 2009), linear elastic characterization of base results in stiffer behavior in pavement simulation. The effect gets even more significant for the pavement with thinner AC layer as in this section. The stain gauge measurements are dependent on installation and type of the strain gauge used and field measurements seem to be high.

### 4.5.5    Thick Section at Ohio

The last validation of the developed FEM was done on a thick driving mainline section in Ohio. This section has a total of 6 layers including subgrade: 1 in of fine graded polymer AC, 2 in of AC intermediate course, 8 in of AC base, 4 in of fatigue resistant base layer, 6 in of aggregate base. The load case selected was DTA with axle load of 10 kip and tire pressure of 110 psi.

The AC was characterized by the Prony series, which were derived from the complex modulus test. However, the information provided for base material characterization was not sufficient for obtaining the model parameters given in 4.1.2. The elastic modulus values were assumed to be 74.4 ksi and 111 ksi for base and subgrade, respectively. These values were reported by Xue and Weaver (2001). Despite the differences that might exist between these sections, it was considered an appropriate approximation.

A total of four pressure cells were installed in the section, two were located at the bottom of the fatigue-resistant base layer and the other two cells were installed at the bottom of the aggregate base layer. The average vertical pressure measurement for these two locations is 7 psi and 4.5 psi. The FEM approximation for these responses is 8.4 psi and 7.3 psi, respectively.

Additionally, transverse strain measurements were used to validate the FE model. Transverse strains were measured at three different locations: bottom of AC layer, bottom of AC base, and bottom of fatigue-resistant base layer. There were 300 measurements for transverse strain at the bottom of AC showing great variability. The measurements varied between 50 με and 350 με with an average of 173 με and a standard deviation of 76 με. The FME predicted this strain at 40.2 με. The measured transverse strains at the bottom of the AC base and fatigue resistant layers were 46 με and 123 με, respectively. FEM's predictions, on the other hand, were 27 and 15 με. High discrepancy between the measurement and FEM results was alluded to the unavailability of data for the base and subgrade material characterizations.

### 4.6    SUMMARY

In order to perform accurate FE simulations of the loaded pavement, an adequate numerical model must be generated. Based on the assumptions made in this study with regard to model geometry, material characterization, temperature profile, layer interaction, and boundary conditions, the FE models used in this study are considered appropriate. Model accuracy was further supported by the validation phase of various field test sections across the U.S., wherein sample critical responses compared relatively well to measured field responses, except for the sections that were lacking some data.

# 5 EFFECT OF TIRE CONFIGURATION ON PAVEMENT RESPONSE

The FE analysis matrix included pavement structure (thin and thick pavements), thickness of pavement layers (see Table 4-6), material properties (see Sections 4.1.1 and 4.1.2), and 12 loading conditions for a total of 576 cases. The loading conditions consisted of very high and low loads (6 and 18 kip) and tire inflation pressure (80 and 125 psi) for developing the artificial neural network model. A loading case with $P$=10 kip and $S$=110 psi was included to evaluate the pavement responses at normal loading conditions. Finally, two loading cases with differential tire inflation pressure were added to the loading matrix. Table 5-1 shows the 12 loading cases, type of tire, applied load, tire inflation pressure, and the resultant. The resultant was obtained as the reaction force of the measured vertical contact stresses/forces.

Table 5-1. Loading Cases Used in Finite Element Analysis

| Loading Case | Tire | $P$ (kN) | $S$ (kPa) | Resultant (kN) |
|---|---|---|---|---|
| L1 | NG-WBT | 26.7 | 552 | 24.5 |
| L2 | NG-WBT | 26.7 | 862 | 26.6 |
| L3 | NG-WBT | 79.9 | 552 | 79.4 |
| L4 | NG-WBT | 79.9 | 862 | 79.4 |
| L5 | DTA | 26.7 | 552 | 25.7 |
| L6 | DTA | 26.7 | 862 | 25.4 |
| L7 | DTA | 26.7 | 552/758 | 26.4 |
| L8 | DTA | 79.9 | 552 | 77.8 |
| L9 | DTA | 79.9 | 862 | 77.3 |
| L10 | DTA | 79.9 | 552/758 | 76.6 |
| L11 | NG-WBT | 44.4 | 758 | 43.7 |
| L12 | DTA | 44.4 | 758 | 39.3 |

Note: 1 kN=224 lb, 1 kPa=0.145 psi

The studied pavement responses are linked to various pavement distresses. The tensile surface strain in the longitudinal ($\varepsilon_{11,surf}$) and transverse ($\varepsilon_{33,surf}$) is associated with near-surface cracking. In addition, the tensile strain at the bottom of the AC in the longitudinal ($\varepsilon_{11,AC}$) and transverse ($\varepsilon_{11,AC}$) direction relates to the pavement's fatigue life (bottom-up fatigue cracking). Permanent deformation is mainly defined by the vertical strain in the pavement structure ($\varepsilon_{22,AC}$, $\varepsilon_{22,base}$, and $\varepsilon_{22,subg}$ for the AC, base, and subgrade, respectively). The vertical shear strain in each layer was included, even though it is not formally related to any pavement distress in the MEPDG procedure.

The effect of pavement structure, layer thickness, material properties, and type of tire on critical pavement responses was studied. Under the same loading condition and layer thicknesses, the change in critical pavement responses with various material properties was plotted, as shown in Figure 5-1 for the Mises stresses. In this figure, the horizontal axis represent the various material properties ($W$=weak and $S$=strong), with the top letter corresponding to the AC, the middle to the base, and the bottom one to the subgrade. The values considered an adjustment caused by the small difference between the applied load and the resultant (compared columns 3 and 5 in Table 5-1). Similar drawings were prepared for each one of the 576 analysis cases, and the results are provided in Appendices B and C.

Box plot were used to have a global assessment of the difference between NG-WBT and DTA (Figure 5-1). For each pavement responses under a fixed loading case, the percentage difference was calculated using DTA as reference. The box plot shows the first and third quartile along with the median of the percentage difference. In addition, the disparity between the maximum and minimum difference with the third and first quartile, respectively, are shown. For instance, in the case shown in Figure 5-1, there are more values with difference less than the median, with a minimum difference of 15.8% and a maximum difference of 45.6%. In addition, the mean and the median are close to one another (34.0% vs. 34.8%).
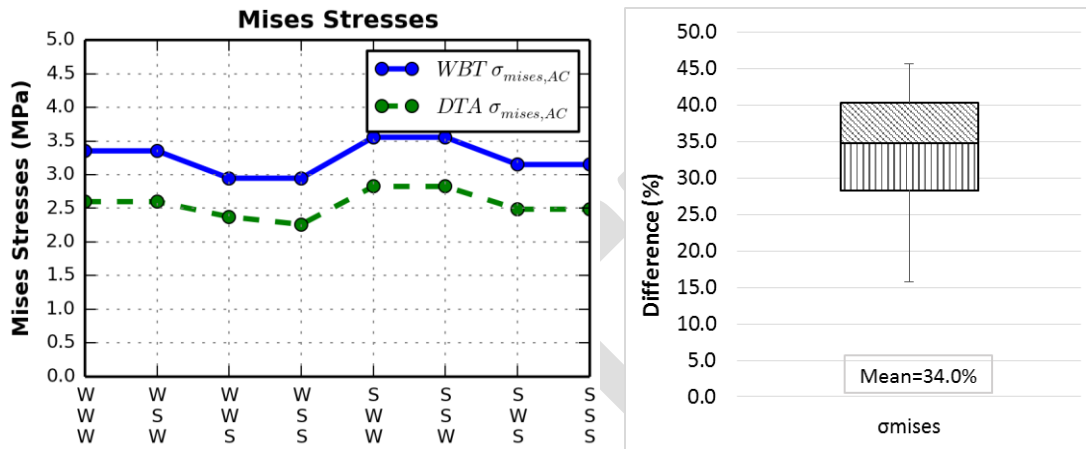


**Figure 5-1. Variation of Mises stresses in thin pavement for $AC$=125 mm, $B$=150 mm, $P$=44.4 kN, and $S$=110 psi (L11 and L12) and box chart.**

## 5.1 THIN PAVEMENT STRUCTURES

### 5.1.1 Longitudinal and Transverse Strains at the Surface and Bottom of the AC

Figure 5-2 shows the variation of the longitudinal and tensile strains on the surface and at the bottom of the AC for NG-WBT and DTA. This figure corresponds to $P$=10 kip and $S$=110 psi, but the same variation for other loading cases is presented in Appendix B. The magnitude of the surface strain did not significantly change between weak and strong base when its thickness was 150 mm; however, when the base thickness was 600 mm, the only material significantly affecting the surface strain was the AC layer. The effect of tire inflation pressure on surface strain was not important for almost any combination of the considered variables, but the effect of applied load was clear.

The tensile strain at the bottom of the AC, in both the longitudinal and transverse directions, was higher for NG-WBT than DTA. The $\varepsilon_{33,AC}$ for NG-WBT was also higher than $\varepsilon_{11,AC}$ and $\varepsilon_{33,AC}$ for DTA. The tire inflation pressure had more influence on $\varepsilon_{33,AC}$ than on $\varepsilon_{11,AC}$ for both tires, but again, load was the most relevant factor. For the thickest layers ($AC$=5 in and $B$=24 in), the only parameter affecting the tensile strain at the bottom of the AC was the AC material, but this behavior changed as the thickness of AC and base changed.

Figure 5-3 summarizes the behavior of the percentage difference between NG-WBT and DTA for the longitudinal and transverse tensile strains at the pavement surface and at the bottom of the AC. For $\varepsilon_{33,surf}$, a reduction in the difference was observed as the AC thickness increases. If the AC thickness was 5 in., the difference tended to be higher for the weak AC; however, if $AC$=3 in the difference was not as sensitive.

The fact that the tensile strain at the bottom of the AC was not greatly affected by tire inflation pressure translated into relatively constant difference between both tires as the inflation pressure changed. The highest discrepancy between both tires for $\varepsilon_{11,AC}$ was observed at loads of small magnitude. In addition,

the impact of the tire type on $\varepsilon_{11,AC}$ did not depend on the material property of any layer. On the other hand, $\varepsilon_{33,AC}$ showed the highest average difference among all the pavement responses, 52.5%, ranging between 33.8 and 67.7%. The information in Figure 5-3 also allows to conclude that: i) the tensile strain at the surface of the AC had a smaller range of values; ii) for $\varepsilon_{33,surf}$, more values above the mean than below; and iii) the average difference in the longitudinal strain at the bottom of the AC, which was consistently higher than the transverse strain, was 23.2%
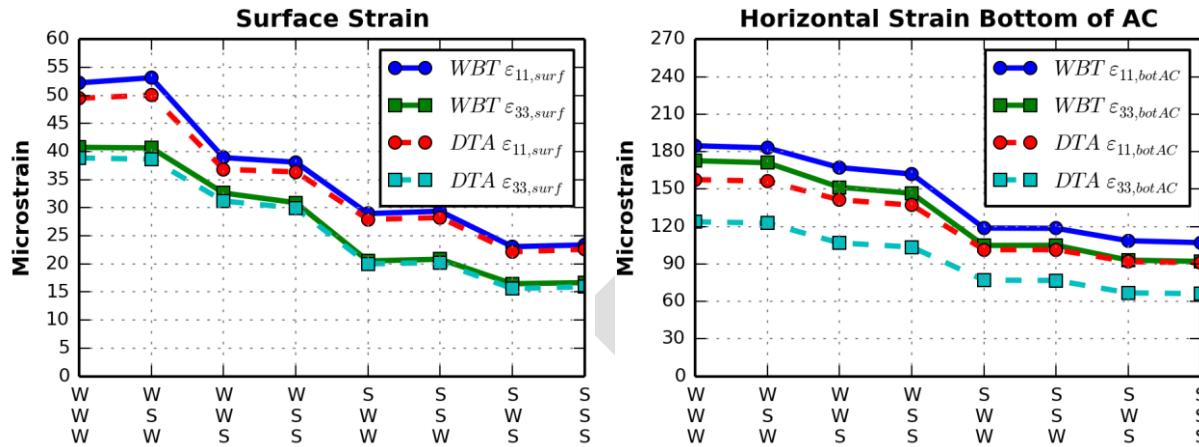


**Figure 5-2. Longitudinal and transverse strains at the pavement surface and bottom of AC for $AC$=125 mm, $B$=150 mm, $P$=44.4 kN, and $S$=110 psi.**
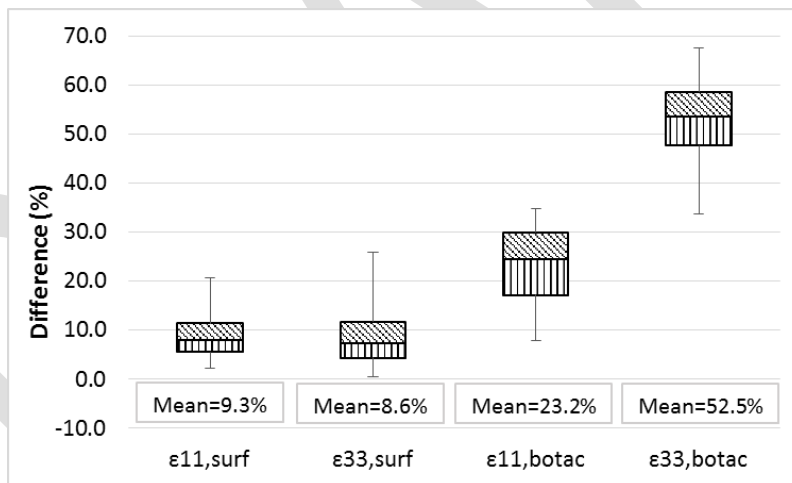


**Figure 5-3. Box plots for difference between NG-WBT and DTA for tensile strain on the surface and bottom of the AC.**

### 5.1.2    Shear Strain in the AC, Base, and Subgrade

Figure 5-4 shows the same variation as in Figure 5-2; but for the vertical shear strain in each layer. The tire inflation pressure slightly affected the vertical shear strain in the pavement layers for NG-WBT more than for DTA, and this effect was more noticeable in the subgrade and base. Conversely, the effect of $S$ on $\varepsilon_{23,subg}$ was almost nonexistent in the thickest pavement structure, regardless of the material properties. The shear strain in the AC was mainly affected by the AC material, but $\varepsilon_{23,base}$ was sensitive to change in material properties in any layer for both type of tires for thin AC layer, $AC$=3 in and $B$=24 in Furthermore, the shear strain in the subgrade was not only affected by the subgrade but also by the AC. As in tensile strain, the load was the most relevant parameter, and the tire inflation pressure played a secondary role.

43
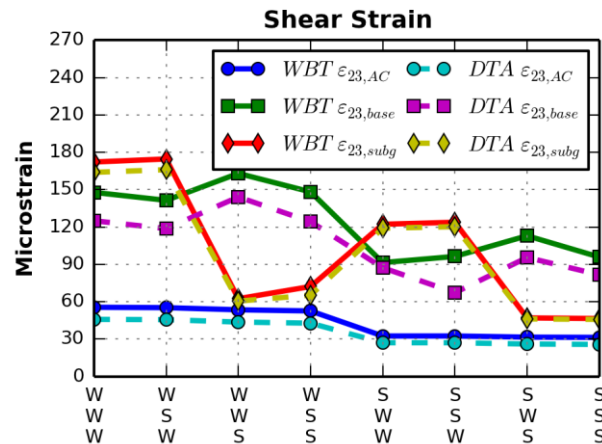
**Figure 5-4. Vertical shear strain in the AC, base, and subgrade for $AC$=125 mm, $B$=150 mm, $P$=44.4 kN, and $S$=110 psi.**

The variation of the percentage difference between NG-WBT and DTA is provided in Figure 5-5 for vertical shear strain. Once more, the mean difference decreased with depth from 26.3% in the AC to 11.2% in the subgrade. However, the range of values in the AC was the smallest. The difference in the $\varepsilon_{23,AC}$ was mainly affected by load and tire inflation pressure, and material properties did not significantly affect the results once thicknesses were fixed. In some cases, the shear strain in the subgrade was smaller for NG-WBT than for DTA (negative difference). Specifically, for high load and the AC thickness of 125 mm, the difference was small (less than 10%), and sometimes negative (as low as -4.7%).
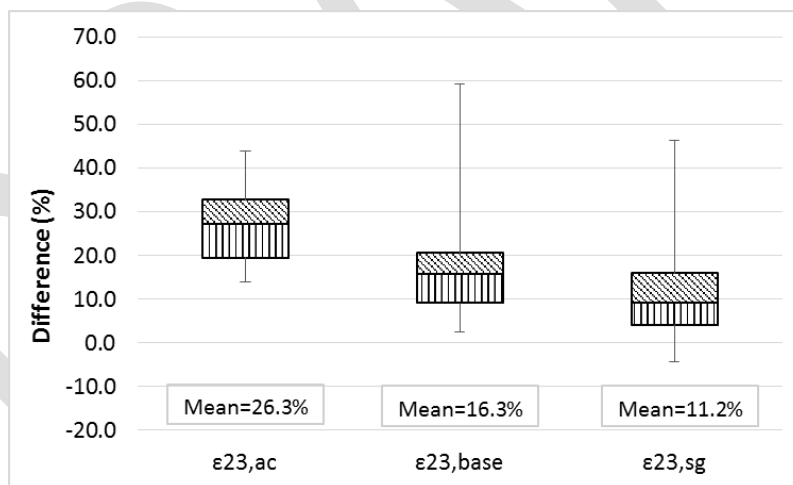


**Figure 5-5. Box plots for difference between NG-WBT and DTA for shear strain in each layer.**

### 5.1.3    Vertical Strains in the AC, Base, and Subgrade

The variation of the vertical strain in each layer for loading cases $L11$ and $L12$ when $AC$=5 in and $B$=6 in is shown in Figure 5-6 (see Appendix B for other loading cases and pavement structures). The applied load was the most relevant factor. Tire inflation pressure affected $\varepsilon_{22,base}$ base when the applied load was high. The base layer showed the highest vertical compressive strain, and $\varepsilon_{22,AC}$ was mainly defined by the applied load. Regarding the vertical strain on top of the subgrade, the material of each layer affected its magnitude differently, with subgrade being the most important, followed by AC, and base being the least important. Base properties had a slight effect when its thickness was 600 mm.

44
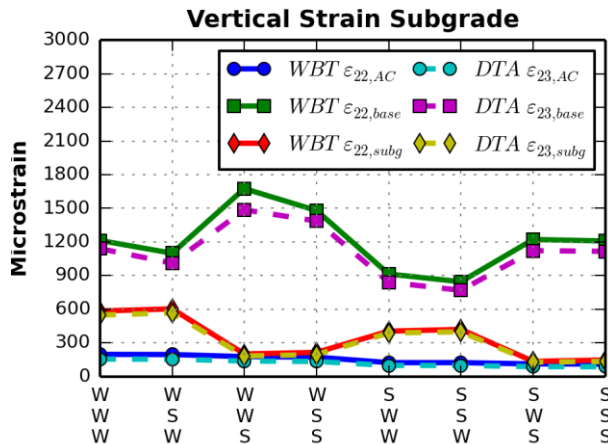
**Figure 5-6. Vertical strain in the AC, base, and subgrade for *AC*=125 mm, *B*=150 mm, *P*=44.4 kN, and *S*=110 psi.**

Figure 5-7 shows the behavior of the difference between NG-WBT and DTA for the vertical strains in each layer. The highest average difference was 36.3%, which corresponded to the AC. This average difference decreased with depth, reaching 14.5% in the base and 13.0% in the subgrade, respectively. For $\varepsilon_{22,subg}$, smaller difference occurred for thickest AC, and the difference was more sensitive to the material property selection when *AC*=3 in It was also noticed that, even though the subgrade had the smallest average percentage difference, it had the highest difference (59.3%) and the largest range (59.0%). In addition, the difference in the vertical strain was more uniform closer to the surface and the average difference decreased with depth, for all thicknesses, loads, tire inflation pressures, and materials.
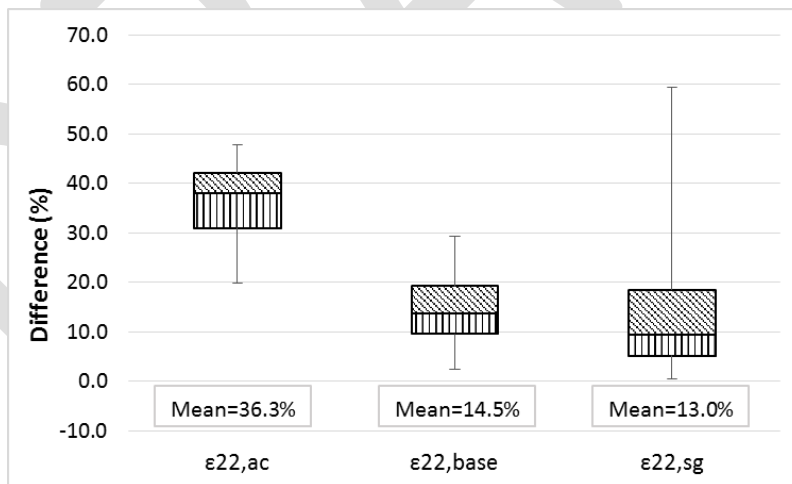


**Figure 5-7. Box plots for difference between NG-WBT and DTA for vertical strain in each layer.**

## 5.2    THICK PAVEMENT STRUCTURES

The simulation factorial for the thick pavement consisted of 192 cases with varied input parameters. Only selective cases are analyzed to present the key findings as the general trends for the same categories are similar. The complete set of plots are shown in Appendix C. The plots presented in this section reflects the NG-WBT (*L*11) and DTA (*L*12) cases with *P*=10 kip and *S*=110 psi.

### 5.2.1 Longitudinal and Transverse Tensile Strains at the Surface and Bottom of the AC

AC and granular base material characterization varied by using weak and strong properties. In Figure 5-8, the top row on the horizontal axis denotes the AC materials, whereas the bottom row indicates the granular base layer materials.

As expected, the transition of AC material properties from strong to weak increased the strain magnitudes. Moreover, AC material property induced a higher change in responses than base material alteration. Similar strain response evolution was evident for NG-WBT and DTA cases, although NG-WBT had a higher magnitude than DTA. In addition, the disparity between the NG-WBT and DTA responses increased as both AC and granular base layers were characterized as *weak* materials and even more significantly for the $\varepsilon_{33,AC}$ at the surface, and $\varepsilon_{11,AC}$ at the bottom.

The horizontal strains at the surface and bottom of the AC were more significantly impacted when the AC layer thickness varied than the base thickness was altered. For AC layer thickness of 16.2 in., the strain magnitudes for both NG-WBT and DTA were relatively similar, whereas the NG-WBT responses were evidently greater than the DTA for a 5-in-thick AC layer.

Comparing the impact of the applied load and tire inflation pressure, it was observed that the applied load governs the change in pavement response. In comparison with tire inflation pressure variation, there was a steeper increase in the strains when the applied load increased. Moreover, a notable difference between the NG-WBT and DTA cases became apparent as the applied load was altered from 6 to 18 kip, specifically for the $\varepsilon_{33,AC}$ at the surface, and $\varepsilon_{11,AC}$ at the bottom.
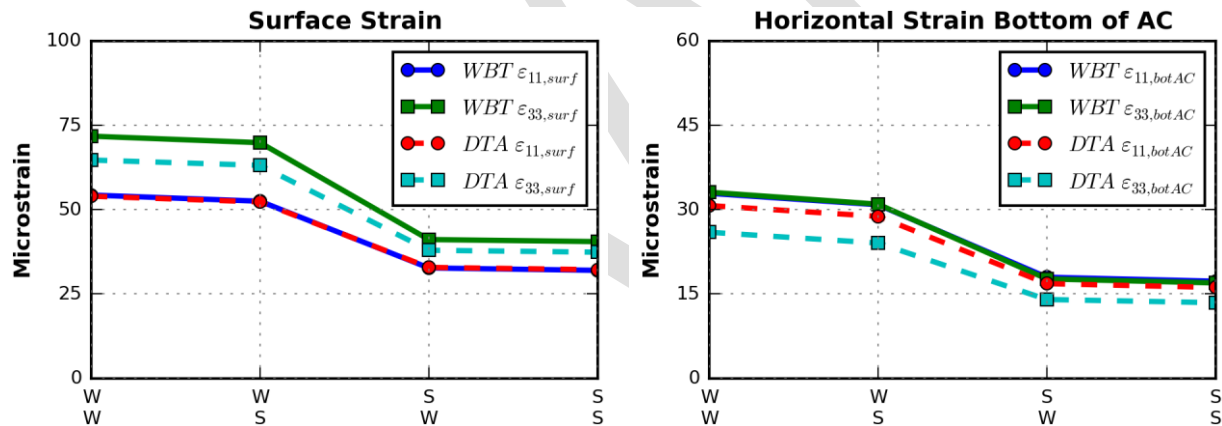


**Figure 5-8. Longitudinal and transverse strains at the pavement surface and bottom of *AC*=412.5 mm, *B*=600 mm, *P*=44.4 kN, and *S*=110 psi.**

Figure 5-9 presents the relative percentage difference between NG-WBT and DTA responses. $\varepsilon_{11,AC}$ were impacted less as the mean difference was 14.2% and 18.3% for the surface and bottom of the AC, respectively. On the other hand, not only the percent difference increased for $\varepsilon_{33,AC}$ but the spread was also greater.
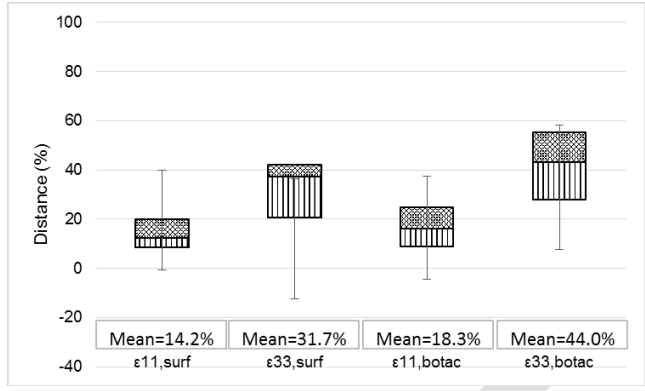
**Figure 5-9. Box plots for difference between NG-WBT and DTA for tensile strains on the surface and bottom of the AC.**

### 5.2.2 Shear Strains in the AC, Base, and Subgrade

Similar to the horizontal strains at the surface and bottom of the AC, the shear strains for all three pavement layers increased as their materials were characterized from *strong* to *weak*. However, only the vertical shear strain of the AC layer changed significantly throughout the material progression in contrast with the coincidental and almost flat evolution of the strains for the granular base and subgrade layers. The disparity between the NG-WBT and DTA cases also increased as the material became *weaker* (Figure 5-10). It was observed that the effect of the applied load on the vertical shear strain response exceeded that of the tire inflation pressure alteration.

The impact of varying the pavement layer thickness also indicated that the structure with $AC$=16.2 in and $B$=24 in induced the highest vertical shear strain in the AC. The subgrade vertical shear strain also resulted in higher strain magnitudes than the AC and granular base layers, when the base layer thickness was reduced to 6 in (with $AC$ = 5 in.). On the other hand, the base layer shear strain was significantly greater than that of the AC and subgrade layers for $AC$ = 5 in and $B$ = 24 in In addition, the NG-WBT responses became significantly greater than the DTA cases as the AC and granular base layer thicknesses decreased.
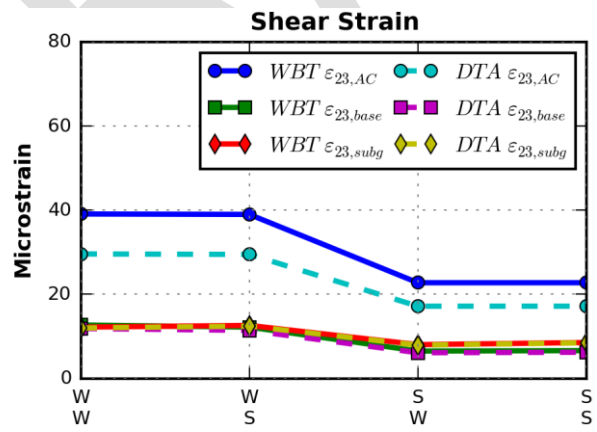


**Figure 5-10. Vertical shear strain in the AC, base, and subgrade for $AC$=412.5 mm, $B$=600 mm, $P$=44.4 kN, and $S$=110 psi.**

In comparison with the NG-WBT impact on vertical shear strains, Figure 5-11 indicates that the percentage difference for the base and subgrade layers was less affected than the ones in the AC layer, wherein the average percentage difference were 18.4% and 8.4%, respectively. This behavior was anticipated as at a greater pavement depth, the applied load becomes the significant factor, whereas contact stresses have a

greater effect at the near-surface region of the AC layer leading to an average percent difference of 39.8% and higher range of 15.5% and 79.0%.
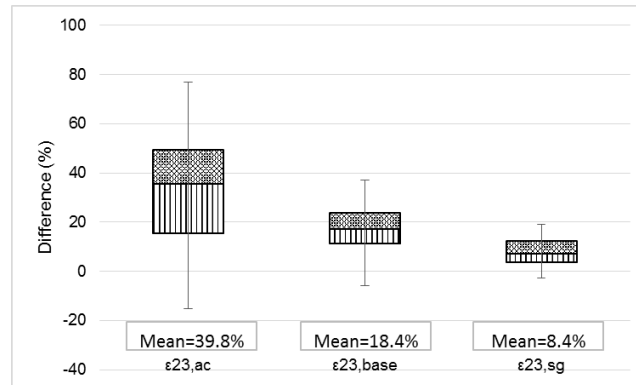


**Figure 5-11. Box plots for difference between NG-WBT and DTA for shear strains in each layer.**

### 5.2.3 Vertical Strains in the AC, Base, and Subgrade

For the last critical pavement response considered, the vertical strains of the subgrade layer were generally higher than the ones in the AC and base layers; this difference is more significant when the base layer is characterized as strong. The trends presented in Figure 5-12 are even more exacerbated when the pavement layer thickness is lower. In addition, when the AC layer material was held constant and the base layer material varied, the difference between the vertical compressive strains in the subgrade and base layers did not change significantly.

Additionally, at a high AC layer thickness of 16.2 in., the strain magnitude range between the AC, base, and subgrade layers was significantly limited compared with that of a 125-mm-thick AC layer. Similar to the vertical shear strain, the case of $AC$=5 in and $B$=24 in generated the highest vertical compressive strain in the base layer more than the ones in the AC and subgrade layers, whereas the subgrade response became significantly greater than the other layers when $AC$=5 in and $B$=6 in Moreover, as the AC and base layer thicknesses were reduced, the responses from the NG-WBT cases increases more significantly than that of the DTA.

In contrast with the percentage difference of the NG-WBT and DTA vertical compressive strain responses in the AC and base layers, the range of the ones for the subgrade layer was significantly less with an average of 10.3%. On the other hand, the average percent difference for the AC and base layers increased to 34.3% and 20.9%, respectively, with a larger spread as well.

Based on the impact of the loading conditions, the applied load was most influential for both the pavement structures in contrast with the tire inflation pressure. In addition, for both cases, the factors inducing higher disparity between the NG-WBT and DTA responses, included an increase in the applied load, reduced pavement layer thicknesses, and *weak* material characterization.

48
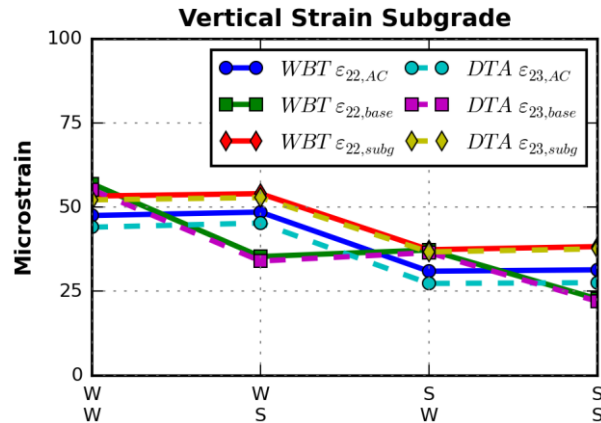
**Figure 5-12. Vertical compressive strain in the AC, base, and subgrade for *AC*=412.5 mm, *B*=600 mm, *P*=44.4 kN, and *S*=110 psi.**
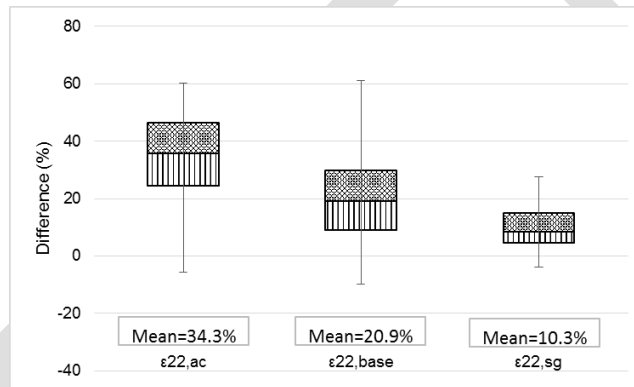


**Figure 5-13. Box plots for difference between NG-WBT and DTA for vertical compressive strain in each layer.**

## 5.3   SUMMARY

The influence of load, tire inflation pressure, loading conditions on the various pavement structures on critical pavement responses was studied. Special focus was given to the comparison between NG-WBT and DTA not only for the magnitude of the responses but also the percentage difference.

For thin pavements, the difference decreased with depth, as the influence of the contact stresses decreased. It was also observed that the highest average difference was in the transverse strain at the bottom of the AC, while in the longitudinal direction it was 23.2%. Even though the difference was higher close to the surface, the values were uniform. Shear strain in the subgrade had small difference, and in some cases it was smaller for NG-WBT than for DTA.

The combination of the low thickness and weak pavement material characterization induced the highest strain values for the thick pavement structure. For instance, the transition of AC material properties from strong to weak and the reduction in AC layer thickness increased the strain magnitudes. Moreover, altering the AC material property generated a greater impact on responses compared with altering the base material.

Comparing NG-WBT and DTA cases, similar strain response evolution was evident, although NG-WBT had a higher magnitude than DTA. In addition, the disparity between the NG-WBT and DTA cases also increased as the material became *weaker* and AC thickness was reduced to 5 in It was also observed that

the applied load governs the change in pavement response more significantly than the tire inflation pressure. Lastly, the relative percentage difference between the NG-WBT and DTA responses revealed the following:

- The transverse strain at the pavement surface and bottom are more affected compared with the strain in the longitudinal direction,
- The shear strain in the AC layer revealed a higher mean difference and spread than that of the base and subgrade, and
- The vertical strain in the AC resulted to a greater percentage difference than the two supporting granular layers.

# 6 ARTIFICIAL NEURAL NETWORKS (ANN)

Calculation of pavement responses to the applied loading condition is a key step in the pavement design procedure, where these responses are used to quantify the pavement damage, which is the final criterion in the mechanistic-empirical pavement design procedure. Pavement damage quantification is typically done using empirical equations while response prediction is carried out based on mechanistic models. As explained earlier, FE modeling provides realistic consideration of 3D tire loading and nonlinear pavement structure. However, running FE models is computationally expensive and, depending on the complexity of the models, can take days to run and obtain the responses of the structure. Also, the user must have technical knowledge about finite elements and details of the modeled structures.

Considering these difficulties for pavement designers, it is necessary to have a simple model to replace this procedure, provided that the model maintains a high level of accuracy and robustness. The recently developed nonlinear, mathematical data-driven models seem to provide the tool needed by researchers to infer data and establish a model that captures underlying nonlinear relationships. Artificial neural networks (ANN) are a soft computing technique introduced in past decades for providing rapid solutions to complex problems. Soft computing techniques, in general, and ANN, in specific, have been increasingly used for solving complex civil engineering problems.

ANN modeling was used in this project to predict pavement responses for a given loading condition. FE database was used for developing neural network models. The developed FE models covered the material properties and loading of the extreme pavement structures for two typical DTA and WBT. Given these extreme cases, ANN models would interpolate the responses for any arbitrary intermediate cases in a fraction of a second without the need for running FE models.

Unlike regression methods, ANN is highly nonlinear. ANN is a statistical learning technique that infers from data and can efficiently handle noisy and erroneous data to describe the underlying phenomena. In fact, ANN is a mathematical representation of human neurons; it is a layered structured of parallel processing units called neurons. A number of neurons are arranged in layers to make a network. A typical three-layer ANN is shown in Figure 6-1.
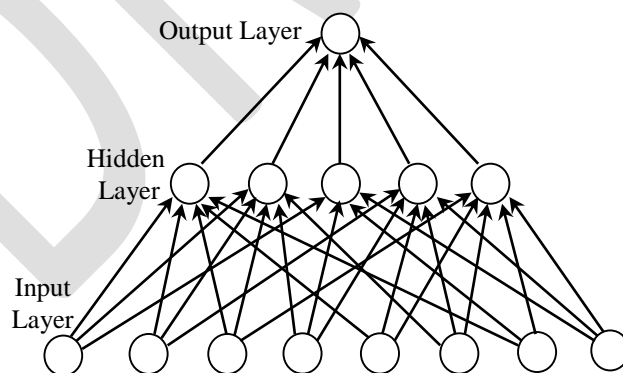


**Figure 6-1. Typical three-layer ANN model structure.**

The first layer is called the input layer and has as many neurons as the same number of independent variables defined in the problem. The middle layer is called the hidden layer and contains an arbitrary number of neurons, defined by trial and error. And the last layer is called the output layer and has the same number of neurons as the dependent variables of the problem. Neurons in one layer are connected to the neurons in the next layer through links called weight factors. ANN modeling is used for determining the

weight factors in a way so that the output of the ANN network is as close as possible to the target value for a specific set of input variables. This is accomplished through an optimization algorithm which adjusts the weights to minimize error between the output and the target. Neurons receive the weighted inputs from previous layer and pass them through a function called activation function; then, the weighted inputs are summed up and passed to the next layer.

Development of an ANN model involves three steps: training, validation, and testing. Accordingly, the database is divided into three datasets. Training data are used to train the network and acquire the weights. Cross-validation data are used for testing the network during training, this dataset represents a measure for training termination, overtraining, and overall generalization ability of the network. Finally, network performance is checked with test data that the network has not seen; this dataset represents a measure for network generalization ability.

In general, training the network consists of the following steps:
1. Weights are randomly generated in each link.
2. Each data sample is set to the input layer.
3. Value of each independent variable $x_i$ in each neuron of the input layer is multiplied by the weight links to the next layer ($w_{ij}x_i$ for $j = 1, 2, \ldots, m$).
4. Each neuron in hidden layer calculates the weighted sum as:

$$net_j = \sum_{i=1}^{n} w_{ij}x_i + bias_j \tag{6.1}$$

where $net_j$ is the weighted sum of the $j$-th neuron and $w_{ij}$ is the weight between neuron $i$ in the preceding layer and the neuron $j$.

5. The output of the $j$-th neuron is calculated with an activation function:

$$out_j = F(net_j) \tag{6.2}$$

where $F$ is the activation function. Two of the most popular activation functions based on their simplicity in calculations are:

   a. Sigmoidal function: $out_j = F(net_j) = \dfrac{1}{1+e^{-net_j}}$ \hfill (6.3)

   b. Hyperbolic tangent: $out_j = F(net_j) = \tanh(net_j)$ \hfill (6.4)

6. The output of the hidden layer proceeds forward to the output layer and Steps 4 and 5 are repeated to calculate the final outputs in the output layer.
7. The output of the network is compared with a target (desired) value to produce an error. The performance function for feed forward networks is the sum of square errors ($SSE$):

$$SEE = \sum_{k=1}^{l} (target_k - out_k)^2 \tag{6.5}$$

8. The error is back-propagated to the network and weights are altered until the desired sum of square errors is reached.

The performance function shown in Eq. 6.5 is a minimization problem where the weights are the decision variables. Several training algorithms are implemented for solving this problem, including gradient descent and gradient descent with momentum, which are popular, but slow (Caglar et al., 2008). An adaptive fast training algorithm known as Levenberg-Marquardt is also available. For more details on ANN methodology, one may refer to Schalkoff (Schalkoff , 1997), Tabatabaee et al. (Tabatabaee et al., 2013), and Moghaddam et al. (Moghaddam et al., 2010).

## 6.1    DATABASE

ANN modeling data include thin and thick pavement structures. According to FE test matrix, the database for ANN modeling consists of 12 load cases. Each load case has 16 and 32 cases (data samples) for thick and thin structures, respectively, totaling 192 thick and 384 thin case data samples. Also, eight cases of medium structure were added to the database to account for some intermediate cases. Table 6-1 through Table 6-3 show the pavement structure for thin, thick, and medium cases, respectively. Two different materials were defined as part of the test matrix to represent weak and strong material limits. Figure 6-2 shows dynamic modulus ($|E^*|$) master curve for weak and strong materials for different layers obtained from analysis of hundreds of mixes from LTPP database. Weak and strong cases were selected to represent extreme cases, where all materials in the analyzed LTPP database fall within the ranges defined by strong and weak materials. Medium cases are basically a combination of weak and strong cases.

**Table 6-1. Weak and Strong Cases - Thin Pavement Structures**

|  | Materials | Thicknesses (mm) |
|---|---|---|
| **AC Layer** | WS-Weak WS-Strong | 75 and 125 mm |
| **Base Granular** | 140 and 415 MPa | 150 and 600 mm |
| **Subgrade** | 35 and 140 MPa | -- |

**Table 6-2. Weak and Strong Cases - Thick Pavement Structures**

|  | Materials | Thicknesses (mm) |
|---|---|---|
| **AC Wearing Surface** | WS-Weak WS-Strong | 25 and 62.5mm |
| **AC Intermediate Layer** | IM-Weak IM-Strong | 37.5 and 100 mm |
| **AC Binder Layer** | BM-Weak BM-Strong | 62.5 and 250 mm |
| **Base Granular** | 140 and 415 MPa | 150 and 600mm |
| **Subgrade** | 70 MPa | -- |

**Table 6-3. Medium Cases – Thin Structures**

| Layer | Materials | Thickness (mm) |
|---|---|---|
| **AC** | IM-Strong | 102 |
| **Base Granular** | 277.5 MPa | 203 |
| **Subgrade** | 65 MPa | -- |

**Table 6-4. Medium Cases –Thick Structures**

| AC Wearing Surface | WS-Weak | 50.8 |
|---|---|---|
| AC Intermediate | IM-Strong | 50.8 |
| AC Binder | BM-Weak | 254 |
| Base Granular | 277.5 MPa | 12 |
| Subgrade | 70 MPa | -- |
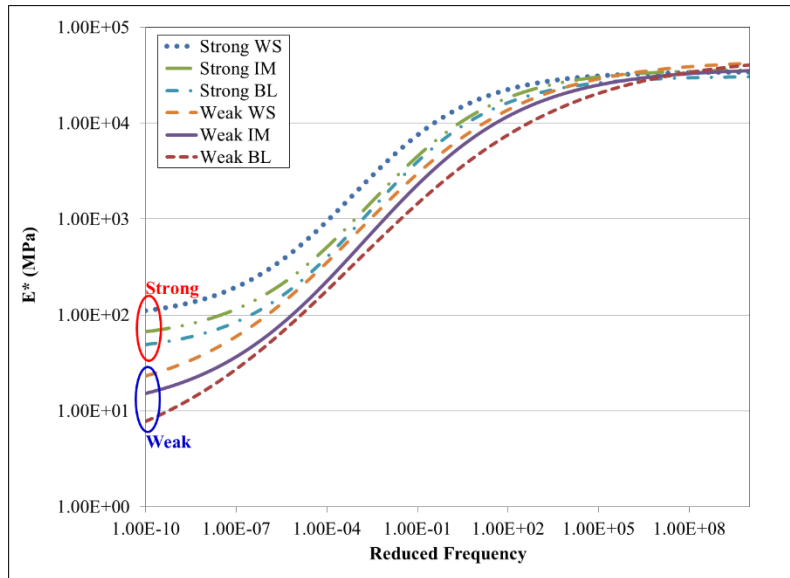


**Figure 6-2. Dynamic modulus |$E^*$| master curve for weak and strong AC layers.**

## 6.2   MODEL DEVELOPMENT AND TRAINING

For each pavement response, an ANN model was developed based on FEM results. Eleven responses, including longitudinal and transverse strains at surface and bottom of AC and vertical and shear strain in base and top of subgrade, were modeled. Critical variables affecting the responses were used as input variables. Variables are categorized under loading or structure. Table 6-5 summarizes the dependent and independent variables.

**Table 6-5. Dependant and Independant Variables Defined for Modeling**

| Category | Independent Variable | Type | Range | Dependent Variable | Type |
|---|---|---|---|---|---|
| Loading | Tire Type (WBT/DTA) | Binary | 0-1 | Long-Strain-Surface | Continuous |
| Loading | Differential Tire Pressure | Binary | 0-1 | Trans-Strain-Surface | Continuous |
| Loading | Axle Load (kN) | Continuous | 24.5-79.3 | Long-Strain-BttmAC | Continuous |
| Loading | Tire Pressure (kPa) | Continuous | 552-862 | Trans-Strain-BttmAC | Continuous |
| Thin Structure | AC Thickness (mm) | Continuous | 75-125 | Vert-Strain-AC | Continuous |
| Thin Structure | AC Material Properties | Continuous | Weak-Strong (master curve) | Vert-Strain-Base | Continuous |
| Thin Structure | Base Thickness (mm) | Continuous | 150-600 | Vert-Strain-SG | Continuous |
| Thin Structure | Base Material (modulus MPa) | Continuous | 140-415 | Shear-Strain-AC | Continuous |
| Thin Structure | Subgrade Material (modulus MPa) | Continuous | 35-140 | Shear-Strain-Base | Continuous |

54

| Thick Structure | Wearing Surface Thickness (mm) | Continuous | 25-62.5 | Shear-Strain-SG | Continuous |
|---|---|---|---|---|---|
| Thick Structure | Intermediate Course Thickness (mm) | Continuous | 37.5-100 | Mises-Stress-AC | Continuous |
| Thick Structure | Binder Course Thickness (mm) | Continuous | 62.5-250 | | |
| Thick Structure | Wearing Surface Material Properties | Continuous | Weak-Strong (master curve) | | |
| Thick Structure | Intermediate Course Material Properties | Continuous | Weak-Strong (master curve) | | |
| Thick Structure | Binder Course Material Properties | Continuous | Weak-Strong (master curve) | | |
| Thick Structure | Base Thickness (mm) | Continuous | 150-600 | | |
| Thick Structure | Base Material (modulus MPa) | Continuous | 140-415 | | |

As part of the material property inputs for ANN modeling, three representative dynamic modulus values were used at reduced frequencies of 100, 0.01, and 1E-9 Hz from the master curves. The material properties for the medium cases are a combination of weak and strong cases. For thin structure, the corresponding AC material property is IM-Strong. Conversely, for thick structure, WS-Weak, IM-Strong and BM-Weak were used for wearing surface, intermediate layer, and binder layer, respectively, as shown in Figure 6-2.

The material properties, especially complex modulus, are not readily available. Therefore, two levels of input properties were defined to account for data availability issues, Level 1 for detailed material properties and Level 2 for receiving modulus of each layer at room temperature only. Level 1 is the most detailed input level where $|E^*|$, in terms of sigmoidal function coefficients, is required as input. $|E^*|$ is a fundamental material property that defines the stiffness as a function of temperature and loading time. Details are presented in section 3.1.1. For each response, a separate ANN model was designed and named Net1, Net2, and so on. All networks have three layers with one hidden layer. Levenberg-Marquardt was chosen as the training algorithm for all models. The number of neurons in the hidden layer was chosen on trial-and-error basis. A different number of neurons was tried, and the network with the least error in training was selected as the optimum number of neurons for that model. Figure 6-3 shows the variation of a sample training error versus the number of neurons, which was used as a criterion for selecting the number of neurons in the hidden layer for Net3 (Long-Strain-BttmAC). Sixteen is the optimum number of neurons for Net3. Similarlry, the optimum number of neurons was determined for all networks.

After deciding on each network configuration, training data were fed into the model. Using an algorithm, the network was trained to build the input-output realtionship. The next step was performance evaluation of models. In this step, prediction accuarcy was measured. The normalized root mean square error ($NRMSE$) and R-square were used as the performance measure for the models.
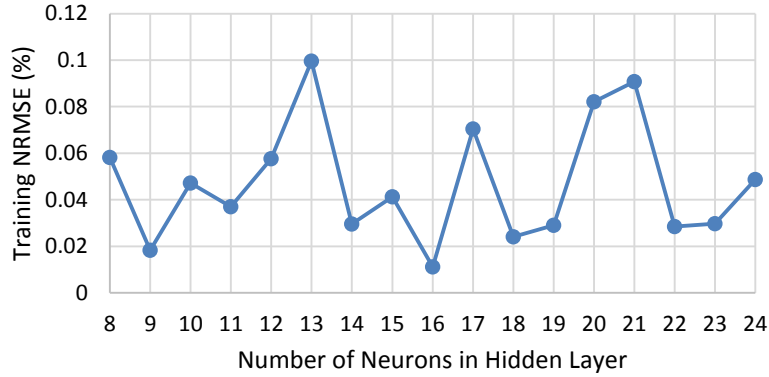
**Figure 6-3. Number of neurons in hidden layer versus training error for Net3 (long-strain, bottom of AC).**

$$NRMSE = \frac{N^2 \cdot RMSE}{N \sum_{i=1}^{N} d_i^2 - \left(\sum_{i=1}^{N} d_i\right)^2} \tag{6.6}$$

where:

$$RMSE = \sqrt{\frac{\sum_{i=1}^{N}(d_i - y_i)^2}{N}} \tag{6.7}$$

and: $d_i$ = desired output of $i$-th data
$y_i$ = Network output of i-th data
$N$ = number of data set.

Training data were used to train the networks, and test data were used to evaluate the networks' performance and validate the models. Therefore, the k-fold cross-validation technique was implemented.

### 6.2.1 K-fold Cross-Validation

The K-fold cross-validation technique was used to evaluate performance of the trained networks. In this technique, the database is divided into number of folds, and each fold is used as the test set one at a time. The best model is considered the one demonstrating the best performance on test data. Data are usually divided randomly into different folds to ensure unbiased comparison of models. In this study, however, unlike random approach, 12 folds corresponding to 12 load cases were used. If test and training sets were randomly assigned, some data samples from a load case would be part of the training dataset while others from the same load case would be part of the test dataset. During training, the model adapts itself to the load cases in the training set. Since data samples in each load case has identical loading information and only some of the variables have varying values, this would cause overtraining and better performance on the test data from the same load case and poor performance on the other load cases, thus adversely affecting the generalization ability of the model.

### 6.3 RESULTS

For each response, an ANN model was developed and tested for validation. Figure 6-4 shows sample performance results for all responses using thick and thin models with one standard deviation band. Vertical axis is the average percentage of error on all test folds. Figure 6-5 shows the scatter plot and R-square result of the thick and thin models for three responses. Figure 6-5 is based on the best trained model and corresponding load case. Table 6-5 summarizes the test results for all models based on average performance on all 12 folds.
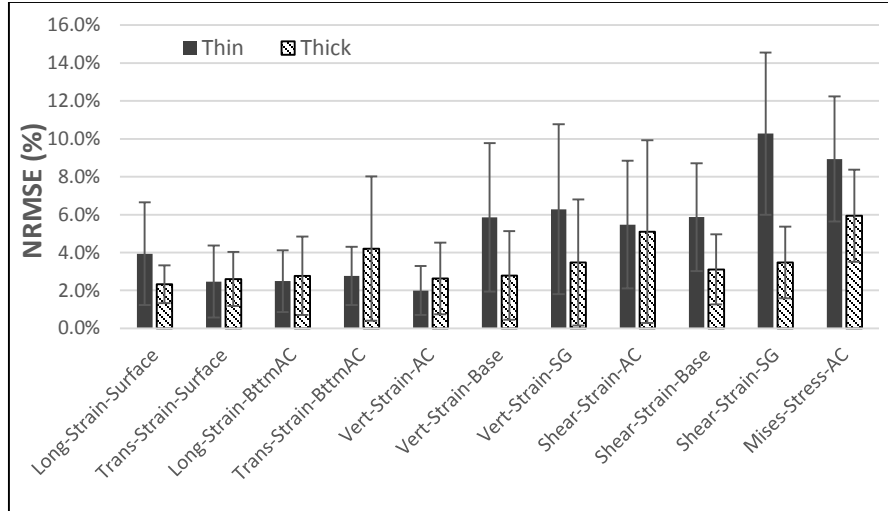
**Figure 6-4. Sample prediction error for all responses using thin and thick models with Level 1 inputs.**
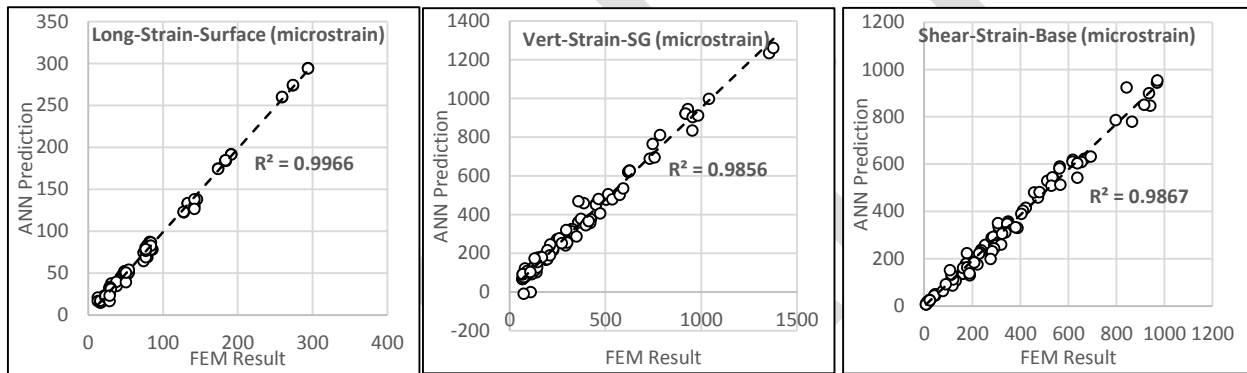


**Figure 6-5. Scatter plot of FEM simulation versus ANN prediction for thick Level 1 model.**

**Table 6-6. Summary of Average  Performance of Models for All Folds**

|  | Thick Level 1 | Thick Level 1 | Thick Level 2 | Thick Level 2 | Thin Level 1 | Thin Level 1 | Thin Level 2 | Thin Level 2 |
|---|---|---|---|---|---|---|---|---|
|  | $R^2$ | %NRMSE | $R^2$ | %NRMSE | $R^2$ | %NRMSE | $R^2$ | %NRMSE |
| Long-Strain-Surface | 0.9955 | 1.61 | 0.9953 | 3.05 | 0.9855 | 4.08 | 0.9970 | 1.65 |
| Trans-Strain-Surface | 0.9907 | 2.34 | 0.9978 | 2.86 | 0.9971 | 2.46 | 0.9789 | 3.09 |
| Long-Strain-BttmAC | 0.9997 | 2.41 | 0.9998 | 3.14 | 0.9953 | 2.52 | 0.9906 | 2.56 |
| Trans-Strain-BttmAC | 0.9966 | 2.89 | 0.9990 | 5.53 | 0.9995 | 2.90 | 0.9984 | 2.33 |
| Vert-Strain-AC | 0.9590 | 1.51 | 0.9988 | 3.74 | 0.9974 | 1.99 | 0.9994 | 1.73 |
| Vert-Strain-Base | 0.9934 | 2.66 | 0.9917 | 2.92 | 0.9993 | 6.58 | 0.9991 | 4.04 |
| Vert-Strain-SG | 0.9999 | 2.92 | 0.9980 | 4.03 | 0.9990 | 6.77 | 0.9960 | 5.48 |
| Shear-Strain-AC | 0.9655 | 4.68 | 0.9971 | 5.53 | 0.9977 | 6.35 | 0.9980 | 5.19 |
| Shear-Strain-Base | 0.9983 | 3.23 | 0.9946 | 2.98 | 0.9740 | 6.34 | 0.9657 | 4.59 |
| Shear-Strain-SG | 0.9756 | 3.35 | 0.9894 | 3.59 | 0.9844 | 11.37 | 0.9997 | 4.19 |
| Mises-Stress-AC | 0.9467 | 6.21 | 0.9678 | 5.69 | 0.9839 | 9.66 | 0.9884 | 6.14 |
| **Average** | **0.9837** | **3.07** | **0.9936** | **3.92** | **0.9921** | **5.55** | **0.9919** | **3.73** |
| **STD** | **0.0180** | **1.29** | **0.0087** | **1.08** | **0.0082** | **2.94** | **0.0103** | **1.48** |

According to the results, the models trained well and no overtraining was observed . The average error for all models was 3.85% with standard deviation of 1.38. In general, the prediction error for shear strains was

the highest, which might be attributed to the complex nature of the shear strians within the pavement structure. No specific trends were obsererved for thin and thick cases and between Level 1 and Level 2. Although Level 1 models are more informative about material properties than Level 2 models, this does not neccesserly lead to better performance. Level 1 used three variables to describe material properties while Level 2 used one material property only. Additional information means more input variables added to the model (in this case 2 and 6 additional variables for thin and thick cases, respectively) without adding extra observations (data samples), thus increasing the complexitiy of the model. Furthermore, all material propeties correlate with each other, which in modeling prospective does not necessarily result in better performance. However, using three variables is a good representation of a viscoleastic material when dealing with data other than that used for modeling. In this case, two materials with the same modulus at room temperature, may have completely different viscoelastic behavior.

## 6.4   SENSITIVITY ANALYSIS

To investigate the importance of the input variables in ANN modeling scheme, a series of sensitivity analyses were conducted. The missing data problem and incremental sensitivity [also called one-at-a-time (OAT) analysis] method were implemented to analyze sensitivity. In the former, one variable was removed from the model at a time and output error was calculated. The relative importance of the variables was evaluated by comparing the output errors. The higher the error, the more important the variable. Figure 6-6 shows the missing data sensitivity results for thin and thick structures with variables aggregated into four categories: pavement structure, load, tire type, and tire pressure.



| | Pavement Structure | Load | TireType (WBTvsDTA) | Tire Inflation Pressure |
|---|---|---|---|---|
| ■ Missing Data_Thin | 18.5% | 16.5% | 8.9% | 5.2% |
| ⊠ Missing Data_Thick | 21.0% | 15.9% | 10.3% | 3.3% |
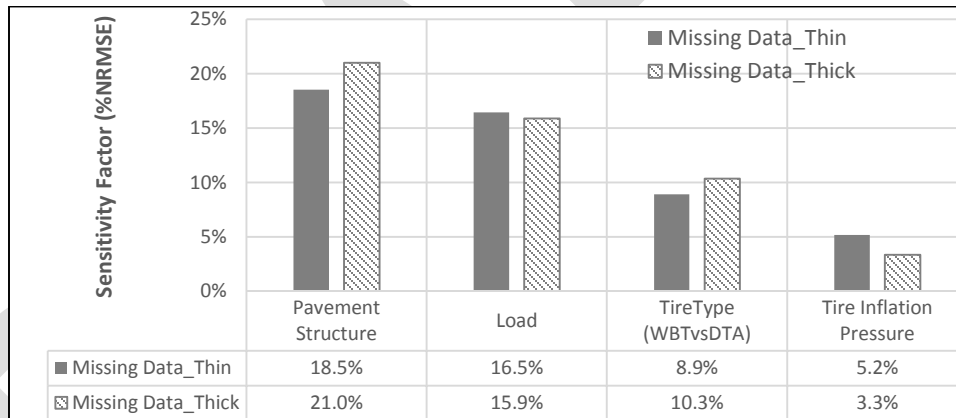
**Figure 6-6. Missing data sensitivity analysis results for thin and thick structures averaged over all responses and Level 1 and Level 2 models.**

The vertical axis shows the amount of error incurred as a result of a missing variable, such as in the thick structures case. If there were no information about "pavement structure", the error would be 20.9%, making "pavement structure" the most important variable. It should be noted that, missing a specific variable is conditional on knowing the variable range; otherwise, it would be impossible to know the response without knowing, for instance, how much load is applied.

In OAT analysis, each variable gradually increases one step at a time from low to high values in the input range. The change in output is recorded while all other variables are kept at baseline values. Step length may vary for different variables depending on the unit, but the same number of steps should be used for all variables to obtain consistent results. At each step, a normalized sensitivity ratio (SR) was calculated using the following equation:

$$SR = \% \frac{\dfrac{y_{i+1}(x) - y_i(x)}{y_i(x)}}{\dfrac{x_{i+1} - x_i}{x_i(x)}} \tag{6.8}$$

where: $y_{i+1}(x)$= model output in step $i + 1$ due to variable $x$
$\quad\quad y_i(x)$= model output in step $i$ due to variable $x$
$\quad\quad x_{i+1}$= value of variable in step $i + 1$
$\quad\quad x_i$= value of variable in step $i$

The $SR$ average over all steps is an indicator of the effect of the input on output; the higher the $SR$, the more important the variable. Figure 6-7 shows variable importance for thick and thin pavements in terms of SR. Twenty steps were used for this study.

According to the results of OAT analysis, an example trend analysis is provided in Figure 6-8 for one of the responses. This example shows the change of longitudinal strain at the bottom of the AC wearing surface layer with change of tire inflation pressure, load, and AC thickness.



| | Pavement Strucutre | Load | Tire Type | Tire Inflation Pressure |
|---|---|---|---|---|
| OAT_Thin | 0.04 | 0.02 | 0.01 | 0.00 |
| OAT_Thick | 0.10 | 0.05 | 0.01 | 0.01 |
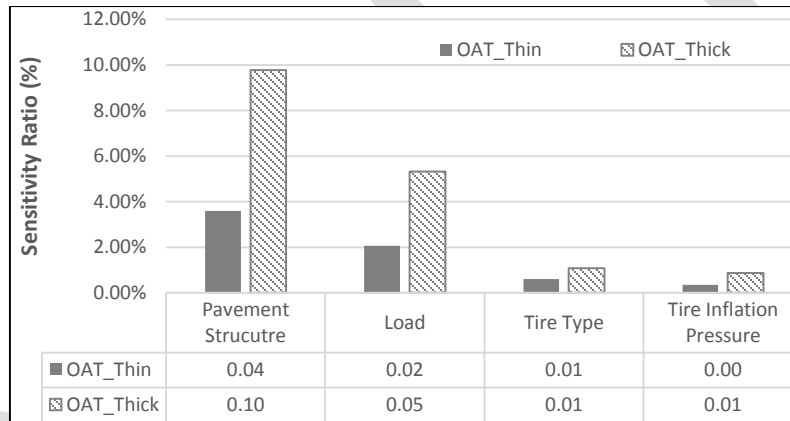
**Figure 6-7. OAT sensitivity analysis results for thin and thick pavement structures averaged over all responses and Level 1 and Level 2 models.**

Both sensitivity methods use different scales to determine the importance of variables; therefore, a sensitivity factor in a scale from 0 to 1 was defined, and the results were normalized to this scale. Figure 6-9 shows a comparison of the sensitivity factor from both methods in one scale averaged over thin and thick structures, all responses, and all levels. According to sensitivity factor results, the pavement structure had the highest effect in both cases. Load is a little more emphasized in the missing data problem. It can also be noted that tire type plays an important role in pavement response calculation. This means that 10 to 30% influence on responses is caused by wide-base tire versus dual-tire, which is somewhat equal to the effect of tire pressure.

## 6.5    ICT-WIDE TOOL

To assist agencies and designers in the evaluation of the effect of WBT on pavements, all trained models were incorporated into a tool called the Illinois Center for Transportation wide-base tool (ICT-wide tool). The tool is a stand-alone Matlab-based tool that can be installed on any Windows operating system. Snapshots and a step-by-step procedure to use the tool are provided in Appendix D.
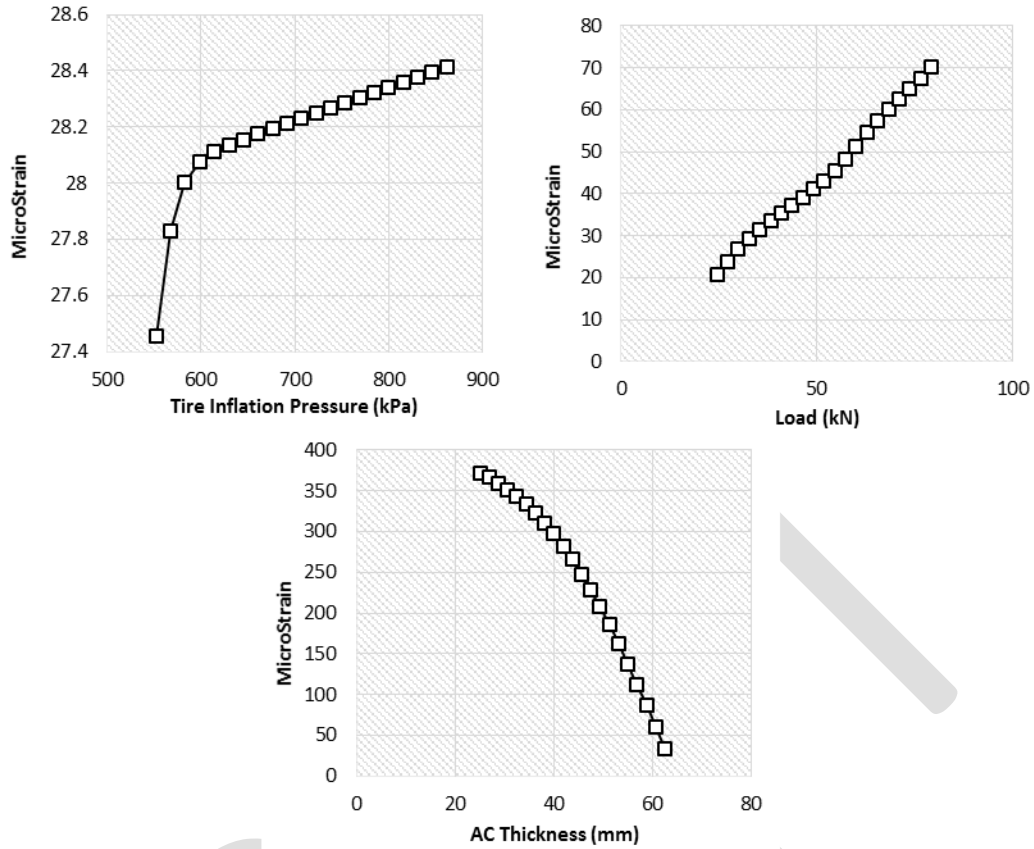
**Figure 6-8. Change of longitudinal strain at bottom of surface with change in: tire inflation pressure, load, and AC thickness.**



| | Pavement Structure | Load | Tire Type (WBTvsDTA) | Tire Inflation Pressure |
|---|---|---|---|---|
| ■ Missing Data | 1.00 | 0.82 | 0.49 | 0.22 |
| ▨ One-at-a-time | 1.00 | 0.55 | 0.13 | 0.09 |
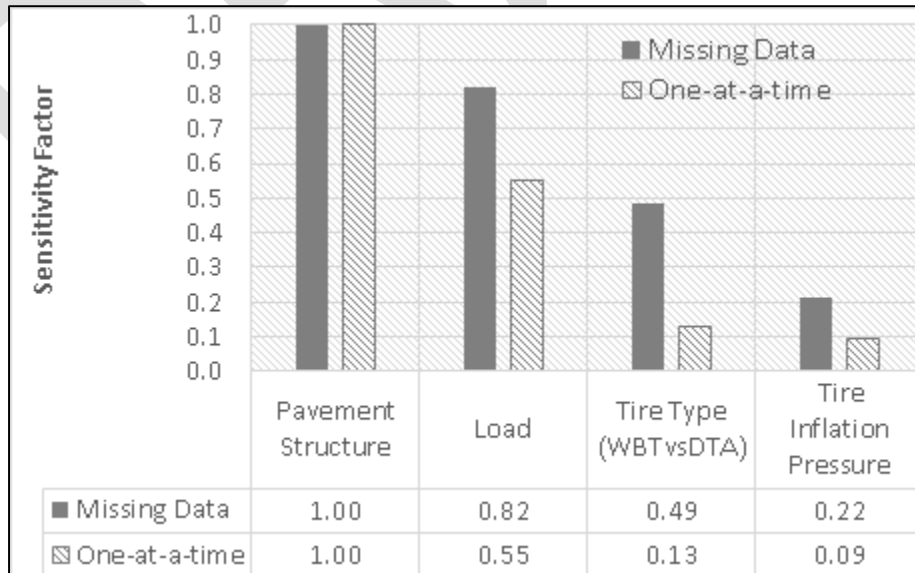
**Figure 6-9. Sensitivity factor averaged over all models.**

## 6.6 SUMMARY

A nonlinear mathematical model, ANN, was developed to replace the more sophisticated numerical FE model. The test matrix developed for FE models was used as the database for ANN modeling. A total of 44 ANN models was developed for each response (11 responses in total), pavement structure (thin and thick), and input level (Levels 1 and 2). Pavement loading information as well as pavement structure and material information were used as model variables. A 12-fold cross-validation technique was used in developing the models. One loading case out of the 12 load cases was set aside as a test dataset and 11 load cases were used as training dataset.

The results showed the ability of ANN models to predict responses in agreement with FE model results. Two sensitivity analysis, the missing data problem and OAT, were conducted to evaluate the variable effect on responses. The results indicate the significance of tire type (wide-base versus dual) on the responses as the selection of a tire type on the other one can cause up to 10% difference in response prediction and hence in pavement damage. This indicates the importance of the dual versus wide-base tire assumption.

# 7 ADJUSTMENT FACTOR FOR AASHTOWARE

## 7.1 INTRODUCTION

All AASHTO pavement design guides issued between early 1960s and 1993 are based on empirical equations, which rely heavily on the results of the AASHO Road Test conducted in Ottawa, Illinois, in the late 1950s (AASHTO, 2008). In order for empirical design guides to deliver accurate performance prediction, design inputs for new pavement structure should be similar to the ones used in the AASHO Road Tests. However, tire type, truck type, axle load limits, and materials have significantly changed since AASHO Road Test.

The need to have a pavement design guide that incorporates changes in materials and loadings and considers direct climate effects on pavement performance was clearly recognized by researchers, engineers, and transportation institutions in 1986 (AASHTO, 2008). Consequently, NCHRP Project 1-37A was launched in 1998 under the sponsorship of the AASHTO, NCHRP and FHWA for the development of an advanced and comprehensive design guide. The MEPDG was released in 2004. Afterwards, MEPDG was reviewed and revised under NCHRP 1-40A, 1-40B and 1-40D, which resulted in the development of MEDPG design software in 2007 (later known as DARWin-ME) and MEPDG - A Manual of Practice, Interim Edition in 2008. In August 2013, the current version, AASHTOWare Pavement ME Design software, was released.

In MEPDG, the user assumes a pavement structure as a trial design and provides all other inputs to the software, such as traffic, material properties, and environmental conditions. Structural responses (strain, stress, and/or deflections) are then calculated within the pavement, which refers to the mechanistic part of the guide. By exploiting empirical models, these responses are linked to distress propagations over a design period and are consequently used for IRI assessment. Finally, the user checks design criteria against predicted ones. If design requirements are not satisfied, trial design should be modified and the steps should be repeated until design requirements are met. Figure 7-1 illustrates the MEPDG procedure.

Accurate prediction of the pavement responses is key for realistic simulation of distress propagation over time. Although MEDPG has a grounded methodology for pavement analysis, it has a number of limitations and unrealistic simplifications that result in inaccurate response predictions. On the other hand, and as indicated earlier, FE analysis simulates pavement responses more realistically in terms of loading conditions and material characterization. Therefore, a correction factor must be developed for structural pavement responses calculated by the MEPDG in accordance with FE results.

## 7.2 MECHANISTIC PART OF THE DESIGN GUIDE AND ITS LIMITATIONS

The mechanistic part of the Guide refers to pavement analysis conducted for obtaining critical responses. MEPDG exploits the multi-layered linear elastic theory (MLET) to compute pavement responses under tire loads. Several types of software implement MLET, such as MnLayer, KenLayer, BISAR, and JULEA; MEPDG uses the JULEA in its framework.

MEPDG considers AC as viscoelastic, its behavior depends on time, temperature, and frequency of loading. MEPDG incorporates the stiffening of AC layer with time through global aging model. On the other hand, temperature within the pavement is determined using the integrated climate model (ICM). Frequency of loading is calculated as a function of vehicle speed, axle type (single, tandem, or tridem) and pavement structure. In addition, the pavement is divided into sub-layers to account for temperature and frequency changes with respect to depth. Dynamic modulus ($E^*$) is computed at the mid-depth of each sublayer by considering aging, temperature and frequency and injecting into JULEA along with other inputs such as layer thicknesses, loads, and tire pressures.
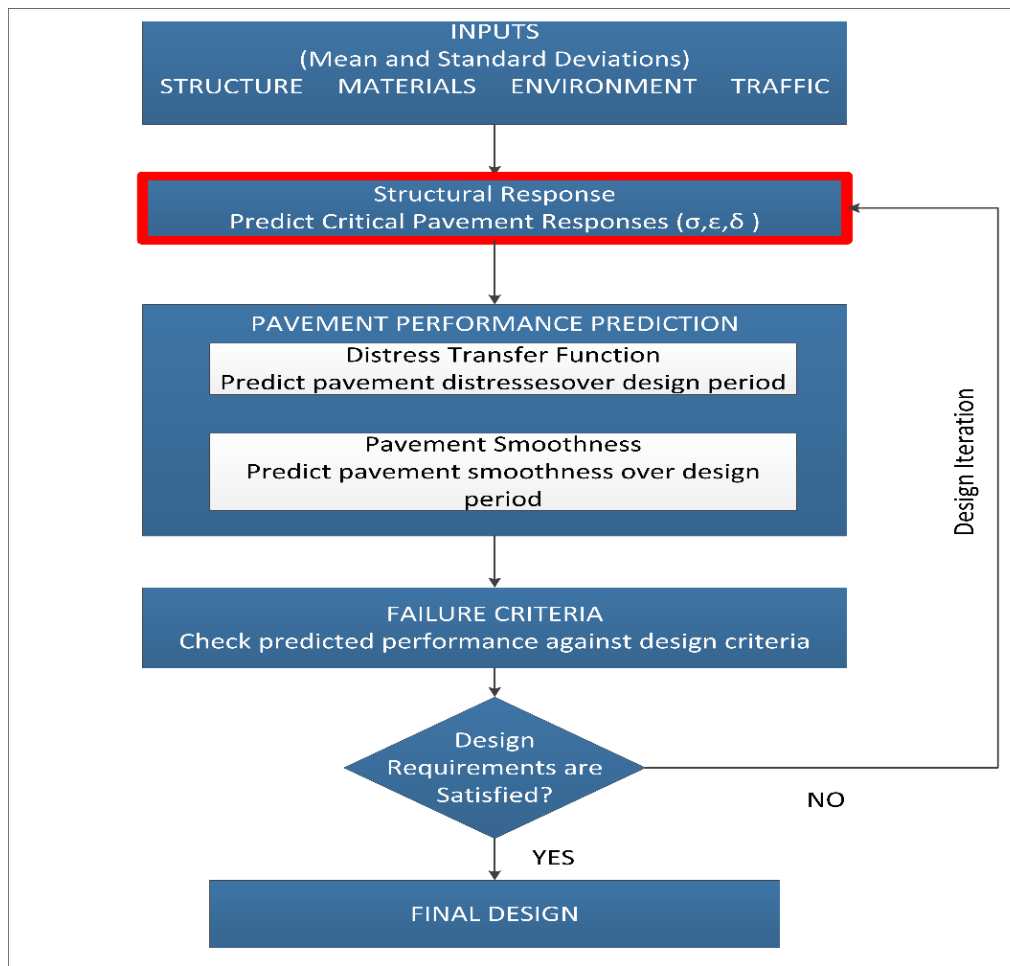
**Figure 7-1. MEPDG flowchart.**

The mechanistic part of the Guide also consists of a three-step procedure: i) subdivision of pavement structure; ii) calculation of modulus at the mid-depth of each sublayer considering aging, temperature and frequency of loading; and iii) running the JULEA with calculated dynamic modulus and other inputs such as thicknesses and load. Figure 7-2 shows MEDPG procedure for computing pavement responses.

Although the mechanistic part of the guide provides a theoretically sound procedure for computing critical pavement responses, it still has a number of limitations and simplifications, which may lead to unrealistic response prediction. These limitations and simplifications are mostly caused by the assumptions behind the MLET used in MEPDG's framework. On the other hand, FE method can simulate tire-pavement interaction more realistically by overcoming most of MEPDG's limitations.

### 7.2.1 Limitations of MEPDG Procedure for Loading Frequency Calculation

Table 7-1 demonstrates the limitations of MEPDG by comparing it with FEA. Tire-pavement interaction is simulated unrealistically because of the assumptions behind the MLET, such as uniform 2-D vertical tire pressure and circular contact area. In addition, Al-Qadi et al. (Al-Qadi et al., 2008a; Al-Qadi et al., 2008b) proved that additional errors are introduced by MEPDG procedure for calculating loading frequency, which translates into inaccurate dynamic modulus calculation. The error in frequency calculation varies from 40% to 140% depending on vehicle speed and depth of calculation. There are two main sources of error in

frequency calculation procedure: i) conversion from time domain to frequency domain, and ii) assuming stress distribution with 45° through the pavement's depth.
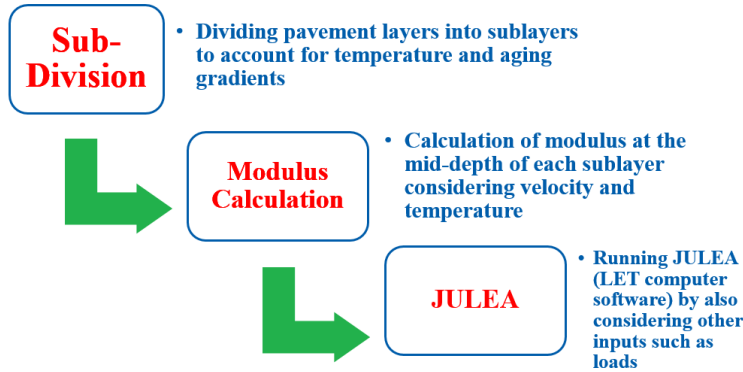


**Figure 7-2. MEPDG procedure.**

MEPDG calculates loading frequency using Eq. 7.1. Al-Qadi et al. (2008) proved that this conversion does not realistically simulate loading frequency and is, thus, the first source of error. In the same study, a novel approach is suggested based on Fast Fourier Transformation and validated by FE simulations:

$$f = \frac{1}{t} \tag{7.1}$$

where: $t$ = time of loading (s) and $f$ = frequency of loading (Hz).
Time of loading is calculated as follows:

$$t = \frac{L_{eff}}{17.6 \, v_s} \tag{7.2}$$

where: $v_s$ = vehicle speed, $L_{eff}$=Effective Length.

**Table 7-1. Limitation of MEPDG Procedure by Comparing FEA**

|  | FEA | MEPDG Procedure |
|---|---|---|
| **Analysis Type** | Dynamic analysis, considering motion of tire and viscoelasticity of AC | Linear Elastic Analysis |
| **Tire Type** | Both WBT and DTA can be simulated | Only DTA can be considered |
| **Contact Stress** | Nonuniform realistic measured 3-D contact stresses | 2-D uniform vertical pressure |
| **Contact Area** | True measured tire contact area | Circular contact area |
| **Speed and Temperature** | Directly considered in viscoelastic dynamic analysis | Implicitly considered in dynamic modulus calculations |
| **Friction Between Layers** | Elastic Stick Model, defined by $\tau_{max}$ and $d_{max}$ | Distributed Spring Model |

| AC Layer Material Properties | Viscoelastic characterization using Prony Series | Dynamic modulus obtained from master curve (MEPDG procedure)** |
|---|---|---|
| **Base Layer** | Stress-dependent, nonlinear model for base – especially important for thin pavement | Linear elastic |

To calculate effective length, all layer thicknesses are transformed into their equivalent thicknesses based on stiffness of the subgrade layer. This process is known as Odemark's method of thickness equivalency (Figure 7-3).
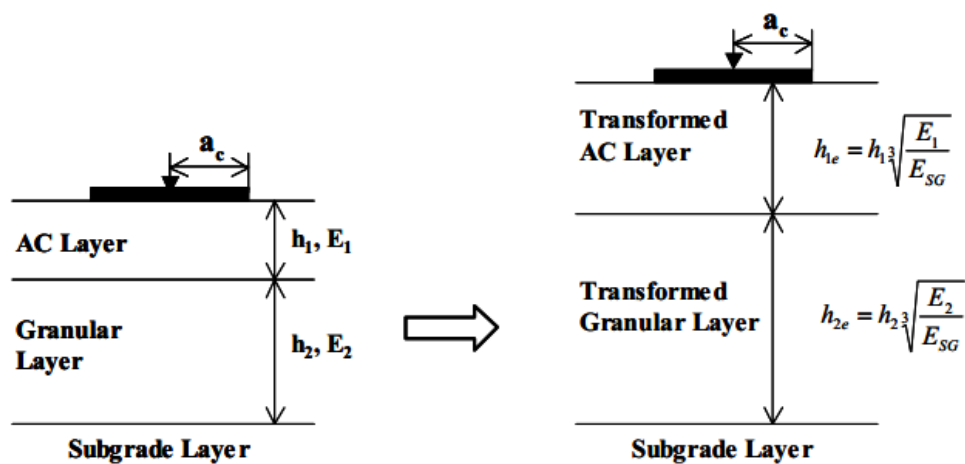


$$h_e = h_{1e} + h_{2e} = h_1 \sqrt[3]{\frac{E_1}{E_{SG}}} + h_2 \sqrt[3]{\frac{E_2}{E_{SG}}} = \sum_{i=1}^{i=n-1} h_i \sqrt[3]{\frac{E_i}{E_{SG}}}$$

**Figure 7-3. Odemark's method of thickness equivalency (NCHRP, 2004).**

After transforming all layer thicknesses, the effective length (Eq. 7.3) is computed by assuming that stress is distributed at $45°$ through the soil depth (Figure 7-4). This assumption is considered the second source of error in frequency calculation. The assumption especially fails to capture far-field effect of approaching-leaving rolling wheel (Al-Qadi et al., 2008). The detailed procedure for calculating frequency of loading is found in NCHRP 2004 (NCHRP Appendix CC).

$$L_{eff} = 2 * (a_c + Z_{eff}) \tag{7.3}$$
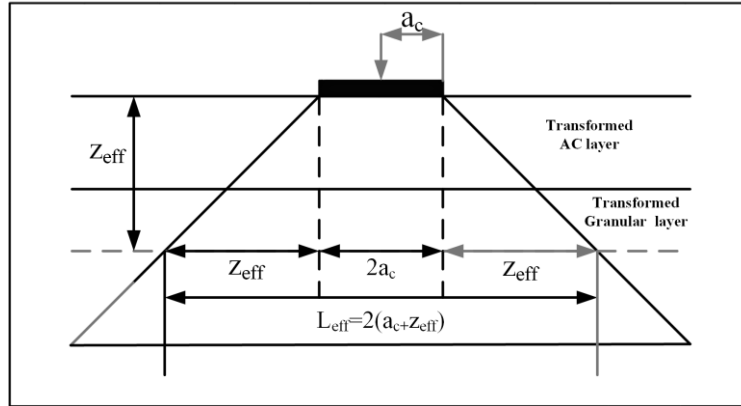
**Figure 7-4. Stress distribution through soil depth.**

## 7.3 DEVELOPMENT OF THE ADJUSTMENT FACTORNT

Pavement ME Design procedure for computing pavement responses has a number of limitations, including the two-dimensional uniform vertical tire pressure with circular contact area, linear elastic analysis of AC layer, and static tire loading. In addition, the procedure is incapable of considering WBT. Therefore, two adjustment factors are proposed: i) adjust to DTA based on FE results when using a wide-base tire; and ii) convert to MEPDG from FE results of DTA. The proposed method is summarized in Figure 7-5.
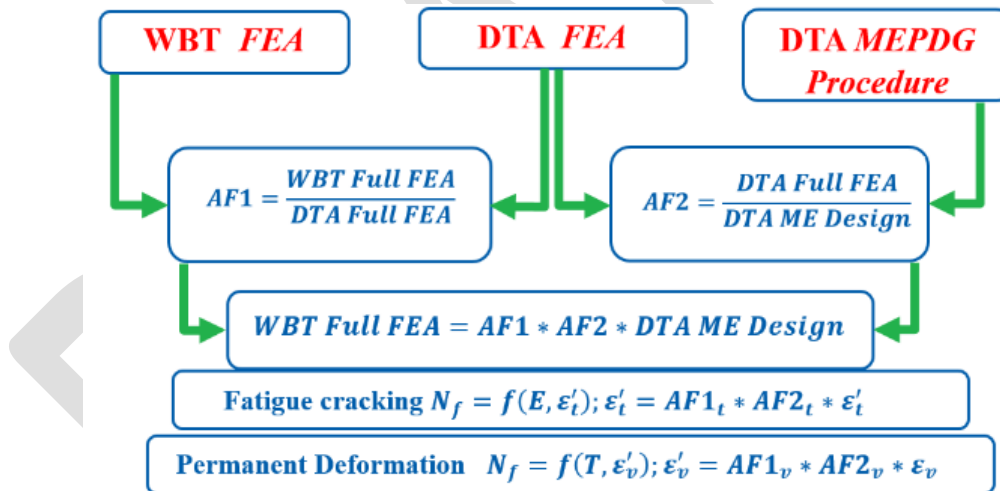

**Figure 7-5. Adjustment factor approach.**

### 7.3.1 Adjustment Factor 1

Adjustment Factor 1 ($AF1$) was developed to convert the response resulting from DTA into NG-WBT. For $AF1$, only FE simulations were used because MLET is not capable of simulating the response NG-WBT properly. $AF1$ was developed using the ABAQUS, which runs considering the same material properties and pavement structures. The only difference was the contact stresses and contact areas which were measured under the same axle load for NG-WBT and DTA. $AF1$ is presented as linear function of the DTA response. Figure 7-6 through Figure 7-9 show the result for each pavement response. It should be noted that all plots have a line of equality ($y = x$) and a fitted straight line. The unity line is solid while the fitted line is dashed. The purpose of the equality line is to demonstrate the significance of applying an adjustment factor to each particular response.
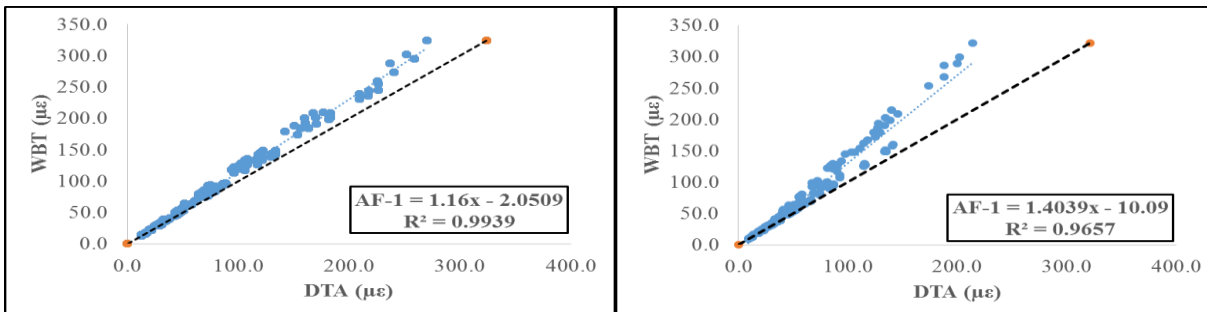
**Figure 7-6. Maximum tensile strain in traffic and transverse direction at AC surface.**
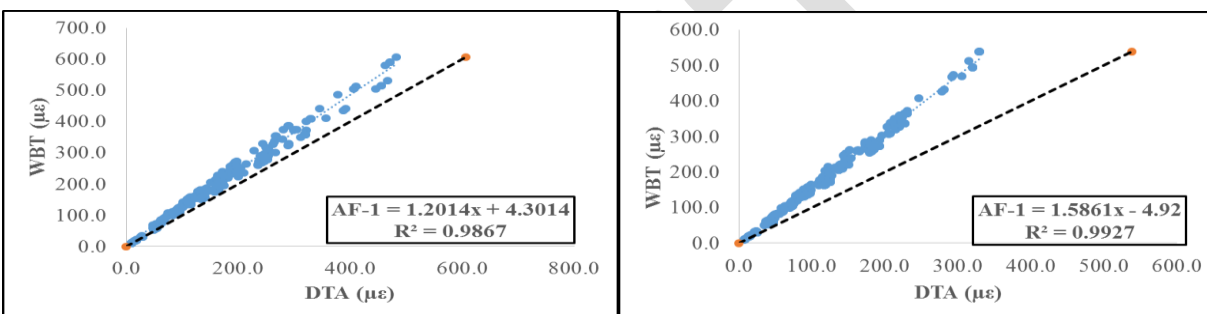


**Figure 7-7. Maximum tensile strain in traffic and transverse direction at bottom of AC.**
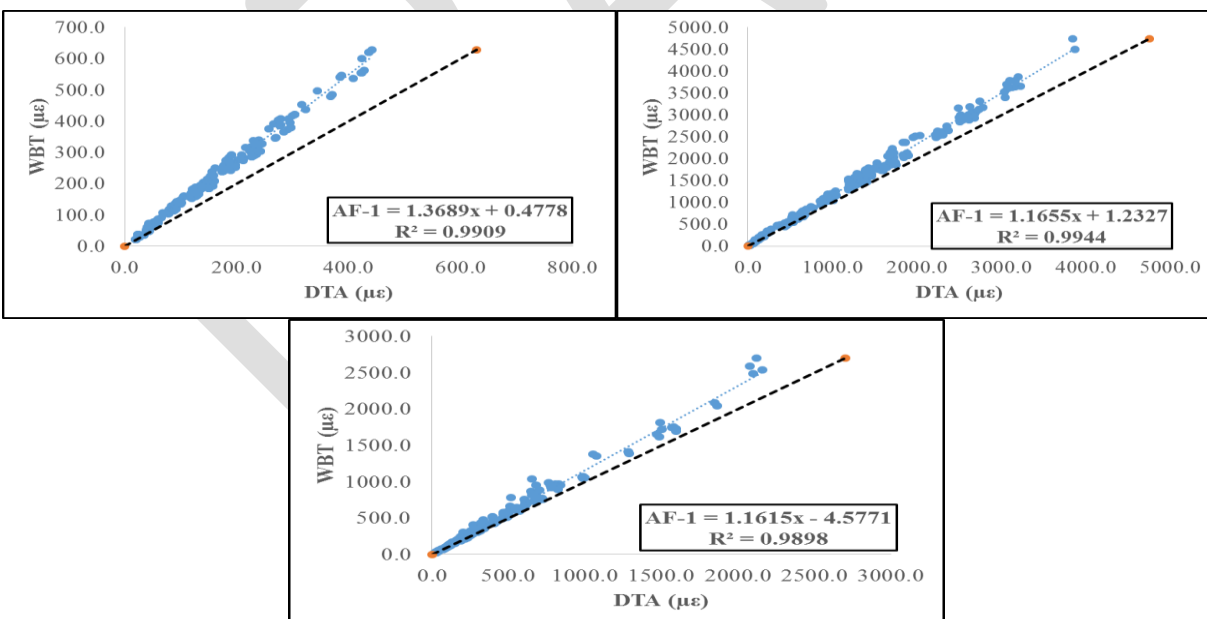


**Figure 7-8. Maximum compressive strain within AC, base, and subgrade.**
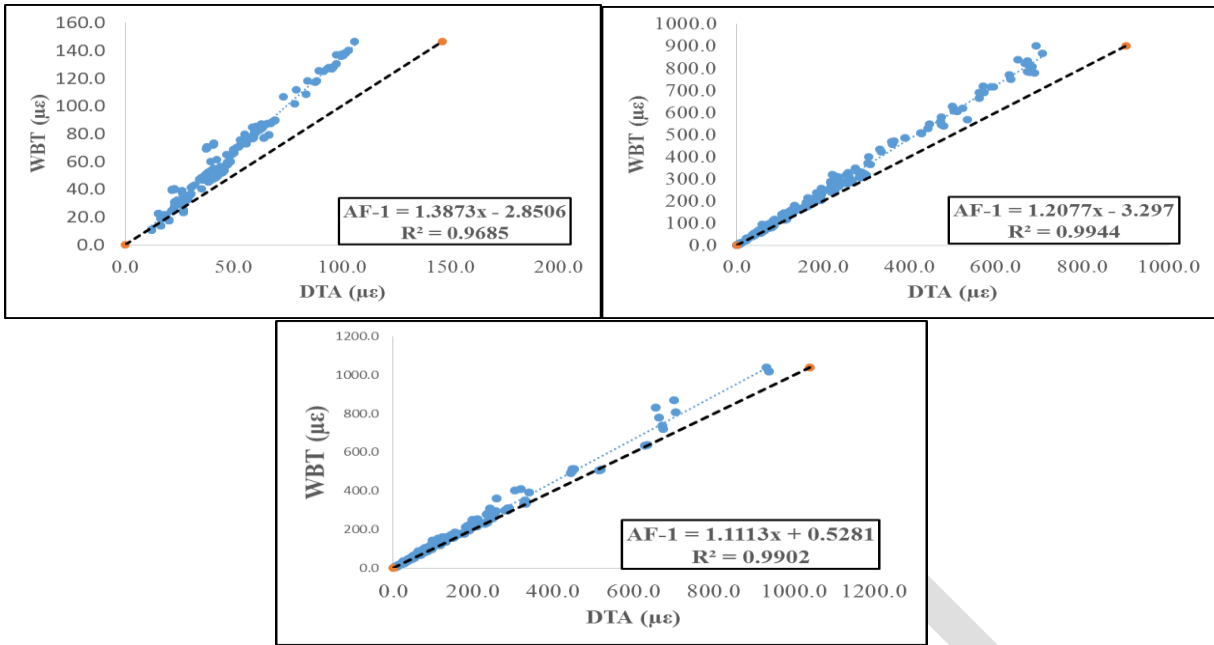
**Figure 7-9. Maximum shear strain within AC, base, and subgrade.**

### 7.3.2 Adjustment Factor 2

Adjustment factor 2 ($AF2$) was developed to modify the responses obtained from MEPDG procedure in accordance with FE analysis where tire-pavement interactions are simulated more accurately. The FE runs using DTA capturing extreme conditions (i.e., thick and thin pavement structures with strong and weak material properties) were used.

Initially, the AASHTOWare software was considered to obtain responses for the 336 cases. However, the implementation of MEPDG procedure as a separate numerical tool was needed for two reasons. First, it is time-consuming and cumbersome to run the AASHTOWare software for 336 cases, because the software uses a significant amount of inputs that make comparison to FE results impossible. For instance, the software uses axle load spectra, and only one set of contact stresses belonging to the specific axle load/tire pressure combination is considered in each FE simulation. In addition, AASHTOWare has temperature-based models for material characterization of base and subgrade. Conversely, in FE analysis, the base and subgrade are characterized without taking temperature into account as it would take tremendous effort and time to adopt ICM into FE model. Second, the AASHTOWare software only gives critical pavement responses (e.g., tensile strain at the bottom AC or compressive strain within base layer); however, comparing shear strain within the pavement is of interest in this study; which is not provided as an output in the software. It is believed that shear strain in AC is relevant to near-surface or near-surface cracking.

Therefore, the MEPDG procedure was implemented by exploiting Matlab and AutoHotkey. The main steps of the MEPDG's procedure implementation are listed below:
1. Subdivision of pavement structure in sub-layers.
2. Calculation of dynamic modulus at mid-depth of each sublayer.
3. Creation of input file.
4. Running JULEA (Linear Elastic Computer Program used by MEPDG).
5. Post-processing to obtain pavement responses.

Pavement structures were sub-divided by applying the algorithm provided in MEPDG. Moreover, dynamic moduli were computed based on the frequency calculation guidance given in section 7.2.1.

### 7.3.2.1 Input Conversion from FE Model to MEPDG

It is critical to convert all inputs used in the FE analysis into the MEPDG procedure to be able to run comparable cases. Table 7-2 compares all inputs from FEA with the MEPDG's procedure.

The same axle load and tire inflation pressure, applied during experiments to measure contact stresses, were used as loading inputs for MEPDG. The contact area was calculated by dividing the axle load over tire pressure. While speed was used to calculate frequency of loading using Eq.7.4, the temperature was embedded into shift factor calculation. The same material parameters (e.g., elastic modulus and master curve) were given as input to both FE model and MEPDG.

The elastic stick model (ESM) was represented in MEPDG procedure. The ESM is an improved version of the well-known Coulomb friction model, presented in Eq. 7.4:

$$\mu = \frac{\tau_{max}}{\sigma} \tag{7.4}$$

where:  $\mu$: friction coefficient
   $\tau_{max}$= maximum shear stress
   $\sigma$=normal stress at the interface

ESM allows tangential stress and a certain amount of elastic slip before the surfaces defining the interface start to slip (see Figure 7-10). In Romanoschi et al. (2001), $\tau_{max}$ and $d_{max}$ are suggested as 205 psi and 0.063 in for pavement modeling based on direct shear test results. Conversely, MLET assumes uniformly distributed shear spring to connect the interfaces and allow relative horizontal movement between two layers. The spring works in radial direction and follows the relationship in Eq. 7.5:

$$\tau_i = k_i * (u_i - u_{i+1}) \tag{7.5}$$

where:  $\tau_i$= radial shear stress at the interface between layers $i$ and $i+1$
   $u_i - u_{i+1}$= relative radial displacement across the interface
   $k_i$= interface spring stiffness

This law can be implemented in any layered elastic computer programs, including JULEA. To reduce numerical complications, JULEA converts Eq. 7.5 to Eq. 7.6 by using the variable $l$ given in Eq. 7.7:

$$(1 - l_i) \cdot \tau_i = l_i \cdot (u_i - u_{i+1}) \tag{7.6}$$
$$k_i = \frac{l_i}{1 - l_i} \tag{7.7}$$

The variable $l$ is computed using user-defined parameter $m$:

$$l = \begin{cases} 0 & \text{for } m \geq 100,000 \\ 10^{-m/E_2} & \text{for } m < 100,000 \end{cases} \tag{7.8}$$

Where, $E_2$= modulus of layer 2 (below the surface layer).

The spring stiffness is basically the slope of $\tau/d$ (Figure 7-10), i.e., ratio of $\tau_{max}$ and $d_{max}$. After computing spring stiffness, the user parameter $m$ is calculated using Eq. 7.9.

**Table 7-2. FEA and MEPDG Input Comparison**

|  | **FE (Reference)** | **MEPDG Procedure** |
|---|---|---|
| **Axle Load (P)** | Known | Known |
| **Contact Stress (p)** | Nonuniform, 3-D stresses (pressure + traction) – measured for each axle load-known | 2D uniform vertical stresses – applied inflation pressure |
| **Contact Area (A)** | True contact area – measured for each axle load | Circular (P/p) |
| **Motion of Tire (Speed)** | Tire is moved of a given velocity | Implicitly considered in dynamic modulus calculations |
| **Temperature** | Directly considered in viscoelastic analysis | Considered in dynamic modulus calculations |
| **Friction Between Layers** | Elastic Stick Model, defined by $\tau_{max}$ and $d_{max}$ | Friction coefficient (user input) |
| **AC Layer Material Properties** | Viscoelastic | Dynamic modulus obtained from master curve |
| **Base Layer** | Thick = Linear elastic | Linear elastic |
|  | Thin = Stress-dependent nonlinear model |  |
| **Subgrade** | Linear elastic | Linear elastic |
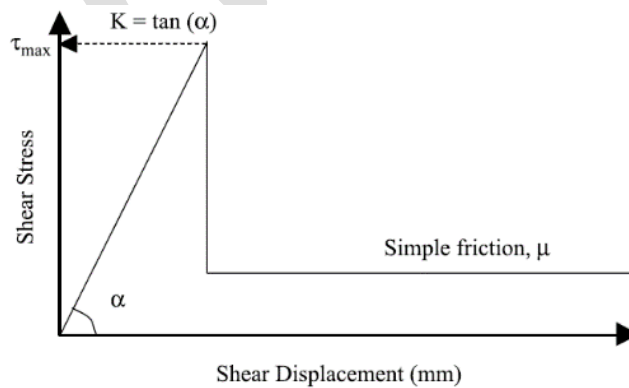


**Figure 7-10. Elastic stick model.**

Differences in loading conditions between FE and MEPDG (three-dimensionality and non-uniformity of the contact stresses), material characterization, and layer interaction, introduce serious challenges that complicate the development of *AF*2. To obtain statistically good correlation for *AF*2, the cases were divided into thick pavement, thin pavement with strong base material, and thin pavement with weak base material. The reasoning behind this division is discussed in the following section.

## 7.3.2.2.1  *AF*2 *for thick pavement*
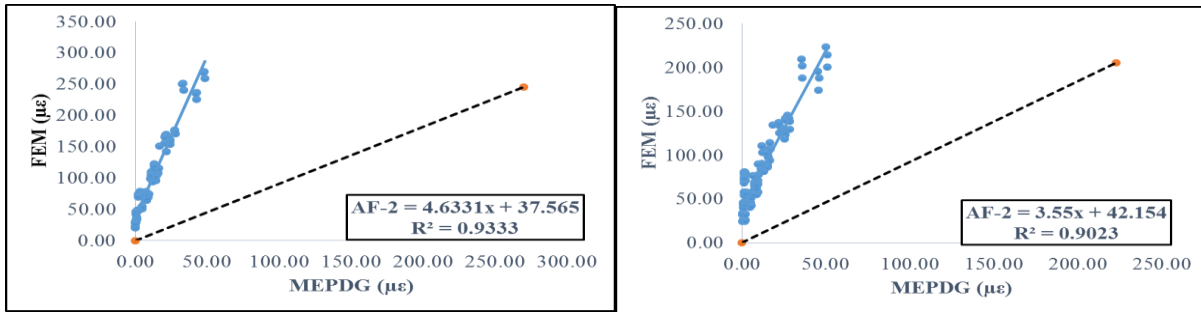


**Figure 7-11. Maximum tensile strain in traffic and transverse direction at AC surface.**
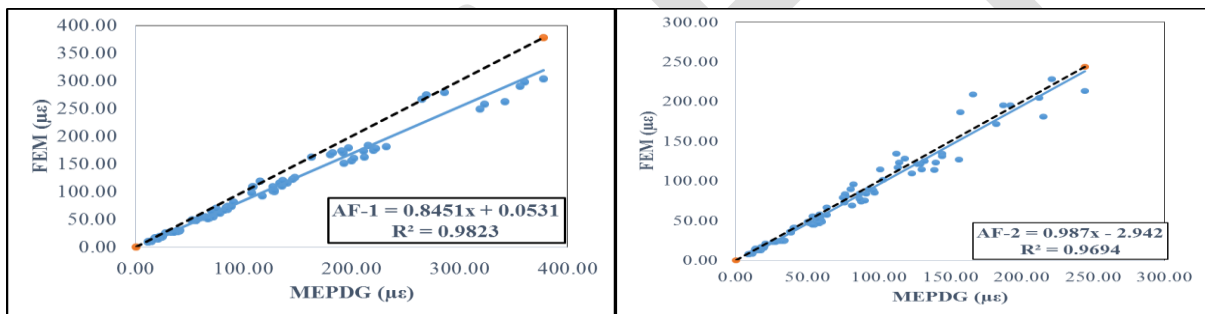


**Figure 7-12. Maximum tensile strain in traffic and transverse direction at bottom of AC.**
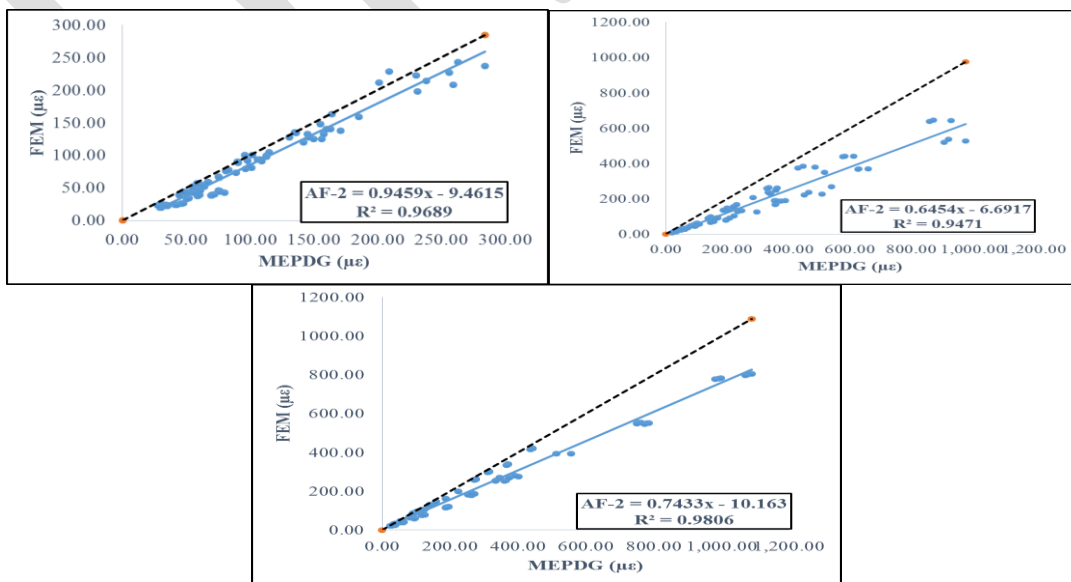


**Figure 7-13. Maximum compressive strain within AC, base, and subgrade.**

71
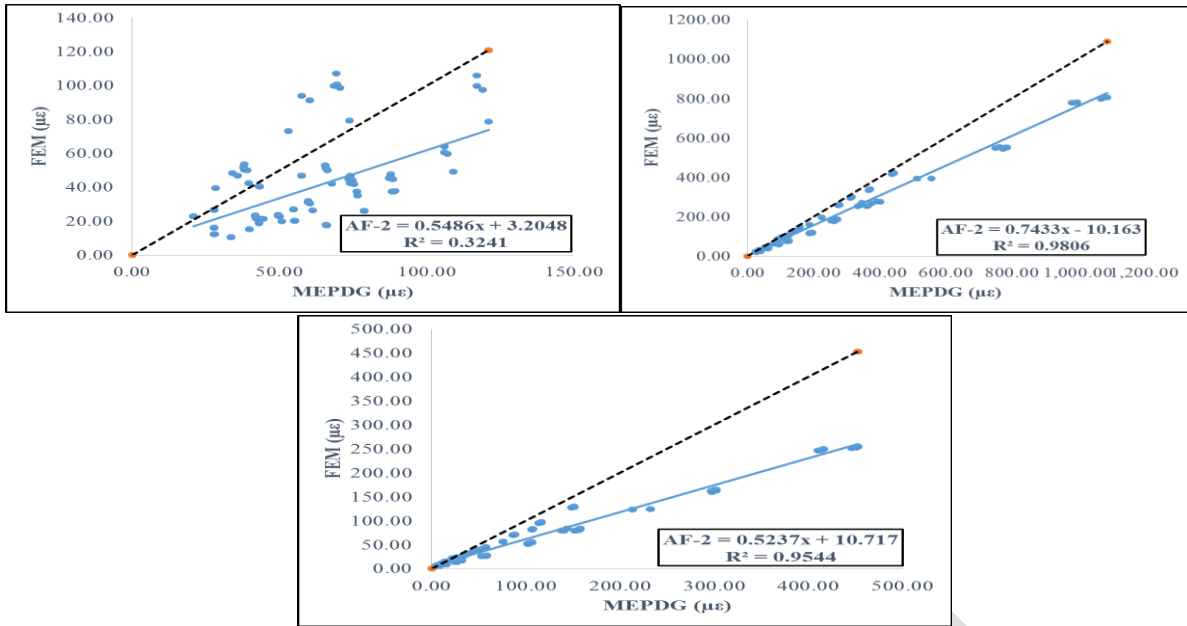
**Figure 7-14. Maximum shear strain within AC, base, and subgrade.**

### 7.3.2.2.2 $AF2$ for thin pavement: weak and strong base
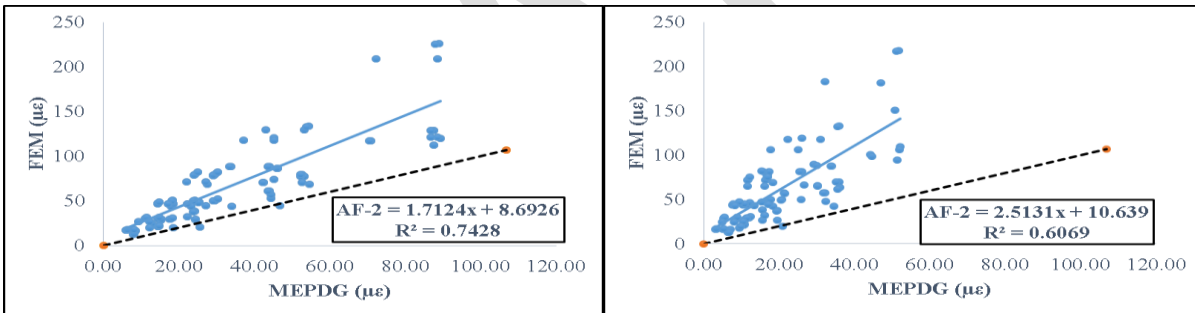

**Figure 7-15. Maximum tensile strain in traffic direction at AC surface for weak and strong base layers.**
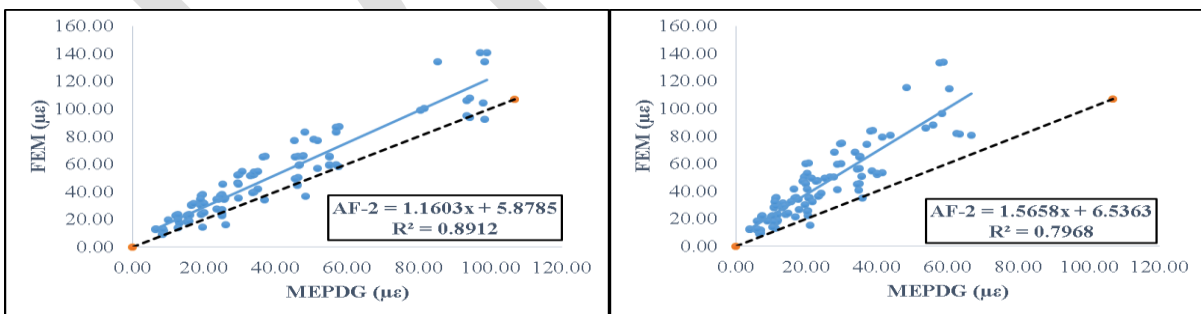

**Figure 7-16. Maximum tensile strain in transverse direction at AC surface for weak and strong base layers.**

72
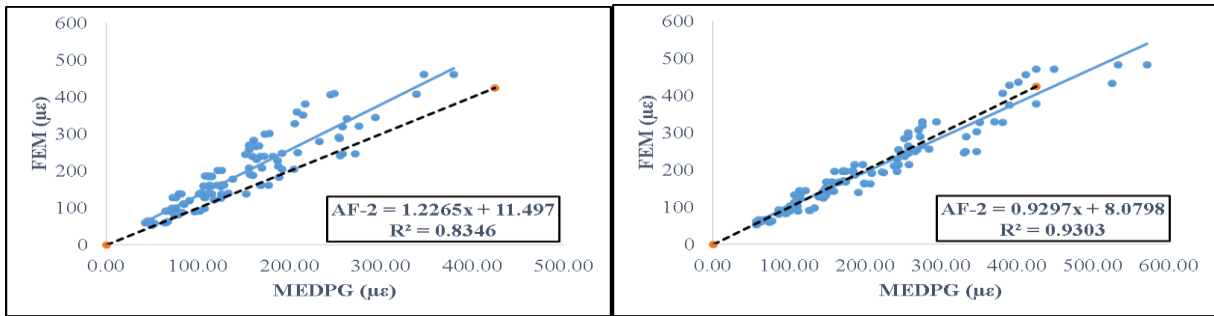
**Figure 7-17. Maximum tensile strain in traffic direction at bottom of AC for weak and strong base layers.**
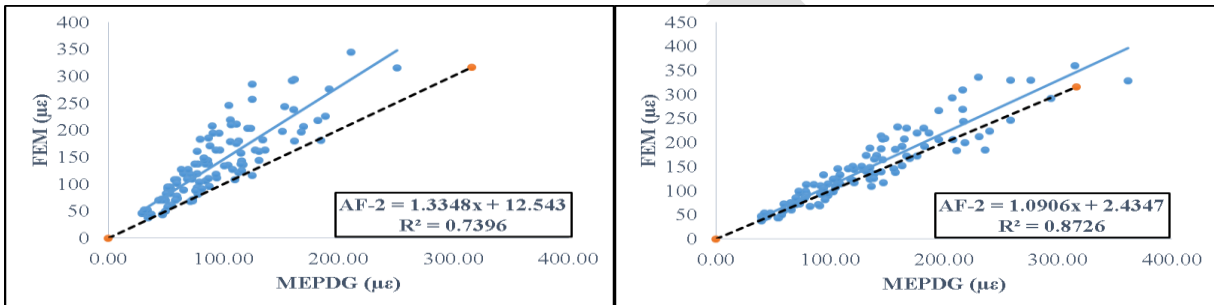


**Figure 7-18. Maximum tensile strain in transverse direction at bottom of AC for weak and strong base layers.**
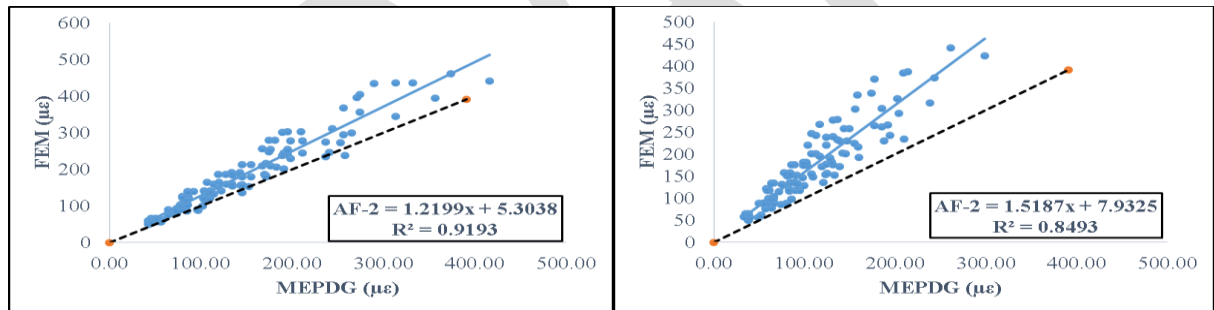


**Figure 7-19. Maximum compressive strain within AC for weak and strong base layers.**
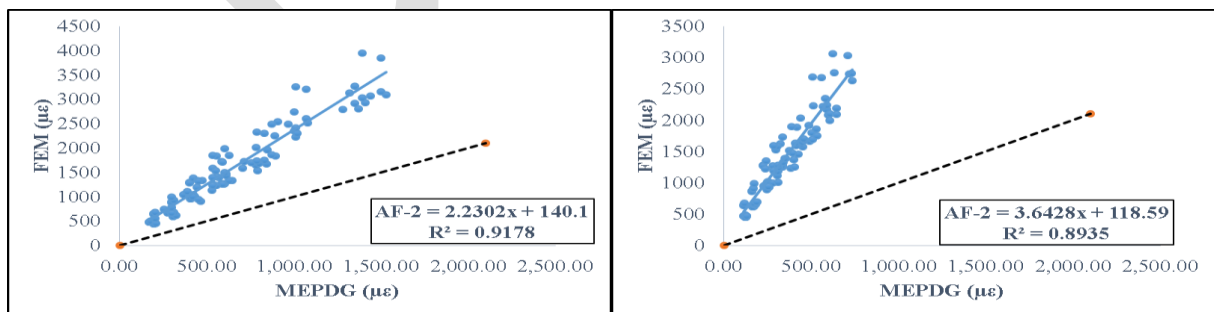


**Figure 7-20. Maximum compressive strain within base for weak and strong base layers.**
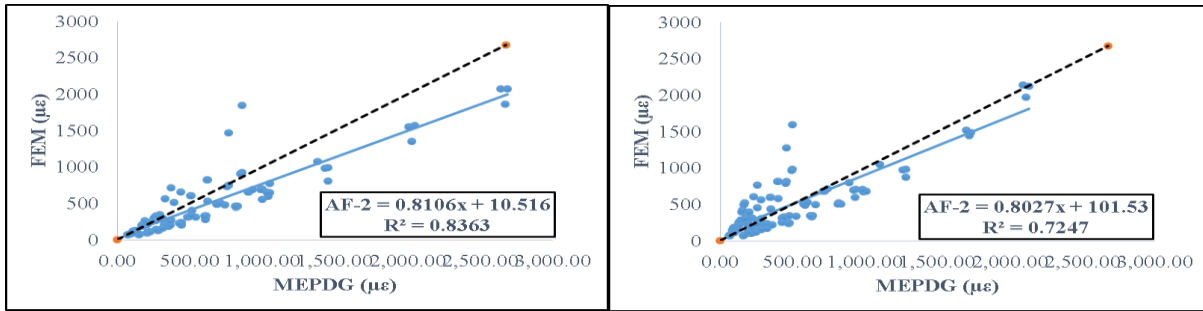
**Figure 7-21. Maximum compressive strain within subgrade for weak and strong base layers.**
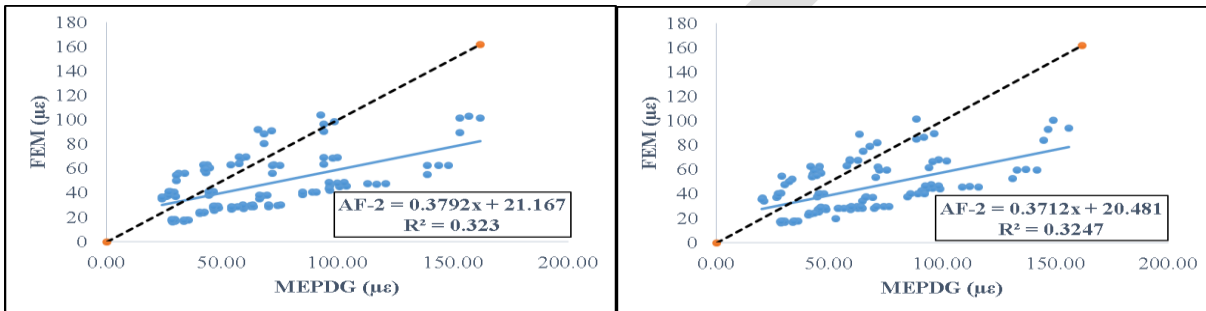

**Figure 7-22. Maximum shear strain within AC for weak and strong base layers.**
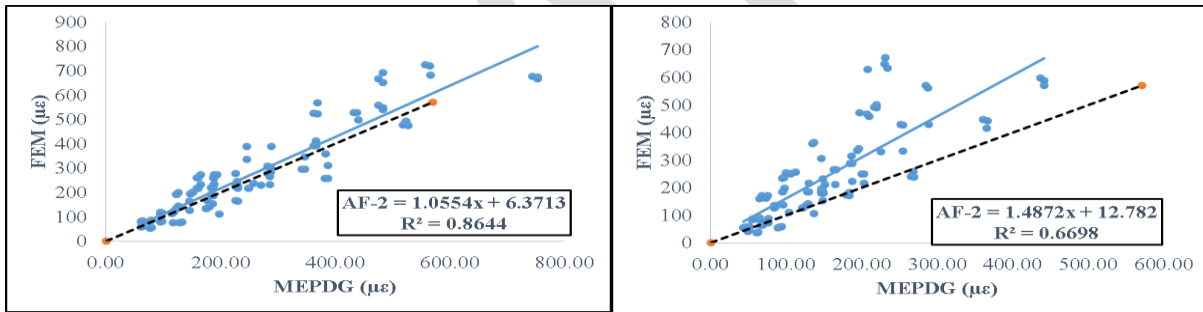

**Figure 7-23. Maximum shear strain within base for weak and strong base layers.**
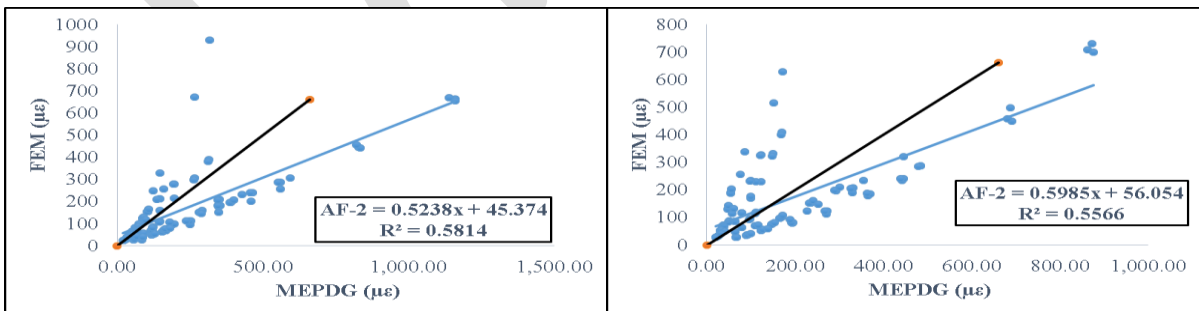

**Figure 7-24. Maximum shear strain within subgrade for weak and strong base layers.**

## 7.4 DISCUSSION OF RESULTS

### 7.4.1 Importance of Using Advanced Analysis

As discussed earlier, FE and MEPDG procedures have significant differences regarding tire-pavement interaction. Among many others, 3-D nonuniform contact stress and nonlinear material characterization for

base layer (in the case of thin pavement) seem to result in the highest differences in pavement responses between the two methods. Observations and comments on AF-2 results are presented as follows:

- After performing analyses on all cases (MEPDG versus FE analysis), two different trends were clearly observed based on AC thickness (thick or thin pavement). The effect of contact stresses diminishes as depth increases. Similar observations were reported by Al-Qadi et al. (2007). Therefore, the thick cases were separated from the thin cases when developing $AF2$.
- Thin pavement was separated into two different groups depending on its base material characterization (i.e., strong or weak) because of its nonlinear stress-dependent behavior.
- Higher $R^2$-values were obtained for thick pavement than for thin pavement because thick pavement responses were less affected by nonuniform contact stresses. Besides, stress-dependent, nonlinear characterization complicates the comparison between FE and MEPDG for thin pavement.
- The coefficients of the independent variable in the fitted equations for thick pavement is smaller than 1 for all the responses except tensile strain at the surface. Consequently, it can be said that MEPDG overestimates the other pavement responses.
- There is no regular trend for thin pavement in terms of the coefficients of independent variable in the fitted equations. While MEPDG procedure yielded higher values for maximum compressive strain within subgrade, FE resulted in higher values for other type of responses such as tensile strain at the bottom of AC and compressive strain within AC and base layers.
- FE provided higher compressive strain within base than MEPDG's procedure for thin pavement. This observation emphasizes the importance of considering stress-dependent, nonlinear characterization for base material.
- The maximum shear strain within AC occurs at shallow depths (around 1 in below the AC surface), so it is governed by the nonuniform, 3-D contact stresses, which are not considered in the MEPDG procedure. Hence, as shown in Figure 7-14 and Figure 7-22, low $R^2$ (between 0.2 and 0.3) was obtained for maximum shear within the AC.
- Maximum tensile strains at AC surface occurred far away from the loaded area, where the axle load was the dominant factor on pavement responses. Therefore, the $R^2$ value is generally high for maximum tensile strain at the surface.
- MEPDG procedure underestimates the maximum tensile strain at the AC surface for both thin and thick cases, which conforms to the literature.

### 7.4.2 Effect of Wide-Base Tire

$AF1$ was developed to convert responses from DTA to WBT. Only FEA simulations were used for $AF1$ because MLET cannot properly simulate WBT loading. Below are significant observations regarding $AF1$:

- $AF1$ was developed for a total of ten different pavement responses. Responses obtained from MEPDG and FE analysis showed a strong correlation, as indicated by the fact that the coefficient of correlation is close to one for all cases.
- The coefficient of the independent variable in the equation for $AF1$ is always higher than 1 for all responses. This indicates that WBT causes higher responses than DTA for the same axle load and tire inflation pressure, which might result in greater pavement damage.
- $AF1$ was developed for all cases without dividing the cases into subgroups. In other words, $AF1$ can be applied to DTA responses for predicting WBT response regardless of the material property and pavement structure used in MEPDG.

## 7.5 DEMOSTRATION OF ADJUSTMENT FACTORS APPLICATION

Table 7-3 presents the numerical example of how adjustment factors can be applied to responses obtained from MEPDG.

**Table 7-3. Numerical Example of Adjustment Factor Application**

| Response | MEPDG | With $AF-1$ | With $AF-2$ | With $AF-1 \times AF-2$ |
|---|---|---|---|---|
| $\varepsilon_{22,subg}$ ($\mu$) | 557.0 | 670.1 | 403.9 | 482.4 |

$\varepsilon_{22,subg}$, the maximum strain at the top of subgrade, is used as an example. MEPDG computes this response as 557.0 $\mu$ for 10 kip axle load, 110 psi tire inflation pressure, 5 in AC thickness and 6 in base layer thickness. This response increased to 670.1 $\mu\varepsilon$ after applying $AF-1$ ($AF-1 = 1.2258 \times MEPDG - 12.681$). It means that $\varepsilon_{22,subg}$ would increase to 670.1 $\mu\varepsilon$ from 557.0 $\mu\varepsilon$ if NG-WBT was used instead of DTA for same axle load and tire inflation pressure. On the other hand, the same response decreased to 403.9 $\mu$ when $AF-2$ ($AF-2 = 0.7443 \times MEPDG - 10.163$) was applied. In other words, $\varepsilon_{22,subg}$ would drop to 430.9 $\mu$ from 557.0 $\mu$ if pavement were analyzed considering realistic loading conditions and material characterization. Finally, the last column shows the combined effect of AF-1 and AF-2. It indicates that $\varepsilon_{22,subg}$ would decrease to 482.4 from 557.0 $\mu$ if the tire were wide-base and the pavement were analyzed considering realistic conditions. Figure 7-25 demonstrates how the adjustment factors may be applied to Pavement ME design software.
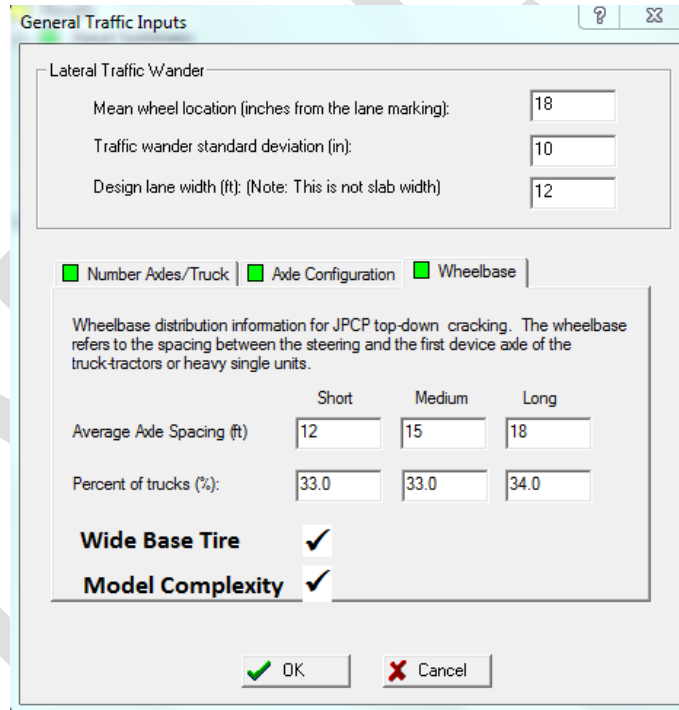


**Figure 7-25. Demonstration of adjustment factors implementation to pavement ME design software.**

## 7.6 SUMMARY

This chapter presents the theoretical background and results of adjustment factors, which may be applied to the pavement ME pavement design software. Two different adjustment factors were developed to correct responses resulting from MEPDG. The first one converts DTA to WBT responses, which are always greater than that of DTA. This adjustment, $AF1$, was developed with high coefficient of determination. The second factor, $AF2$, accounts for the model complexities such as 3-D contact stresses, stress-dependent, nonlinear base material and accurate material and interface models. Although $AF2$ showed high $R^2$-value for thick

pavement, it was slightly lower for thin pavement. Stress-dependent, nonlinear base and the higher influence of nonuniform, 3-D contact stress caused lower coefficient of determination in thin pavements.

# 8   EXPERIMENTAL PAVEMENT SECTIONS

## 8.1   TEST SECTIONS AT FLORIDA DOT

The pavement structure and instrumentation of the typical pavement section built in Florida are presented in Figure 8.1 and 8.2. The sections were built at two locations: test pit and test track. Instrumentation was installed on top of the subgrade in the test pit section. Two pressure cells were placed on top of the subgrade and H-type strain gauges were placed at the bottom of the AC layers (three in each direction).

Three pavement structures were built at the test track. The AC layer of one section had a thickness of less than 1 in (SP-12.5 PG 67-22). No material characterization is available for the existing layer. A new AC layer (SP-12.5) was placed in two lifts, 1.5 in each with PG 76-22 binder. Each lift had various combinations of polymer and rubber to meet PG 76-22 binder. No instrumentation was installed in this section.  Out of the two other sections, only one was instrumented. Each section had an existing 1.5-in. AC (SP 12.5 PG 67-22). Two lifts of AC were placed, the first was 1.5-in. SP-12.5 PG 67-22, and the second one, the surface lift, was either 12.5-, 9.5-, or 1-in. of 0.187 in mix with PG 67-22 binder. One section was instrumented at the bottom of the new AC layers using three strain gauges in both directions. Similar instrumentation was applied at 1 in from the surface. Dynatest H-type strain gauges and Geokon pressure cells were used as pavement responses instrumentation. In addition, surface instrumentation, foil gauges, were installed at various offsets, as presented in Figures 8.1 and 8.2. Six sets of foil gauges, three in each traffic direction, were installed on the surface. Each set had four foil gauges at 3 in intervals from tire edge. The load and tire inflation pressure used during the APT is shown in Table 8-1; the speed during testing was 8 km/h. More details regarding the testing facility, construction, instrumentation and testing are presented in Appendix E

**Table 8-1. Test Matrix for APT at Florida DOT**

| Tire Type | Tire Inflation Pressure (kPa) | Tire Loading (kN) | | | | |
|---|---|---|---|---|---|---|
| WBT and DTA | 552 | 26.6 | 35.6 | 44.4 | 62.2 | 79.9 |
| WBT and DTA | 690 | 26.6 | 35.6 | 44.4 | 62.2 | 79.9 |
| WBT and DTA | 758 | 26.6 | 35.6 | 44.4 | 62.2 | 79.9 |
| WBT and DTA | 862 | 26.6 | 35.6 | 44.4 | 62.2 | 79.9 |
| DTA Only | 552/758* | 26.6 | 35.6 | 44.4 | 62.2 | 79.9 |
| DTA Only | 552/758* | 26.6 | 35.6 | 44.4 | 62.2 | 79.9 |

*Indicates pressure differential in dual tires. 1 kN=224 lb, 1 kPa=0.145 psi

## PLAN VIEW
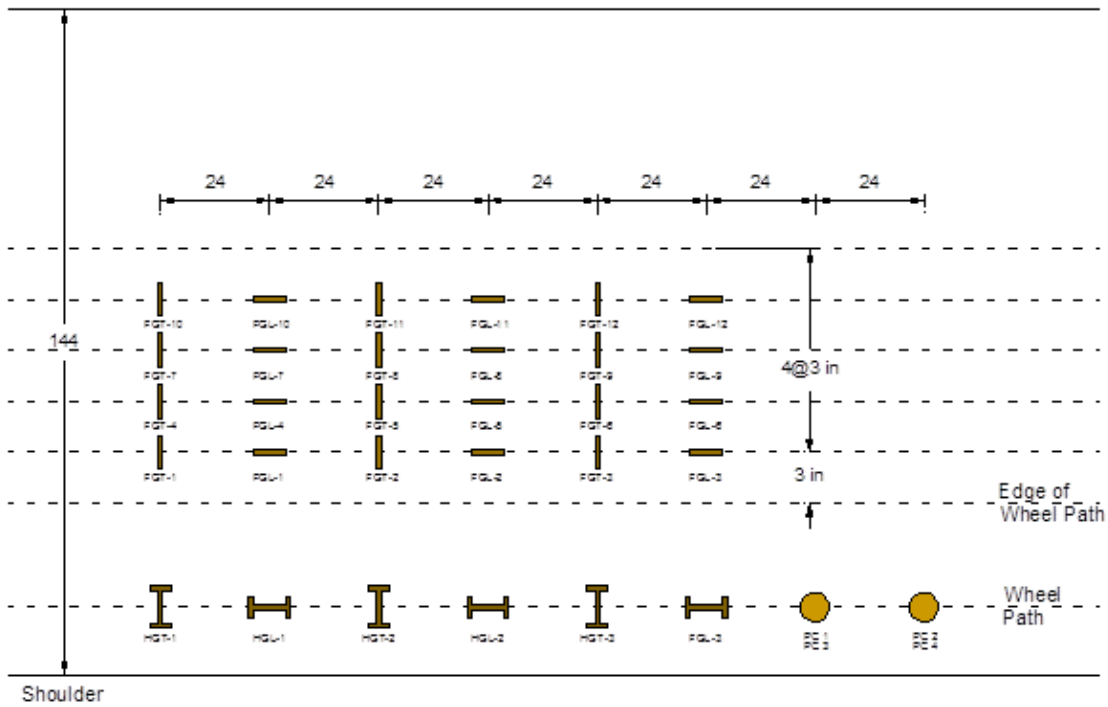


## PROFILE VIEW
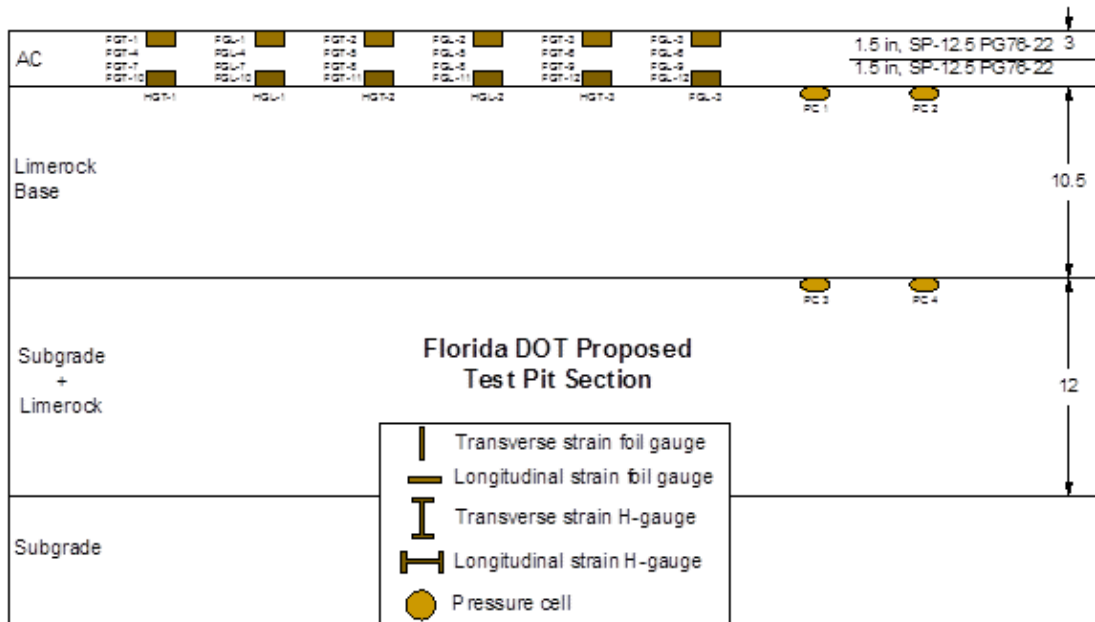


**Figure 8-1. Pavement structure and instrumentation for the test pit section.**
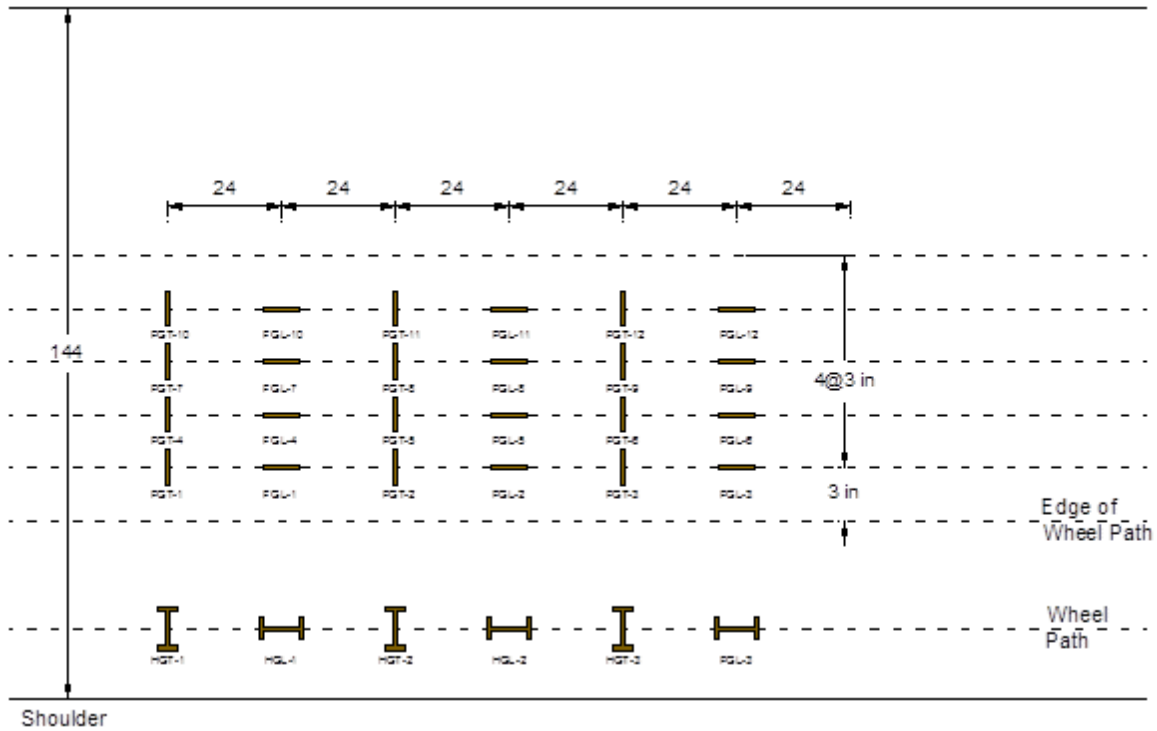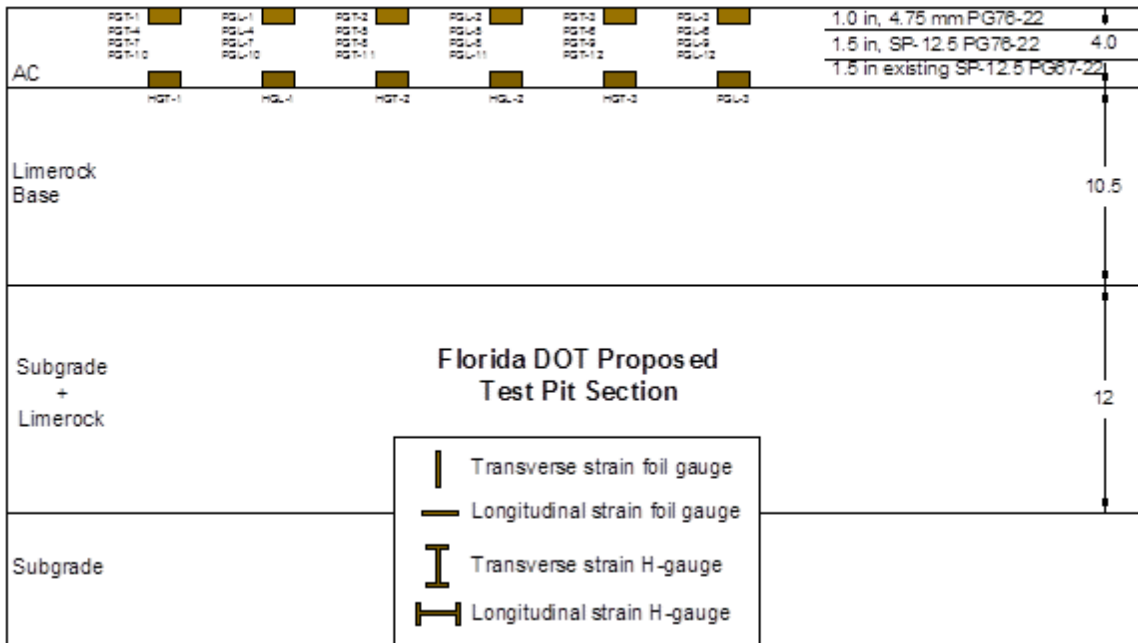
**Figure 8-2. Pavement structure and instrumentation for the test track section.**

## 8.2    TEST SECTIONS AT UC-DAVIS

Figures 8.3 and 8.4 graphically describe the typical pavement structures built at UC-Davis. The two test sections are approximately 48 m long and 4.0 m wide with 10.6 in granular base layer on top of clayey subgrade. In addition, 10 in of granular recycled AC layer was placed on top of the base layer and 4.7 in

wearing surface. The wearing surface of each section was 15% and 50% HMA reclaimed asphalt pavement (RAP). The base was full-depth reclamation with no stabilizer (FDR-NS) for both sections. The instrumentation included strain gauges (Tokyo Sokki KM-100HAS) in both directions under each lift of the AC layer (2.4 in thick), and they were located at the middle of the wheel path. Each section had eight strain gauges, four under each lift of the surface layer. In addition, two pressure cells were installed at the bottom of the recycled granular layer and two at the bottom of the AC wearing surface. To measure deflection at different depths in the pavement structure, multi-depth deflectometers were used to complement the instrumentation response measurements.

The load and tire inflation pressure used during the APT is given in Table 8-1; the speed during testing was 8 km/h, 100 cycles each. The temperature was set at a depth of 0.8 in from the surface as used by SHRP. The traffic load was applied bi-directionally (back and forth) and was performed from low to high load and from low to high temperature to avoid pavement damage. Furthermore, a test was performed at different offsets for WBT and DTA for a specific value of temperature, tire inflation pressure, and load (temperature=122 °F, tire inflation pressure=80 and 125 psi, and load=44.4 kN). The offset, or the distance from sensor line to tire center, was 7 and 12 in for both tires.
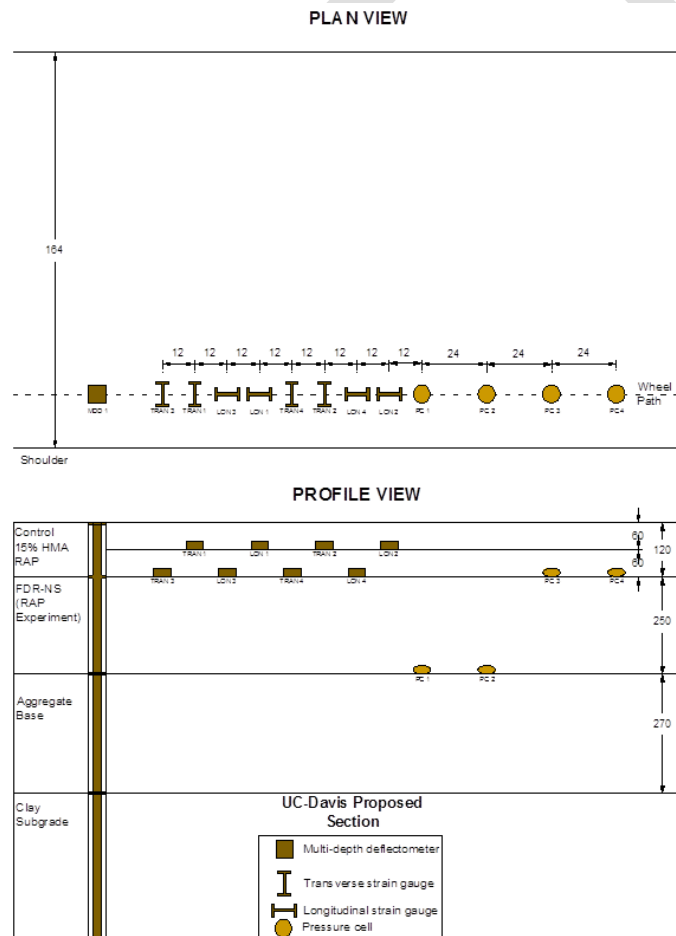


**Figure 8-3. Plan and profile view of pavement structure and instrumentation for the 15%-RAP-HMA test section at UC-Davis.**

**PLAN VIEW**
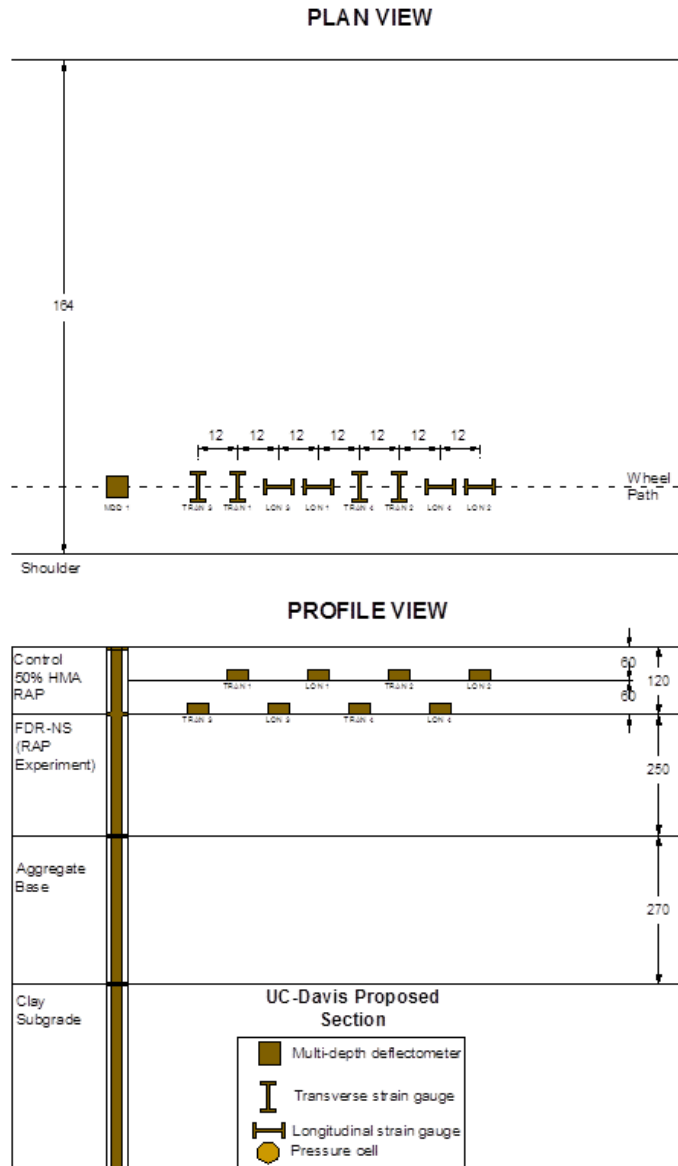


**PROFILE VIEW**



**Figure 8-4. Plan and profile view of pavement structure and instrumentation for the 50%-RAP-HMA test section at UC-Davis.**
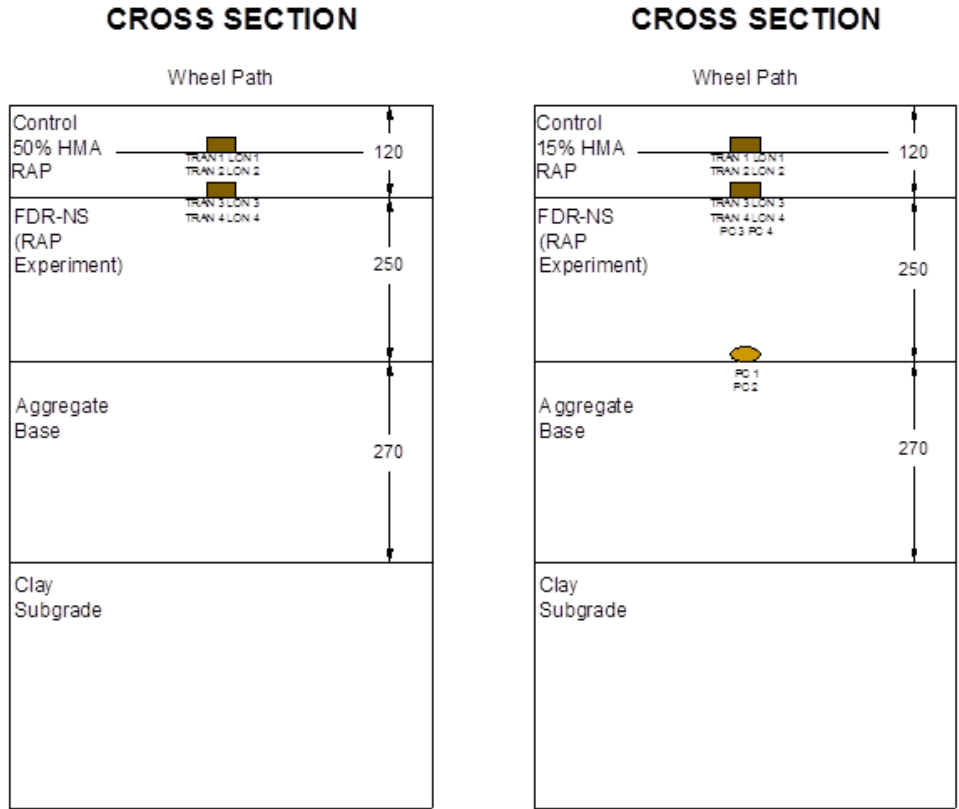
**Figure 8-5. Cross section of pavement structures and instrumentation for the test section at UC-Davis (Multi-depth deflectometer not shown for clarity).**

## 8.3    TEST SECTIONS AT DELAWARE, OHIO

The pavement structure and instrumentation of the three sections built in Ohio are presented in Figures 8.7 and 8.8. The total thicknesses of the AC layer for the sections are 13 in for Sections A and B, and 15 in for Section C. For Sections A and B, the thickness of the asphalt treated base (ATB) is 150 mm, while for Section C is 200 mm. H-type strain gauges were installed at three different depths: the bottom of the fatigue resistant layer (FRL), the bottom of the ATB, and the bottom of upper lift of the surface layer. In addition, six longitudinal sensors were placed at the bottom of the FRL; six at the bottom of the ATB (3 longitudinal and 3 transverse); and four close to the surface (2 longitudinal and 2 transverse).

Instrumentation of these sections also included LVDTs, pressure cells, and strain gauge rosettes (SGR) as shown in Figures 8.9 and 8.10. In addition to the pressure cells on top of the subgrade, another two pressure cells were installed at the bottom of the FRL. A total of 16 SGR were installed in Section A, two holes, and eight rosettes in each hole at four depths. One of the two holes was circular and the other rectangular. Section B had the same number of SGR and distribution as Section A.

During construction and instrumentation of the perpetual pavement sections in Ohio, samples of AC pavement were collected. These samples were used to obtain the material properties used as input in the mechanistic-based finite element software PANDA (Pavement Analysis using a Nonlinear Damage Approach) that was developed by the Asphalt Research Consortium team at Texas A&M University. The materials collected from each AC were used to fabricate specimens which were tested under different loading conditions.

83
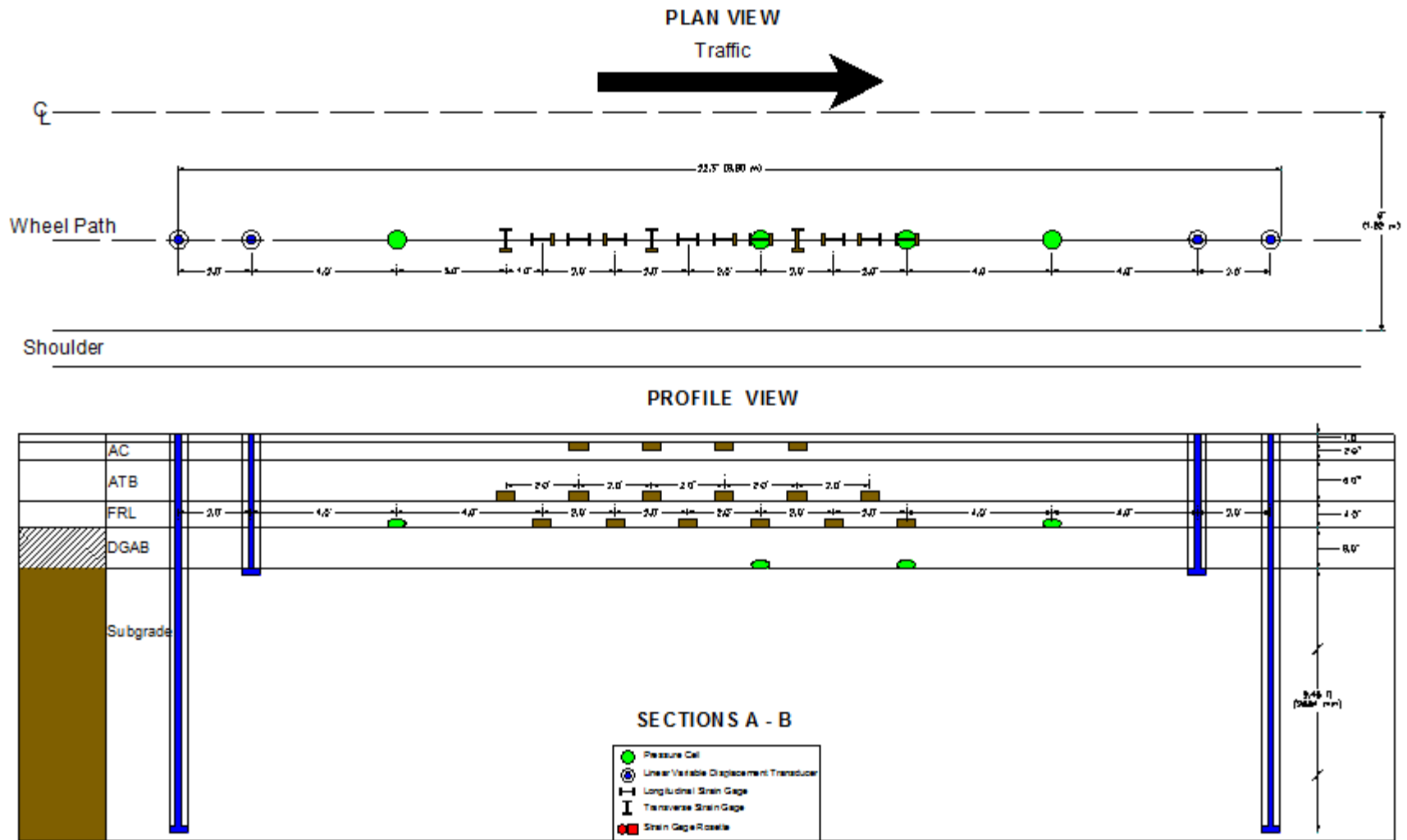
**Figure 8-6. Pavement structure and instrumentation of Sections A and B (13-in-thick).**
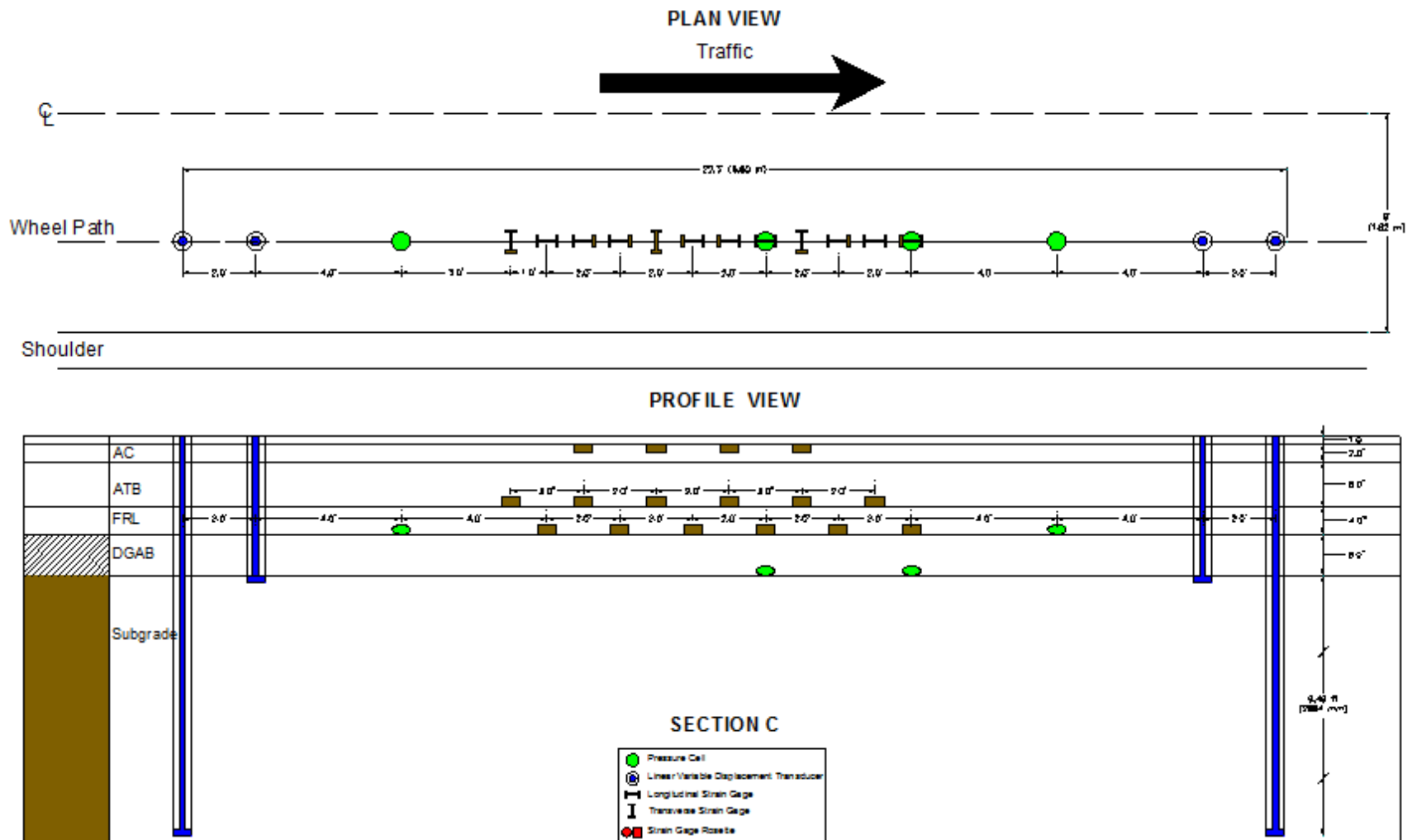
**Figure 8-7. Pavement structure and instrumentation of Section C (15-in-thick).**
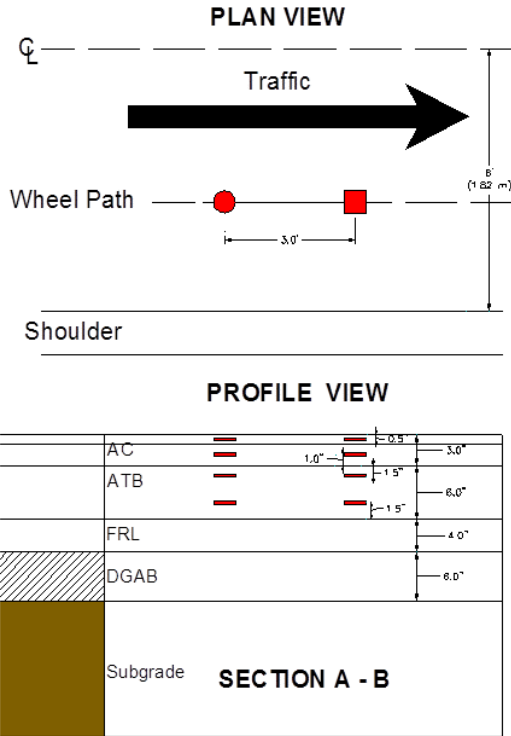
**Figure 8-8. Detail of rosettes instrumentation for Sections A and B.**
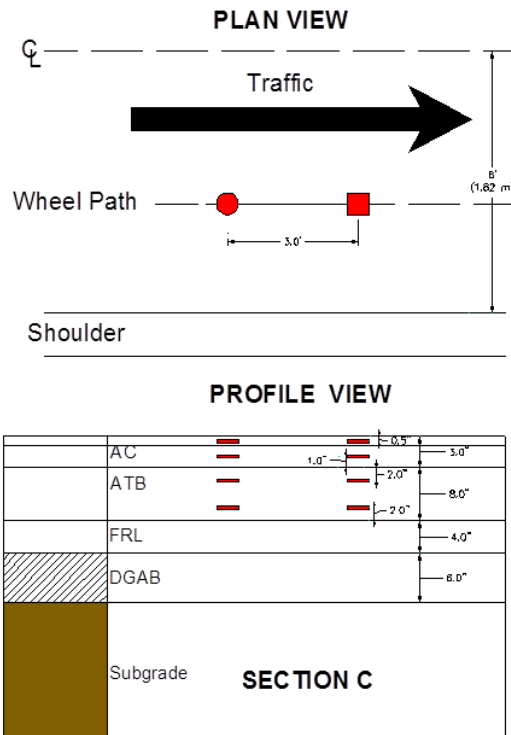


**Figure 8-9. Detail of rosettes instrumentation for Section C.**

## 8.4    DATABASE MANAGEMENT

An online database was developed to organize data and make the most use of both new and existing information that used WBT as part of their testing program. Database management procedure includes pre-processing data, filtering and smoothing, max/min response extraction, post-processing and summary, and online application design. Details of max/min response extraction with an example code and step-by-step database management is provided in Appendices G and H, respectively.

## 8.5    SUMMARY

Three new test sites were built and instrumented in Florida, California, and Ohio as part of this study. Strain, stress, and temperature were measured at various locations in the pavement structures. In addition, the research team gathered pavement responses from previous project that used WBT. Existing and new information and data were compiled and organized in an online database that will be available to the public.

# 9 QUANTIFICATION OF PAVEMENT DAMAGE

Transfer functions are used to bridge the gap between mechanistic strain responses to pavement damage, as recommended by the mechanistic-empirical design guide. Five distresses are considered for evaluating pavement damage: fatigued cracking (including bottom-up and near-surface), AC rutting, and subgrade rutting, wherein each distress is related to a critical pavement response.

## 9.1 FATIGUE CRACKING

As traffic traverses over a pavement, it generates stresses and strains that induce cracking at the bottom of the AC and later on propagating to the surface after being loaded repeatedly – a phenomenon called "bottom-up" cracking. On the other hand, near-surface fatigue cracking originates at near-surface of the pavement and propagates downwards. Two mechanisms are believed to cause near-surface cracking: load-associated tensile strains and stresses at the pavement surface, shear stresses close to the tire edge, and aging of the AC. The authors believe "near-surface" cracking usually occurs close to the surface due the high shear in AC near surface and is frequently mistakenly referred to as "near-surface" cracking.

The transfer function recommended by MEPDG for evaluating the number of repetitions related to fatigue cracking is the following:

$$N_f = k_{f1}(C)(C_H)\beta_{f1}(\varepsilon_t)^{k_{f2}\beta_{f2}}(E_{HMA})^{k_{f3}\beta_{f3}}$$
$$C = 10^M$$
$$M = 4.84\left(\frac{V_{be}}{V_a + V_{be}} - 0.69\right)$$

(9.1)

where:

$N_f$ = allowable number of axle load applications for a flexible pavement and HMA overlays

$\varepsilon_t$ = tensile or shear strain at critical locations calculated by the structural response model, in./in.

$E_{HMA}$ = dynamic modulus of HMA measured in compression, psi

$k_{f1}, k_{f2}, k_{f3}$ = global field calibration parameters (from NCHRP 1-40D recalibration, $k_{f1} = 0.007566$, $k_{f2} = -3.9492$, $k_{f3} = -1.281$)

$\beta_{f1}, \beta_{f2}, \beta_{f3}$ = local or mixture specific field calibration constants, for global calibration effort, these constants were set to 1.0

$V_{be}$ = effective asphalt content by volume, %,

$V_a$ = percent air voids in the HMA mixture

$C_H$ = thickness correction term, dependent on cracking type

Eqs. (9.1) and (9.2) pertain to bottom-up and near-surface cracking, respectively.

$$C_H = \frac{1}{0.000398 + \frac{0.003602}{1 + e^{(11.02 - 3.49H_{HMA})}}}$$

(9.1)

$$C_H = \frac{1}{0.01 + \frac{12.00}{1 + e^{(15.676 - 2.816H_{HMA})}}}$$

(9.2)

where:

$H_{HMA}$         = total HMA thickness, in

## 9.2    AC RUTTING

Another damage parameter is the permanent deformation or rutting within the AC layer, which results from densification, compression, or lateral movement of AC. The following expression is used to evaluate the number of repetitions to failure, by setting a threshold of $\Delta_{p(HMA)}$=0.5 in (12.7 mm) for the AC layer deformation.

$$\Delta_{p(HMA)} = \varepsilon_{p(HMA)}h_{HMA} = \beta_{1r}k_z\varepsilon_{r(HMA)}10^{k_{1r}}n^{k_{2r}\beta_{2r}}T^{k_{3r}\beta_{3r}}$$

(9.3)

$$k_z = (C_1 + C_2D)0.328196^D$$

$$C_1 = -0.1039(h_{HMA})^2 + 2.4868h_{HMA} - 17.342$$
$$C_2 = 0.0172(h_{HMA})^2 - 1.7331h_{HMA} + 27.428$$

where:

| | |
|---|---|
| $\Delta_{p(HMA)}$ | = accumulated permanent deformation in the HMA layer/sublayer, in. |
| $\varepsilon_{p(HMA)}$ | = accumulated permanent axial strain in the HMA layer/sublayer, in./in. |
| $\varepsilon_{r(HMA)}$ | = resilient strain calculated by the structural response model at mid-depth of each HMA sublayer, in./in. |
| $h_{HMA}$ | = HMA layer thickness, in. |
| $n$ | = number of axle load repetitions |
| $T$ | = pavement temperature, °F |
| $k_z$ | = depth confinement factor |
| $k_{1r}, k_{2r}, k_{3r}$ | = global field calibration parameters (from NCHRP 1-40D recalibration, $k_{1r} = -3.35412, k_{2r} = 0.4791, k_{3r} = 1.5606$), and |
| $\beta_{1r}, \beta_{2r}, \beta_{3r}$ | = local or mixture specific field calibration constants, for global calibration effort, these constants were set to 1.0 |
| $D$ | = depth below the surface, in. |

## 9.3    SUBGRADE RUTTING

The last type of pavement distress deals with exceeding the elastic limit of the subgrade and is associated with repetitive shear strain in the subgrade. Using the following equation, subgrade rutting is evaluated.

$$N_f = 1.365 * 10^{-9}\varepsilon_v^{-4.477}$$

(9.4)

where:

| | |
|---|---|
| $N_f$ | = allowable number of axle load applications for subgrade rutting failure |
| $\varepsilon_v$ | = maximum vertical strain on top of subgrade |

## 9.4    COMBINED DAMAGE RATIO

Each of the five distresses mentioned above results in a damage ratio, defined as the quotient between the number of repetitions to failure, which corresponds to a reference load and the allowable number of repetition of the load case in question:

$$DR = \frac{N_{ref}}{N}$$

(9.5)

where:

$$DR \qquad = \text{damage ratio}$$

$$N_{ref} \qquad = \text{allowable number of loading repetitions for a reference load}$$

$$N \qquad = \text{allowable number of loading repetitions for a specific load}$$

In this study, for the same applied load and tire inflation pressure, $N_{ref}$ and $N$ correspond to the DTA and NG-WBT cases, respectively.

In this study, all failure mechanisms considered are combined using a logarithmic damage distribution factor. This is especially beneficial as the variables to be integrated spread over several orders of magnitude. The combined damage ratio is then calculated as follows:

$$CDR = a_1 DR_{BU} + a_2 DR_{TDS} + a_3 DR_{TDT} + a_4 DR_{RS} + a_5 DR_{RH}$$

$$a_i = \frac{\dfrac{1}{\log(N_i)}}{\sum_{j=1}^{n} \dfrac{1}{\log(N_j)}} \tag{9.6}$$

where:

$$CDR \qquad = \text{combined damage ratio}$$
$$DR_{BU} \qquad = \text{damage ratio for bottom-up fatigue cracking}$$
$$DR_{TDS} \qquad = \text{damage ratio for near-surface cracking caused by shear strain}$$
$$DR_{TDT} \qquad = \text{damage ratio for near-surface cracking caused by tensile strain}$$
$$DR_{RS} \qquad = \text{damage ratio for subgrade rutting}$$
$$DR_{RH} \qquad = \text{damage ratio for AC rutting}$$
$$n \qquad = \text{total number of failure mechanisms considered}$$

For a direct comparison between NG-WBT and DTA, the damage ratio was calculated for the same value of load and tire inflation pressure, taking DTA as reference. For instance, the highest load and tire inflation pressure are $P$ =18 kip and $S$=125 psi, respectively. The corresponding loading cases in Table 5-1 are $L4$ and $L9$ for NG-WBT and DTA, respectively. As a consequence, $CDR$ was calculated for $L4$ taking $L9$ as reference.

After implementing the transfer functions, unreasonable high results were obtained for the comparison between NG-WBT and DTA. This could be attributed to a series of drawbacks inherent in the transfer functions:

- Transfer functions consider a particular critical pavement response as input (e.g., compressive strain on top of subgrade for rutting prediction) and predict corresponding distress over time. Transfer functions are empirical equations developed based on laboratory experiments and are, therefore, very sensitive to small changes in strain. Hence, the validity of prediction for the field performance strictly depends on effective calibration, which may increase the sensitivity of transfer functions to inputs,
- Being highly affected by small changes in input, transfer functions can deliver unrealistic comparisons for damage even though the pavement responses are similar,
- The scope of testing program for transfer function's regression coefficient does not cover our study's parametric ranges, thereby leading to highly inaccurate values, and
- Calibration of transfer functions did not consider NG-WBT.

To overcome this limitation, a more theoretically sound approach is proposed and presented.

## 9.5    PROPOSED ANALYSIS APPROACH USING THE STRESS/STRAIN DOMAIN

Although MEPDG provides transfer functions that directly link critical responses to damage, the locality of the point response inputs diminishes the significance of the multi-axial stress states. This behavior is especially important and predominantly influenced at the near-surface region, which is insufficiently quantified by transfer functions, and it is the region where the greatest difference between NG-WBT and DTA lies. Therefore, with the proposed approach, multi-axial stress states are adequately considered and quantified through a normalized scalar parameter.

### 9.5.1    Multi-Axial Stress and Strain States

In general, an element stress state can be represented by normal and tangential stresses. If a material element is rotated in a manner that leads to zero shear stresses, the element stress state can then be characterized using principal stresses, or the normal stresses acting on the element. Using the principal stresses, the hydrostatic stress, $p_\sigma$, and shear stress indicator, $q_\sigma$, can be defined using the following equations:

$$p_\sigma = \frac{1}{3}(\sigma_1 + \sigma_2 + \sigma_3) \tag{9.7}$$

$$q_\sigma = \sqrt{\frac{1}{2}((\sigma_1 - \sigma_2)^2 + (\sigma_2 - \sigma_3)^2 + (\sigma_1 - \sigma_3)^2)} \tag{9.8}$$

where:

$\sigma_1$ = maximum principal stress
$\sigma_2$ = intermediate principal stress
$\sigma_3$ = minimum principal stress

Below, the same form of equations can represent the hydrostatic strain, $p_\varepsilon$, and shear strain indicator, $q_\varepsilon$.

$$p_\varepsilon = \frac{1}{3}(\varepsilon_1 + \varepsilon_2 + \varepsilon_3) \tag{9.9}$$

$$q_\varepsilon = \sqrt{\frac{2}{9}((\epsilon_1 - \varepsilon_2)^2 + (\varepsilon_2 - \varepsilon_3)^2 + (\varepsilon_1 - \varepsilon_3)^2)} \tag{9.10}$$

where:

$\varepsilon_1$ = maximum principal strain
$\varepsilon_2$ = intermediate principal strain
$\varepsilon_3$ = minimum principal strain

From the finite element model, a subdomain was extracted that spans 1 m$^3$ centered on the middle of the wheel path. As the stresses and strains tend to zero at the boundaries, the domain for the multi-axial stress state analysis could be limited to the selected subdomain. Furthermore, the critical loading step is selected when the tire is at the middle of the wheel path. Therefore, the domain of the analysis could be further reduced to a two-dimensional (2-D) plane $(y, z)$ where $x$ in the traffic direction is held constant.

Initially the plane was held at the mid-length of the pavement model; however, the variation of the given plane along the traffic direction indicated that the maximum stress and strain states occur behind the middle of the tire footprint. This observed behavior is alluded to the viscoelastic response of the AC layers. To ensure a fair comparison, the location of the maximum values was considered to be critical and was used in the proposed analysis approach.

Using the centroid of each finite element of the analysis domain, principal values were obtained and the hydrostatic stress and strain, and shear stress and strain indicators were calculated and plotted in the Cartesian plane. Figure 9-1 illustrates a sample $p - q$ diagram in the stress domain.
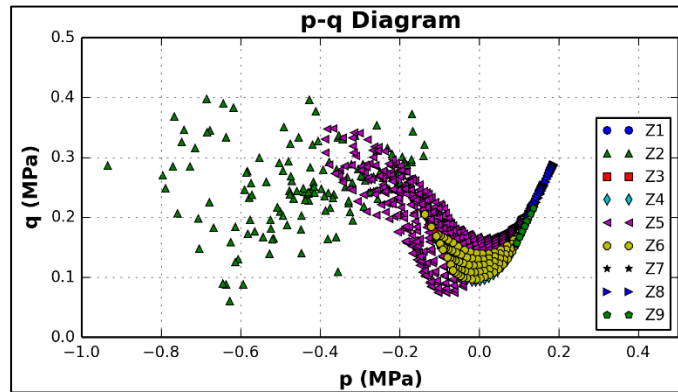


**Figure 9-1. Multi-axial stress state of an AC layer.**

In addition, each pavement layer was divided into nine regions, namely $Z1$ through $Z9$, as presented in Figure 9-2. Using this zoning process, magnitudes throughout the layer depth could be easily differentiated, wherein the most critical regions included near-surface ($Z2$), tire edges ($Z1$ and $Z3$), and mid-bottom of the layer ($Z8$). It is worth noting that the vertical boundaries were defined by the width of the tire footprint with an additional 2 in to the left and right of the tire edges. The horizontal boundaries for the AC, base, and subgrade layers were 1, 2, and 2 in., respectively, from the top and bottom of each layer, to adequately capture the behavior at the near-surface and at the bottom.
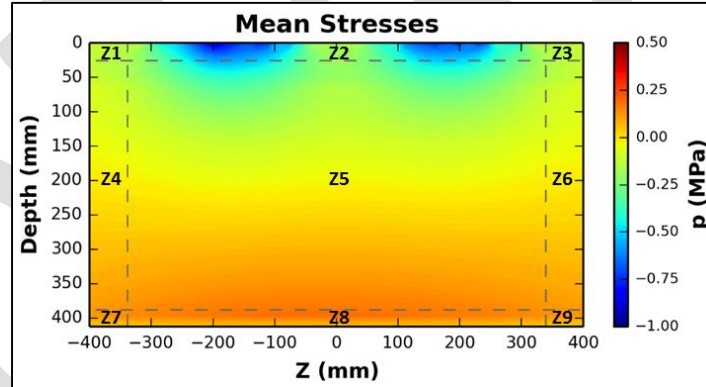


**Figure 9-2. Nine zones are defined for each pavement layer to localize areas with high stress magnitudes.**

### 9.5.2 Modified Drucker-Prager Cap Model
In the Modified Drucker-Prager Cap model, the yield surface consists of three parts: (1) the Drucker-Prager shear failure surface, (2) an elliptical cap limiting the hydrostatic pressure, and (3) a smooth transition zone between the failure surface and the cap (Figure 9-3).

92
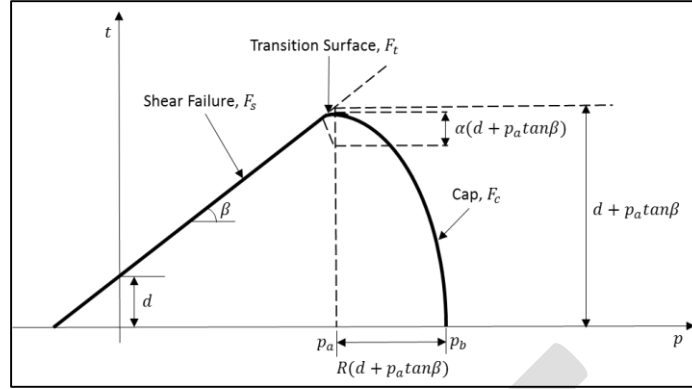
**Figure 9-3. Modified Drucker-Prager Cap Model yield surfaces.**

The Drucker-Prager shear failure surface is defined by:
$$F_s = t - p \tan\beta - d = 0 \tag{9.11}$$

where:

$\beta$ = angle of friction
$d$ = cohesion

Moreover, the cap and transition yield surfaces are estimated by:

$$F_c = \sqrt{(p - p_a)^2 + \left[\frac{Rt}{(1 + \alpha + \alpha/cos\beta)}\right]^2} - R(d + p_a tan\beta) = 0 \tag{9.12}$$

$$F_t = \sqrt{(p - p_a)^2 + \left[t - (1 - \frac{\alpha}{cos\beta})(d + p_a tan\beta)\right]^2} - R(d + p_a tan\beta) = 0 \tag{9.13}$$

$$p_a = \frac{p_b - Rd}{1 + R \tan\beta}$$

where:

$R$ = material parameter that controls the shape of the cap
$\alpha$ = defines the smooth transition surface between the Drucker-Prager shear failure surface and the cap
$p_b$ = mean effective yield stress and defines position of the cap

### 9.5.3 Polar Coordinate Transformation

To effectively relate the $p$-$q$ diagram values to the failure envelope, the values in the Cartesian coordinate were transformed into polar coordinates. Two important parameters can be extracted from the $p$-$q$ diagram in the Cartesian plane: (1) the magnitude of the vector that forms from the point of origin to a specific $p$-$q$ coordinate and (2) the angle $\theta$ between the vector and the horizontal axis. The failure plane (red dashed line in Figure 9-4) was also transformed.

This transformation allowed the relative comparison of the cloud of stress and strain states to the failure plane. It was also realized that depending on the proximity of the point to the failure plane, the material may fail in compression and/or shear. Therefore, a weight factor was created to adequately penalize the stress/strain state point based on its location relative to the failure envelope. Common weight factors that

are independent of the load case were defined by regionalizing the polar coordinate system into 30 sectors, which stemmed from defining six radii boundaries (0, 0.2, 0.4, 0.6, 0.8, and 1.0) and seven angle boundaries $(0, \pi/6, \pi/3, \pi/2, 2\pi/3, 5\pi/6, \pi)$. The midpoint of each sector was estimated and the shortest distance from the centroid to the failure envelope was calculated.
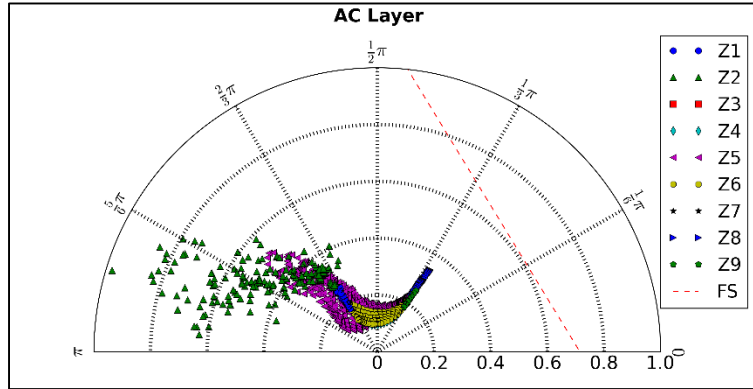


**Figure 9-4. Sample polar coordinate transformation.**

Given the centroidal distances, the reciprocal is calculated by:

$$r = \frac{1}{d}$$

(9.14)

where:

| | |
|---|---|
| $r$ | = reciprocal |
| $d$ | = shortest distance from sector centroid to failure envelope |

Based on these reciprocals, the maximum reciprocal value indicated the shortest distance to the failure envelope and was quantified to be the highest value among the 30 sectors. For instance, from Figure 9-5, $d_1 < d_2$ therefore, $r_1 > r_2$.
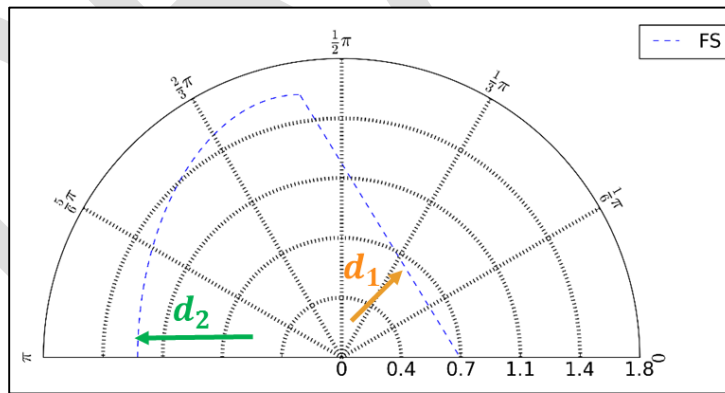


**Figure 9-5. Comparison of the sector centroids relative to the failure envelope.**

The weight factors were then calculated by normalizing the reciprocals to the maximum reciprocal. This indicated a weight of value 1.0 was the closest sector to the failure envelope. Relating back to the example from Figure 9-5, $w_1 > w_2$. It is worth noting that this process was only implemented in the regions within the failure envelope as absolute failure was assumed for the sectors beyond.

Using the vector magnitude and weight factors, the $p$-$q$ point cloud can be combined into one cumulative scalar value, coined as the cumulative stress, $C\sigma$, or cumulative strain, $C\varepsilon$. However, a direct comparison

94

between various loading cases was deemed to be relatively unfair given that their corresponding mesh geometries differ. For instance, the DTA load case would generate a higher number of points in the $p$-$q$ diagram  the NG-WBT case. Therefore, a shift factor was defined to generate similar number of points and make an even comparison between load cases. The shift factor was calculated by normalizing the cumulative stress/strain values to the 2-D area occupied by the point cloud. Also, recall the previously introduced load factor, which accounted for the difference between the applied and resultant loads. The final scalar parameter that compared the $CS$ values is defined as the cumulative ratio, $CR$, which is calculated by:

$$C\sigma/\varepsilon_{case} = \sum_{i=1}^{m} |pq|_i * w_n$$

(9.15)

$$CR = \frac{C\sigma/\varepsilon_{case} * LF_{case}}{C\sigma/\varepsilon_{ref} * LF_{ref}}$$

(9.16)

where:

| | |
|---|---|
| $C\sigma/\varepsilon_{case}$ | = cumulative stress/strain of the specific load case |
| $|pq|_i$ | = vector magnitude of the specific point $i$ |
| $w_n$ | = weight of the specific sector $n$ for a total of $m$ sectors |
| $CR$ | = cumulative stress/strain ratio (unitless) |
| $C\sigma/\varepsilon_{ref}$ | = cumulative stress/strain of the reference load case |
| $LF_{case}$ | = load factor of the specific load case |
| $LF_{ref}$ | = load factor of the reference load case |

The same domain analysis was performed for each pavement layer and for the entire pavement data set to provide a comprehensive understanding of the sensitivity of the $CR$ parameter to the variables considered in the numerical matrix.

### 9.5.4   Preliminary Testing

In lieu of using the transfer functions, the aforementioned domain analysis approach was implemented to several cases considering typical loading conditions on a thick pavement with AC thickness of 16.2 in and granular base thickness of 6 in Both layers were characterized with strong material properties. The typical trailer tire loading condition considered an applied load of 10 kip with a uniform tire inflation pressure of 110 psi (NG-WBT and reference DTA) and differential DTA inflation pressure of 80 and 110 psi. In addition, the loading condition for a steer tire was also evaluated, given the applied load of 7 kip and tire inflation pressure of 100 psi. In total, four cases were considered.

The following figures illustrate the cumulative ratio variation in the stress and strain domains for the individual pavement layer (AC, base, and subgrade), the entire pavement data set, and tire edges – all corresponding to the critical 2-D plane. For the individual pavement layers, critical zones were related to important pavement distresses:
- AC layer: zones 2 and 8 correspond to near-surface and bottom-up fatigue cracking regions, respectively; and
- Base and subgrade layers: zone 2 corresponds to permanent deformation or rutting region.

The vertical axis of the following figures indicates the cumulative ratio normalized to the reference DTA under a typical loading condition, whereas the horizontal axis enumerates the four cases considered. Based on Figure 9-6, both the NG-WBT and the steer tire have higher cumulative stress states in the middle-top zone (or zone 2) than the middle-bottom zone (or zone 8); whereas the two DTA cases (with uniform and

differential tire inflation pressures) generated similar cumulative stress states. In addition, NG-WBT invoked the highest stress state within the AC layer, followed by the steer tire. However, within the supporting granular materials, the disparity between NG-WBT and the steer tire diminishes. Moreover, for the bulk 2-D pavement response, the NG-WBT indicated the highest ratio, followed by the steer tire. This bulk behavior was predominantly due to the high ratios within the AC layer. It is noteworthy that the cumulative stress ratio for the entire pavement plane was not a simple addition of the ratios of the individual pavement layers but the addition of the cumulative stresses normalized to the uniformly inflated DTA case.
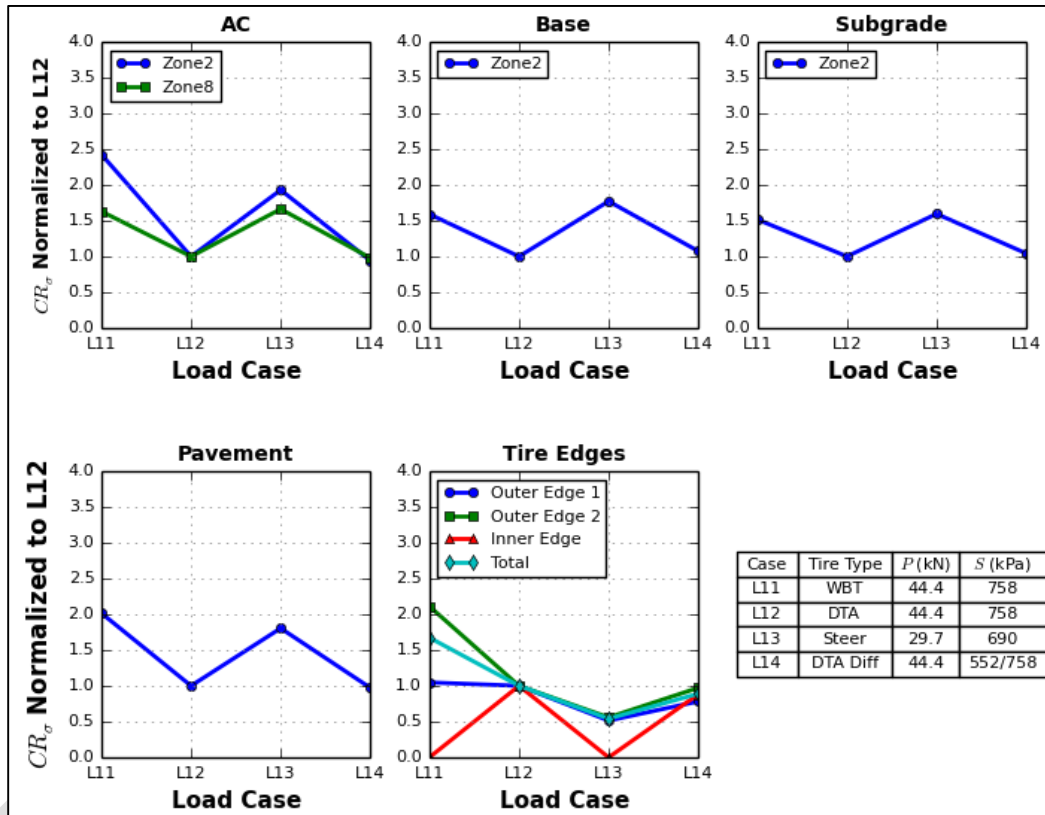


*Note: Conversion factor (4.45 kN = 1 kip; 6.89 kPa = 1 psi)*
**Figure 9-6. Cumulative ratio variation in the stress domain normalized to L12.**

Due to the inherent observation of similar stress states for both the DTA cases, within zone 2, the analysis domain was further localized to tire edges only. Recall that the tire footprint width was extended by 2 in from the tire edges, three local zones within zone 2 were generated by removing the area directly underneath the tire(s). The zones governed by tire edges only included two outer edges (named "Outer Edge 1" and "Outer Edge 2"), and the spacing between the DTA (coined as "Inner Edge").

Figure 9-6 illustrates that the stress state at one of the outer edges of the NG-WBT was twice greater than the other, which could be alluded to the high level of non-uniformity of the stresses at near-surface. Although for the remaining three cases, the stress states at all tire edges were relatively uniform and indicated much lower ratios than the NG-WBT. It is noteworthy that the values for the inner edge of the NG-WBT and steer tire tended to zero as it was non-existent.

As stress is analogous to excitation, strains, on the other hand, correspond to the resulting pavement response. Using the strain domain, a holistic evaluation of the pavement behavior with both stresses and strains is provided. In contrast to the stress domain, the variation between zones 2 and 8 within the AC layer was minimized (see top-left of Figure 9-7). Additionally, the steer tire presented a slightly higher damage

96

potential than the NG-WBT for the three pavement layers. It could also be observed that for the DTA with differential tire pressure, the cumulative ratio increased from the AC layer towards the subgrade layer. This behavior indicated that the additional load being carried by one of the differentially inflated DTA was being manifested at a higher strain state farthest from the surface. Furthermore, as the available load input data for the steer tire considered an inflation pressure of 100 psi, the cumulative ratio did not result to a significant disparity from the NG-WBT.
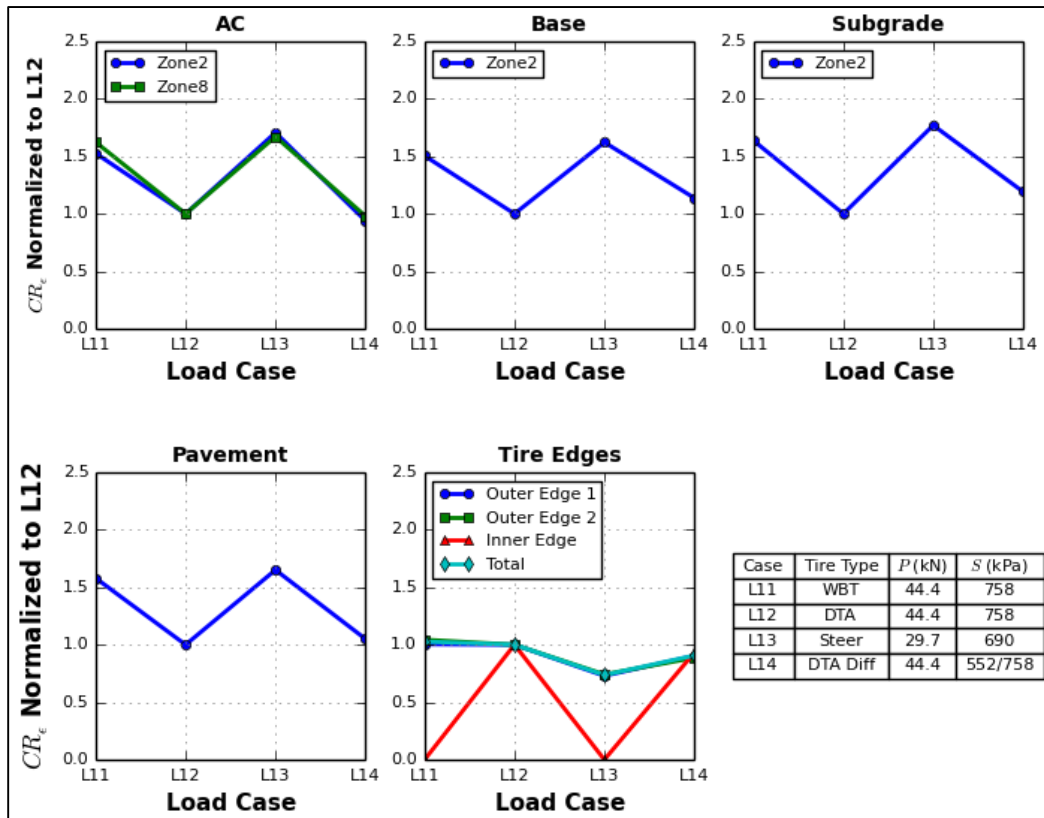


*Note: Conversion factor (4.45 kN = 1 kip; 6.89 kPa = 1 psi)*
**Figure 9-7. Cumulative ratio variation in the strain domain normalized to L12.**

For a bulk single value indicator for the entire pavement data set, a clear disparity between the two DTA cases was not captured (see bottom-left of Figure 9-7). Due to this unexpected behavior, a more in-depth study of its causes was completed. As seen in Figure 9-8, there was a highly uneven distribution of loads for the reference DTA with uniform inflation pressure. From the given load input of L12, the applied and the total resultant loads differed by 13.2%, where each tire carried 4.10 and 4.73 kip. Similar to the point responses, generally the load difference is used as a linear factor to normalize the responses. However, due to increasing the resulting stress and strain states by the aforementioned percent difference, the anticipated disparity between the uniformly and differentially inflated DTA was not observed.

97
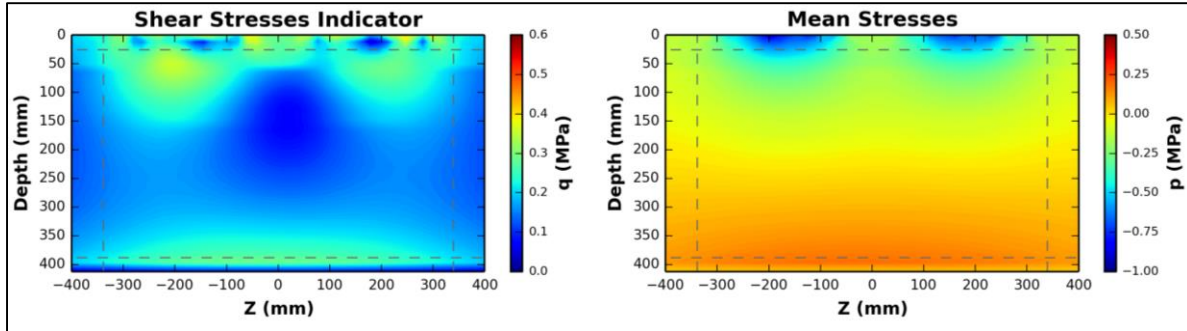
*Note: Conversion factor (25.4 mm = 1 in)*

**Figure 9-8. Shear stress indicator and mean stresses of L12.**

Therefore, another load case was introduced, L12B, which was utilized to simulate an actual uniformly inflated DTA. This was accomplished by using one of L12 tires that garnered a resultant load of 4.73 kip and mirrored the experimentally measured contact loads to the other half of the DTA. Not only was the difference between the applied and resultant forces reduced to 5.3%, but also this pseudo load case inhibited the application of a high-valued linear load factor onto a nonlinear pavement response. Figure 9-9 and Figure 9-10 illustrate the cumulative ratio variation in the stress and strain domains, normalized to the newly defined case, L12B. For the individual layers and entire 2-D pavement, similar trends from the cases normalized to L12 were preserved, although the disparity between zones 2 and 8 within the AC layer was reduced and the tire edges showed a greater variation in their corresponding ratios, thereby supporting the high nonlinear and localized behavior at near-surface.
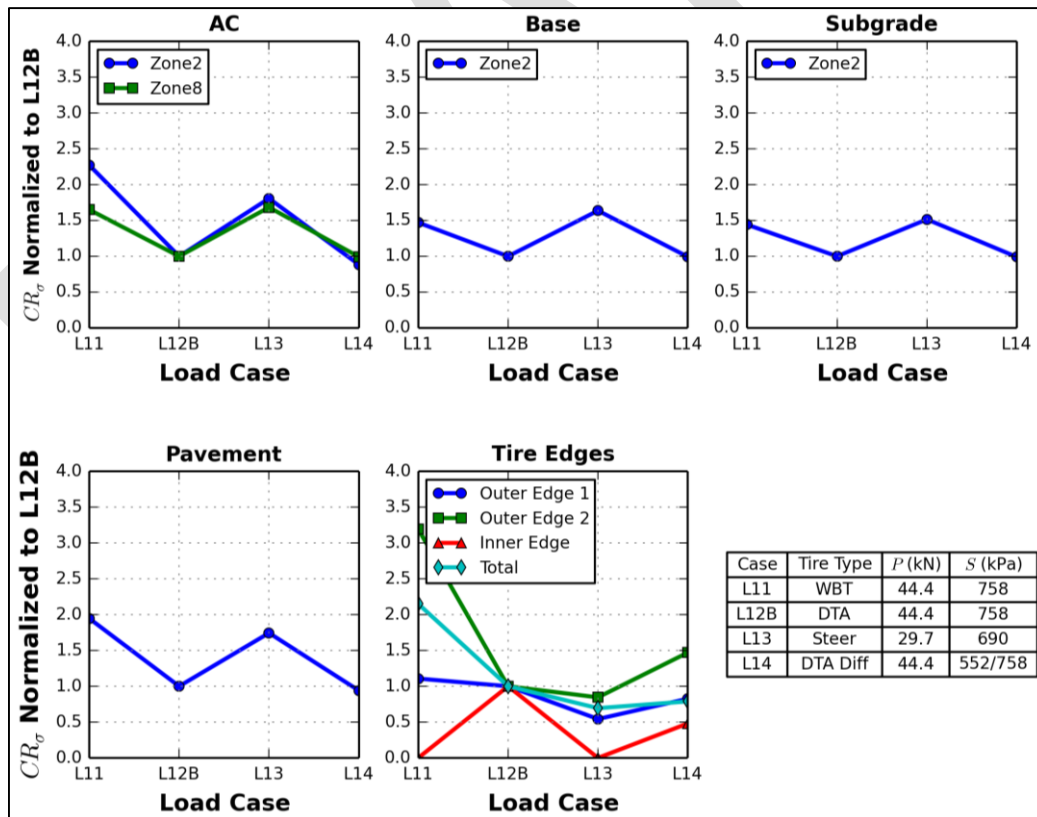


*Note: Conversion factor (4.45 kN = 1 kip; 6.89 kPa = 1 psi)*

**Figure 9-9. Cumulative ratio variation in the stress domain normalized to L12B.**

98
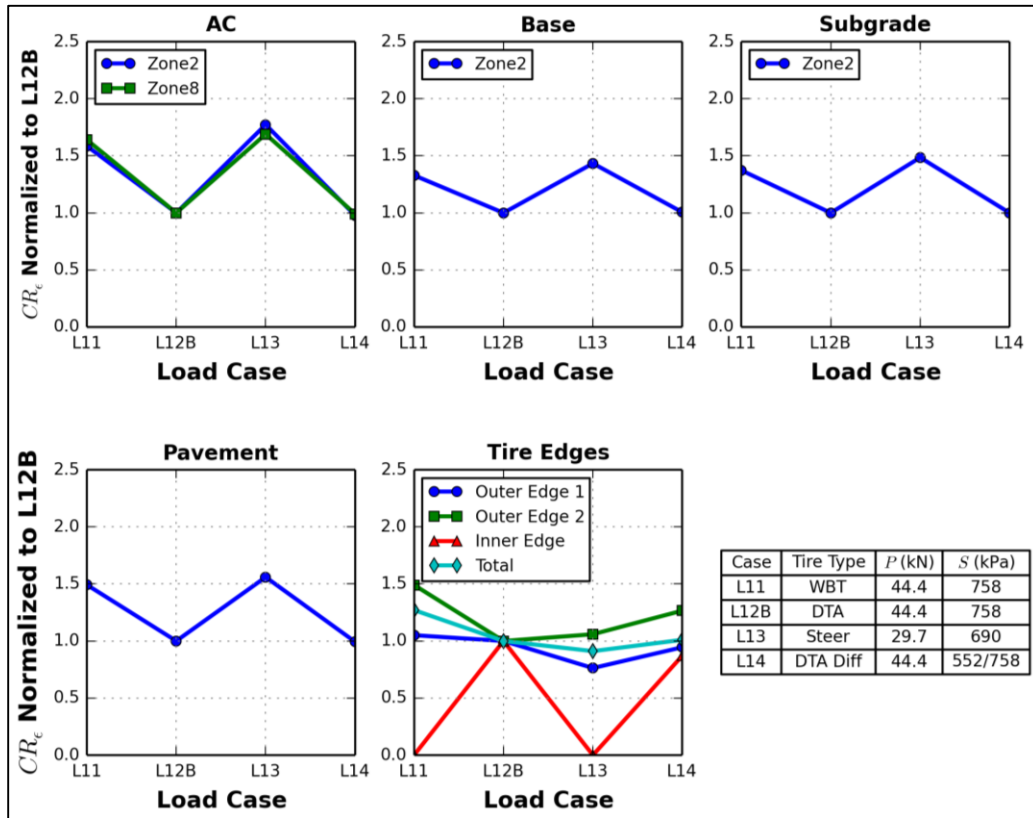
**Figure 9-10. Cumulative ratio variation in the strain domain normalized to L12B.**

However, the given near-surface zone did not fully capture the impact of the differential tire inflation pressure where the tendency of one tire to carry a higher load than the other could be clearly observed (**Error! Reference source not found.**).

**Figure 9-11. Shear strain indicator and mean strains of L14.**

Therefore, solely for the differential DTA case, the normalization is kept to L12B, however, in order to adequately account for the impact of the differential inflation pressure and to isolate individual tire behavior, zones 2 and 5 of the AC layer were subdivided into the left and right regions. The resulting cumulative ratios in the strain domain for the individual tires within zones 2 and 5 were 1.02 and 1.25, indicating that one of the tires could induce a damage potential of 25% greater than the reference DTA (L12B).

## 9.6    SUMMARY

The transfer functions used by MEPDG were proven to be inappropriate for comparing the damage caused by NG-WBT and DTA. An alternative procedure was introduced, which considered the three-dimensional stress and strain states in each layer, including the pavement surface, where the difference between NG-WBT and DTA was generally highest, followed by the steer tire. The zoning process of the proposed approach provided a means of relating areas of high damage potential to critical pavement distresses. However, the bulk value indicator masked the influence of the DTA with differential tire inflation pressure, as the cumulative ratios for the layers and entire pavement plane tended to a value of one – indicating a relatively similar damage to the uniformly inflated DTA. Moreover, the zones related to important pavement distresses did not adequately capture the impact of the differential inflation pressure. Therefore, a combination of two zones (zones 2 and 5) was implemented and resulted to a 25 % higher damage potential by one of the differentially inflated tires carrying a greater load than the other. Given the proposed domain analysis approach, the three-dimensional state of the pavement structure is successfully captured into a single value indicator, with the ability of isolating tensile and shear components.

# 10  LIFE-CYCLE ASSESSMENT AND COST ANALYSIS

The life-cycle assessment (LCA) and life-cycle cost analysis (LCCA) approaches have been used to provide a preliminary evaluation of the environmental and economic effects of NG-WBT. The two approaches are considered to satisfy the following objectives:
- Evaluate life-cycle energy consumption, greenhouse gas emissions (GHG), and cost from pavement when using NG-WBT, while focusing on interactions between the impacts of NG-WBT on the pavement design life and on improvement in fuel economy as a result of vehicle operation during the pavement use phase.
- Produce initial case studies using the approaches developed, examine how NG-WBT can affect the life-cycle impacts of pavement, and use these initial case studies to provide a preliminary indication of the net effects on greenhouse gas emissions, energy use, and cost of changes in the market penetration of NG-WBT, considering the entire life cycle of a preservation treatment as defined by the framework, including material production, construction, and vehicle use.

The University of Illinois at Urbana-Champaign (UIUC) pavement LCA tool was used to evaluate the life-cycle energy consumption, GHG emissions in the material and construction phases based on pavement maintenance and rehabilitation (M&R) strategies affected by implementing NG-WBT. A pavement LCA model based on the guideline presented by Harvey et al. (Harvey et al., 2011) was initially developed to evaluate total energy use and greenhouse gas (GHG) emissions from pavement M&R strategies. This model was used to evaluate roughness-induced energy consumption, GHG emissions, and cost during the use phase. The cost in the material and construction phases was also calculated using the tool.

In this study, international roughness index (IRI) and mean profile depth (MPD) progression models of pavement LCA model were used to calculate extra energy consumption from variations in the pavement surface profile (Tseng, 2012; Lu et al., 2009). In addition to these surface profile progression models, UIUC's pavement LCA tool was used to assess the life-cycle energy consumption and GHG emissions for two case studies, which are derived from two pavement structures used in the APT tests (at UC-Davis) that represent two levels of truck traffic. Three scenarios, representing three possible pavement design lives with different performances, were analyzed along with five different levels of market penetration of NG-WBT.

## 10.1  EXISTING STUDIES

Santero (Santero et al., 2010; Santero et al., 2011), Kendall (Kendall, 2007), Zhang et al. (Zhang et al., 2010), Mukherjee (Mukherjee, 2012), and Wang et al. (Wang et al., 2012) and others evaluated existing pavement LCA studies and models. Wang (Wang, 2013) also performed a review of studies on the concept of rolling resistance. Based on those studies and models, Wang et al. (Wang et al., 2012) developed an approach for considering pavement surface characteristics, vehicle type, traffic conditions, and their impact on rolling resistance, vehicle energy consumption, and GHG emissions in the use phase of pavement LCA.

A few studies evaluated the vehicle fuel consumption of NG-WBT, including the GENIVAR Consulting Group (now rebranded WSP Global) of Montreal, Quebec, which performed an economic study to evaluate the cost and benefits of adopting NG-WBT on heavy duty vehicles in 2005. This study focused on the market for heavy-duty vehicles and road networks in the Quebec area using variables such as number of trips, average distance per trip, and road networks used by heavy duty trucks; the study also included calculations of the benefits and costs to the trucking industry (such as reduced fuel costs and vehicle maintenance costs), increased agency costs (such as increased road damage costs), and increased benefits to society (such as reduced $CO_2$ emissions and reduced tire disposal costs). For the fuel consumption reduction of these economic impacts, the Quebec study first cited a result obtained from Michelin, which

found that NG-WBT can reduce a vehicle's rolling resistance by about 12% and thus reduce its fuel consumption by about 4%. The study then reported that according to a survey conducted among Quebec trucking firms that used NG-WBT, six of the seven firms stated that the fuel economy improvement ranged from 3.5 to 12%. [Note: The final fuel economy improvements adopted in this current study, averaged from nine sources, were 3.2%] The GENIVAR study did not include any mechanistic components of pavement-vehicle interaction, i.e., the impact from pavement and WBT on rolling resistance and fuel consumption, when analyzing the fuel consumption and GHG emissions. The fuel economy improvement was directly applied to calculate the reduced fuel consumption and GHG emissions.
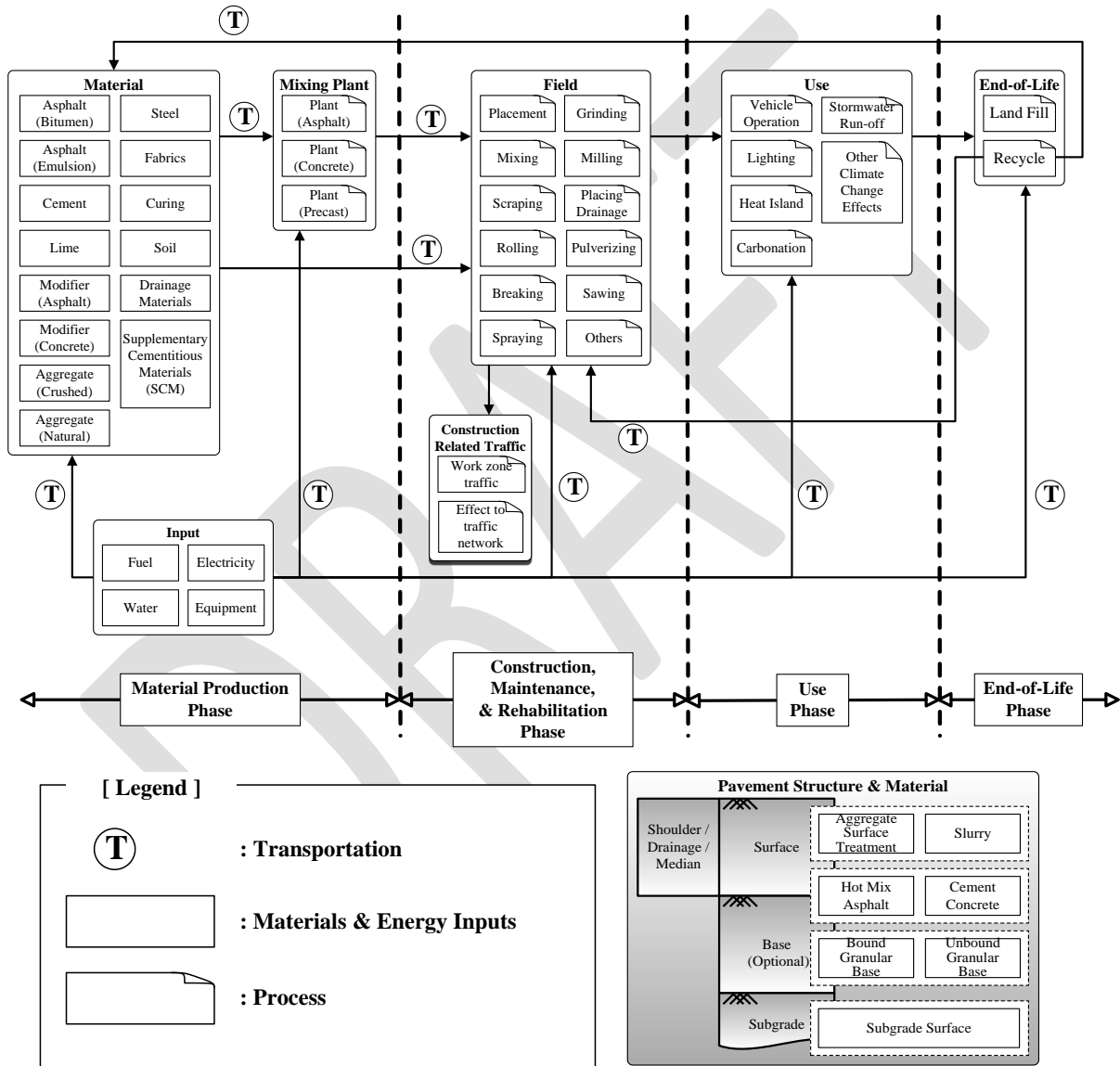


**Figure 10-1. A generic life cycle of a pavement system (Wang et al., 2012)**
**(Note: The lists in this figure are not intended to be comprehensive or exhaustive).**

A study by Franzese et al. (Franzese et al., 2010) evaluated changes in the fuel economy of Class 8 combination trucks when they were equipped with NG-WBT. In this study, instantaneous fuel consumption

monitors were installed on six Class 8 trucks to collect real-world performance data on normal freight operations. This study especially focused on the configuration of truck-trailer tires (combining DTA and WBT) and on load level (tractor only, light, medium, and heavy). The results showed that fuel economy always improved when NG-WBT were included in the truck-trailer tire configuration compared with the basic scenario (standard dual tires on both tractor and trailer) and that the fuel economy improvement increased as the number of NG-WBT increased. When either the truck or the trailer was equipped with NG-WBT, the improvement was around 6%, and when both were equipped with NG-WBT, the improvement reached 9%. In addition, the study showed that these improvements were more significant as load levels increased, although the specific values varied by load level. Thus the study—which included a mix of highway driving conditions and stop-and-go driving conditions—confirmed that NG-WBT can improve fuel economy in real-world situations. However, as with the Quebec study, this study did not include any mechanistic components of pavement-vehicle interaction, and therefore the only direct relationship derived was the one between NG-WBT and changes to fuel consumption.

Bachman et al. (*2005*) tested the fuel economy and nitrogen oxide ($NO_x$) emissions of two similar Class 8 trucks to evaluate the benefits of a variety of technologies, including the NG-WBT. The study found (a) that NG-WBT can increase fuel economy and reduce $NO_x$ emissions for both highway conditions (at both 55 mph and 65 mph) and suburban stop-and-go traffic conditions, and (b) that there appeared to be no significant difference between the improvements for the two drive cycles. But, as with the other studies cited here, this one made no effort to tie rolling resistance to the NG-WBT or to pavement surface characteristics.

The aforementioned studies only focused on the direct fuel consumption savings from using the NG-WBT, without considering any mechanistic approach to evaluating the vehicle fuel consumption of the pavement use phase through analysis of pavement-vehicle interaction. Therefore, in this study's analysis of the fuel economy of pavement, the use phase model developed by the University of California Pavement Research Center (UCPRC) pavement LCA model was only used to evaluate standard dual tires; the fuel consumption of NG-WBT was assessed by applying a direct fuel economy improvement factor based on results derived from the literature for standard dual tires. In addition to UCPRC's use phase model, the life cycle energy consumption and GHG emissions associated with the material and construction phases were calculated using the UIUC pavement LCA tool. To evaluate the life cycle cost of pavement M&R strategies affected by different levels of market penetration of NG-WBT, the same tool was used.

## 10.2 METHODOLOGIES

### 10.2.1 Basic Approach

Any thorough evaluation of the effects of NG-WBT on the environment would have to consider the numerous complex conditions present on a highway network at any given time. Therefore, for a preliminary study such as this one, it would be inaccurate to create an "average" scenario to capture conditions on the entire network. Instead, the following approach was taken:

- The highway network was divided into categories based on factorial variables similar to those in the UCPRC Pavement LCA study (Wang et al., 2012).
- Case studies were performed for each category based on the settings of the factorials. Each case study included all life cycle phases of a pavement segment, and the life cycle impacts from the different tire technologies (i.e., standard DTA and NG-WBT) associated with that segment. The impacts were based on vehicle miles traveled.
- Results from the categorical case studies were applied to the network with additional sensitivity analyses, including different types of tires and traffic levels and congestion.

As a first demonstration of the approach developed for this study, only a few selected variables are considered in the example case studies included in this report. Among the selected variables are two asphalt pavement structures, with two levels of the truck traffic, and five levels of market penetration of NG-WBT.

### 10.2.2 Scope and System Boundary

This study focuses on pavement damage caused by the introduction of NG-WBT and the resultant changes in energy consumption, GHG emissions, and cost. Theoretically, in a study of this kind the environmental impacts that occur over the tire life cycle would also be included. They are not included herein, however, because a life-cycle inventory of tire manufacturing is currently unavailable. Even if it were, the contribution from tires to the results of this evaluation would likely be very small since only a very small portion of a tire's life would be allocated to the pavement segment analyzed.

The life cycle of a generic pavement system includes the material production, construction, use, M&R, and end-of-life (EOL) phases. The modeling in this study considers the material production, construction, and use phases. Because the M&R and EOL phases were assumed to be the same for the selected pavement types, they were omitted.

Only asphalt pavement was included in the current analysis because only that type of pavement was performance-tested under NG-WBT with the APT. This study focused on asphalt mill and overlay treatments.

Selection of an analysis period for the study was problematic as the scenarios for different structures, traffic levels, and tire types each led to a different pavement design life. Theoretically, the analysis period for a pavement LCA study should be based on the design life of the longest-lived pavement in the study (i.e., with *design life* defined as the time period between the end of construction and when the failure criteria for the performance model are reached). Two options for selecting an analysis period were proposed for this study: (1) using a common analysis period for all scenarios and including at least one M&R event in each scenario; and (2) annualizing the total environmental impacts in each scenario within the design life of that scenario, and assuming that the M&R treatment is repeated in the future. Under the first option, it is expected that multiple M&R treatments are performed in some of the scenarios. Therefore, the environmental impacts from the material production and construction phases in the pavement life cycle of the last M&R treatment need to be annualized, and only those within the analysis period should be included to ensure a fair comparison among the different scenarios. In the second option, the total life cycle impacts within the design life of the pavement of each scenario are first calculated and then annualized so that comparisons can be made among the different scenarios. In this study, a range of possible market penetrations of NG-WBT were analyzed, which inevitably led to a range of possible design lives. With the first method, this created the problem of arbitrarily selecting an analysis period to cover all possible service lives and increases the complexity. The second option was used in this study to avoid this problem, with the assumption that these treatments are repeated when they reach their design life.

In terms of environmental impacts, a decision was made to limit this study to energy consumption, measured in mega-joules (MJ), and to GHG emissions, measured in $CO_2$-equivalents ($CO_2$-e), the most common indicator used when discussing global warming. This was decided because the study's scope was limited to evaluating potential contributions from pavements to global warming and was supported by a broad interest in the fossil-energy dependence of on-road transportation systems. $CO_2$-e is a *midpoint indicator* (as opposed to *endpoint indicator*, such as damage to the economy due to sea level rise or damage to ecosystems) and its use is supported by various scientific studies. The GHG emissions assessed in the study include carbon dioxide ($CO_2$), methane ($CH_4$), and nitrous oxide ($N_2O$). The quantities of the emissions were normalized into $CO_2$-e using their 100-year global warming potentials (GWPs) (*IPCC, 2007)*. In terms of economic impacts, the present worth dollar was used as the monetary indicator.

### 10.2.3 Overall Procedure

This study examined the difference in GHG emissions, energy consumption, and cost between two tire technologies: standard DTA and NG-WBT. The life-cycle energy consumption, GHG emissions, and cost from the selected pavement segments were calculated using the following:

- A pavement performance model based on standard DTA and NG-WBT
- Life-cycle inventories (LCIs) of the material production and construction phases
- Vehicle emissions factors based on standard DTA and NG-WBT in the pavement use phase
- Unit cost information for pavement materials and equipment operation activities

The procedure followed is shown in Figure 10-2 and described in detail below.

For the scenario DTA (i.e., 0 percent market penetration of NG-WBT), GHG emissions and energy consumption for the pavement life cycle were calculated using standard DTA, and this was treated as the baseline case. LCIs and costs of unit processes for each pavement life cycle phase were taken from the UIUC's database. The calculated pavement design life was based on different pavement damage scenarios, which are discussed in detail in Section 10.3. For the NG-WBT scenarios, a series of market penetration levels of those tires were evaluated. Calculations for these were similar to those used for standard DTA, but the vehicle fuel economy values in the use phase were higher for NG-WBT.

**Table 10-1. Characteristics Used to Describe the Two Tire Types**

|  | Standard Dual-Tire (Baseline) | Wide-Base Tire |
|---|---|---|
| NG-WBT market penetration | 0% | 5%, 10%, 50%, 100% |
| Design life | Calculated based on different damage scenario using Miner's Law | Calculated based on different damage scenario using Miner's Law |
| LCIs of material production and construction phases | UIUC LCI database | UIUC LCI database |
| Use phase vehicle fuel economy improvement | 0 | 3.2% improvement compared with baseline |

### 10.2.4 Pavement Life Cycle Modeling

#### 10.2.4.1 Material Production

The material production phase of pavement included a detailed investigation of aggregates, asphalt binder, and asphalt mix production. Multiple data sources for each material were reviewed, data sources were disaggregated to the process level, processes were compared with respect to related technologies, and then the data sources were recalculated based on the local condition and redefined system boundary. The results from this phase were considered to represent the LCI up to the time when materials left the "factory gate"; transportation of the processed materials to and from the construction site was considered part of the construction phase.

The spatial scale of materials used in pavement construction ranges from local to global. In this case, aggregates and asphalt are usually produced locally or regionally. LCI data are usually collected through field surveys and laboratory experiments. However, in the absence of such data, data from published LCI data sources and other LCA reports were used. Because each selected data source represents different local conditions, technologies, and system boundaries, they were customized before being used. For example, some were truncated or expanded to make the system boundary the same.
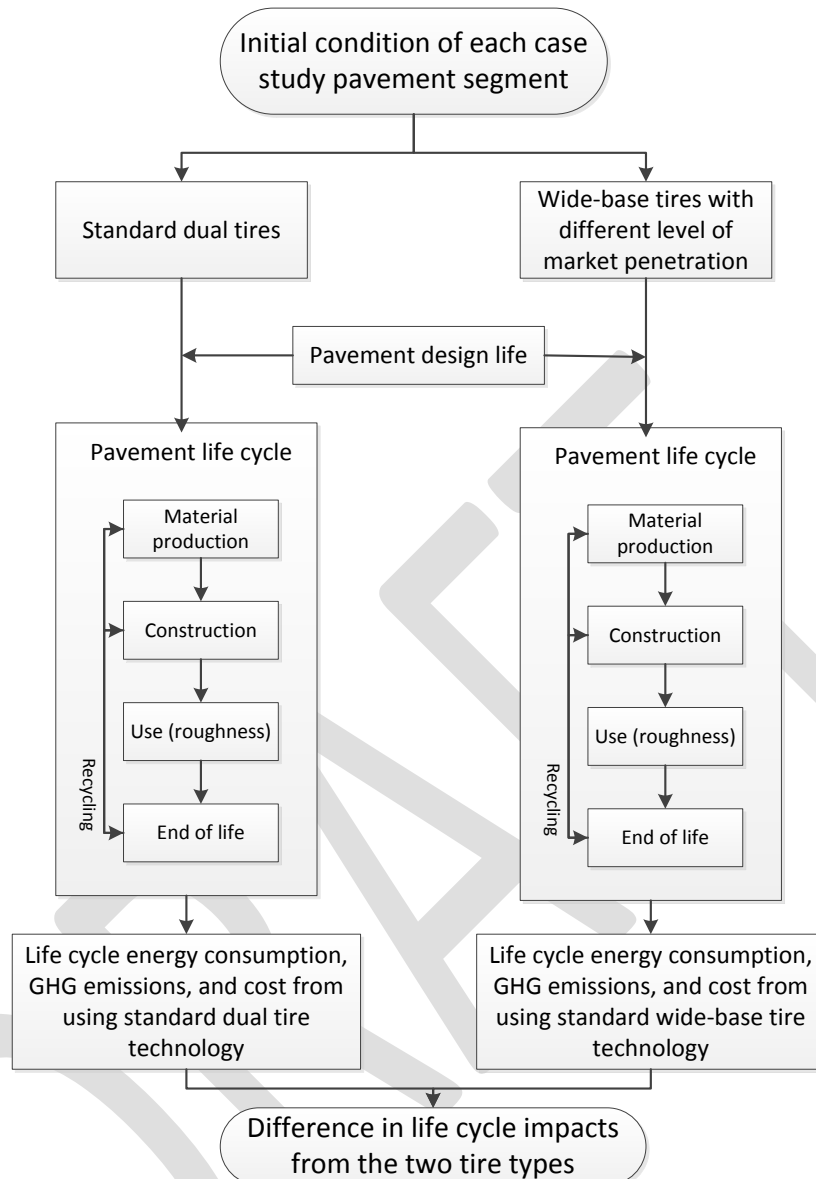
**Figure 10-2. Overall procedure for the LCA and cost analysis.**

In the LCI database developed by UIUC, multiple data sources such as commercial LCI database (Ecoinvent) and survey questionnaires were considered for each material. A number of data sources for the primary energy consumption of major materials are shown in Table 10-2 for comparison purposes. Data sources for this benchmark include the pavement LCI produced by Stripple et al. in Sweden (*1998*), asphalt inventory produced by the Athena Institute in Canada (*2006*), Ecoinvent (*2011*), and the U.S. Life Cycle Inventory (U.S. LCI) produced by the National Renewable Energy Laboratory. Default US-Ecoinvent 2.2 unit processes were used for production of binder, aggregate, and electricity, and material hauling in this study to reflect general conditions of North America. For the asphalt mixing plant, data from survey questionnaires were used, but modified with default US-EI electricity model.

Based on the pavement structures presented in Figure 10-5, UIUC's pavement LCA tool was used to evaluate the economic saving in the material phase from implementing different M&R strategies affected by using NG-WBT. The results of economic savings were annualized in present value with a discount rate of 3%.

**Table 10-2.  Primary Energy Consumption per Mass of Each Material or Process (MJ/kg) (*Lee, 2013*)**

| | Stripple | Athena | EcoInvent | U.S. LCI |
|---|---|---|---|---|
| Crushed aggregate | 0.0786 | 0.0576 | 0.14 | 0.056 |
| Natural aggregate | 0.00767 | 0.0360 | 0.059 | 0.0397 |
| Asphalt: Feedstock | 40.2 | 40.2 | 40.2 | 40.2 |
| Asphalt: Manufacturing | 2.89 | 5.32 | 9.0 | 10.5 |
| Asphalt mixing plant: Hot-mix asphalt (with reclaimed asphalt pavement) | 0.551 | 0.531 | -- | -- |

### 10.2.4.2  Construction

Because pavement may have different performances under standard DTA and NG-WBT, the construction activities triggered by pavement performance were different with different levels of NG-WBT traffic.

The environmental impacts that occur in the pavement construction phase include fuel use and the emissions contributed by both construction equipment and construction-related traffic. An example of the construction phase data flow is shown in Figure 10-3. It was assumed that construction occurs during nine-hour nighttime closures, so there would be minimal impact from construction-related traffic.
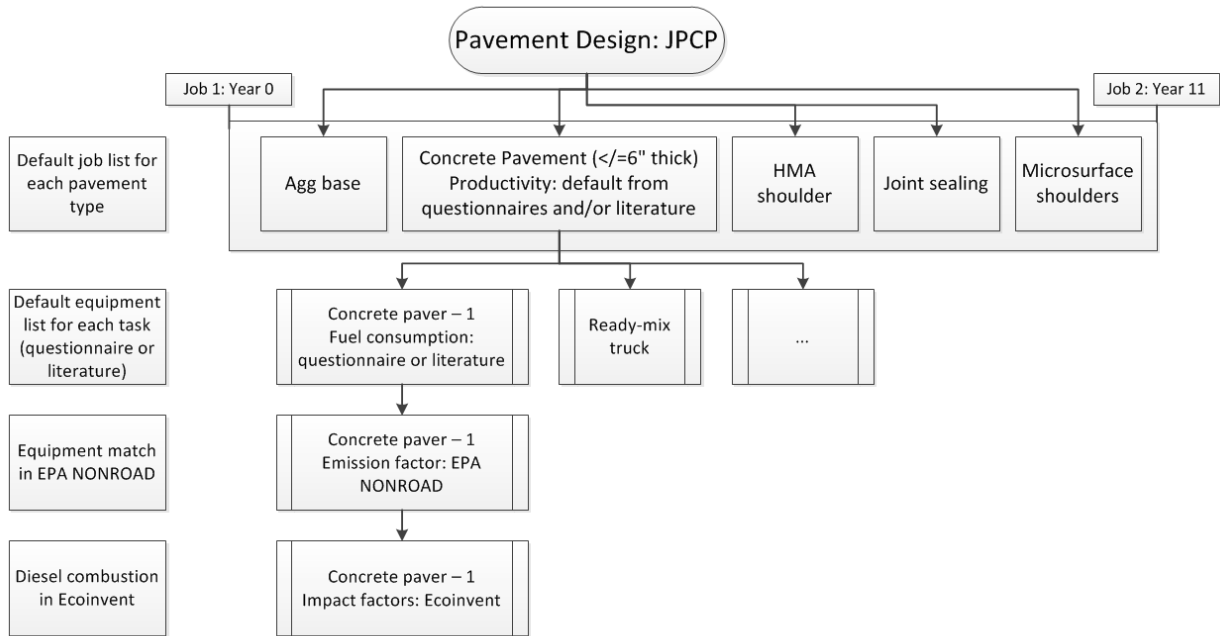


**Figure 10-3.  An example construction phase data flow for JPCP.**

A list of construction tasks was obtained from historic construction data. Information on the productivity and fuel consumption of construction equipment from the National Cooperative Highway Research Program (NCHRP) Report 744 (2013), PaLATE pavement LCA tool (2007), ROADEO road emission optimization tool (2011), and the Athena Institute's Impact Estimator software (2013) were used to calculate inventories of construction activities. EPA's NONROAD (2008) was used to obtain the fuel use and emission factors of construction equipment and environmental impacts associated with diesel combustion was obtained from SimaPro (2013).

As seen in Figure 10-3, construction data flow begins with the design. The design pavement structure is related to a given set of construction, maintenance, and rehabilitation tasks grouped together based on the construction plan. Each task has a productivity rate indicating how fast the task can be done and a set of default equipment is assigned to each task. The task productivity is related to the individual equipment fuel consumption to calculate the fuel usage for the task. Based on the fuel used by each piece of equipment, the emissions and environmental impacts are then computed. Construction tasks used in the study include pavement milling, removal, paving, and hauling. Cost information associated with these tasks were obtained from various sources (Caltrans, 2011; Brock & Richmond, 2006; U.S. DOE, 2009).

Based on the pavement structures presented in Figure 10-5, UIUC's pavement LCA tool was used to evaluate changes in economic performance in the construction phase from implementing different M&R strategies affected by using NG-WBT.

### 10.2.4.3 Use

According to the *UCPRC Pavement LCA Guideline,* the pavement use phase includes additional vehicle operation resulting from deterioration of the pavement (including increases in fuel consumption, pollutant emissions, damage to vehicles, damage to freight, tire wear), the heat island effect from the pavement, non-GHG-related climate change effects from the pavement albedo, roadway lighting effects from pavement albedo, and water pollution from leachate and runoff. But when these case studies were conducted, the only quantitatively reliable model available was the one that considered additional fuel consumption and GHG emissions. As a result, this study only considers the effect of pavement on fuel economy during the use phase.

Figure 10-4 shows the modeling procedure. First, the time progression of pavement surface characteristics under standard DTA on a road segment was generated from a pavement condition survey or pavement performance model. At the same time, using different M&R strategies and percentages of NG-WBT, different scenarios were developed based on these surface characteristics under standard DTA. Using a rolling resistance model, rolling resistance values were calculated based on these surface characteristics, and the values were used to update the relevant parameters in a vehicle emissions model, which simulates an engine's running status. The vehicle emissions model selected had to be capable of analyzing emissions at the microscopic level to allow for updating the rolling resistance parameters. However, the updating procedure could vary among different vehicle emissions models.
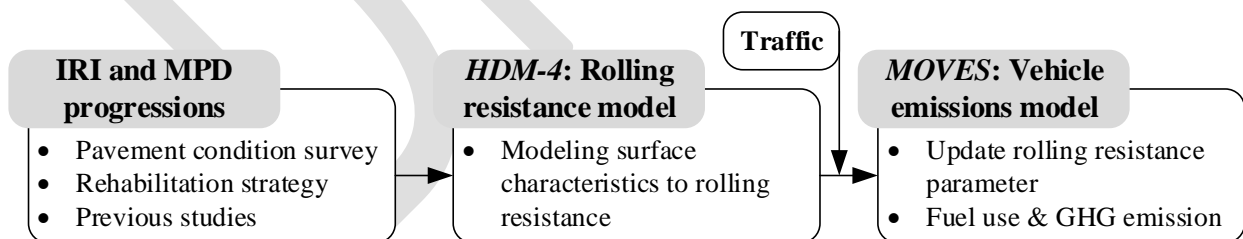


**Figure 10-4. Procedure to address additional fuel consumption and GHG emission.**

Next, traffic data for this road segment were extracted from a traffic database. Once this was done and the rolling resistance parameter was updated, fuel consumption and emissions could be modeled through the vehicle emissions model, and the net difference between different M&R strategies could be evaluated.

In the UCPRC approach, the *HDM-4* was adopted as the rolling resistance model and *MOVES* (Motor Vehicle Emission Simulator) by the U.S. Environmental Protection Agency (U.S. EPA, 2014), was adopted as the vehicle emissions model. *HDM-4* was developed by PIARC (World Road Association) for conducting cost analyses for the maintenance and rehabilitation of roads. HDM-4 has a rolling resistance

model that simulates rolling resistance based on IRI and MPD and an engine model that considers rolling resistance as it addresses vehicle fuel consumption. It calculates the vehicle fuel consumption and emissions based on emissions factors and vehicle activities.

Because no model of IRI performance has been developed based on NG-WBT, three scenarios were developed for evaluating the potential impacts from NG-WBT on pavement IRI. Further, because the relationships among pavement surface characteristics, rolling resistance, and vehicle fuel consumption for vehicles equipped with NG-WBT have not been fully developed to date either, this study adopted an average reduction in vehicle fuel consumption from NG-WBT of 3.2%, a typical range of fuel saving from NG-WBT in literature, derived from nine data sources. The fuel consumption and GHG emissions resulting from use of standard DTA were calculated by applying the existing UCPRC pavement LCA use phase model. The results obtained were then lowered by 3.2% for NG-WBT.

The economic saving from fuel economy improvement of 3.2% was calculated by converting the energy savings to the amount of fuel using a higher heating value of diesel. The upstream energy associated with diesel production was not included. The amount of fuel saved was then multiplied by the unit price of diesel to compute the monetary value saving in the use phase.

### 10.2.5 Pavement Performance Model

*10.2.5.1 MPD and IRI*

To assess energy consumption and GHG emissions reduction in the use phase, it is necessary to evaluate IRI and MPD performance with and without pavement treatment activities. Because of the lack of sufficient performance data on pavement surface characteristics under NG-WBT, some of the scenarios in this study assume that IRI and MPD have the same progression model under standard DTA and NG-WBT.

The IRI progression model for medium thickness asphalt overlays is obtained from a study by Tseng at UCPRC (*Tseng, 2012*). This model uses the number of ESALs, IRI value before the overlay, overlay type, and climate region as inputs. Equation (10.1) and Equation (10.2) show the models for initial IRI after construction and IRI progression, respectively.

$$IRI_{initial} = a \times IRI_{previous} + b \tag{10.1}$$

$$IRI_t = IRI_{initial} + c \times Age^d \tag{10.2}$$

where:

| | |
|---|---|
| $IRI_{initial}$ | = IRI immediately after construction of the overlay, in in/mi |
| $IRI_{previous}$ | = IRI value before the overlay, in in./mi |
| $a$ and $b$ | = coefficients in the overlay progression model, which are different for each type of overlay defined in the pavement management system |
| $IRI_t$ | = IRI value at Age *t* years, in units of in./mi |
| $Age$ | = age of the pavement section after last treatment, years |
| $c$ and $d$ | = coefficients in the progression model, which are different for each type of treatment, ESAL level (as defined by the model), and climate region group |

**Table 10-3. Coefficients of IRI Model for Asphalt Overlay**

| Overlay Type[1] | ESAL Level[2] | Climate Region Group[3] | a | b | c | d |
|---|---|---|---|---|---|---|
| Medium Overlay (0.1 to 0.25 ft.) | A | Severe | 0.40 | 42.23 | 6.175 | 1.44 |
| Medium Overlay (0.1 to 0.25 ft.) | A | Mild | 0.40 | 42.23 | 5.89 | 1.35 |
| Medium Overlay (0.1 to 0.25 ft.) | B | Severe | 0.40 | 42.23 | 6.5 | 1.44 |
| Medium Overlay (0.1 to 0.25 ft.) | B | Mild | 0.40 | 42.23 | 6.2 | 1.35 |
| Medium Overlay (0.1 to 0.25 ft.) | C | Severe | 0.40 | 42.23 | 6.825 | 1.44 |
| Medium Overlay (0.1 to 0.25 ft.) | C | Mild | 0.40 | 42.23 | 6.51 | 1.35 |
| Thick Overlay (> 0.25 ft.) | A | Severe | 0.62 | 12.18 | 0.76 | 2.07 |
| Thick Overlay (> 0.25 ft.) | A | Mild | 0.62 | 12.18 | 0.76 | 1.98 |
| Thick Overlay (> 0.25 ft.) | B | Severe | 0.62 | 12.18 | 0.8 | 2.16 |
| Thick Overlay (> 0.25 ft.) | B | Mild | 0.62 | 12.18 | 0.8 | 1.98 |
| Thick Overlay (> 0.25 ft.) | C | Severe | 0.62 | 12.18 | 0.84 | 2.16 |
| Thick Overlay (> 0.25 ft.) | C | Mild | 0.62 | 12.18 | 0.84 | 1.98 |

Note:

1: These treatments are defined in the pavement management system based on the thickness of the overlay. Because this study used two pavement designs with different thicknesses, the corresponding type of overlay was selected in the modeling process.

2. Annual ESAL level is defined in accordance with the pavement management system:

A: Annual ESAL ≤ 100,000;

B: 100,000 < Annual ESAL ≤ 500,000; and

C: Annual ESAL > 500,000.

3. Climate region group is defined as:

Severe climate: Central Coast, Desert, Inland Valley, South Mountain;

Mild climate: High Desert, High Mountain, Low Mountain, North Coast, South Coast.

The climate regions are defined by Caltrans to show the impact of temperature, precipitation, freezing/thawing, and solar radiation on pavement (*2013*). The climate region group is defined by Tseng (*2012*).

The progression of MPD over time for asphalt surfaces was taken from a previous study performed by the UCPRC (Lu et al., 2009). The model of MPD progression for an HMA overlay is shown in Equation (10.3).

$$
\begin{aligned}
MPD(micron) = &-93.7089 - 4.2910 \times AirVoid(\%) + 47.8933 \\
&\times Age(year) + 28.2136 \times FinenessModulus - 9.9487 \\
&\times NMAS(mm) - 5.4209 \times Thickness(mm) - 0.7087 \\
&\times NumberOfDays > 30C - 0.0402 \times AADTTinLane
\end{aligned}
\tag{10.3}
$$

where NMAS is the nominal maximum aggregate size, and others variables are indicated by their names.

### 10.2.5.2 Fatigue Cracking

Because a range of market penetration levels of NG-WBT was assessed, which would lead to a range of service lives of pavement, the performance model for fatigue and rutting was also used in this study.

The Asphalt Institute fatigue equations were used to determine cracking life. MEPDG was not used because it provided unreasonable results. The equations are shown in Equation (10.4) and Equation (10.5), where $N_f$ is the maximum allowed repetition; $C$ is the correction factor; $V_a$ is the volume of asphalt in the mix; $V_b$ is the volume of air in the mix; $\varepsilon_t$ is the tensile strain; and $E^*$ is the dynamic modulus in units of psi, which is the stiffness of the asphalt. To account for the difference between laboratory and field conditions, a factor of 18.4 was included in Equation 10.4.

$$N_f = 0.0796 \times C \varepsilon_t^{-3.291} |E^*|^{-0.854} \qquad (10.4)$$

$$C = 10^{4.84\left(\frac{V_b}{V_a+V_b}-0.69\right)} \qquad (10.5)$$

### 10.2.5.3 Rutting

The Asphalt Institute rutting model was used to determine rutting performance because, as in the case of fatigue cracking, MEPDG transfer functions provided unreasonable results for rutting. The maximum number of axle load repetitions to reach 0.5 in rut depth ($N_d$) is:

$$N_d = 1.365 \times 10^{-9} \varepsilon_c^{-4.447} \qquad (10.6)$$

where $\varepsilon_c$ is the vertical compressive strain on top of the subgrade.

## 10.3  CASE STUDIES

Two case studies that focused on asphalt pavements were performed using the described LCA approach. The case studies were undertaken to obtain a preliminary indication of the net effects on GHG emissions, cost, and energy use of NG-WBT and different truck traffic levels.

### 10.3.1  Functional Unit and System Boundary

Both case studies considered an asphalt overlay treatment. In this type of treatment, an old asphalt layer is milled and a new asphalt overlay is applied. The LCA phases considered in the modeling included material production, construction, and use. The routine maintenance and EOL phases were assumed to be the same for each pavement type, so they were omitted. Transportation of materials removed during the treatments in the EOL phase was considered in the material production and construction phases. Annualized impacts were used from the pavement life cycle to avoid inconsistent pavement design lives among the different scenarios, assuming that these treatments will be repeated when the pavements reach the end of their design lives.

The two case studies were based on the following two structure designs used in the APT experiments (see Table 10-4 for a detailed description and Figure 10-5 for cross section of the pavement structures):
- A segment, case study 671HC, using a thick asphalt layer for a high truck traffic volume
- A segment, designated case study 670HC, using a thin asphalt layer for a low truck traffic volume

Two criteria were used for selecting the segments: (1) the truck traffic level on the segment would lead to a reasonable design life; and (2) the roughness level on the segment was high enough to trigger an M&R treatment. The designs were applied to two segments in the highway network that met these criteria. The design for case 671HC was applied on a segment of westbound Interstate 80 (I-80) in Nevada County in California with two lanes per direction. The segment is a two-mile rural highway with an IRI value of about 146 in./mi in Lane 1 and 228 in./mi in Lane 2. The one-way AADT on this segment was 13,500 with 19% truck percentage. The design for case 670HC was applied to a two-mile segment of southbound State Route 213 in Los Angeles County, California with two lanes per direction. The IRI before the treatment

was 184 in./mi in the inner lane (Lane 1) and 196 in./mi in the outer lane (Lane 2). The one-way AADT on this segment was 15,750 with 2% trucks.

Each case study considered an asphalt overlay treatment carried out in 2012 with the same thickness as the AC layer in the original pavement. Each case also modeled standard DTA as the baseline (i.e., where a 0% market penetration of NG-WBT is in place), and four levels of market penetration of NG-WBT (5%, 10%, 50%, and 100%). These market penetrations were assumed to be constant throughout the analysis period. The differences in energy consumption and GHG emissions were evaluated between the NG-WBT and standard DTA. Because roughness was not included in the APT tests and because of the unavailability of an IRI performance model for NG-WBT, the following three scenarios were designed for and analyzed in this study to assess the potential impacts from NG-WBT.

**Table 10-4. Summary of the Two Case Studies**

| Case Study | 671HC (Thick Asphalt) | 670HC (Thin Asphalt) |
|---|---|---|
| County | Nevada | Los Angeles |
| Route | I-80 Westbound | SR-213 Westbound |
| Surface | Asphalt concrete | Asphalt concrete |
| Section length | 3,129 m (2 miles) | 3,129 m (2 miles) |
| Number of lanes in each direction | 2 | 2 |
| Lane width | 3.66 m | 3.66 m |
| AADT (one-way) | 13,500 | 15,750 |
| Truck percentage | 19% | 2% |
| Construction type | Mill and asphalt overlay | Mill and asphalt overlay |
| HMA layer thickness | 120 mm | 60 mm |
| Tire types analyzed | Standard DTA and four levels of market penetration of NG-WBT | Standard DTA and four levels of market penetration of NG-WBT |



| 120 mm HMA with 15% reclaimed asphalt pavement |
|---|
| 250 mm recycled base, milled and recompacted, no stabilization |
| 320 mm old aggregated base Class 2 |
| Top 200 mm subgrade tipped and recompacted |
| Clay subgrade |

| 60 mm HMA with 15% reclaimed asphalt pavement |
|---|
| 250 mm recycled base, milled and recompacted, no stabilization |
| 320 mm old aggregated base Class 2 |
| Top 200 mm subgrade tipped and recompacted |
| Clay subgrade |
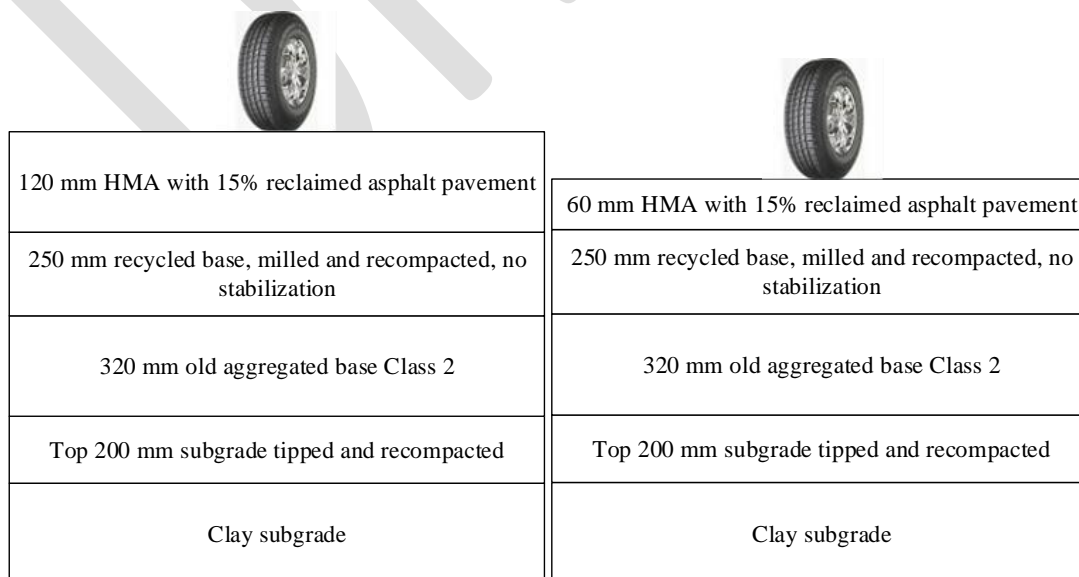
**Figure 10-5. Cross-sections of the two studies: (a) 671HC (thick asphalt) and (b) 670HC (thin asphalt).**

- Scenario I: standard DTA and NG-WBT have the same impact on the pavement's fatigue cracking and roughness (indicated by IRI) performance. In this scenario, any level of market penetration of NG-WBT results in the same level of damage to the pavement, and therefore the pavement has the same design life, which is calculated based on the fatigue cracking performance under standard DTA. The only difference expected from the different levels of NG-WBT market penetration would be the fuel economy improvement gained from their use.
- Scenario II: standard DTA and NG-WBT have different impacts on pavement's cracking performance and the same impacts on the pavement's roughness performance. The pavement design life is determined by the maximum allowed repetitions calculated from the fatigue cracking model. In this scenario, different levels of market penetration of NG-WBT lead to different design lives of pavement, calculated using Miner's rule. Annualized life cycle inventory was used in this study, i.e., the annualized GHG emissions from the material production and construction phases and the annualized GHG emissions reduction from the use phase, therefore avoiding the problem of adopting an analysis period that covers the different design lives resulting from different use levels of NG-WBT.
- Scenario III: standard DTA and NG-WBT have the same impacts on pavement's fatigue cracking performance, but different impacts on the pavement's roughness performance. The rutting performance model was used as an approximate indicator for roughness performance. The difference in IRI performance between standard DTA and NG-WBT was considered proportionate to the difference in their respective rutting life. The annual IRI value under NG-WBT was calculated using Equation (10.7).

$$\Delta \text{IRI}_{NGWBT \text{ between year } j \text{ and } 1} = \Delta IRI_{DTA \text{ between year } j \text{ and } 1} \times \frac{Rutting \ life_{DTA}}{Rutting \ life_{NGWBT}} \qquad (10.7)$$

Where:

$\Delta \text{IRI}_{NGWBT \text{ between year } j \text{ and } 1}$ = increase of IRI value between Year j and Year 1 under NG-WBT, in m/km

$\Delta IRI_{DTA \text{ between year } j \text{ and } 1}$ = increase of IRI value between Year j and Year 1 under DTA, in m/km

$Rutting \ life_{DTA}$ = pavement design life in years under standard DTA calculated based on the rutting model shown in Equation (10.6)

$Rutting \ life_{NGWBT}$ = pavement design life in years under NG-WBT calculated based on the rutting model shown in Eq. (10.6)

### 10.3.2 Material Production Phase

The material production phase includes the extraction and initial processing of aggregates, asphalt, and the AC mixing process at the mixing plant. Processes in this phase include raw material acquisition, transport of raw materials to and from the plant, and material manufacturing. The transport of AC to and from the site was attributed to the construction phase.

### 10.3.3 Construction Phase

LCIs of the construction phase of each pavement segment were calculated on a prorated basis depending on the size of each construction event. Calculation was based on the total amount of asphalt material needed. Hauling of asphalt materials from plants to the construction site was considered. Based on the number of hours of equipment operation for each construction task, the amount of fuel used was calculated and the corresponding impacts were computed.

### 10.3.4 Use Phase

As noted in the discussion of the system boundary, this study focused on assessing life-cycle energy consumption, GHG emissions, and cost under three scenarios. The greatest difference between these three

scenarios occurred in the pavement performance of the use phase. In each scenario, both passenger cars and trucks were assigned to each lane because each lane had a different level of pavement performance.

In the use phase, case studies focused on the effects of pavement surface characteristics, IRI and MPD, on fuel economy. In order to simplify the study, some assumptions and adjustments were made for items that were common to all the scenarios:
- Use of NG-WBT instead of standard dual tires resulted in an average improvement in vehicle fuel economy of 3.2% when all other conditions are kept constant.
- Routine maintenance activities in the use phase were assumed to be equal and were therefore ignored.
- Traffic volume and fleet composition were the same during weekdays and weekends.
- Hourly traffic distribution was the same for all types of vehicles.
- The average hourly speed distribution on rural freeways was applied in the case study.
- Alternative fuel vehicles were not considered.

For each scenario, it was necessary to determine the pavement design life and roughness performance in order to calculate the annualized emissions based on the market penetration of NG-WBT. The following steps were used to calculate the design life under each situation:
- The maximum repetitions allowed were calculated using either the maximum tensile strain on the bottom of the AC layer or the maximum compressive strain on top of the subgrade (depending on whether it is fatigue cracking or rutting, respectively) using the results obtained from the UIUC ANN tool, based on the specific performance equation.
- The number of repetitions that the pavement receives each year was calculated based on the ESAL count, and that result was divided by the maximum allowed repetitions (as shown in Table 10-6) to calculate the annual damage to the pavement.
- Using Miner's Law, the design life was calculated by counting how many years it would take the cumulative damage to reach a value of 1. Because a series of market penetrations of NG-WBT were assessed, the damage from standard DTA and NG-WBT were calculated separately and then summed when Miner's rule was applied.

The UIUC's ANN tool was used to predict the maximum tensile strain and maximum compressive strain in cases 670HC and 671HC (Table 10-5). Maximum tensile strain values were obtained under 18-kip axle load, temperature of 68 °F, and 100 psi tire pressure. The maximum allowed repetitions and the design life for each scenario are shown in Table 10-6 through 10-8, respectively.

Figure 10-6 shows the IRI progression over five years for cases 671HC and 670HC for Scenarios I and II (these two scenarios have the same IRI performance), using the pavement performance previously discussed. Figure 10-7 shows the IRI progression over five years for Scenario III of cases 671HC and 670HC, using rutting performance to predict IRI performance under WBT. Figure 10-8 shows the MPD progression over five years under all tires.

**Table 10-5. Maximum Tensile and Compressive Strain in Cases 670HC and 671HC**

| Tire Type | Distress Type | Location and Type of Strain | Case 670HC (Thin Asphalt) | Case 671HC (Thick Asphalt) |
|---|---|---|---|---|
| Standard DTA | Fatigue cracking | Maximum tensile strain on the bottom of HMA (microstrain) | 318 | 196 |
| Standard DTA | Fatigue cracking | Maximum allowed repetitions | 282,405 | 3,042,203 |
| Standard DTA | Rutting | Maximum compressive strain on the top of subgrade (microstrain) | 490 | 403 |
| Standard DTA | Rutting | Maximum allowed repetitions | 714,044 | 1,700,743 |
| NG-WBT | Fatigue cracking | Maximum tensile strain on the bottom of HMA (microstrain) | 403 | 222 |
| NG-WBT | Fatigue cracking | Maximum allowed repetitions | 128,638 | 2,007,418 |
| NG-WBT | Rutting | Maximum compressive strain on the top of subgrade (microstrain) | 560 | 383 |
| NG-WBT | Rutting | Maximum allowed repetitions | 395,690 | 2,125,011 |

**Table 10-6. Annual Damage and Design Life: Scenario I under Different WBT Market Penetrations**

| Case | Market Penetration of NG-WBT | Annual Damage | Design Life (Years) |
|---|---|---|---|
| 671HC (thick asphalt) | 0% (standard dual tires, i.e., baseline) | 0.166 | 7 |
| 671HC (thick asphalt) | 5% | 0.166 | 7 |
| 671HC (thick asphalt) | 10% | 0.166 | 7 |
| 671HC (thick asphalt) | 50% | 0.166 | 7 |
| 671HC (thick asphalt) | 100% | 0.166 | 7 |
| 670HC (thin asphalt) | 0% (standard FTA, i.e., baseline) | 0.374 | 3 |
| 670HC (thin asphalt) | 5% | 0.374 | 3 |
| 670HC (thin asphalt) | 10% | 0.374 | 3 |
| 670HC (thin asphalt) | 50% | 0.374 | 3 |
| 670HC (thin asphalt) | 100% | 0.374 | 3 |

**Table 10-7. Annual Damage and Design Life: Scenario II under Different WBT Market Penetrations**

| Case | Market Penetration of NG-WBT | Annual Damage | Design Life (Years) |
|---|---|---|---|
| 671HC (thick asphalt) | 0% (standard dual tires, i.e., baseline) | 0.166 | 7 |
| 671HC (thick asphalt) | 5% | 0.170 | 6 |
| 671HC (thick asphalt) | 10% | 0.174 | 6 |
| 671HC (thick asphalt) | 50% | 0.208 | 5 |
| 671HC (thick asphalt) | 100% | 0.251 | 4 |
| 670HC (thin asphalt) | 0% (standard dual tires, i.e., baseline) | 0.374 | 3 |
| 670HC (thin asphalt) | 5% | 0.396 | 3 |
| 670HC (thin asphalt) | 10% | 0.418 | 3 |
| 670HC (thin asphalt) | 50% | 0.597 | 2 |
| 670HC (thin asphalt) | 100% | 0.821 | 2 |

**Table 10-8. Annual Damage and Design Life: Scenario III under Different WBT Market Penetrations**

| Case | Market Penetration of Wide-Base Tires | Annual Damage | Design Life (Years) |
|---|---|---|---|
| 671HC (thick asphalt) | 0% (standard dual tires, i.e., baseline) | 0.296 | 4 |
| 671HC (thick asphalt) | 5% | 0.293 | 4 |
| 671HC (thick asphalt) | 10% | 0.290 | 4 |
| 671HC (thick asphalt) | 50% | 0.267 | 4 |
| 671HC (thick asphalt) | 100% | 0.237 | 5 |
| 670HC (thin asphalt) | 0% (standard dual tires, i.e., baseline) | 0.148 | 7 |
| 670HC (thin asphalt) | 5% | 0.154 | 7 |
| 670HC (thin asphalt) | 10% | 0.160 | 7 |
| 670HC (thin asphalt) | 50% | 0.207 | 5 |
| 670HC (thin asphalt) | 100% | 0.267 | 4 |
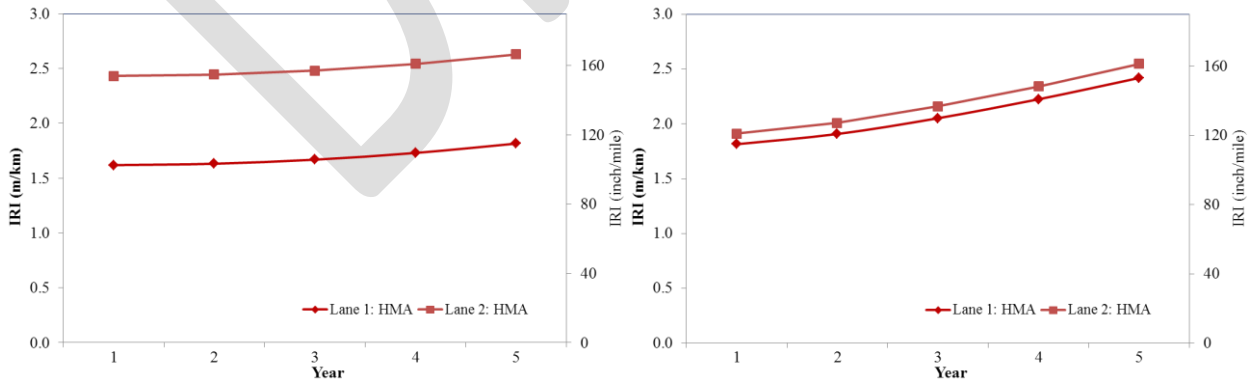


**Figure 10-6. Scenario I and Scenario II IRI progression for case 671HC (thick asphalt) and for case 670HC (thin asphalt).**
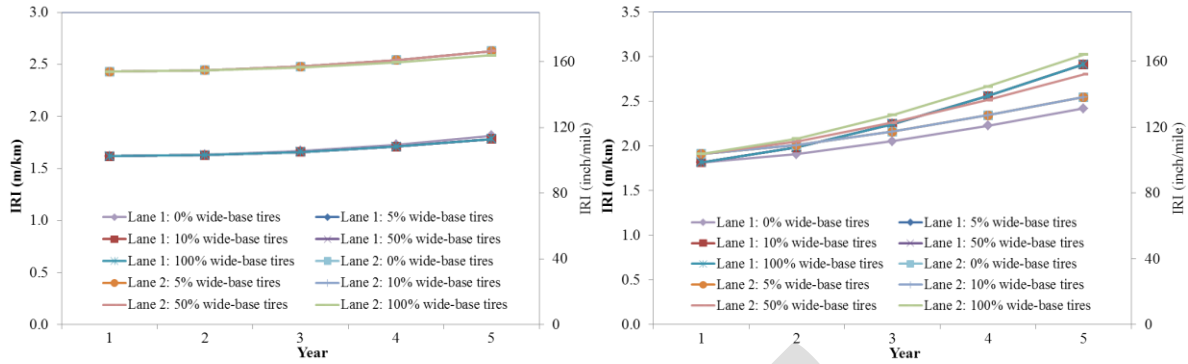
**Figure 10-7. Scenario III IRI progression (a) for case 671HC (thick asphalt) and (b) for case 670HC (thin asphalt).**

Notes:

(1): In case 671HC (thick asphalt), 0% NG-WBT (standard dual-tire), 5% NG-WBT, 10% NG-WBT, 50% NG-WBT, and 100% NG-WBT showed nearly the same IRI progression on each lane. Initial IRI values are different because the two lanes carried different initial IRI values.

(2): In case 670HC (thin asphalt), 0% NG-WBT (standard dual-tire), 5% NG-WBT, and 10% NG-WBT showed the same IRI progression on each lane. The 50% NG-WBT tire and 100% NG-WBT showed the same IRI progression on each lane. Initial IRI values are different because the two lanes carried different initial IRI values.
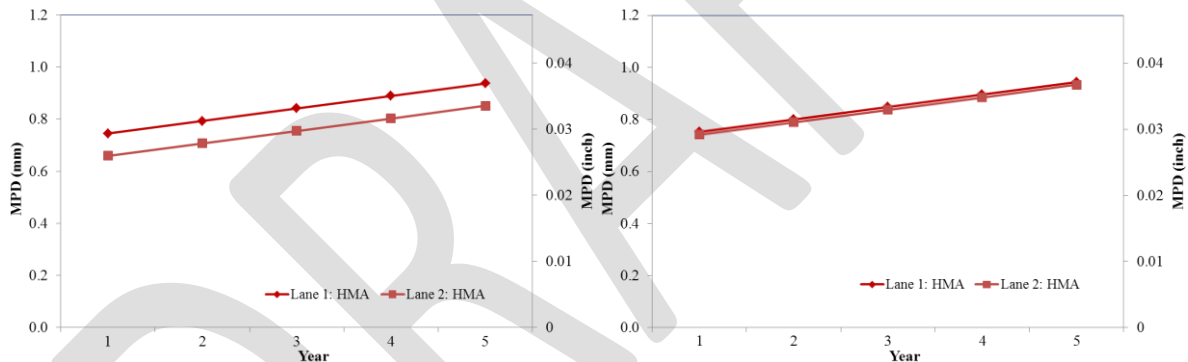


**Figure 10-8. MPD progression in all scenarios:  for case 671HC (thick asphalt) and for case 670HC (thin asphalt).**

## 10.3.5   Results and Discussion

### 10.3.5.1   Scenario I: Same Fatigue and IRI Performance Between Two Tires

In this scenario, the pavement performed the same under the standard DTA and NG-WBT. Therefore, the only difference in the results is the improved fuel economy due to use of the NG-WBT. Table **10-9** and 10-10 show the results for cases 671HC and 670HC, respectively, and Figure **10-9** shows the GHG emissions reduction for each case.

The results are intuitive: since no other impacts on the pavement from use of NG-WBT were included, the only benefits were improved fuel economy and an expected reduction in GHG emissions (due to less fuel consumed) for both cases. Also, because only trucks were equipped with NG-WBT, the higher the truck traffic volume and the greater the market penetration of NG-WBT, the greater the fuel savings (both environmentally and economically) and the greater the anticipated emissions reduction.

117

**Table 10-9. Scenario I Results for Case 671HC (Thick Asphalt): Energy Savings and GHG Emissions Reductions Compared with the Baseline (Standard Dual Tires)**

| | Market Penetration of Wide-Base Tires | Use Phase | Life Cycle Result |
|---|---|---|---|
| Energy saving compared with the baseline (MJ) | 5% | 127,654 | 127,654 |
| Energy saving compared with the baseline (MJ) | 10% | 255,308 | 255,308 |
| Energy saving compared with the baseline (MJ) | 50% | 1,276,540 | 1,276,540 |
| Energy saving compared with the baseline (MJ) | 100% | 2,553,079 | 2,553,079 |
| GHG reduction compared with the baseline (metric ton $CO_2$-e) | 5% | 9 | 9 |
| GHG reduction compared with the baseline (metric ton $CO_2$-e) | 10% | 19 | 19 |
| GHG reduction compared with the baseline (metric ton $CO_2$-e) | 50% | 94 | 94 |
| GHG reduction compared with the baseline (metric ton $CO_2$-e) | 100% | 187 | 187 |
| Economic saving compared with the baseline ($ Present) | 5% | 3,108 | 3,108 |
| Economic saving compared with the baseline ($ Present) | 10% | 6,216 | 6,216 |
| Economic saving compared with the baseline ($ Present) | 50% | 31,079 | 31,079 |
| Economic saving compared with the baseline ($ Present) | 100% | 62,158 | 62,158 |

**Table 10-10. Scenario I Results for Case 670HC (Thin Asphalt): Energy Savings and GHG Emissions Reductions Compared with the Baseline (Standard DTA)**

| | Market Penetration of Wide-Base Tires | Use Phase | Life Cycle Result |
|---|---|---|---|
| Energy saving compared with the baseline (MJ) | 5% | 8,694 | 8,694 |
| Energy saving compared with the baseline (MJ) | 10% | 17,388 | 17,388 |
| Energy saving compared with the baseline (MJ) | 50% | 86,941 | 86,941 |
| Energy saving compared with the baseline (MJ) | 100% | 173,881 | 173,881 |
| GHG reduction compared with the baseline (metric ton $CO_2$-e) | 5% | 1 | 1 |
| GHG reduction compared with the baseline (metric ton $CO_2$-e) | 10% | 1 | 1 |
| GHG reduction compared with the baseline (metric ton $CO_2$-e) | 50% | 6 | 6 |
| GHG reduction compared with the baseline (metric ton $CO_2$-e) | 100% | 13 | 13 |
| Economic saving compared with the baseline ($ Present) | 5% | 225 | 225 |
| Economic saving compared with the baseline ($ Present) | 10% | 449 | 449 |
| Economic saving compared with the baseline ($ Present) | 50% | 2,246 | 2,246 |

| | | | |
|---|---|---|---|
| Economic saving compared with the baseline ($ Present) | 100% | 4,493 | 4,493 |

### 10.3.5.2 Scenario II: Fatigue Performance Determines the Design Life

In this scenario, the pavement life is determined by fatigue cracking performance. Because the NG-WBT introduced a higher tensile strain at the bottom of the asphalt layer, which increased the expected amount of fatigue cracking and shortened pavement life, as market penetration of NG-WBT increases, the pavement design life decreases. As noted, this study annualized the energy consumption and GHG emissions were annualized from the material production and construction phases to avoid having different pavement design lives. Therefore, as the market penetration of NG-WBT increases, the annualized energy consumption and GHG emissions from the material production and construction phases increase. At the same time, the pavement's IRI performance was the same for NG-WBT and the DTA. Since the annualized use phase energy consumption and GHG emissions were calculated based on the pavement design life, the use phase results for Scenarios I and II differed slightly. Table 10-11 and Table 10-12 show the results for cases 671HC and 670HC, respectively, and Figure 10-10 shows the GHG emissions reduction for each case.

The results show that the damage to pavement from NG-WBT imposed a very significant impact on the material production and construction phases. When this impact was included in the analysis, various consequences were observed for the thin and thick sections. For the 671HC section, net savings in energy consumption and GHG were negative at lower market penetrations (5% and 10%) of NG-WBT and positive at higher market penetrations (50% and 100%). Thus, depending on the market penetration of NG-WBT, the life cycle impacts could also vary. However, the net economic saving for any market penetration was negative as the ratio of calorific or energy value and unit cost of fuel is very high compared with that of pavement materials. On the other hand, for the 670HC section, net savings in energy consumption and GHG were positive at lower market penetrations (5% and 10%) and negative at higher market penetrations (50% and 100%) because the savings from NG-WBT for the thin overlay section is minor due to low truck percent. Thus, the increased impacts from the reduced overlay service life at higher market penetrations surpass the fuel saving from NG-WBT. As the overlay service life remained constant, the net economic savings were positive at lower market penetrations (5% and 10%) and negative at high market penetrations (50% and 100%) due to reduced overlay service life.

It should be noted that this conclusion is heavily dependent on the pavement design life calculated from the performance model. If the pavement has the same design life for both DTA and NG-WBT, the difference in the material production and construction phases between the baseline and the other scenarios will be zero, and the benefit from the use phase will dominate the results. Further, not only is the tensile strain introduced by NG-WBT larger than that from DTA, the NG-WBT also have larger traffic wander. Therefore when the damage from NG-WBT was calculated, the cumulative damage might have been overestimated, thus resulting in a shortened pavement design life.

**Table 10-11. Scenario II Results for Case 671HC (Thick Asphalt): Energy Savings and GHG Emissions Reductions Compared with the Baseline (Standard Dual Tires)**

| | Market Penetration of Wide-Base Tires | Material Production Phase | Construction Phase | Use Phase | Life Cycle Result |
|---|---|---|---|---|---|
| Energy saving compared with the baseline (MJ) | 5% | -317,900 | -112,644 | 127,551 | -302,993 |
| Energy saving compared with the baseline (MJ) | 10% | -317,900 | -112,644 | 255,103 | -175,442 |
| Energy saving compared with the baseline (MJ) | 50% | -635,800 | -225,288 | 1,274,605 | 413,516 |
| Energy saving compared with the baseline (MJ) | 100% | -953,701 | -337,933 | 2,547,635 | 1,256,002 |
| GHG reduction compared with the baseline (metric ton $CO_2$-e) | 5% | -18 | -9 | 9 | -18 |
| GHG reduction compared with the baseline (metric ton $CO_2$-e) | 10% | -18 | -9 | 19 | -8 |
| GHG reduction compared with the baseline (metric ton $CO_2$-e) | 50% | -36 | -18 | 93 | 39 |
| GHG reduction compared with the baseline (metric ton $CO_2$-e) | 100% | -55 | -26 | 187 | 106 |
| Economic saving compared with the baseline ($ Present) | 5% | -128,642 | -39,408 | 3,108 | -164,942 |
| Economic saving compared with the baseline ($ Present) | 10% | -128,642 | -39,408 | 6,216 | -161,834 |
| Economic saving compared with the baseline ($ Present) | 50% | -257,283 | -78,817 | 31,079 | -305,021 |
| Economic saving compared with the baseline ($ Present) | 100% | -385,925 | -118,225 | 62,158 | -441,993 |

**Table 10-12. Scenario II Results for Case 670HC (Thin Asphalt): Energy Savings and GHG Emissions Reductions Compared with the Baseline (Standard Dual Tires)**

| | Market Penetration of Wide-Base Tires | Material Production Phase | Construction Phase | Use Phase | Life Cycle Result |
|---|---|---|---|---|---|
| Energy saving compared with the baseline (MJ) | 5% | 0 | 0 | 8,694 | 8,694 |
| Energy saving compared with the baseline (MJ) | 10% | 0 | 0 | 17,388 | 17,388 |
| Energy saving compared with the baseline (MJ) | 50% | -370,884 | -131,417 | 86,865 | -415,436 |
| Energy saving compared with the baseline (MJ) | 100% | -370,884 | -131,417 | 173,731 | -328,570 |
| GHG reduction compared with the baseline (metric ton $CO_2$-e) | 5% | 0 | 0 | 1 | 1 |
| GHG reduction compared with the baseline (metric ton $CO_2$-e) | 10% | 0 | 0 | 1 | 1 |
| GHG reduction compared with the baseline (metric ton $CO_2$-e) | 50% | -21 | -10 | 6 | -25 |
| GHG reduction compared with the baseline (metric ton $CO_2$-e) | 100% | -21 | -10 | 13 | -19 |
| Economic saving compared with the baseline ($ Present) | 5% | 0 | 0 | 217 | 217 |
| Economic saving compared with the baseline ($ Present) | 10% | 0 | 0 | 433 | 433 |
| Economic saving compared with the baseline ($ Present) | 50% | -194,606 | -59,123 | 2,164 | -251,565 |
| Economic saving compared with the baseline ($ Present) | 100% | -194,606 | -59,123 | 4,326 | -249,403 |
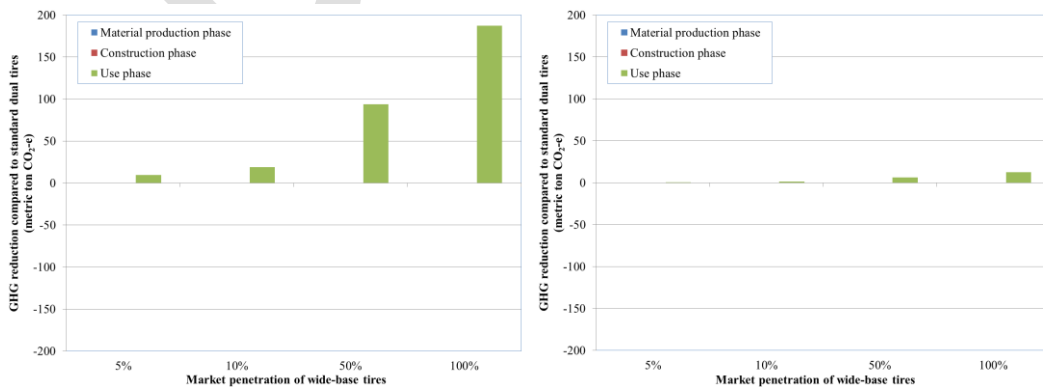


**Figure 10-9. Scenario I GHG emissions reduction compared with the baseline (*standard dual tires*): case 671HC (thick asphalt) and case 670HC (thin asphalt).**
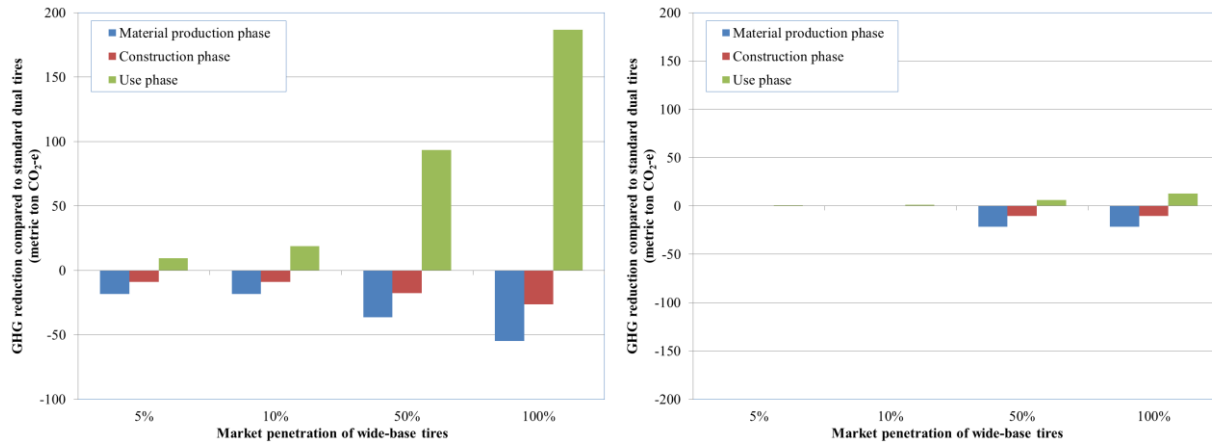
**Figure 10-10: Scenario II GHG emissions reduction compared with the baseline (standard dual tires): case 671HC (thick asphalt) and case 670HC (thin asphalt).**

### 10.3.5.3  Scenario III: IRI Performance Determines Design Life

In this scenario, the pavements have the same fatigue cracking performance for DTA and NG-WBT, and IRI performance is the determining factor for design life. This part of the study used rutting life to estimate the IRI performance under NG-WBT. Table 10-13 and Table 10-14 show the results for cases 671HC and 670HC, respectively, and Figure 10-11 shows the GHG emissions reduction for each case.

The results of scenario III for cases 671HC and 670HC were contrasting. The 671HC case experienced positive savings in energy and GHG from fuel economy improvement as well as extended overlay rutting life. This also resulted in economic savings from less material production and equipment operation (at 100% market penetration of NG-WBT) as well as fuel economy improvement. Fuel economy improvement and energy saving from a slower IRI progression due to NG-WBT, the savings in the overall use phase were slightly greater than scenario II. The opposite was observed for the 670HC case. Savings in energy and GHG were negative because of reduced rutting life and the energy loss from a faster IRI progression that surpassed the fuel economy improvement by using NG-WBT. Therefore, resulting economic savings were also negative for the material, construction, and use phases.

**Table 10-13. Scenario III Results for Case 671HC (Thick Asphalt): Energy Savings and GHG Emissions Reductions Compared with the Baseline (Standard Dual Tires)**

| | Market Penetration of NG-WBT | Material Production Phase | Construction Phase | Use Phase | Life Cycle Result |
|---|---|---|---|---|---|
| Energy saving compared with the baseline (MJ) | 5% | 0 | 0 | 137,472 | 137,472 |
| Energy saving compared with the baseline (MJ) | 10% | 0 | 0 | 264,933 | 264,933 |
| Energy saving compared with the baseline (MJ) | 50% | 0 | 0 | 1,284,617 | 1,284,617 |
| Energy saving compared with the baseline (MJ) | 100% | 556,325 | 197,127 | 2,575,624 | 3,329,077 |
| GHG reduction compared with the baseline (metric ton $CO_2$-e) | 5% | 0 | 0 | 10 | 10 |
| GHG reduction compared with the baseline (metric ton $CO_2$-e) | 10% | 0 | 0 | 19 | 19 |
| GHG reduction compared with the baseline (metric ton $CO_2$-e) | 50% | 0 | 0 | 94 | 94 |
| GHG reduction compared with the baseline (metric ton $CO_2$-e) | 100% | 32 | 15 | 189 | 236 |
| Economic saving compared with the baseline ($ Present) | 5% | 0 | 0 | 3,497 | 3,497 |
| Economic saving compared with the baseline ($ Present) | 10% | 0 | 0 | 6,740 | 6,740 |
| Economic saving compared with the baseline ($ Present) | 50% | 0 | 0 | 32,681 | 32,681 |
| Economic saving compared with the baseline ($ Present) | 100% | 180,098 | 55,172 | 64,584 | 299,854 |

**Table 10-14. Scenario III Results for Case 670HC (Thin Asphalt): Energy Savings and GHG Emissions Reductions Compared with the Baseline (Standard Dual Tires)**

| | Market Penetration of NG-WBT | Material Production Phase | Construction Phase | Use Phase | Life Cycle Result |
|---|---|---|---|---|---|
| Energy reduction compared with the baseline (MJ) | 5% | 0 | 0 | -300,383 | -300,383 |
| Energy reduction compared with the baseline (MJ) | 10% | 0 | 0 | -291,648 | -291,648 |
| Energy reduction compared with the baseline (MJ) | 50% | -317,900 | -112,644 | -380,996 | -811,540 |
| Energy reduction compared with the baseline (MJ) | 100% | -476,850 | -168,965 | -432,971 | -1,078,787 |
| GHG reduction compared with the baseline (metric ton $CO_2$-e) | 5% | 0 | 0 | -22 | -22 |
| GHG reduction compared with the baseline (metric ton $CO_2$-e) | 10% | 0 | 0 | -21 | -21 |
| GHG reduction compared with the baseline (metric ton $CO_2$-e) | 50% | -18 | -9 | -27 | -54 |
| GHG reduction compared with the baseline (metric ton $CO_2$-e) | 100% | -27 | -13 | -31 | -71 |
| Economic saving compared with the baseline ($ Present) | 5% | 0 | 0 | -7,319 | -7,319 |
| Economic saving compared with the baseline ($ Present) | 10% | 0 | 0 | -7,106 | -7,106 |
| Economic saving compared with the baseline ($ Present) | 50% | -166,805 | -50,677 | -9,553 | -227,035 |
| Economic saving compared with the baseline ($ Present) | 100% | -250,208 | -76,015 | -11,015 | -337,238 |

Because NG-WBT causes a higher tensile strain at the bottom of the AC layer, the interaction between the pavement damage caused by NG-WBT−which affects the pavement design life and the environmental impacts in the material production and construction phases−and fuel economy improvements resulting from NG-WBT was investigated. A developed LCA model was applied to evaluate AC overlays for two case studies. Two pavement segments were analyzed in this study: 671HC and 670HC, which were based on two pavement structures used in APT testing and represented two levels of truck traffic volume (high and low, respectively). Three analysis scenarios were considered where (I) pavement design life was considered the same for standard DTA and NG-WBT; (II) pavement design life was determined for fatigue cracking performance; and (III) pavement design life was determined by IRI performance. Various market penetration levels of NG-WBT were also analyzed within each scenario. Annualized energy consumption and GHG emissions were used to compare the different scenarios.
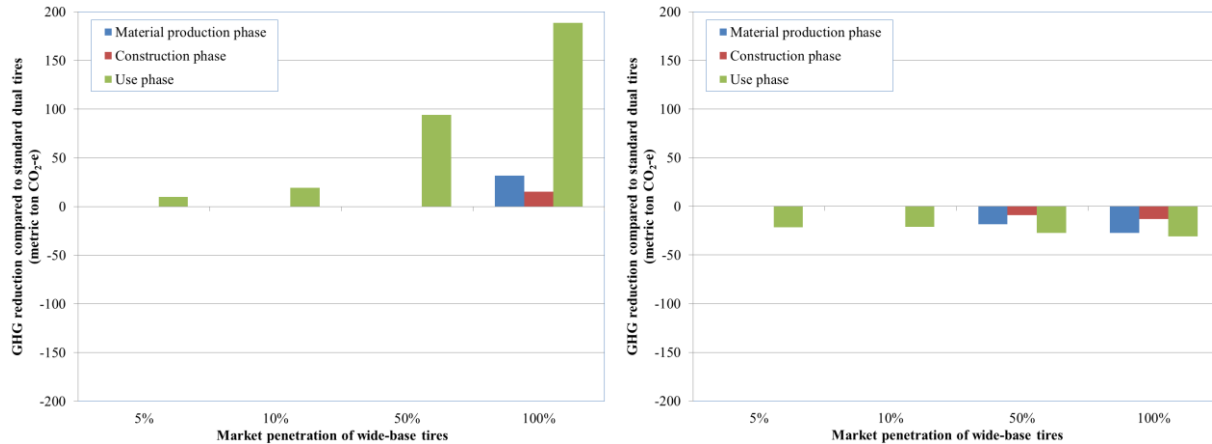
**Figure 10-11: Scenario III GHG emissions reduction compared with the baseline (DTA): case 671HC (thick asphalt) and case 670HC (thin asphalt).**

The results indicated the following:

- Scenario I resulted in significant cost and fuel consumption savings and GHG emissions reductions when NG-WBT was used.
- Scenario II showed that 670HC had higher annual energy consumption and GHG emissions compared with the baseline, while 671HC experienced an overall saving in energy consumption and GHG emissions when NG-WBT was used.
- Scenario III resulted in NG-WBT having lower life cycle energy consumption and cost and GHG emissions for 671HC, while it was higher for 670HC.

In summary, it is evident that NG-WBT results is significant savings in life cycle energy consumption and cost, and GHG emissions; however, these benefits are sensitive to the method used to determine pavement performance, especially that a small change in pavement strain may result in significant changes in pavement life.

## 10.4 SUMMARY

To assess the environmental and economic impacts of adopting NG-WBT, an approach was developed to evaluate the life-cycle energy consumption and cost, and GHG emissions from their use. The life cycle phases analyzed in this study include pavement material production, pavement construction, and pavement use phases. The life cycle of tires was not included due to unavailability of data, and the contribution of tires to the results would be very limited since only a very small portion of a tire's life would be allocated to the pavement segments analyzed in the study. The impacts from pavement roughness and macrotexture on vehicle fuel consumption, as well as the fuel economy improvement from using NG-WBT, are included in the pavement use phase.

125

# 11 CONCLUSIONS AND RECOMMENDATIONS

The main objective of this study was to perform a comprehensive approach to compare the impact of NG-WBT and DTA on road infrastructure. Contact stresses of the NG-WBT and DTA were measured. A numerical model was generated to simulate realistic pavement structures, materials, and applied loading conditions. The model was validated with various field test sections across the United States. Good agreement was noted between finite element analysis results and pavement field instrument responses when using proper material characterization parameters, especially for vertical pressure and tensile strain in transverse direction. The FE model is capable of realistically simulating tire-pavement interaction in the field when accurate data are used

It was evident that NG-WBT responses were generally greater than DTA for thin and thick pavements. The difference decreased with depth, and a few cases showed higher responses for DTA (e.g., shear strain in the subgrade in thin pavement). A small change in pavement responses resulted in enormous changes in pavement performance or life when using transfer functions, and therefore the impact of pavement response was presented in stresses and strain changes. The following conclusions summarize the findings of this study:

1) Elastic theory and empirical transfer function may not be accurate for predicting the impact of NG-WBT. Hence, realistic models should be used to quantify the impact of NG-WBT including 3-D finite element modeling, proper material cauterization (e.g., viscoelastic asphalt properties and anisotropic unbound materials for thin pavements, etc.), and moving nonuniform three-dimensional tire loading.

2) Considering the smaller contact area of NG-WBT, near-surface strain should be carefully investigated during the design method. While increasing AC thickness reduces bottom-up cracking potential, it may increase near-surface cracking and, therefore, a proper wearing surface should be used. On the other hand, building pavements with strong granular base layer may diminish changes in potential subgrade rutting.

3) DTA with differential tire inflation pressure produces higher damage than DTA with the same tire inflation pressure.

4) For local roads, subgrade rutting is the controlling distress of the pavement life; the difference between the two tires impact on subgrade failure is not significant. The impact of NG-WBT is greater than that of DTA on interstate highways where the controlling distress in asphalt concrete for perpetual pavement is top-down or near-surface cracking and possible AC rutting. Durable, high-performance surface materials, usually implemented in the interstate system, can control this damage. For typical (non-perpetual) pavement, the impact of NG-WBT is still greater than DTA but to a lesser degree.

5) MEPDG may not be used directly for predicting responses of NG-WBT. Therefore, two adjustment factors were developed to modify the pavement responses obtained from MEPDG to FE NG-WBT: i) adjustment of MEPDG results to FE results; and ii) adjustment of MEPDG DTA results to NG-WBT.

6) To simplify the process of using NG-WBT and allow for implementation by agencies, an ANN tool was developed to predict the pavement response without running FE. The tool results rendered by the ANN surrogate models were highly accurate with average prediction error less than 5% and R-square values higher than 0.95. The ANN tool can be incorporated in mechanistic design methods, such as the AASHTOWare.

7) Based on the life cycle assessment (LCA) models developed and applied and the NG-WBT market penetration percentages considered, NG-WBT can save energy and reduce GHG and emissions, depending on corresponding pavement performance.

8) Although NG-WBT may cause more distresses than DTA for some roads, NG-WBT demonstrate significant improvement compared with FG-WBT.

# 12  REFERENCES

AASHTO. (2008). "Mechanistic-Empirical Pavement Design Guide: A Manual of Practice." Interim Edition, American Association of Highways and Transportation Officials.

Al-Qadi I.L., Dessouky S. H., Kwon J., and Tutumluer E., (2008). "Geogrid in Flexible Pavements Validated Mechanism." *Transportation Research Record: Journal of the Transportation Research Board*, No. 2045, Transportation Research Board of the National Academies, Washington, DC.

Al-Qadi, I. L., Elseifi, M. A., Yoo, P. J., Dessouky, S. H., Gibson, N., Harman, T., and Petros, K. (2008). Accuracy of Current Complex Modulus Selection Procedure from Vehicular Load Pulse: NCHRP project 1-37a mechanistic-empirical pavement design guide. *Transportation Research Record: Journal of the Transportation Research Board*, *2087*(1), 81-90.

Al-Qadi, I. L., Wang, H., Yoo, P., Dessouky, S. (2008). "Dynamic Analysis and In Situ Validation of Perpetual Pavement Response to Vehicular Loading." *Transportation Research Record: Journal of the Transportations Research Board*, 2087(2008), 28-39.

Al-Qadi, I. L., Xie, W., and Elseifi, M. A. (2008). Frequency Determination from Vehicular Loading Time Pulse to Predict Appropriate Complex Modulus In MEPDG. *Journal of the Association of Asphalt Paving Technologists*, *77*.

Al-Qadi, I. L., and Yoo, P. J. (2007). Effect of Surface Tangential Contact Stresses on Flexible Pavement Response (With Discussion). Journal of the Association of Asphalt Paving Technologists, 76.

Asia Sustainable and Alternative Energy Program (ASTAE). (2011). "ROADEO Toolkit User Manual".

Athena Sustainable Materials Institute. (2013). Impact Estimator [software], <http://calculatelca.com/software/impact-estimator/download-impact-estimator/>

Athena Institute. (2006). "A Life Cycle Perspective on Concrete and Asphalt Roadways: Embodied Primary Energy and Global Warming Potential" <www.cement.ca/images/stories/ athena%20report%20Feb.%202%202007.pdf>.

Bachman, L. J., Erb, A., and Bynum, C. L. (2005). "Effect of Single Wide Tires and Trailer Aerodynamics on Fuel Economy and NOx Emissions of Class 8 Line-Haul Tractor-Trailers." SAE Paper Number 05CV-45. American Society for Testing and Materials, Warrendale, PA.

Bonaquist, R. (1992). "An Assessment of the Increased Damage Potential of Wide Base Single Tires." 7th International Conference on Asphalt Pavements, Nottingham, UK, pp. 1-16.

Bathe, K.J. (1982).  Finite Element Procedures in Engineering Analysis, Prentice-Hall, New Jersey.

Brock, J. D., and Richmond, J. R. (2006). "Milling and Recycling." Technical Paper T-127. An Astec Industries Company. U.S.A.

Caglar, N., M. Elmas, Z. Dere Yaman, and M. Saribiyik (2008). "Neural Networks in 3-Dimensional Dynamic Analysis of Reinforced Concrete Buildings." *Construction and Building Materials,* (22), pp. 788–800.

California Department of Transportation (Caltrans). (2011). Contract Cost Data - A Summary of Cost by Items for Highway Construction Projects. Division of Engineering Services, CA.

Caltrans. (n.d.) Caltrans Pavement Climate Regions Map. <www.dot.ca.gov/hq/maint/Pavement/ Offices/Pavement_Engineering/Climate.html>. (Feb. 24, 2013).

De Beer, M., C. Fisher, and F. J. Jooste. Determination of Pneumatic Tyre/Pavement Interface Contact Stresses under Moving Loads and Some Effects on Pavements with Thin Asphalt Surfacing. In

*Proceedings of the 8th International Conference on Asphalt Pavements*, Seattle, Washington. 1997, pp. 179–227.

Emissions and Generation Resources Integrated Database (eGRID). (2012). U.S. Environmental Protection Agency. Washington, D.C.

EPA. (2008). NONROAD Model (Nonroad engines, equipment, and vehicles), NONROAD 2008a Model (Version 2008a) [software], <http://www.epa.gov/otaq/nonrdmdl.htm>.

Fakhri, M. and Ghanizadeh, A. R. (2014). "Modelling of 3D Response Pulse at the Bottom of Asphalt Layer Using a Novel Function and Artificial Neural Network." *International Journal of Pavement Engineering*, 15(8), 671-688.

FHWA (2012). "Long Term Pavement Performance Program Standard Data Release (SDR) 26.0". CD-ROM.

Franzese, O., Knee, H. E., and Slezak, L. (2010). "Effect of Wide-Based Single Tires on Fuel Efficiency of Class 8 Combination Trucks." *Transportation Research Record*, No. 2191, pp. 1-7.

GENIVAR Consulting Group (2005). "Economic Study Use of Supersingle Tires by Heavy Vehicles Operating in Québec." Report published by GENIVAR Consulting Group, Montreal, QC, Canada.

Greene J., Toros U., Kim S., Byron T., and Choubane B., (2010). "Impact of Wide-Base Single Tires on Pavement Damage." *Transportation Research Record: Journal of the Transportation Research Board*, No. 2155, Transportation Research Board of the National Academies, Washington, DC.

Greenhouse Gases, Regulated Emissions, and Energy Use in Transportation (GREET) 1. (2013). Argonne National Laboratory. [Software]. Chicago, IL.

Harvey, J., Kendall, A., Lee, I.-S., Santero, N., Van Dam, T., and Wang, T. (2010). "Pavement Life Cycle Assessment Workshop: Discussion Summary and Guidelines." UCPRC-TM-2010-03. <www.dot.ca.gov/research/researchreports/reports/2010/2010-05_task_1897_pavement.pdf>. University of California Pavement Research Center, Davis and Berkeley, CA.

Harvey J., and Popescu L., (2000). *Rutting of Caltrans Asphalt Concrete and Asphalt-Rubber Hot Mix under Different Wheels, Tires and Temperatures – Accelerated Pavement Testing Evaluation*. Pavement Research Center Institute of Transportation Studies University of California, Berkeley

Helwany, S. (2007). Applied Soil Mechanics with ABAQUS® Applications. John Wiley & Sons, Inc, Hoboken, New Jersey.

Horvath, A. (2007). PaLATE Pavement Life Cycle Assessment Tool for Environmental and Economic Effects (ver 2.2) [software], <http://www.ce.berkeley.edu/~horvath/palate.html>.

IPCC. (2007). IPCC Fourth Assessment Report: Climate Change 2007 (AR4): The Physical Science Basis. Contribution of Working Group I to the Fourth Assessment Report of the IPCC. <www.ipcc.ch/publications_and_data/publications_ipcc_fourth_assessment_report_wg1_report_the_physical_science_basis.htm>. Cambridge University Press, Cambridge, United Kingdom and New York, NY, USA.

Kendall, A. (2007). "Concrete Infrastructure Sustainability: Life Cycle Metrics, Materials Design, and Optimized Distribution of Cement Production." Ph.D Dissertation. University of Michigan.

Kim, Minkwan, Erol Tutumluer, and Jayhyun Kwon. (2009). "Nonlinear Pavement Foundation Modeling for Three-Dimensional Finite-Element Analysis of Flexible Pavements." *International Journal of Geomechanics*.

Lee, I.-S. (2013). "Approaches to Life Cycle Inventory Development for Sustainable Highway

Infrastructure: Protocol Development, Regionalization, and New Inventories." Ph.D. Dissertation. University of California, Davis, Davis, CA.

Lu, Q., Kohler, E., Harvey, J. T., and Ongel, A. (2009). "Investigation of Noise and Durability Performance Trends for Asphaltic Pavement Surface Types: Three-Year Results." UCPRC-RR-2009-01. <www.ucprc.ucdavis.edu/pdf/UCPRC-RR-2009-01.pdf>. Report published by University of California Pavement Research Center, Davis and Berkeley, CA.

Moghaddam, F. R., S.H. Afandizadeh, and M. Ziyadi, (2011). "Prediction of Accident Severity Using Artificial Neural Networks", *International Journal of Civil Engineering*, Vol. 9, No. 1.

Motor Vehicle Emissions Simulator (MOVES) 2014 Model. (2014). U.S. Environmental Protection Agency. [Software]. Washington, D.C.

Mukherjee, A., and Cass, D. (2012). "Project Emissions Estimator Implementation of a Project-Based Framework for Monitoring the Greenhouse Gas Emissions of Pavement." *Transportation Research Record*, No. 2282, pp. 91-99.

National Renewable Energy Laboratory. (n.d.). U.S. Life Cycle Inventory Database <www.nrel.gov/lci/>. (Jul. 30, 2011.)

National Cooperative Highway Research Program (NCHRP). (2004). "Guide for the Mechanistic-Empirical Design for New and Rehabilitated Pavement Structure". 1-37A, Transportation Research Board, Washington, DC

NCHRP. (2013). "2013 Fuel Usage Factors in Highway and Bridge Construction", NCHRP report 744, Washington, D.C.

Organization for Economic Co-Operation and Development (OECD) (1992). "OECD Report." Dynamic Loading of Pavements. OECD, Paris, France.

PRe Constultants. (2013). SimaPro8.0 [software], <http://www.pre-sustainability.com/software>.

Santero, N., Masanet, E., and Horvath, A. (2010). "Life Cycle Assessment of Pavements: A Critical Review of Existing Literature and Research." <www.escholarship.org/uc/item/8632v9cc.pdf>. Portland Cement Association, Skokie, IL.

Santero, N. J., Masanet, E. and Horvath, A. (2011). "Life-cycle Assessment of Pavements. Part I: Critical Review." *Resources, Conservation and Recycling*, Vol. 55, No. 9-10, pp. 801-809.

Stripple, H. (1998). "Life Cycle Assessment of Road (Swedish)." <www.ivl.se/webdav/files/B-rapporter/B1210E.pdf>. Swedish Environmental Research Institute, Stockholm, Sweden.

Schalkoff, R.J. (1997). *Artificial Neural Networks*. McGraw-hill, N. Y.

Swiss Centre for Life Cycle Inventories. (2011). EcoInvent. <www.ecoinvent.org>. (Sep. 15, 2013.) Swiss Centre for Life Cycle Inventories, Dubendorf, Switzerland.

Tabatabaee, N., M. Ziyadi, and Y Shafahi (2013). "Two-Stage Support Vector Classifier and Recurrent Neural Network Predictor for Pavement Performance Modeling." *Journal of Infrastructure Systems*. 19(3), 266–274.

Tseng, E. (2012). "The Construction of Pavement Performance Models for the California Department of Transportation New Pavement Management System." Master's Thesis. University of California, Davis, Davis, CA.

Tutumluer, E. (2008). State of the Art: Anisotropic Characterization of Unbound Aggregate Layers in Flexible Pavements. *Engineering Mechanics Conference*. Minneapolis, MN

Tutumluer, E. and Thompson, M. (1998). Anisotropic Modeling of Granular Bases. Final Report for the Federal Highway Administration

U.S. Department of Energy. (2009). Transportation Energy Data Book. 2008. U.S. Department of Transportation, National Transportation Statistics.

U.S. Energy Information Administration. (2014). Petroleum & Other Liquids. Online Database. [Jun. 2014]. <http://www.eig.gov/petroleum/gasdiesel/>.

Wang, T., Lee, I. S., Kendall, A., Harvey, J., Lee, E. B., and Kim, C. (2012). "Life Cycle Energy Consumption and GHG Emission from Pavement Rehabilitation with Different Rolling Resistance." *Journal of Cleaner Production*, Vol. 33, pp. 86-96.

Wang, T. (2013). "Reducing Greenhouse Gas Emissions and Energy Consumption Using Pavement Maintenance and Rehabilitation: Refinement and Application of A Life Cycle Assessment Approach." Ph.D. Dissertation. University of California, Davis, Davis, CA.

Wang, T., Lee, I.-S., Harvey, J., Kendall, A., Lee, E. B., and Kim, C. (2012). "UCPRC Life Cycle Assessment Methodology and Initial Case Studies on Energy Consumption and GHG Emissions for CAPM Treatments with Different Rolling Resistance." UCPRC-RR-2012-02. <www.ucprc.ucdavis.edu/PDF/UCPRC-RR-2012-02.pdf>. University of California Pavement Research Center (UCPRC), Davis and Richmond, CA.

Wang, H. (2011). "Analysis of Tire-Pavement Interaction and Pavement Responses Using a Decoupled Modeling Approach." PhD Dissertation. University of Illinois at Urbana-Champaign, Urbana, Illinois.

Xiao, Y., Tutumluer, E., Siekmeier, J. (2011) Mechanistic–Empirical Evaluation of Aggregate Base and Granular Subbase Quality Affecting Flexible Pavement Performance in Minnesota. *Transportation Research Record.* 2227, 97-106.

Xue W., and Weaver E., (2011). "Pavement Shear Strain Response to Dual and Wide-Base Tires." Presented in *90th Annual Meeting*, *Transportation Research Board of the National Academies*, Washington, DC.

Yoo, P.J. and Al-Qadi, I.L. (2007). "Effect of Transient Dynamic Loading on Flexible Pavements." *Transportation Research Record: Journal of the Transportations Research Board*, 1990(2007), 129-140.

Yoo, P. J., and I. L. Al-Qadi. The Truth and Myth of Fatigue Cracking Potential in Hot-Mix Asphalt: Numerical Analysis and Validation. *Journal of Association of Asphalt Paving Technologists*, Vol. 77, 2008, pp. 549–590.

Yoo, P. J., Al-Qadi, I. L., Elseifi, M. A., and Janajreh, I. (2006). Flexible Pavement Responses to Different Loading Amplitudes Considering Layer Interface Condition and Lateral Shear Forces. The International Journal of Pavement Engineering, 7(1), 73-86.

Zhang, H., Lepech, M. D., Keoleian, G. A., Qian, S. Z., and Li, V. C. (201). "Dynamic Life-Cycle Modeling of Pavement Overlay Systems: Capturing the Impacts of Users, Construction, and Roadway Deterioration." *Journal of Infrastructure Systems*, Vol. 16, No. 4, pp. 299-309.

# Appendix A:    Three-Dimensional Contact Stresses



**WBT Load=26 kN, and Inflation Pressure=552 kPa**
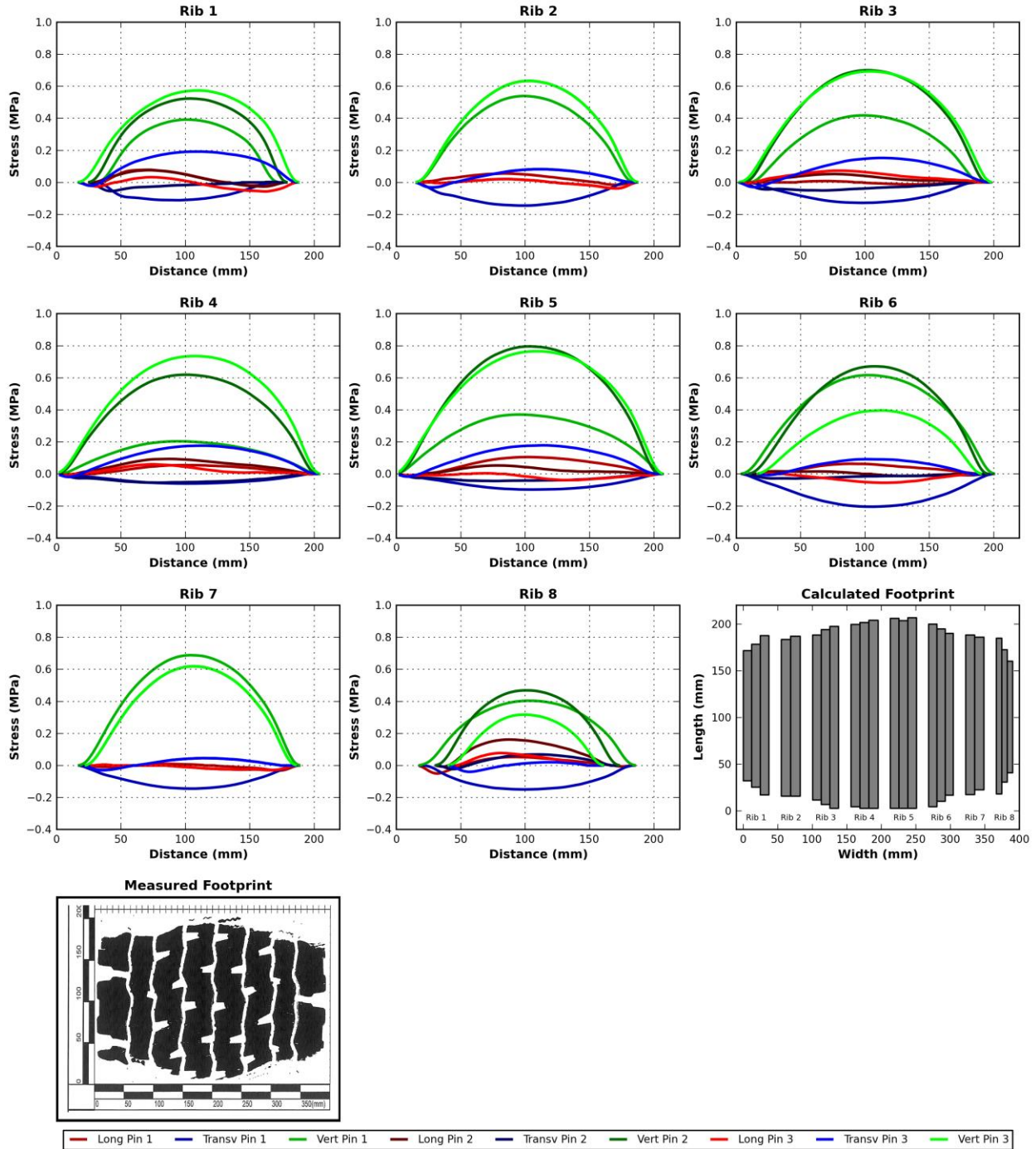
Figure A- 1. Three-dimensional contact stresses when *P*=6 kip and *S*=80 psi for NG-WBT.

# Appendix B: Modeling Results Thin Pavement
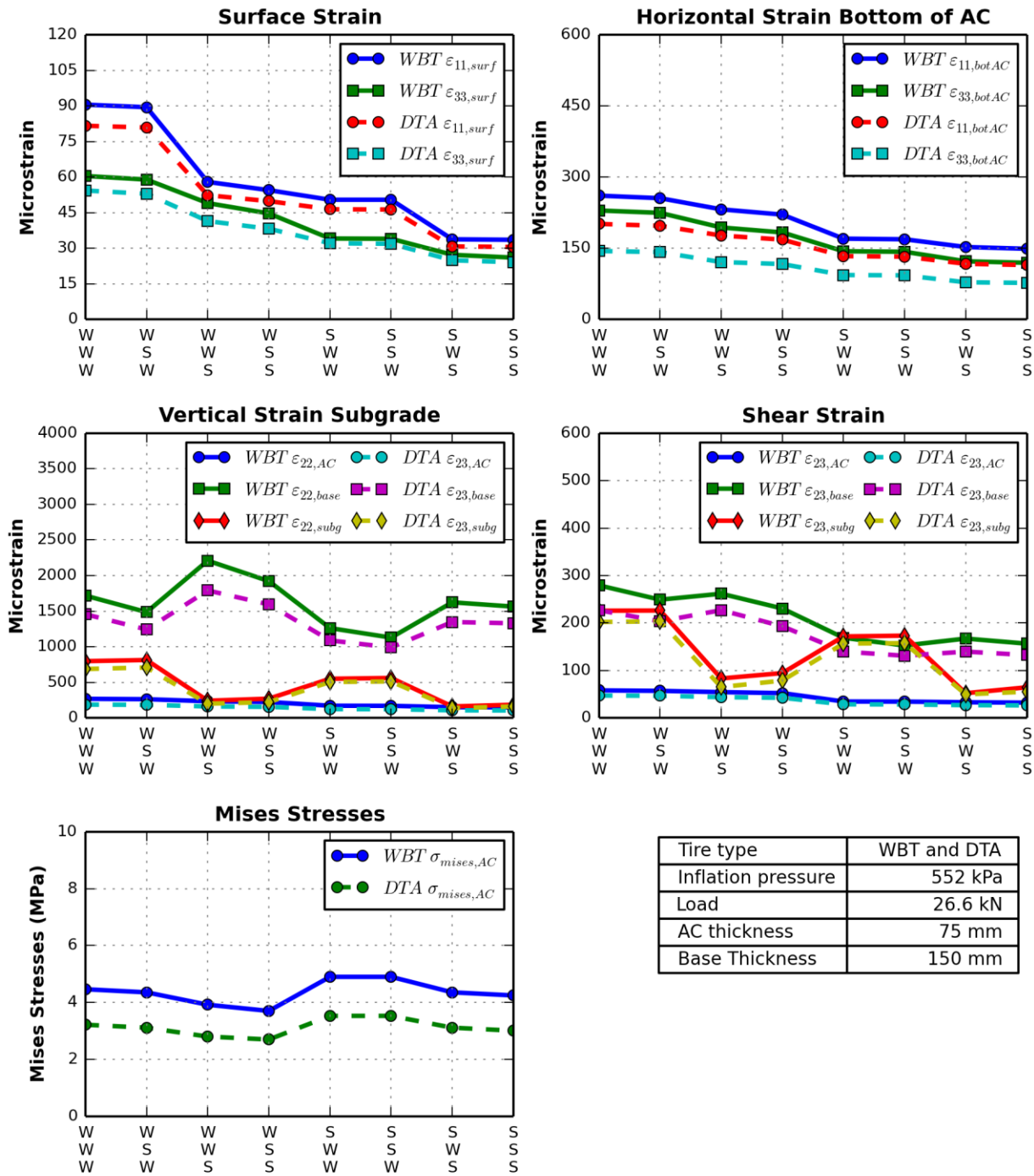


Figure B-1. Critical pavement responses for AC=3 in., B=6 in., *P*=6 kip, and *S*=80 psi.

# Appendix C:    Modeling Results Thick Pavement

## L1 and L5, AC=125mm, Base=150mm
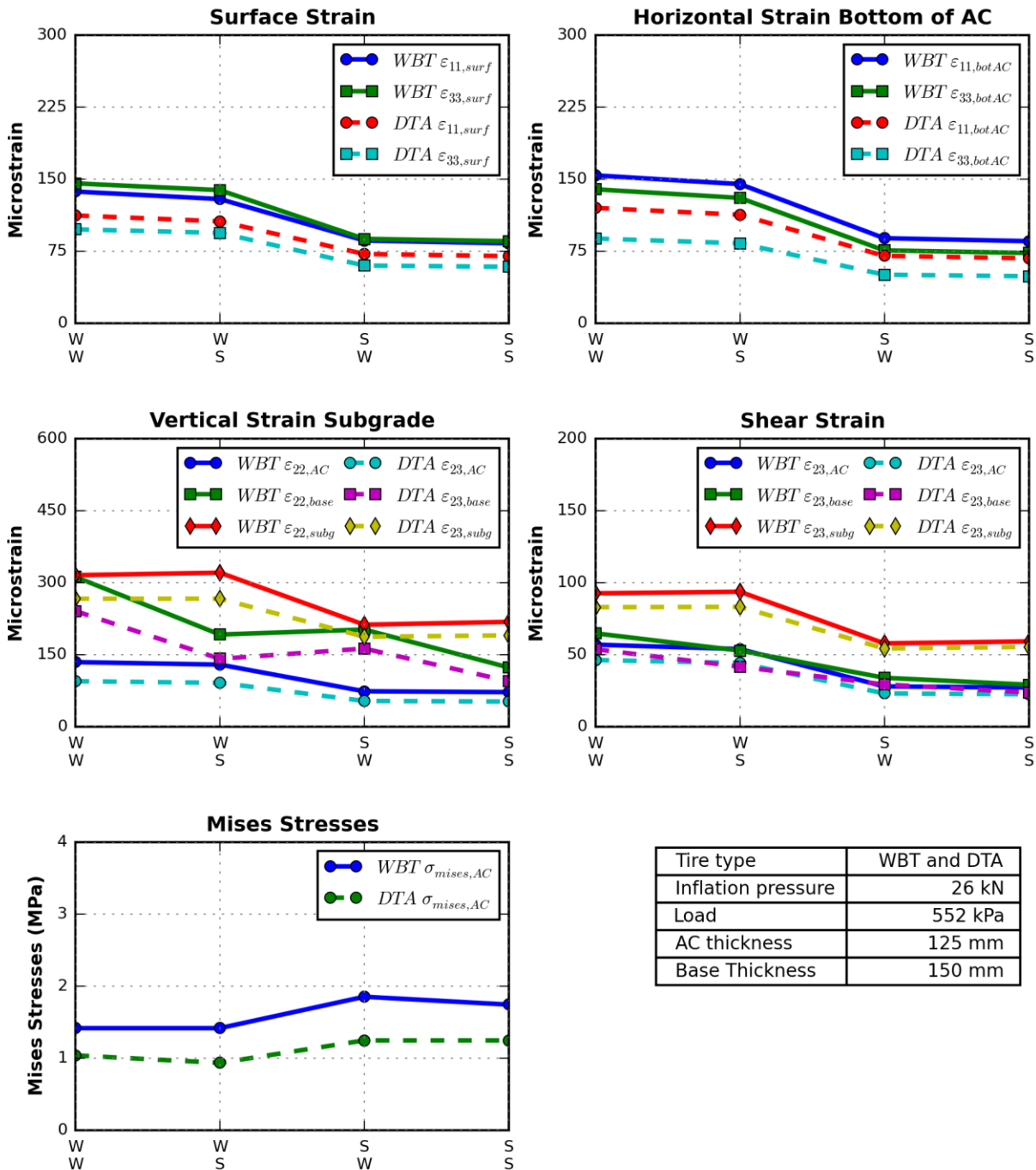


**Figure C-1. Critical pavement responses for AC=5 in., B=6 in., *P*=6 kip, and S=80 psi.**

# Appendix D:    ICT-Wide Tool

Installation guide: the software package includes the following files:
- Application file 'ICT-Wide.exe
- MyAppInstaller_mcr.exe
- MyAppInstaller_web.exe
- splash.png and
- readme.txt file

First, install the file 'MyAppInstaller_mcr'. In case of error, the updated version can be found on the internet by searching the key word 'mcr Matlab R2014a'. After installing mcr file, run the application ICT-Wide to use the tool.

Figure D-2 to Figure D-5 show a few snapshots of the tool. There are two main input modules; the output module is located at the bottom. The user provides inputs in the load and structure modules and specifies the outputs in the responses module. There are two options for inputting structure information: low-volume (thin) or interstate (thick) structures. Accordingly, two levels of inputs, Level 1 and Level 2, are provided to enter material properties. Upon selecting input level, details can be entered by pressing "open" (Figure D-2). After completing inputs, the tool will generate the selected responses.

Three possible windows can be seen as a result. If the model runs successfully, a window will appear requesting a destination folder to save the results. If any of the inputs is entered incorrectly, a window will appear asking for correcting possible mistakes. Finally, if the user enters invalid or out-of-range inputs, which might lead to unrealistic output, a window will appear warning the user. The output will be saved as a csv file including the inputs specified by user and predicated responses. Different cases can be appended to the same file.
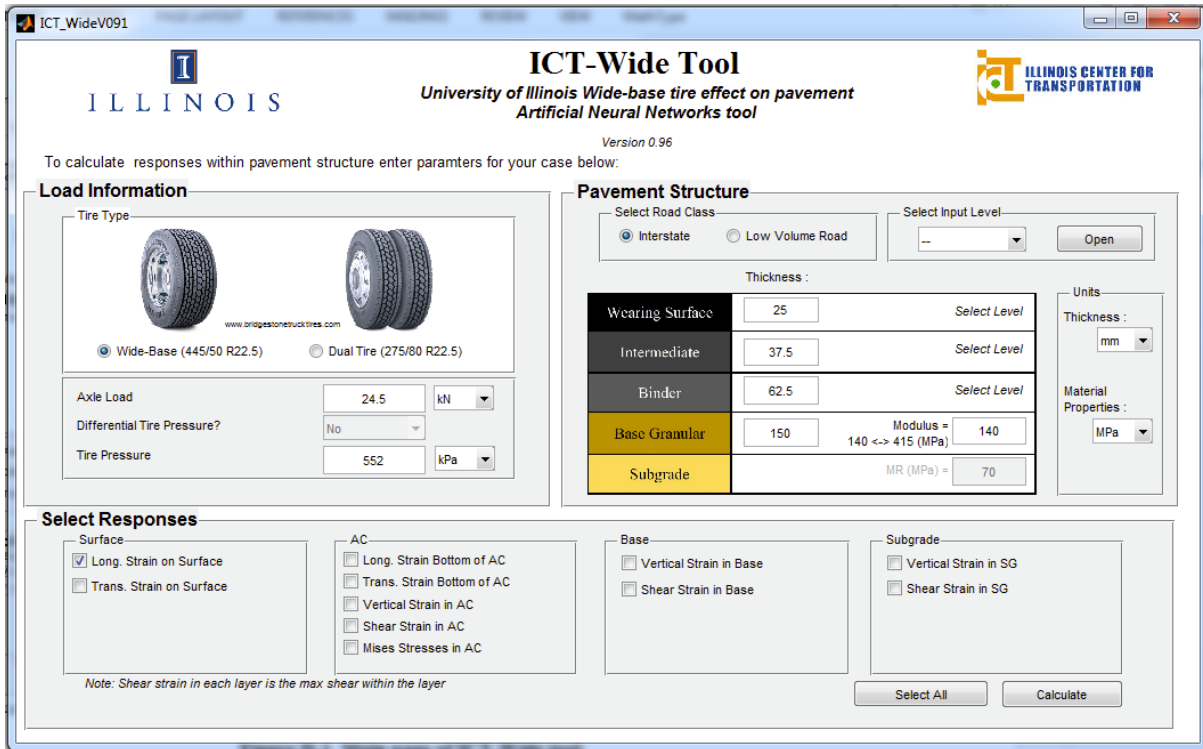
**Figure D-2. Main page of ICT-Wide tool.**
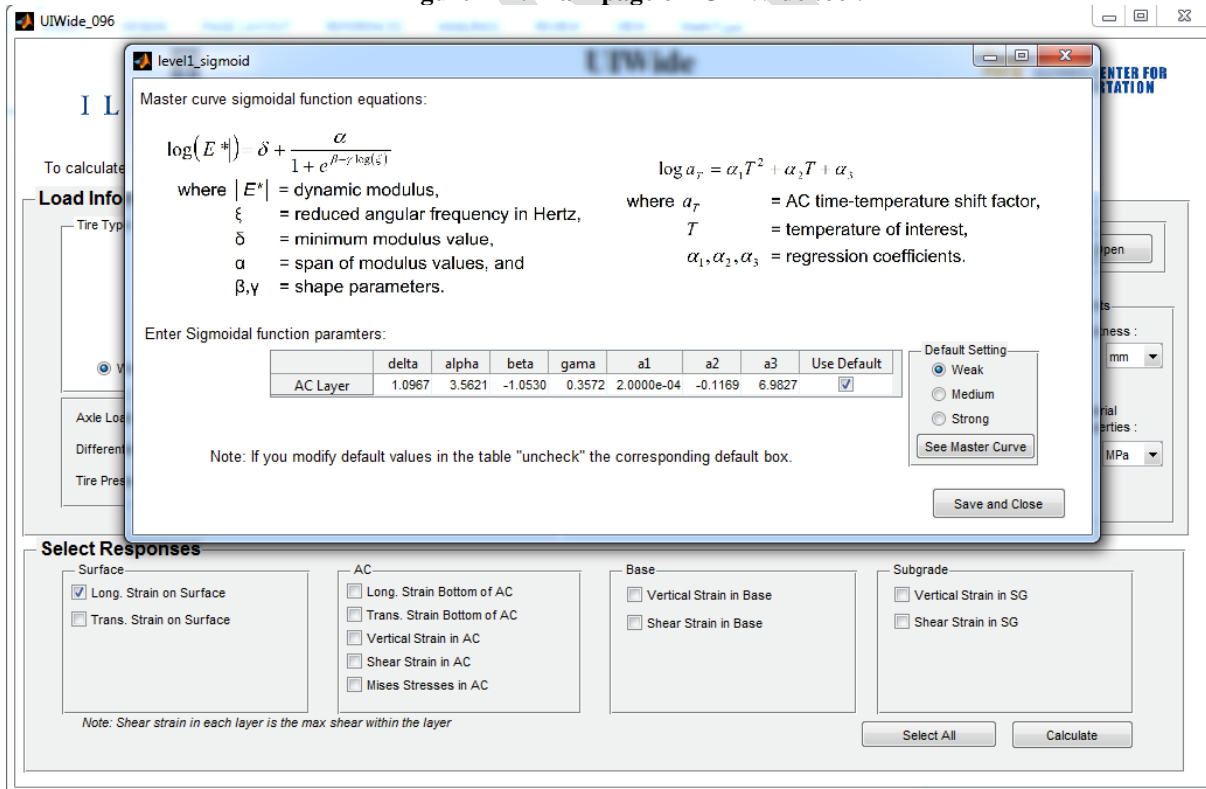


**Figure D-3. Prompt for Level 1 input.**
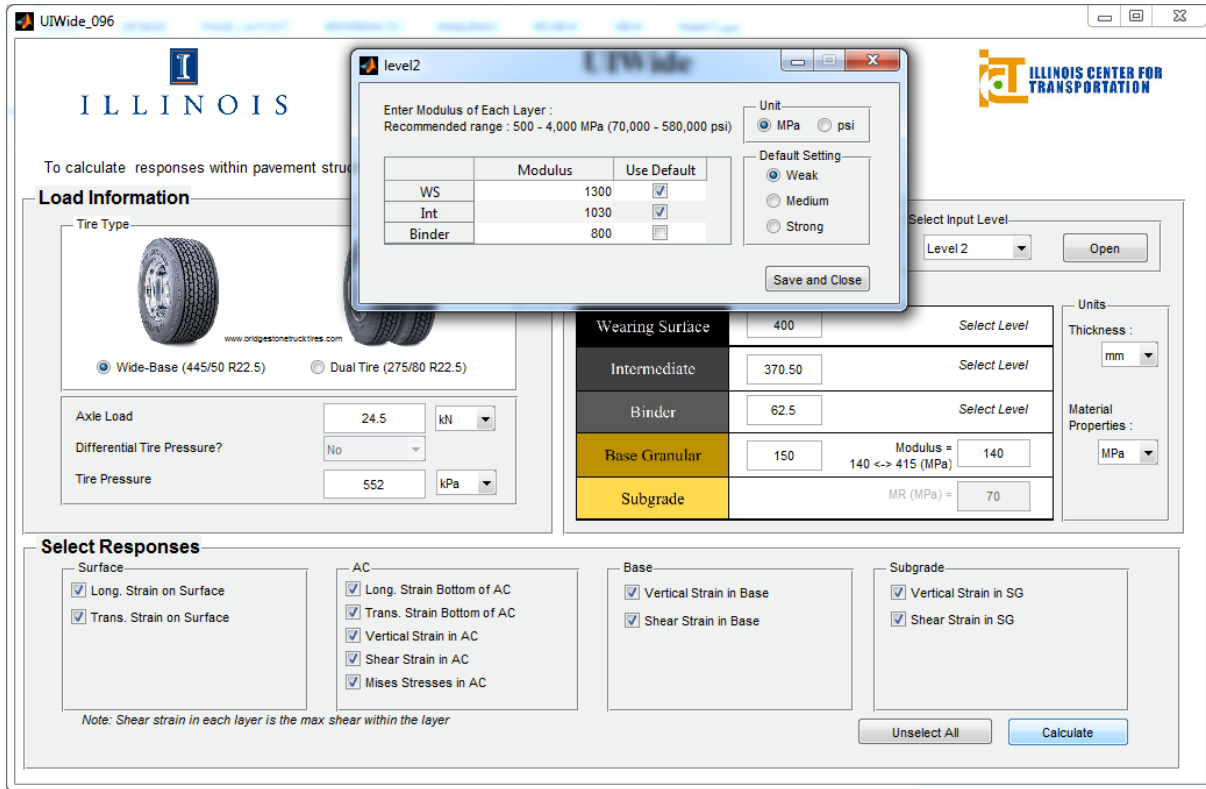
**Figure D-4. Prompt for Level 2 input.**
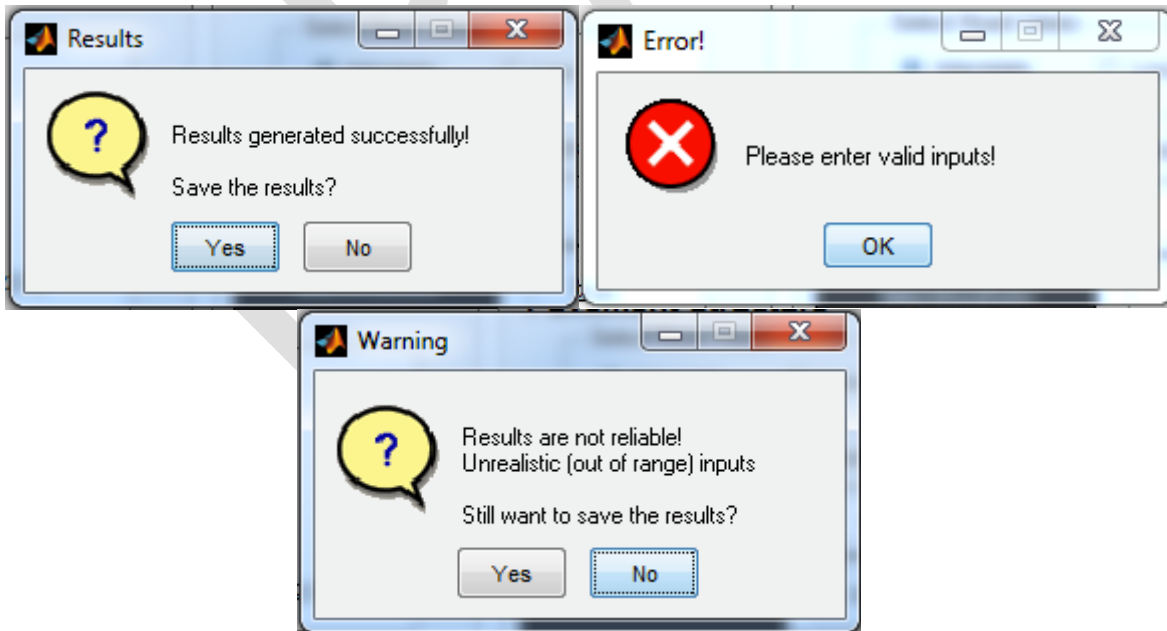


**Figure D-5. Three possible windows to appear after running tool.**

# Appendix E:    Florida DOT Pavement Sections

As part of this study, the Florida Department of Transportation (FDOT) constructed and instrumented two test sections to measure pavement response. The effort made to construct, instrument, and test these sections are documented.

**FDOT ACCELERATED PAVEMENT TESTING FACILITY**
Florida's APT facility is housed within the State Materials Research Park in Gainesville. The original test lanes measured 150 ft. long and 12 ft. wide. A recent expansion of the test track extended each lane an additional 300 ft. The supporting soil layers consist of a 10.5 in limerock base over a 12 in mixture of limerock and native A-3 soil.  Two additional 50 ft. long test tracks (referred to as the test pits) are enclosed by a sump with an interconnecting channel system for controlling the water table. A photograph of the original test tracks and empty test pits are shown in Figure E-1.



**Figure E-1. HVS test tracks and test pits.**

Accelerated loading was performed using a heavy vehicle simulator (HVS), Mark IV model.  The HVS can apply wheel loads between 7 and 45 kips at speeds of 2 mph to 8 mph along a 30 ft. test strip.  The effective test segment within this span is approximately 20 ft.  The remaining 5 ft., at either end of the test strip, allows the load wheel to reach programmed parameters controlling load and speed levels.  Wheel wander of up to 30 in can be induced.  A heater system and insulated panels, shown in Figure E-2, maintain a constant testing temperature within the test section area.

**Figure E-2. Insulated panels on HVS.**

## CONSTRUCTION
### Test Section Construction

Two test sections were constructed in October, 2012. One section was built on the east test pit while the second was constructed on Lane 7 of the test track extension. The test pit pavement consisted of two similar 1.5 in Superpave (SP-12.5) layers with a PG 67-22 asphalt binder. The test track consisted of a 1.5 in SP-12.5 layer with a PG 67-22 asphalt binder, a 1.5 in SP-12.5 layer with a PG 76-22, and a 1.0 in., 0.187 in mixture with a PG 76-22. The pavement sections were constructed in accordance with FDOT specifications and standards. The pavement structures for these sections are shown in Figure E-3.

| Test Pit Section | Test Track Section |
|---|---|
| | 1.0 inch 4.75 mm with PG 76-22 |
| 1.5 inch SP-12.5 with PG 67-22 (Gradation B) | 1.5 inch SP-12.5 with PG 76-22 (Gradation B) |
| 1.5 inch SP-12.5 with PG 67-22 (Gradation B) | 1.5 inch SP-12.5 with PG 67-22 (Gradation A) |
| 10.5 inch limerock base | 10.5 inch limerock base |
| 12 inch mixture of limerock and subgrade | 12 inch mixture of limerock and subgrade |
| A-3 subgrade | A-3 subgrade |

**Figure E-3. Pavement structure of test sections.**

### Material Sampling

Both test sections had similar supporting granular layers as indicated in Figure E-3. A summary of laboratory test results is included in Table E-1. The resilient modulus values listed in this table were obtained using the relationship developed from each individual test (resilient modulus versus bulk stress-

with bulk stress, $\theta$, defined as $\theta = \sigma_1 + \sigma_2 + \sigma_3$). The resilient modulus values are an average of two individual tests from each sample location. The resilient modulus samples were compacted to within 1 pound per cubic foot (pcf) of the maximum density and 0.5 percent of the optimum moisture content as determined by AASHTO T99 for the embankment and AASHTO T180 for the subgrade and base. The bulk stresses typically used to represent in-situ stresses of embankment, subgrade, and base layers are 11 psi, 16 to 18 psi, and 20 to 30 psi, respectively. The resilient modulus is determined by the following equation:

$$M_r = k_1 \theta^{k_2}$$
(1)

**Table E-1a. Granular Layer Properties AASHTO T99 or AASHTO T180**

| | AASHTO T99 or AASHTO T180 | | | |
|---|---|---|---|---|
| Material | Max Density (pcf) | Opt. Moist. (%) | Actual Density (pcf) | Actual Moisture (%) |
| Limerock Base | 114 | 12 | 112.5 | 10.3 |
| Stabilized Subgrade | 114 | 11 | 113.8 | 9.3 |
| Embankment | 115 | 11 | 113.3 | 9.3 |

**Table E-1b. Granular Layer Properties AASHTO T307**

| Material | Bulk Stress 11 psi | Bulk Stress 18 psi | Bulk Stress 40 psi | Avg. | $k_1$ | $K_2$ |
|---|---|---|---|---|---|---|
| Limerock Base | 13,083 | 17,365 | 27,482 | 27,482 | 3,297 | 0.5752 |
| Stabilized Subgrade | 14,332 | 18,553 | 28,197 | 18,553 | 4,079 | 0.5244 |
| Embankment | 12,806 | 16,538 | 25,035 | 12,806 | 3,687 | 0.5193 |

HMA material was sampled from delivery trucks during construction (Figure E-4) for mixture performance tests and three random cores were retrieved from each lane to verify in-situ density. In addition, 30 cores from each test section were extracted and shipped to the University of Illinois for further testing. Table E-2 summarizes the gradations and volumetric properties of the asphalt mixtures.



**Figure E-4. Loose mixes sampled from trucks.**

**Table E-2a. Gradation and Volumetric Property Data**

| Sieve | Test Pit SP-12.5 JMF, % Passing | Test Pit SP-12.5 Plant Avg, % Passing | Test Track 4.75 JMF, % Passing | Test Track 4.75 Plant Avg, % Passing | Test Track SP-12.5 JMF, % Passing | Test Track SP-12.5 Plant Avg, % Passing | Test Track SP-12.5[1] JMF, % Passing | Test Track SP-12.5[1] Plant Avg, % Passing |
|---|---|---|---|---|---|---|---|---|
| 3/4" | 100 | 100.0 | 100 | 100.0 | 100 | 100.0 | 100 | 99.9 |
| 1/2" | 100 | 98.3 | 100 | 100.0 | 100 | 98.4 | 98 | 96.8 |
| 3/8" | 87 | 86.0 | 100 | 100.0 | 87 | 87.5 | 88 | 85.0 |
| #4 | 62 | 59.6 | 99 | 98.7 | 62 | 61.9 | 59 | 57.0 |
| #8 | 41 | 39.7 | 77 | 78.2 | 41 | 42.4 | 40 | 38.8 |
| #16 | 29 | 28.7 | 56 | 55.0 | 29 | 31.1 | 29 | 28.4 |
| #30 | 22 | 22.2 | 39 | 40.0 | 22 | 24.0 | 22 | 21.7 |
| #50 | 12 | 13.2 | 26 | 26.0 | 12 | 13.8 | 12 | 12.9 |
| #100 | 4 | 5.3 | 15 | 15.6 | 4 | 5.2 | 4 | 4.9 |
| #200 | 2 | 2.9 | 8.9 | 9.5 | 2 | 2.9 | 2 | 2.9 |

**Table E-3b. Gradation and Volumetric Property Data – Binder Content**

| Binder Type | PG 67-22 (unmodified) | | PG 76-22 (Modified) | | PG 76-22 (modified) | | PG 67-22 (unmodified) | |
|---|---|---|---|---|---|---|---|---|
| %AC | 5.1 | 4.7 | 6.5 | 6.3 | 5.1 | 4.9 | 5.1 | 4.9 |
| %AV | 4.0 | 4.0 | 4 to 6 | 4.6 | 4.0 | 3.9 | 4.0 | 3.3 |

**Table E-4c. Gradation and Volumetric Property Data – Core Density and Lift Thickness**

| Core Property | SP-12.5 | 4.75 | SP-12.5 | SP-12.5[1] |
|---|---|---|---|---|
| % Density | 94.2 | 11.5 | 94.8 | 94.6 |
| Lift Thickness, Inch | 1.5 | 0.9 | 1.6 | 1.4 |

Note: The SP-12.5 mixture placed on the test track was paved approximately 1 year prior to the mixture placed on the test pit.

The AMPT is a testing device designed to determine the asphalt mixture dynamic modulus for use in pavement structural design (e.g., the MEPDG) and the flow number for the evaluation of potential mixture performance. The AMPT test provides a dynamic modulus master curve that indicates the modulus of asphalt mixture for any combinations of temperature and load frequency. AASHTO PP 61 standardizes the construction of dynamic modulus master curve using the AMPT. In addition, the flow number measured from the AMPT enables the evaluation of rutting resistance of asphalt mixtures.

Dynamic modulus and flow number tests were conducted in accordance with AASHTO TP 79. The plant mix sampled during construction was compacted using the Superpave Gyratory Compactor (SGC). Three replicates were made for dynamic modulus tests and one replicate was prepared for the flow number test according to AASHTO PP 60. The AMPT test setup is shown in Figure E-5. The dynamic modulus master curves generated for the three different mixtures and flow number results are also presented in the same figure.
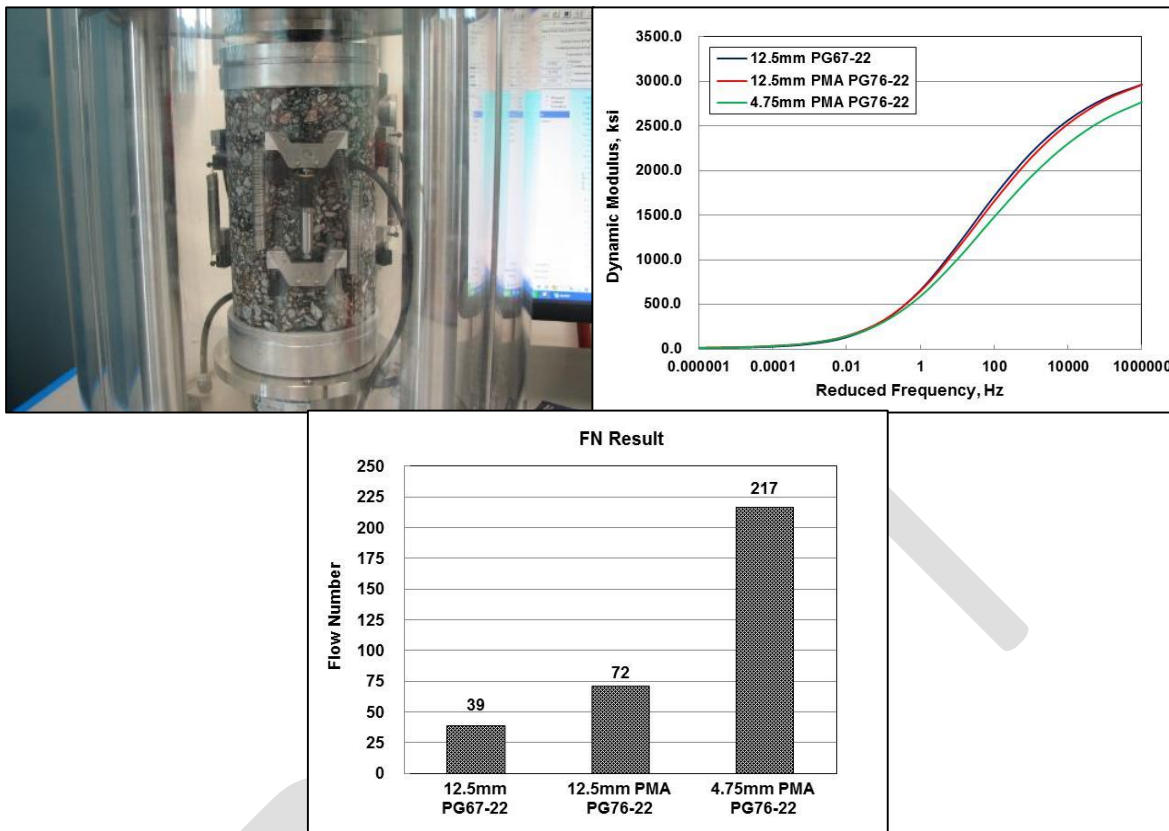
**Figure E-5. AMPT test setup, dynamic modulus master curve, and flow number results.**

Superpave IDT tests were conducted on mixtures to determine key mixture fracture properties. The standard Superpave IDT tests, including resilient modulus, creep compliance and strength test, were performed at 50 °F. A complete description of test procedures and data analysis are presented by Roque et al. (Roque et al., 1997). The plant mixes sampled from truck were compacted using the SGC. Three replicates per mixture type were prepared and tested. Table E-5 summarizes the information of three cut specimens for testing and Figure E-6 shows the configuration of Superpave IDT test setup.

**Table E-5. Information of Cut Specimens for Superpave IDT Tests**

| Mixture Types | Specimen Number | Air Voids (%) | Average Diameter (inch) | Average Thickness (inch) |
|---|---|---|---|---|
| 12.5mm PG67-22 | 1 | 6.9 | 5.93 | 1.53 |
| 12.5mm PG67-22 | 2 | 6.8 | 5.92 | 1.57 |
| 12.5mm PG67-22 | 3 | 6.5 | 5.92 | 1.51 |
| 12.5mm PMA PG76-22 | 1 | 7.0 | 5.93 | 1.49 |
| 12.5mm PMA PG76-22 | 2 | 6.7 | 5.92 | 1.51 |
| 12.5mm PMA PG76-22 | 3 | 6.9 | 5.92 | 1.48 |

141

| 4.75mm PMA PG76-22 | 1 | 7.3 | 5.92 | 1.51 |
|---|---|---|---|---|
| 4.75mm PMA PG76-22 | 2 | 6.7 | 5.92 | 1.50 |
| 4.75mm PMA PG76-22 | 3 | 6.9 | 5.92 | 1.54 |



**Figure E-6. Superpave IDT test setup.**

Table E-6 summarizes the results of Superpave IDT tests and Figure E-7 presents three key mixture fracture properties most strongly related to cracking performance of asphalt pavements. Generally, a higher *ER* value is associated with a higher *FE* and a lower creep rate. The aforementioned trend is consistent with the results shown in Figure E-7. In particular, it was found that 0.187 in mixture with polymer-modified PG 76-22 binder had a relatively higher *FE*, lower creep rate, and higher entities and relationships (ER) values that may result in better fracture resistance than the 0.5 in mixtures.

**Table E-6. Superpave IDT Test Results**

| Mixture Types | Temp. (°F) | m-value | $D_1$ (1/psi) | Creep Compl. (1/GPa) | $S_t$ (MPa) | $M_R$ (GPa) | $\varepsilon_f$ ($10^{-6}$) | FE (KJ/m³) | $DCSE_f$ (KJ/m³) | Creep Rate (1/psi·sec) | ER |
|---|---|---|---|---|---|---|---|---|---|---|---|
| 12.5mm PG67-22 | 50 | 0.46 | 3.55E-07 | 1.281 | 2.44 | 13.97 | 1300.23 | 2.30 | 2.09 | 3.83E-09 | 2.81 |
| 12.5mm PMA PG76-22 | 50 | 0.41 | 4.17E-07 | 1.058 | 2.54 | 13.16 | 1533.00 | 2.80 | 2.55 | 2.77E-09 | 4.16 |
| 4.75mm PMA PG76-22 | 50 | 0.35 | 3.84E-07 | 0.658 | 2.90 | 14.21 | 2050.62 | 4.40 | 4.10 | 1.47E-09 | 10.93 |

Note: 1 MPa=145 psi,

142
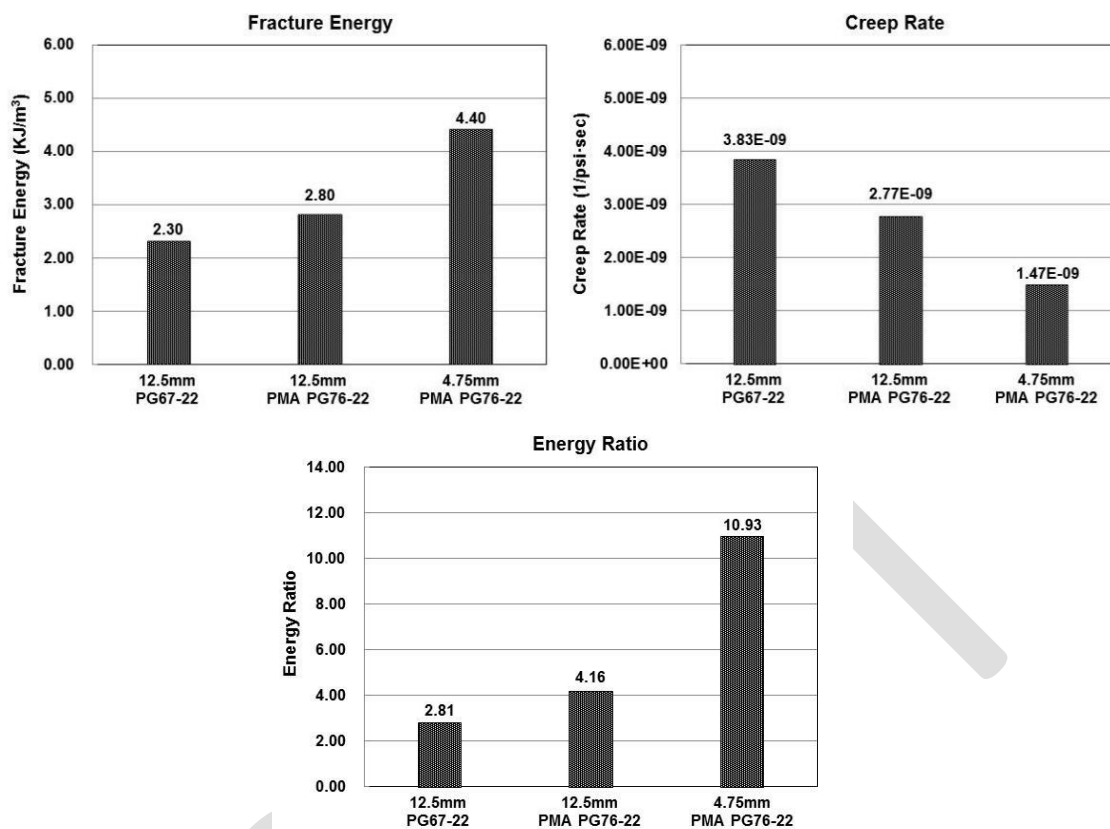
**Figure E-7. Key mixture fracture properties determined from Superpave IDT tests: Fracture energy, creep rate, and energy ratio.**

## INSTRUMENTATION

Each test section was instrumented to measure pavement response resulting from wheel loading. Prior to construction, each embedded sensor was placed in the appropriate location, labeled, and checked for adequate response. Immediately after construction, the response was again checked to make sure each embedded sensor survived the compaction and heat associated with the placement of HMA. Standard sensor installation methods used by FDOT can be found on the State Materials Office website. Table E-7 summarizes the types and locations of sensors. Diagrams of the exact sensor locations are shown in Figure E-8 and Figure E-9. Instrumentation data were collected with a mobile National Instruments data acquisition (DAQ) system (Figure E-10) at 200 Hz for the surface gauges and pressure cells and at 100 Hz for the embedded H-gauges.

**Table E-7. Sensor Types and Locations**

| Sensor Type | Number of Sensors per Test Section | Model | Vertical Location | Offset from Wheel Path |
|---|---|---|---|---|
| Surface strain gauge | 24 | Tokyo Sokki PFL-30-11-5L | HMA surface | Transverse and longitudinal orientations at various offsets from wheel path edge |
| Asphalt strain gauge | 6 | Tokyo Sokki KM-100HAS | Bottom of new HMA | Transverse and longitudinal orientations below tire center |

143

| Pressure cell | 2 | RST Instruments LPTPC09-S | Bottom of new HMA | Below tire center |
|---|---|---|---|---|
| Pressure cell (Test Pit only) | 2 | Geokon 3500 | Bottom of base | Below tire center |
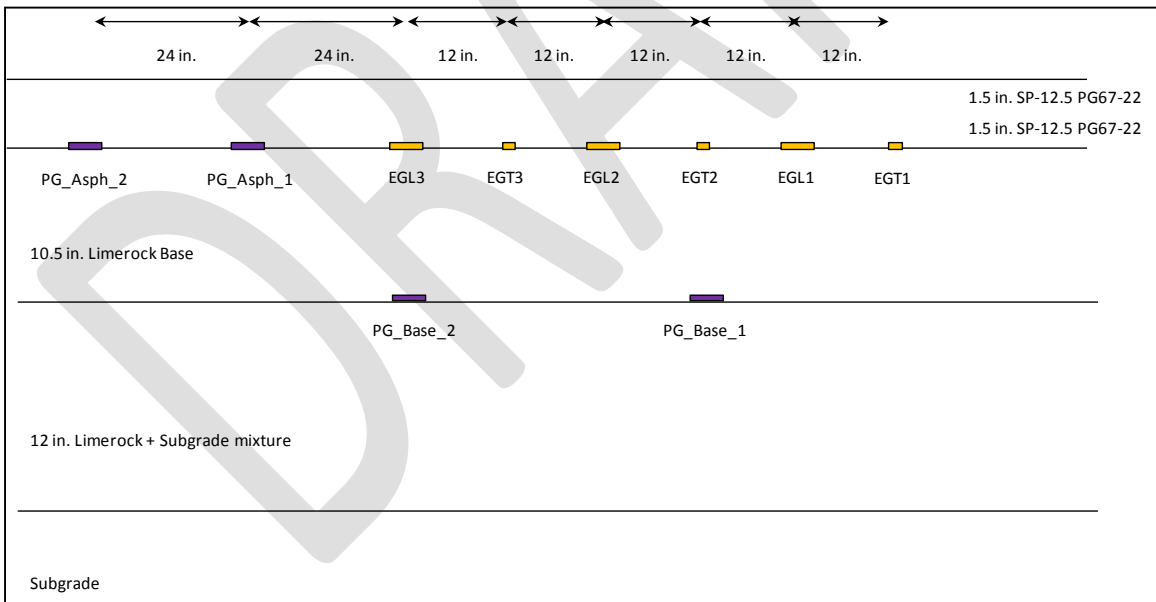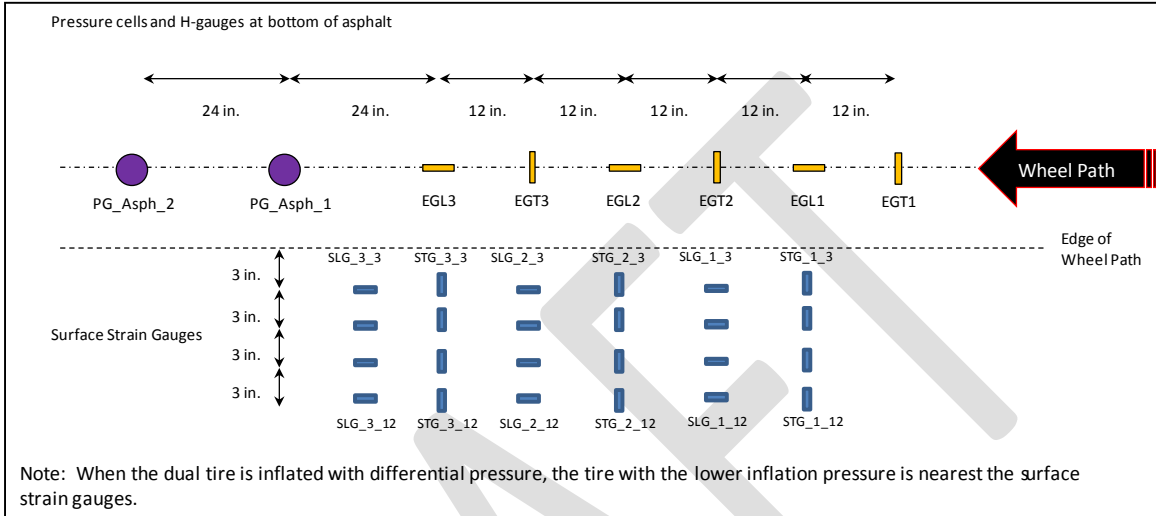


**Figure E-8. Test pit instrumentation layout.**
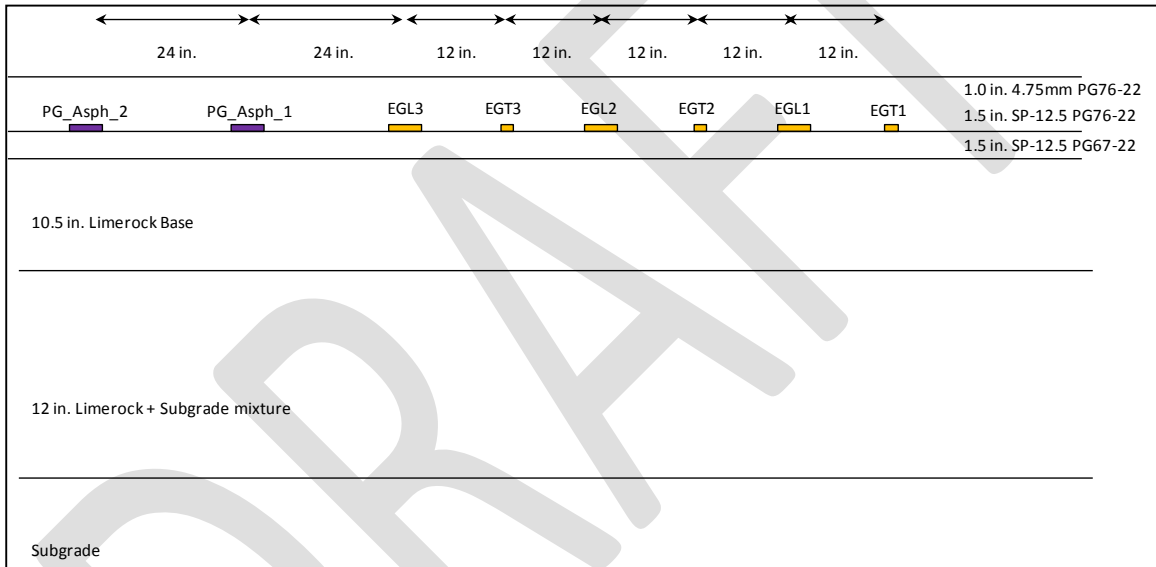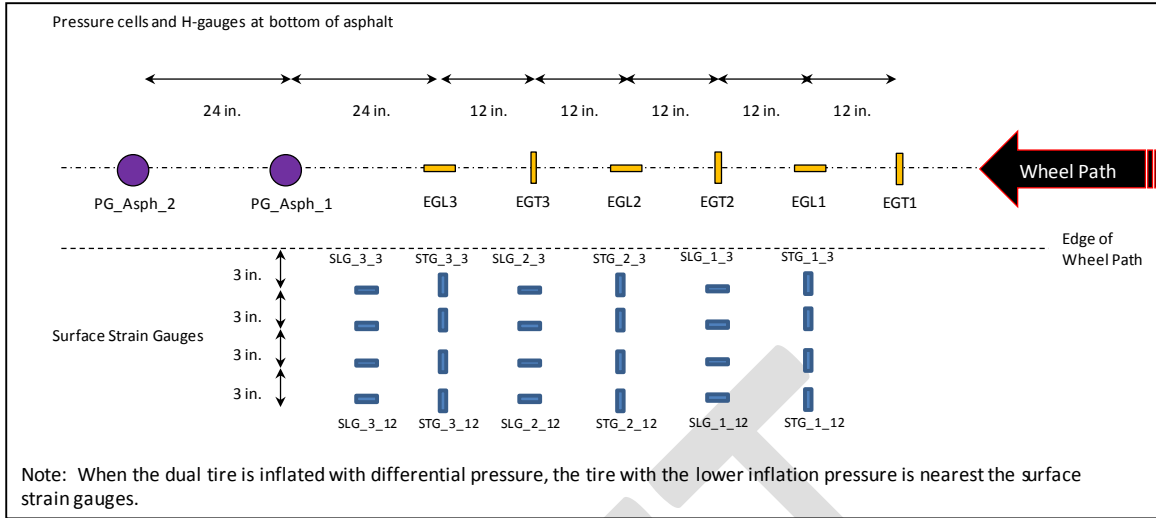
**Figure E-9. Test track instrumentation elevation view.**

**Figure E-10. Mobile DAQ system.**

## HVS LOADING

Several combinations of inflation pressure, tire load, and pavement temperature were used for each tire type, as shown in Table E-8. HVS loading was initiated on January 24 on the test pit using the dual-tire and was completed on February 12. HVS loading on the test track started on February 20 using the 445 mm wide base tire and was completed on April 10. A main motor failure during loading of the test track delayed testing for more than two weeks. Table E-8 shows the load and temperature combinations that were used.

**Table E-8. HVS Test Matrix**

| Tire Type | Inflation Pressure (psi) | Tire Load (kips) | Tire Load (kips) | Tire Load (kips) | Tire Load (kips) | Tire Load (kips) |
|---|---|---|---|---|---|---|
| NGWB & Dual | 80 | 6 | 8 | 10 | 14 | 18 |
| NGWB & Dual | 100 | 6 | 8 | 10 | 14 | 18 |
| NGWB & Dual | 110 | 6 | 8 | 10 | 14 | 18 |
| NGWB & Dual | 125 | 6 | 8 | 10 | 14 | 18 |
| Dual Only | 60/110 | 6 | 8 | 10 | 14 | 18 |
| Dual Only | 60/110 | 6 | 8 | 10 | 14 | 18 |

Each loading combination was conducted at 25℃, 40℃, and 55℃

# Appendix F: UC-Davis Pavement Sections

## TEST TRACK LOCATION, DESIGN, AND CONSTRUCTION
### Experiment Location

The wide-base tire experiment is located on the North Test Track at the University of California Pavement Research Center facility in Davis, California. An aerial view of the site is shown in Figure F-1. This was the second test undertaken on this test track and the original pavement was reconstructed for this study.



**Figure F-1. Aerial view of the UCPRC research facility.**

### Test Track Layout

The North Test Track is 361 ft. (110 m) long and 49.2 ft. (15 m) wide. It has a two percent crossfall in the north-south direction. The track was first constructed as part of the third phase of a Caltrans/UCPRC warm-mix asphalt study, and it was used to investigate and compare differences in the performance of seven different warm-mix asphalt technologies in gap-graded rubberized asphalt mixes against that of two gap-graded rubberized hot-mix asphalt control sections *(2, 3)*.

The test track was recycled in place to investigate four different full-depth reclamation strategies (no stabilizer [FDR-NS], foamed asphalt with cement [FDR-FA], engineered emulsion [FDR-EE], and Portland cement [FDR-PC]). The track was divided into four lanes for this study. The track layout is shown in Figure F-2 (The two test sections for the wide-base tire study are situated in Cells #1 and #2, respectively). All test track measurements and locations discussed in this technical memorandum are based on this layout.

The wide-base tire study was undertaken on Lane #1 with FDR-NS. Two sections were selected for testing, one within Cell #1 and one within Cell #2.
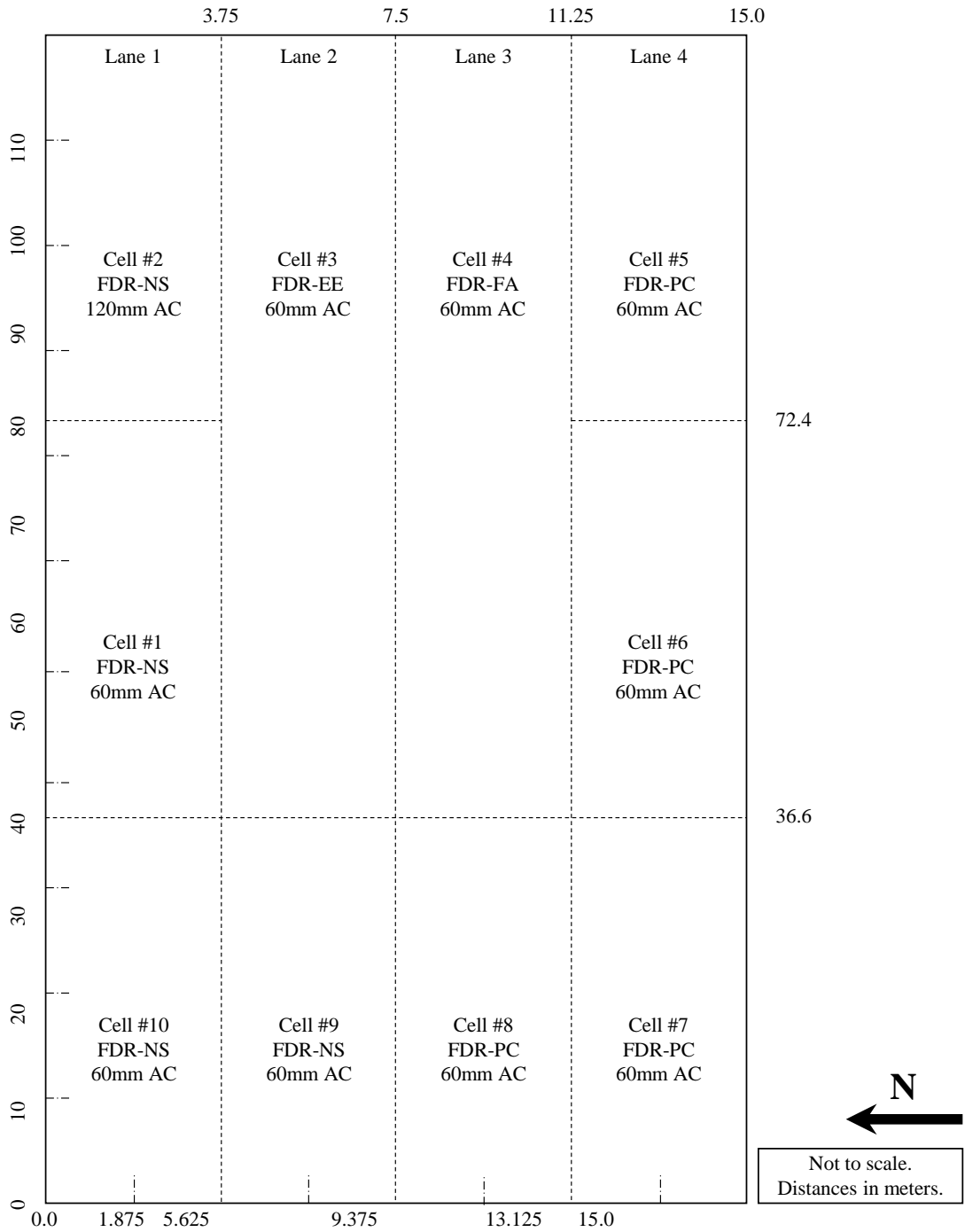
**Figure F-2. Test track layout.**

## Pavement Design

Pavement design for the FDR study was based on typical Caltrans practice. Recycle depth was set at 0.83 ft. (250 mm), resulting in a new recycled base layer consisting of 0.4 ft. (120 mm) of recycled AC and 0.43 ft. (130 mm) of the existing base. Given that the study was dedicated to understanding the behavior and performance of the recycled base, a relatively thin (0.2 ft. [60 mm]) AC surfacing was used in the design. Part of the FDR-NS lane was surfaced with 0.4 ft. (120 mm) of AC to compare performance of FDR-NS

with two surfacing thicknesses. The pavement designs for the original and recycled test track are shown in Figure F-3 and Figure F-4. Details for the subgrade and original base material are provided below.



**Layer: RHMA-G/RWMA-G**
Thickness: 60 mm (0.2 ft)

**Layer: HMA**
Thickness: 60 mm (0.2 ft)

**Layer: Imported Class 2 Aggregate Base Course**
Thickness: 450 mm (1.5 ft.), Modulus: 300 MPa (43.5 ksi)

**Layer: Prepared Subgrade**
Thickness: Semi-infinite, Modulus: 60 MPa (8.7 ksi)
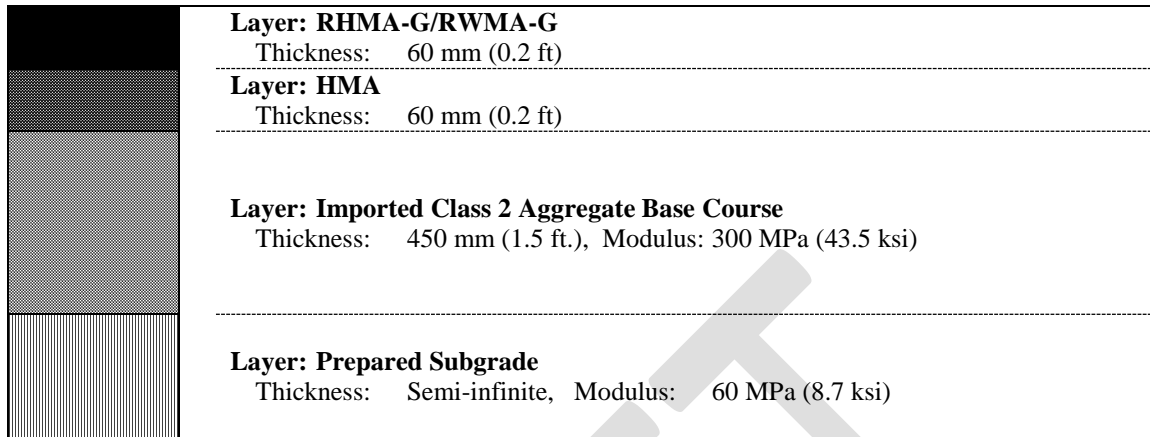
**Figure F-3. Original pavement structure for rubberized warm-mix asphalt test sections.**



**Layer: HMA**
Thickness: 60 mm (0.2 ft.) or 120 mm (0.4 ft.) HMA

**Layer: Recycled**
Thickness: 250 mm (0.83 ft)

**Layer: Imported Class 2 Aggregate Base Course**
Thickness: 320 mm (0.9 ft)

**Layer: Prepared Subgrade**
Thickness: Semi-infinite
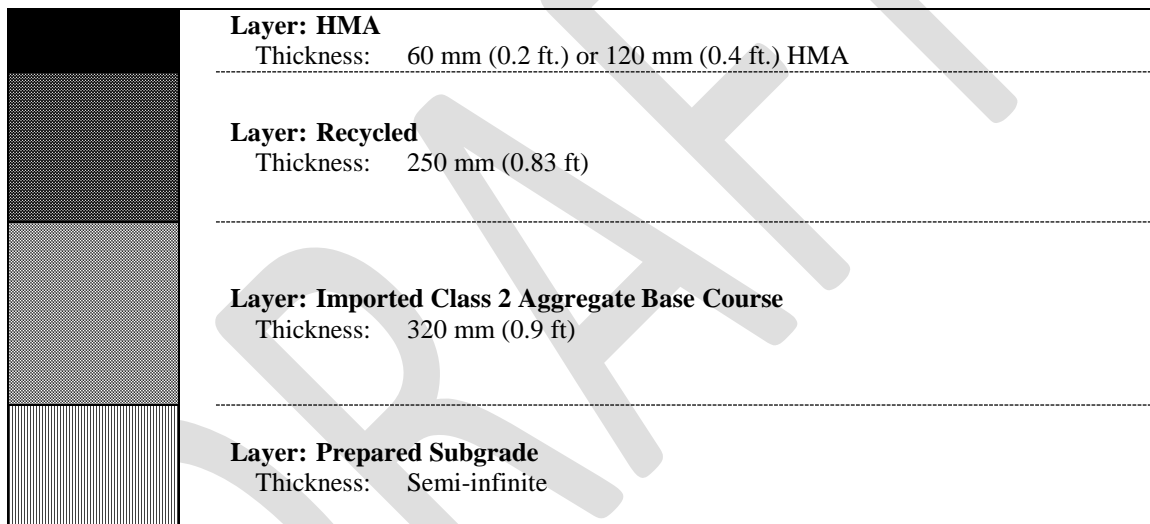
**Figure F-4. Pavement structure for FDR and wide-base tire study test sections.**

**Subgrade and Base Course Properties (Original Pavement)**

Dynamic cone penetrometer (DCP) tests were performed along the center lines of each the three lanes over the length and width of the test track prior to construction to obtain an indication of the in-situ subgrade strength. Results are summarized in Table F-1. Penetration rates varied between 0.43 in per blow and 1.2 in per blow, with the weakest areas in the middle of the track. Variation was attributed to the degree of soil mixing, to temporary stockpiling of lime-treated soils used during adjacent building pad construction (lime treatment was used to dry the soil in some areas of the site), to compaction from equipment during construction of the adjacent facility, and to varying subgrade moisture contents.

**Table F-1. Summary of DCP Survey on Subgrade Material**

| Test Location[1] (m) | mm/blow Lane #1 | mm/blow Lane #2 | mm/blow Lane #3 | CBR[2] Lane #1 | CBR Lane #2 | CBR Lane #3 | Stiff.[2] (MPa) Lane #1 | Stiff. (MPa) Lane #2 | Stiff. (MPa) Lane #3 |
|---|---|---|---|---|---|---|---|---|---|
| 10 | 17 | 21 | 19 | 11 | 9 | 9 | 56 | 41 | 44 |
| 20 | 16 | 18 | 15 | 12 | 10 | 13 | 60 | 46 | 63 |
| 30 | 14 | 16 | 13 | 14 | 12 | 15 | 66 | 60 | 71 |

| 40 | 13 | 22 | 16 | 15 | 8 | 12 | 71 | 40 | 60 |
| 50 | 13 | 26 | 15 | 15 | 6 | 13 | 71 | 36 | 63 |
| 60 | 12 | 25 | 16 | 17 | 6 | 12 | 77 | 37 | 60 |
| 70 | 15 | 30 | 15 | 13 | 5 | 13 | 63 | 30 | 63 |
| 80 | 14 | 28 | 15 | 14 | 5 | 13 | 66 | 34 | 63 |
| 90 | 12 | 26 | 14 | 17 | 6 | 14 | 77 | 36 | 66 |
| 100 | 11 | 20 | 15 | 19 | 9 | 13 | 85 | 42 | 63 |

[1] Measured from southwest corner of the track.

[2] Estimated from DCP software tool.

## Subgrade Preparation for the Original Pavement

Subgrade preparation included vegetation removal, preliminary leveling, ripping, watering and mixing, compaction, and final leveling to include a two percent north-south crossfall as follows:
- Removing vegetation with a grader, windrowing of the deleterious material towards the center of the track, collecting this material with a scraper and dumping it in a temporary stockpile for removal
- Preliminary leveling with a grader followed by watering
- Ripping to a depth of 12 in (300 mm)
- Watering and mixing using both the scraper and grader. Pockets of high clay content soils were observed during this process, which required additional working with the grader and scraper to break up the clods
- Initial compaction with a padfoot roller. Despite extensive mixing, some clay pockets were still observed after completion of the initial compaction, with padfoot impressions clearly visible. Clay pockets appeared to predominate on the eastern half of the track
- Final compaction with a vibrating smooth drum roller
- Final leveling with a grader
- Density checks on the finished surface with a nuclear density gauge

Quality control of the subgrade preparation was limited to density checks with a nuclear gauge following California Test 231 (CT 231) and comparison of the results against a laboratory maximum density of 134.2 lb/ft$^3$ (2,150 kg/m$^3$) determined according to California Test 216 (CT 216). Nuclear gauge measurements were taken at ten different locations selected according to a nonbiased plan. Samples for laboratory density determination were taken at the first three locations. The results summarized in Table F-2 indicate that the subgrade density was generally consistent across the test track. Relative compaction varied between 95.4 percent and 99.2 percent with an average of 97.0 percent, two percent above the Caltrans-specified minimum density of 95 percent for subgrade compaction. No location had a relative compaction lower than this minimum.

**Table F-2. Summary of Subgrade Density Measurements**

| Location | Wet Density (lb/ft$^3$) | Wet Density (kg/m$^3$) | Moisture Content (%) | Dry Density (lb/ft$^3$) | Dry Density (kg/m$^3$) | Relative Compaction (%) |
|---|---|---|---|---|---|---|
| 1 | 130.5 | 2,091 | 15.6 | 112.6 | 1,804 | 97.3 |
| 2 | 132.6 | 2,124 | 17.3 | 113.1 | 1,811 | 98.8 |
| 3 | 131.3 | 2,103 | 16.8 | 112.4 | 1,801 | 97.8 |
| 4 | 130.2 | 2,086 | 16.2 | 112.1 | 1,796 | 97.0 |
| 5 | 133.2 | 2,133 | 15.2 | 115.6 | 1,852 | 99.2 |
| 6 | 128.9 | 2,065 | 17.8 | 109.5 | 1,754 | 96.0 |
| 7 | 132.2 | 2,117 | 17.9 | 112.1 | 1,795 | 98.5 |
| 8 | 128.1 | 2,052 | 18.7 | 107.9 | 1,728 | 95.4 |

| | | | | | | |
|---|---|---|---|---|---|---|
| 9 | 132.3 | 2,120 | 16.5 | 113.6 | 1,820 | 98.6 |
| 10 | 128.7 | 2,062 | 15.0 | 111.9 | 1,793 | 95.9 |
| Average | 130.8 | 2,095 | 17.0 | 112.1 | 1,795 | 97.0 |
| Std. Dev. | 1.8 | 29 | 1.2 | 2.1 | 34 | 1.3 |

## Base Course Construction for the Original Pavement

Base course aggregates were sourced from the Teichert Cache Creek quarry near Woodland, California. Key material properties are summarized in Table F-3. The material met Caltrans specifications, except for the percent passing the #200 sieve, which exceeded the specification operating range by 3.0 percent, and just met the contract compliance limits.

The warm-mix asphalt test track base course was constructed two days after the subgrade preparation. The construction process included aggregate spreading, watering, compaction, and final leveling to include a two percent north-south crossfall as follows:

- Transporting crushed base course material (alluvial) that complied with Caltrans Class 2 aggregate base course specifications from the Teichert Cache Creek aggregate source to the test track with a fleet of bottom-dump trucks and trailers
- Dumping the aggregate in windrows
- Spreading the aggregate with a grader to a thickness of approximately 4.0 in (100 mm)
- Adding water to bring the aggregate to the optimum moisture content and re-mixing with the grader to ensure even distribution of the moisture throughout the material
- Initial compaction of the spread material with a vibrating steel wheel roller
- Repeating the process until the design thickness of 1.5 ft. (450 mm) was achieved
- Applying a generous application of water followed by compaction to pump fines to the surface to provide good aggregate interlock (slushing)
- Final leveling with a grader. Final levels were checked with a total station to ensure that a consistent base course thickness had been achieved
- Removal of excess material with a scraper followed by final compaction
- Density checks on the finished surface with a nuclear density gauge

**Table F-3. Base Course Material Properties**

| Property | | | Result | Operating Range | Contract Compliance |
|---|---|---|---|---|---|
| Grading: | 1" | (25 mm) | 100 | 100 | 100 |
| | 3/4" | (19 mm) | 99.1 | 90 – 100 | 87 – 100 |
| | 1/2" | (12.5 mm) | 90.1 | – | – |
| | 3/8" | (9.5 mm) | 83.5 | – | – |
| | #4 | (4.75 mm) | 63.3 | 35 – 60 | 30 – 65 |
| | #8 | (2.36 mm) | 48.8 | – | – |
| | #16 | (1.18 mm) | 39.2 | – | – |
| | #30 | (600 μm) | 30.8 | 10 – 30 | 5 – 35 |
| | #50 | (300 μm) | 21.6 | – | – |
| | #100 | (150 μm) | 15.6 | – | – |
| | #200 | (75 μm) | 12.3 | 2 – 9 | 0 – 12 |
| Liquid Limit | | | | – | – |
| Plastic Limit | | | Non-plastic | – | – |
| Plasticity Index | | | | – | – |
| Maximum Dry Density | | | 140.6 (2,252) | – | – |
| (lb/ft$^3$)(kg/m$^3$) | | | 6.0 | – | – |

| | | | |
|---|---|---|---|
| Optimum Moisture Content | | | |
| R-Value | 79 | – | >78 |
| Sand equivalent | 30 | 25 | >22 |
| Durability index – course | 78 | – | >35 |
| Durability index – fine | 52 | – | >35 |

Quality control of the base course construction was limited to density checks with a nuclear gauge following CT 231 and comparison of the results against a laboratory maximum wet density of 150.5 lb/ft³ (2,410 kg/m³) determined according to CT 216. Nuclear gauge measurements were taken at ten different locations selected according to a nonbiased plan. A sample for laboratory density determination was taken at the first location. Results are summarized in Table F-4 and indicate that the base course density properties were generally consistent across the test track, but that the material was relatively wet compared with the laboratory-determined optimum moisture content. Relative compaction varied between 96.7 percent and 99.4 percent with an average of 98.0 percent, three percent above the Caltrans-specified minimum density of 95 percent for base compaction. No location had a relative compaction lower than this minimum.

**Table F-4. Summary of Nuclear Gauge Density Measurements on Base Course Layer**

| Location | Wet Density (lb/ft³) | Wet Density (kg/m³) | Moisture Content (%) | Dry Density (lb/ft³) | Dry Density (kg/m³) | Relative Compaction (%) |
|---|---|---|---|---|---|---|
| 1 | 146.5 | 2,346 | 6.6 | 137.4 | 2,201 | 97.3 |
| 2 | 148.5 | 2,379 | 7.0 | 138.8 | 2,223 | 98.7 |
| 3 | 148.0 | 2,371 | 8.0 | 137.0 | 2,195 | 98.4 |
| 4 | 147.1 | 2,356 | 7.8 | 136.5 | 2,186 | 97.8 |
| 5 | 148.7 | 2,382 | 6.3 | 139.9 | 2,241 | 98.8 |
| 6 | 145.5 | 2,330 | 6.8 | 136.2 | 2,182 | 96.7 |
| 7 | 149.0 | 2,387 | 8.2 | 137.7 | 2,206 | 99.0 |
| 8 | 145.6 | 2,332 | 7.7 | 135.2 | 2,165 | 96.8 |
| 9 | 149.5 | 2,395 | 6.9 | 139.8 | 2,240 | 99.4 |
| 10 | 145.7 | 2,334 | 7.8 | 135.2 | 2,165 | 96.8 |
| Average | 147.4 | 2,361 | 7.3 | 137.3 | 2,200 | 98.0 |
| Std. Dev. | 1.5 | 25 | 0.7 | 1.7 | 27.6 | 1.0 |

Follow-up DCP measurements were also undertaken on the base at the same locations as the original subgrade DCP survey. The results are summarized in Table F-5 and indicate that although average penetration rates (mm/blow) were consistent across the track, there was considerable difference in the average calculated stiffness of the base from the redefined layers based on actual penetration. Consequently, the contractor was requested to re-compact the track with a static steel drum roller prior to priming to consolidate the base layer and accelerate movement of any infiltrated water to the surface. A significant improvement in subgrade stiffness attributed to the subgrade preparation and confinement by the base was also noted.

**Table F-5a. Summary of DCP Survey on Base and Subgrade Material – Penetration Rate (mm/blow)**

| Test Location (m)[1] | Base Lane #1 | Base Lane #2 | Base Lane #3 | Subgrade Lane #1 | Subgrade Lane #2 | Subgrade Lane #3 |
|---|---|---|---|---|---|---|
| 10 | 3 | - | - | 9 | - | - |
| 20 | - | 3 | - | - | 8 | - |
| 30 | - | - | 3 | - | - | 7 |
| 40 | 4 | - | - | 9 | - | - |
| 50 | - | 4 | - | - | 9 | - |
| 60 | - | - | 4 | - | - | 9 |
| 70 | 4 | - | - | 10 | - | - |

| | | | | | |
|---|---|---|---|---|---|
| 80 | - | 4 | - | - | 10 | - |
| 90 | - | - | 4 | - | - | 7 |
| 100 | 4 | - | - | 11 | - | - |

[1] Measured from southwest corner of the track.

**Table F-6b. Summary of DCP Survey on Base and Subgrade Material – Stiffness (MPa [ksi])[2]**

| Test Location (m)[1] | Base Stiff. Lane #1 | Base Stiff. Lane #2 | Base Stiff. Lane #3 | Subgrade Stiff. Lane #1 | Subgrade Stiff. Lane #2 | Subgrade Stiff. Lane #3 |
|---|---|---|---|---|---|---|
| 10 | 430 (62) | - | - | 111 (16) | - | - |
| 20 | - | 395 (57) | - | - | 119 (17) | - |
| 30 | - | - | 320 (46) | - | - | 139 (20) |
| 40 | 332 (48) | - | - | 114 (17) | - | - |
| 50 | - | 299 (43) | - | - | 107 (16) | - |
| 60 | - | - | 279 (41) | - | - | 137 (20) |
| 70 | 255 (37) | - | - | 99 (14) | - | - |
| 80 | - | 260 (38) | - | - | 105 (15) | - |
| 90 | - | - | 273 (40) | - | - | 148 (22) |
| 100 | 259 (38) | - | - | 116 (17) | - | - |

[2] Estimated from DCP software tool.

## Full-Depth Reclamation

Conventional FDR construction procedures were followed on the FDR-NS lane (). The recycler and connected water tanker made a single pass to pulverize and mix the material to optimum moisture content for compaction. Initial rolling was completed with a pad foot roller, followed by vibrating smooth drum and rubber-tired rollers. Final levels were achieved with a grader after initial rolling. Compaction was measured with a nuclear gauge. Material properties and nuclear gauge compaction results are provided in Table F-7 and Table F-7, respectively.



**Figure F-5. Test track recycling.**

**Table F-7. Recycled Layer Material Properties**

| Property | | | Result | Operating Range | Contract Compliance |
|---|---|---|---|---|---|
| Grading: | 1" | (25 mm) | 100 | 100 | 100 |
| | 3/4" | (19 mm) | 99 | 90 – 100 | 87 – 100 |
| | 1/2" | (12.5 mm) | 91 | – | – |
| | 3/8" | (9.5 mm) | 82 | – | – |
| | #4 | (4.75 mm) | 66 | 35 – 60 | 30 – 65 |
| | #8 | (2.36 mm) | 46 | – | – |
| | #16 | (1.18 mm) | 31 | – | – |
| | #30 | (600 μm) | 21 | 10 – 30 | 5 – 35 |
| | #40 | (425 μm | 14 | – | – |

153

| | | | | |
|---|---|---|---|---|
| #50 | (300 μm) | 11 | – | – |
| #100 | (150 μm) | 8 | – | – |
| #200 | (75 μm) | 5 | 2 – 9 | 0 – 12 |
| Liquid Limit | | | – | – |
| Plastic Limit | | Non-plastic | – | – |
| Plasticity Index | | | – | – |
| Maximum Dry Density (lb/ft³) (kg/m³) | | 135.5 (2,171) | – | – |
| Optimum Moisture Content | | 4.8 | – | – |

**Table F-8. Summary of Nuclear Gauge Density Measurements on Recycled Layer**

| Location | Wet Density (lb/ft³) | Wet Density (kg/m³) | Moisture Content (%) | Dry Density (lb/ft³) | Dry Density (kg/m³) | Relative Compaction (%) |
|---|---|---|---|---|---|---|
| 1 | 135.6 | 2,172 | 8.0 | 125.4 | 2,008 | 100.3 |
| 2 | 130.1 | 2,083 | 9.3 | 120.8 | 1,935 | 96.7 |
| 3 | 144.3 | 2,311 | 11.7 | 132.6 | 2,124 | 106.1 |
| 4 | 139.1 | 2,229 | 9.8 | 126.8 | 2,030 | 101.4 |
| 5 | 140.2 | 2,246 | 8.7 | 129.0 | 2,066 | 103.2 |
| 6 | 127.8 | 2,046 | 7.3 | 119.0 | 1,906 | 95.2 |
| 7 | 141.6 | 2,268 | 9.6 | 129.3 | 2,071 | 103.4 |
| 8 | 140.3 | 2,247 | 8.9 | 128.8 | 2,063 | 103.0 |
| 9 | 131.0 | 2,098 | 7.0 | 122.4 | 1,960 | 97.9 |
| Average | 136.6 | 2,189 | 8.9 | 126.0 | 2,018 | 100.8 |
| Std. Dev. | 5.8 | 93 | 1.4 | 4.5 | 72 | 3.6 |

## Material Properties of AC During Construction

Dense-graded AC was sourced from the Teichert Perkins Asphalt Plant in Sacramento, California. Key material design parameters are summarized in Table F-9. The material met Caltrans specifications for Type-A HMA with three-quarter inch aggregate gradation and contained 15 percent RAP.

**Table F-9. Key HMA Mix Design Parameters**

| Parameter | | | Wearing Course Actual | Wearing Course Compliance |
|---|---|---|---|---|
| Grading: | 1" | (25 mm) | 100 | 100 |
| | 3/4" | (19 mm) | 99 | 94 – 100 |
| | 1/2" | (12.5 mm) | 85 | 94 – 100 |
| | #4 | (4.75 mm) | 49 | 44 – 58 |
| | #8 | (2.36 mm) | 32 | 31 – 41 |
| | #30 | (600 μm) | 18 | 16 – 24 |
| | #200 | (75 μm) | 4 | 3 – 7 |
| Asphalt binder grade | | | PG 64-16 | – |
| Asphalt binder content (% by aggregate mass) | | | 4.8 | – |
| Hveem stability at optimum bitumen content | | | 37.0 | >37 |
| Air void content (%) | | | 4.9 | 2 – 6 |
| Voids in mineral aggregate (LP-2) (%) | | | 13.8 | >13 |
| Voids filled with asphalt (LP-3) (%) | | | 64.9 | 65 – 75 |
| Sand equivalent (%) | | | 72.0 | >47 |
| Specific gravity (compacted, Gmb) | | | 2.451 | – |
| Specific gravity (Max, Gmm) | | | 2.576 | – |

154

## Prime Coat Application

Prior to prime coat application, the surface was broomed to remove all loose material (Figure F-6). An SS-1H asphalt emulsion prime coat was applied to the surface at a rate of 0.15 gal/yd$^2$ (0.68 L/m$^2$). Although a consistent application was achieved (Figure F-7), some differential penetration, which was attributed to patches of near-surface moisture, was observed.



**Figure F-6. Broomed surface.**



**Figure F-7. Primed surface.**

## AC Placement

AC was placed on November 14, 2012. Construction started at approximately 8:30 a.m. ambient air temperature was 45 °F and the relative humidity was 86 percent. Construction was completed at approximately 11:00 a.m., when ambient temperature was 55 °F and the relative humidity was 70 percent.

The mix was transported using end-dump trucks. Paving started in Lane #1, followed by Lanes #2, #3, and #4. The second lift on Lane #1 was placed after completion of the first lift on the other lanes. Paving was carried out in a west-east direction and followed conventional procedures. A breakdown roller closely followed the paver applying about four passes. A single pass was made with an intermediate rubber-tired roller, followed by another four passes with a finish roller. Compaction of the lower lift appeared to be consistent and no problems were noted. On the short section with the second lift (see Cell #2 in Figure F-2), the mix appeared tender and some shearing was noted in the vicinity of the instrumentation cables.

## Construction Quality Control

Compaction was measured by the UCPRC using a nuclear gauge on the day of construction using the mix design specific gravity values. Measurements were taken at 60 ft. (18 m) intervals along the center line of each lane, with a focus on checking densities in the areas that would be used for HVS testing. A summary of the results is provided in Table F-10. The results indicate that there was some variability in the measurements in the first lift, but that satisfactory compaction had been achieved. Density measurements were generally lower on the second lift and were attributed to tenderness in the mix and problems with shearing in the vicinity of the instrumentation cables.

**Table F-10. Summary of AC Density Measurements**

155

| Position | Lane #1 First Lift | Lane #1 First Lift | Lane #1 First Lift | Lane #1 Second Lift | Lane #1 Second Lift | Lane # Second Lift |
|---|---|---|---|---|---|---|
| | Gauge | Gauge | Relative | Gauge | Gauge | Relative |
| | lb/ft$^3$ | kg/m$^3$ | lb/ft$^3$ | lb/ft$^3$ | kg/m$^3$ | (%) |
| 1 | 146.0 | 2,339 | 92.8 | 141.6 | 2,269 | 90.0 |
| 2 | 145.3 | 2,328 | 92.4 | 142.5 | 2,283 | 91.0 |
| 3 | 147.8 | 2,367 | 93.9 | 142.3 | 2,280 | 90.5 |
| 4 | 143.0 | 2,290 | 90.9 | – | – | – |
| 5 | 146.1 | 2,341 | 92.9 | – | – | – |
| 6 | 146.5 | 2,346 | 93.1 | – | – | – |
| Average | 145.8 | 2,335 | 92.7 | 142.1 | 2,277 | 90.5 |
| Std. Dev. | 1.6 | 25.6 | 1.0 | 0.5 | 7.4 | 0.5 |
| RICE | 2.520 | | | | | |

Temperatures were systematically measured throughout the placement of the AC using infrared temperature guns, thermocouples, and an infrared camera. Mix temperature behind the paver screed was 297 °F. Temperatures at the start and completion of rolling were 295 °F and 141 °F, respectively. The thermal camera image (*FLIR Systems ThermaCAM PM290*) of the mat behind the paver, in Figure F-8, clearly shows consistent temperature across the mat.
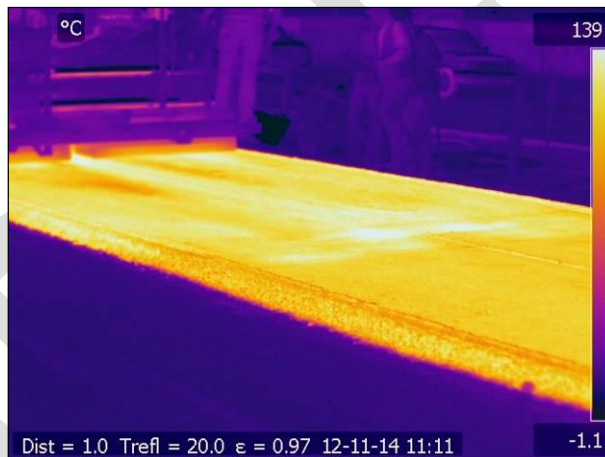


**Figure F-8. Thermal images of test track during construction.**

Thickness was monitored with probes by the paving crew throughout the construction process. The thickness of cores removed for laboratory testing after construction was measured for quality control purposes. Average thicknesses of the bottom and top lifts were 2.6 in (67 mm) and 2.5 in (64 mm), respectively.

## TEST TRACK LAYOUT, INSTRUMENTATION, AND SAMPLING

Accelerated Pavement Testing was conducted on two test sections on the lane with full-depth reclaimed aggregate base with no stabilization (FDR-NS). One of the test sections had a single 0.2 ft. lift of HMA and the second one had two 0.2 ft. lifts.

### Protocols and Coordinate System

The HVS test section layout, test setup, trafficking, and measurements followed standard UCPRC protocols. A schematic in Figure F-9 shows the HVS test section along with the stationing and coordinate system. The thermocouple tree locations and coordinate system are also presented; the z-axis points upward following the right-hand convention with zero at the pavement surface. Station numbers (0 to 16) refer to fixed points on the test section and are used for measurements and as a reference for discussing performance. Stations

156

were placed at 1.6 ft. (0.5 m) increments. The test section is 26.2 ft. (8.0 m) long and 3.3 ft. (1.0 m) wide. A sensor installed at the center of the test section has an *x*-coordinate of 13.1 ft and a *y*-coordinate of 1.6 ft.
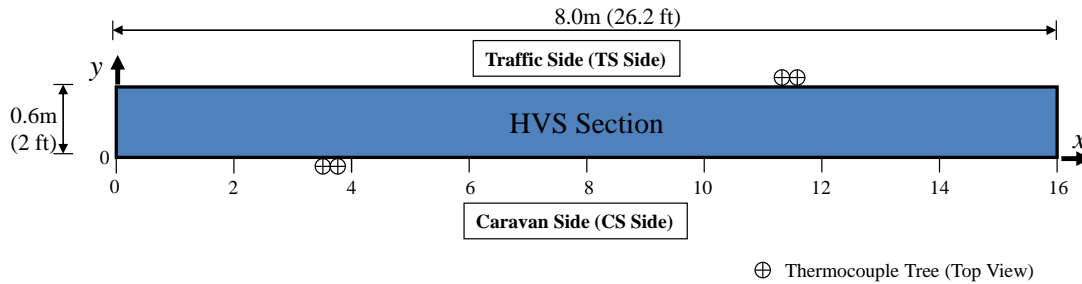


**Figure F-9. Schematic of an HVS test section and stations.**

## Test Track Layout

The FDR study test track layout is shown in Figure F-10. Two HVS test sections were demarcated for the wide-base tire testing (Sections 670HC and 671HC). All test sections were situated at the center of the lane.
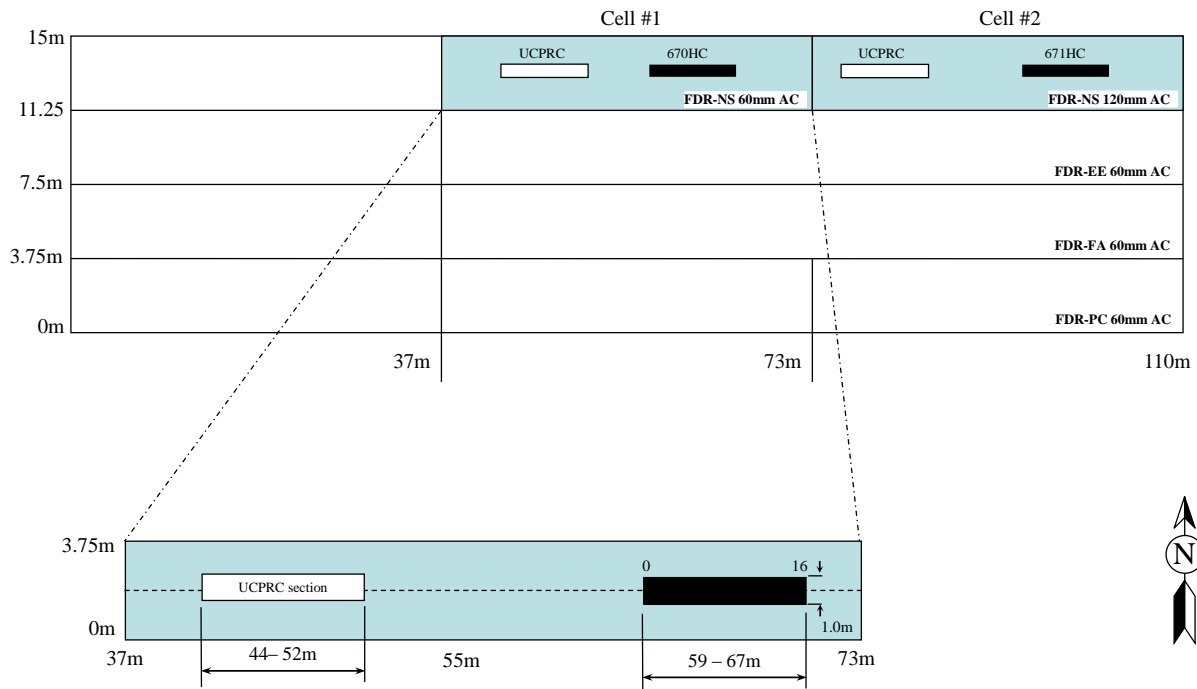


**Figure F-10. Layout of test sections.**

## Instrumentation Layout

Measurements were taken with embedded instruments including a multi-depth deflectometer (MDD), strain gauges, a pressure cell, and thermocouple trees. The layout of the embedded instruments is shown in Figure F-11 and Figure F-12, respectively for the two test sections. Photographs of the layout of the strain gauges and pressure cells in Section 670HC and Section 671HC are shown in Figure F-13 and Figure F-14, respectively. The exact coordinates of the instruments are listed in Table F-1 and Table F-2.
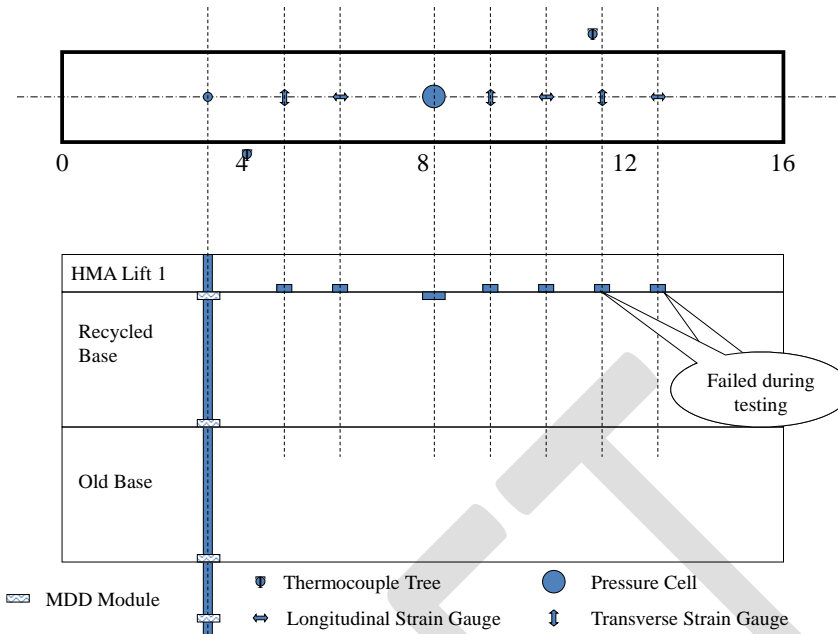
**Figure F-11. Layout of embedded instruments for Section 670HC (one lift of HMA).**



**Figure F-12. Layout of embedded instruments for Section 671HC (two lifts of HMA).**

158

**Figure F-13. View of strain gauges and pressure cells installed on Section 670HC during construction.**



(a) **Instruments on top of the recycled base**  (b) **Strain gauges on top of the bottom lift of HMA**
**Figure F-14. View of strain gauges and pressure cells installed on Section 671HC during construction.**

159

**Table F-11. Coordinates of Embedded Instruments for Section 670HC**

| Section | Type | Name | PosX (mm) | PosY (mm) | PosZ (mm) | Orientation |
|---------|------|------|-----------|-----------|-----------|-------------|
| 670HC | MDD | MDD3-70 | 1,500 | 500 | -70 | Vertical |
| 670HC | MDD | MDD3-310 | 1,500 | 500 | -310 | Vertical |
| 670HC | MDD | MDD3-550 | 1,500 | 500 | -550 | Vertical |
| 670HC | MDD | MDD3-850 | 1,500 | 500 | -850 | Vertical |
| 670HC | Pressure Cell | PC8CL_RAB_T | 4,000 | 500 | -60* | Vertical |
| 670HC | Strain Gauge | SG5CL_T_HMA_B | 2,500 | 500 | -50$^x$ | Transverse |
| 670HC | Strain Gauge | SG6CL_L_HMA_B | 3,000 | 500 | -50$^x$ | Longitudinal |
| 670HC | Strain Gauge | SG9CL_T_HMA_B | 4,610 | 500 | -50$^x$ | Transverse |
| 670HC | Strain Gauge | SG10CL_L_HMA_B | 5,219 | 500 | -50$^x$ | Longitudinal |
| 670HC | Strain Gauge | SG12CL_T_HMA_B | 5,829 | 500 | -50$^x$ | Transverse |
| 670HC | Strain Gauge | SG13CL_L_HMA_B | 6,438 | 500 | -50$^x$ | Longitudinal |
| 670HC | Thermocouple | 4CS-0 | 2,000 | -100 | 0 | N/A |
| 670HC | Thermocouple | 4CS-20 | 2,000 | -100 | -20 | N/A |
| 670HC | Thermocouple | 4CS-50 | 2,000 | -100 | -50 | N/A |
| 670HC | Thermocouple | 4CS-90 | 2,000 | -100 | -90 | N/A |
| 670HC | Thermocouple | 4CS-120 | 2,000 | -100 | -120 | N/A |
| 670HC | Thermocouple | 12TS-0 | 6,000 | 1,100 | 0 | N/A |
| 670HC | Thermocouple | 12TS-20 | 6,000 | 1,100 | -20 | N/A |
| 670HC | Thermocouple | 12TS-50 | 6,000 | 1,100 | -50 | N/A |
| 670HC | Thermocouple | 12TS-90 | 6,000 | 1,100 | -90 | N/A |
| 670HC | Thermocouple | 12TS-120 | 6,000 | 1,100 | -120 | N/A |

*: installed flush with the top of the recycled base
$^x$: installed on top of the recycled base

**Table F-12. Coordinates of Embedded Instruments for Section 671HC**

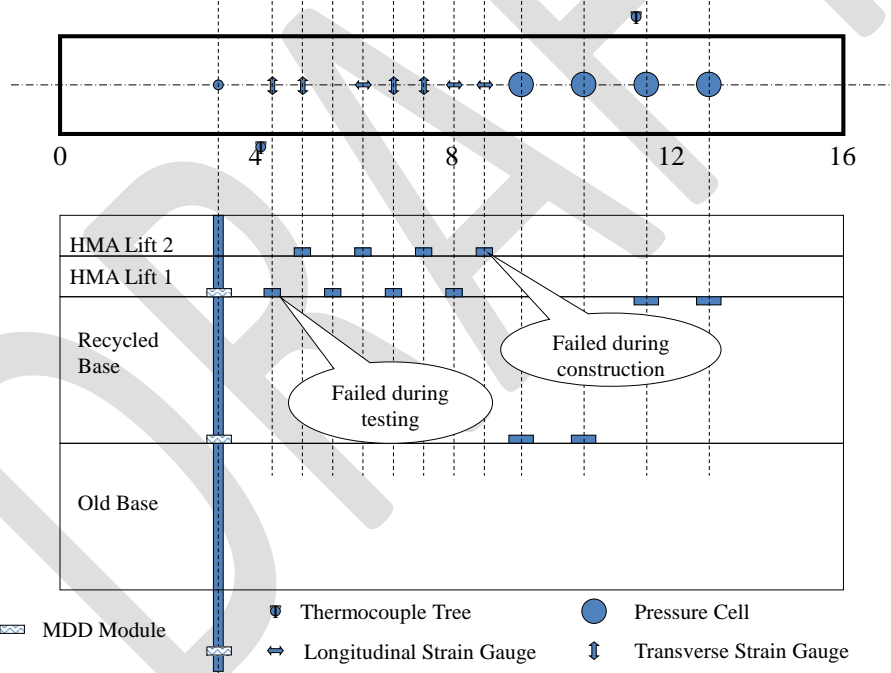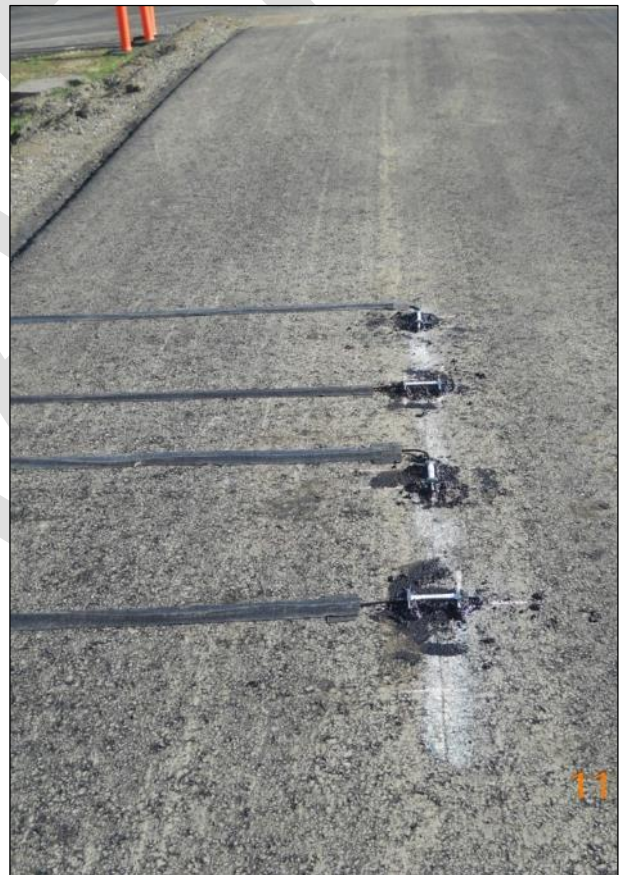| Section | Type | Name | PosX (mm) | PosY (mm) | PosZ (mm) | Orientation |
|---------|------|------|-----------|-----------|-----------|-------------|
| 671HC | MDD | MDD3-100 | 1,500 | 500 | -100 | Vertical |
| 671HC | MDD | MDD3-365 | 1,500 | 500 | -365 | Vertical |
| 671HC | MDD | MDD3-1000 | 1,500 | 500 | -1,000 | Vertical |
| 671HC | Pressure Cell | PC9CL_RAB_B | 4,671 | 500 | -365 | Vertical |
| 671HC | Pressure Cell | PC11CL_RAB_B | 5,281 | 500 | -365 | Vertical |
| 671HC | Pressure Cell | PC12CL_RAB_T | 5,890 | 500 | -135 | Vertical |
| 671HC | Pressure Cell | PC13CL_RAB_T | 6,500 | 500 | -135 | Vertical |
| 671HC | Strain Gauge | SG4CL_T_HMA_BL_B | 2,233 | 500 | -116 | Transverse |
| 671HC | Strain Gauge | SG5CL_T_HMA_TL_B | 2,538 | 500 | -65 | Transverse |
| 671HC | Strain Gauge | SG6CL_L_HMA_BL_B | 2,842 | 500 | -116 | Longitudinal |
| 671HC | Strain Gauge | SG6CL_L_HMA_TL_B | 3,147 | 500 | -65 | Longitudinal |
| 671HC | Strain Gauge | SG7CL_T_HMA_BL_B | 3,452 | 500 | -116 | Transverse |
| 671HC | Strain Gauge | SG8CL_T_HMA_TL_B | 3,757 | 500 | -65 | Transverse |
| 671HC | Strain Gauge | SG8CL_L_HMA_BL_B | 4,062 | 500 | -116 | Longitudinal |
| 671HC | Thermocouple | 4CS-0 | 2,000 | -100 | 0 | N/A |

| 671HC | Thermocouple | 4CS-20 | 2,000 | -100 | -20 | N/A |
|-------|--------------|--------|-------|------|-----|-----|
| 671HC | Thermocouple | 4CS-50 | 2,000 | -100 | -50 | N/A |
| 671HC | Thermocouple | 4CS-90 | 2,000 | -100 | -90 | N/A |
| 671HC | Thermocouple | 4CS-120 | 2,000 | -100 | -120 | N/A |
| 671HC | Thermocouple | 12TS-0 | 6,000 | 1,100 | 0 | N/A |
| 671HC | Thermocouple | 12TS-20 | 6,000 | 1,100 | -20 | N/A |
| 671HC | Thermocouple | 12TS-50 | 6,000 | 1,100 | -50 | N/A |
| 671HC | Thermocouple | 12TS-90 | 6,000 | 1,100 | -90 | N/A |
| 671HC | Thermocouple | 12TS-120 | 6,000 | 1,100 | -120 | N/A |

*: installed flush with the top of the recycled base
x: installed on top of the recycled base

- **Thermocouples**

Type-K thermocouples were used to measure pavement and air temperatures (both inside and outside the temperature chamber). Five thermocouples were bundled together to form a "thermocouple tree" (Figure F-15) for measuring pavement temperatures at multiple depths at each location.



**Figure F-15. Thermocouple tree with five Type-K thermocouples on a plastic dowel.**

- **Laser Profilometer**

A laser profilometer was used to the measure transverse surface profile of the test section at every station, (i.e., from Station 0 to Station 16). The difference between the surface profile after HVS trafficking and the initial surface profile is the permanent change in surface profile. Based on the change in surface profile, the maximum total rut was determined for each station, as illustrated in Figure F-16.
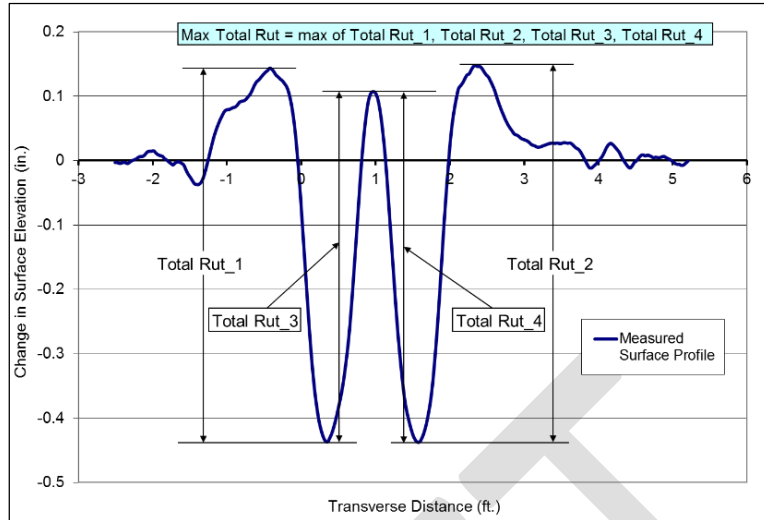
**Figure F-16. Illustration of maximum rut depth for a leveled profile.**

- **Strain Gauges**

*Tokyo Sokki Kenkyujo Inc. KM100-HAS* 350 Ω full bridge strain gauges were used on both sections. Gauges were attached to the pavement surface using a paste prepared by mixing sand and asphalt emulsion. Installation of a strain gauge on top of the recycled base is shown in Figure F-17.


**Figure F-17. Installation of *Tokyo Sokki KM100-HAS* strain gauge.**

The strain gauges were connected to a *National Instruments NI cDAQ-9237* module. A virtual channel was created for each strain gauge using the *Measurement & Automation Explorer* (NI-MAX) software provided by *National Instruments*. The settings for the virtual channel are shown Figure F-18. Using these settings, the strain gauge virtual channel readings are determined as:

$$Strain = -\frac{V_r}{GF} = -\frac{V_r}{0.5} = -2V_r$$

where $Strain$ is the output of the virtual channel; $GF$ is the gauge factor in the virtual channel setting; and $V_r$ is the ratio between output and input voltages of the Wheatstone bridge inside the strain gauge.
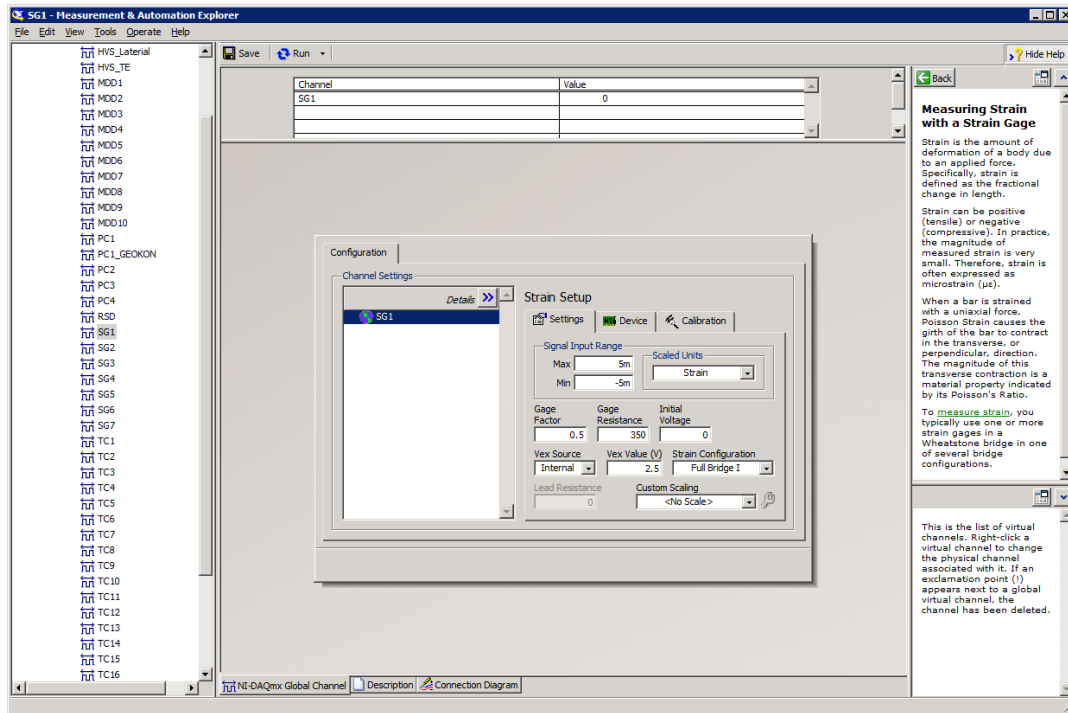
**Figure F-18. Virtual channel settings for strain gauges used in this project.**

A gauge factor ($GF$) of 0.5 was used to configure the virtual channel to accommodate the *Tokyo Sokki* calibration coefficient ($C_\varepsilon$) for each gauge based on the assumption that the voltage ratio ($V_r$) was multiplied by 2.0 when converting to strain. The data acquisition software then converted the virtual channel reading into microstrain by multiplying it by -0.830 x $10^6$. The negative sign was necessary to ensure that tensile strain will increase the final readings. The value of 0.830 was the average calibration coefficient provided by *Tokyo Sokki*. Once the strain readings were recorded, they were loaded into a database where the actual calibration coefficients for each specific strain gauge were stored. When data were extracted from the database, the necessary minor rescaling was built into the query to ensure that the individual gauge factors were used in place of the average value of 0.830.

Example strain data recorded from one of the strain gauges is presented in Figure F-19, which shows the variation of the strain gauge reading versus wheel position as the wheel travels from one end of the test section to the other. Several quantities are summarized based on the raw readings. Specifically, the reference value is the reading when the wheel is at the far end of the test section. The peak and valley are maximum and minimum values deviating from the reference value, respectively.
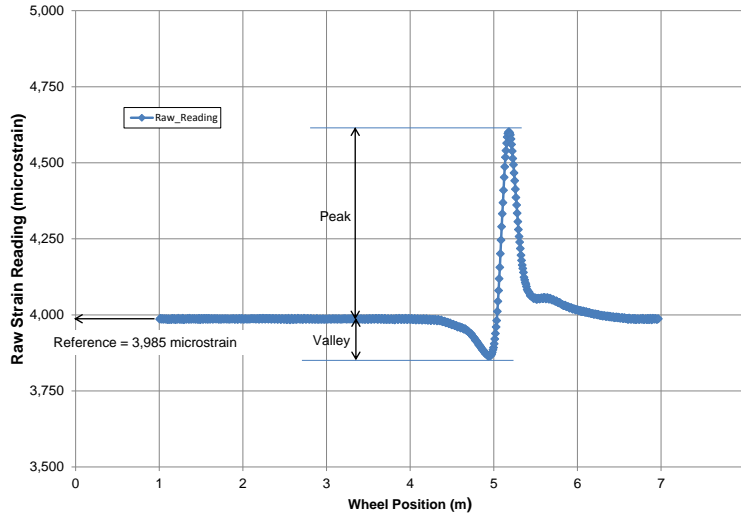
**Figure F-19. Example strain reading and definitions of summary quantities.**

- **Earth Pressure Cells**

Two different types of earth pressure cells were used: *GeoKon 3500-3* pressure cells were installed in the thin AC section (i.e., Section 670HC) and *RST Instruments LPTPC09-SG* pressure cells were used in the thick section (i.e., Section 671HC). Installation of the pressure cells is shown in Figure F-20.



(a) *GeoKon 3500-3* pressure cell on 670HC        (b) *RST* pressure cells on 671HC

**Figure F-20. Installation of earth pressure cells for the two test sections.**

Example data recorded from one of the pressure cells is shown in Figure F-21, which presents variation of the pressure reading versus wheel position as the wheel travels from one end of the test section to the other. Several quantities are summarized based on the raw readings. Specifically, the reference value is the reading when the wheel is at the far end of the test section. The peak and valley are maximum and minimum values deviating from the reference value, respectively.

164
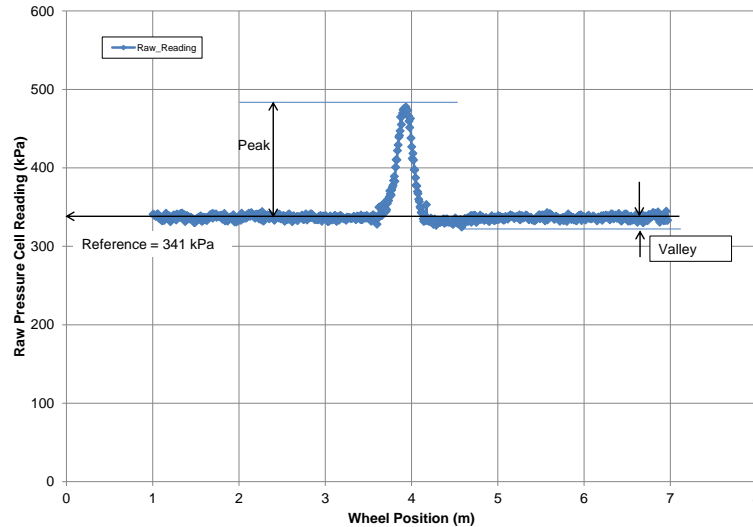
**Figure F-21. Example pressure cell reading and definitions of summary quantities.**

- **Multi-Depth Deflectometers**

A multi-depth deflectometer is essentially a stack of linear variable differential transformer (LVDT) modules fixed at different depths in a single borehole. LVDT modules have nonspring-loaded core slugs linked into one long stick that is fixed at the bottom of a 10 ft. (3.3 m) borehole. The borehole was 1.5 in (38 mm) in diameter. A model MDD with five modules is shown in Figure F-22.mThe LVDT modules were fixed to the pavement, which allowed permanent vertical deformations at various depths to be recorded in addition to measurement of the elastic deformation caused by the passage of HVS wheels.

An example set of MDD data are presented in Figure F-23, which shows the variation of the elastic vertical deflections measured at different depths versus wheel position as the wheel travels from one end of the test section to the other. The elastic vertical deflection is the difference between total vertical deflection and the reference value, defined as the reading when the wheel is at the far end of the test section. The peak values are the maximum elastic vertical deflection for each individual module.

165

**Figure F-22. A model multi-depth deflectometer (MDD), showing five modules.**
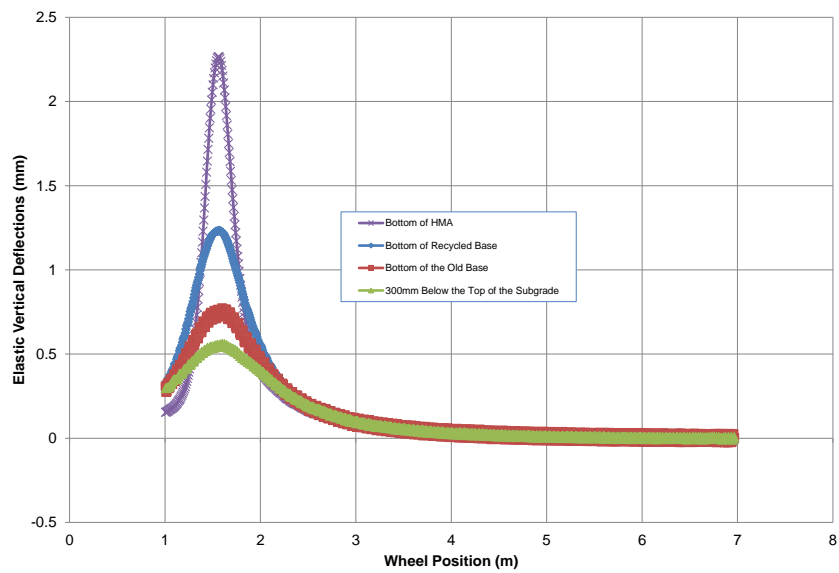


**Figure F-23. Example elastic vertical deflection measured with MDD.**

## Material Sampling

Thirty-two cores were sampled from Section 670HC and 16 cores were sampled from Section 671HC (Figure F-24). All cores were 6 in (150 mm) in diameter and were sampled from untrafficked areas approximately 20 in (0.5 m) away from the HVS test sections after testing was completed.

Edge of the lane

0.5m

0.5m

HVS Test Section

0.5m

0.5m

Edge of the lane

▭▭▭▭▭ Area for coring
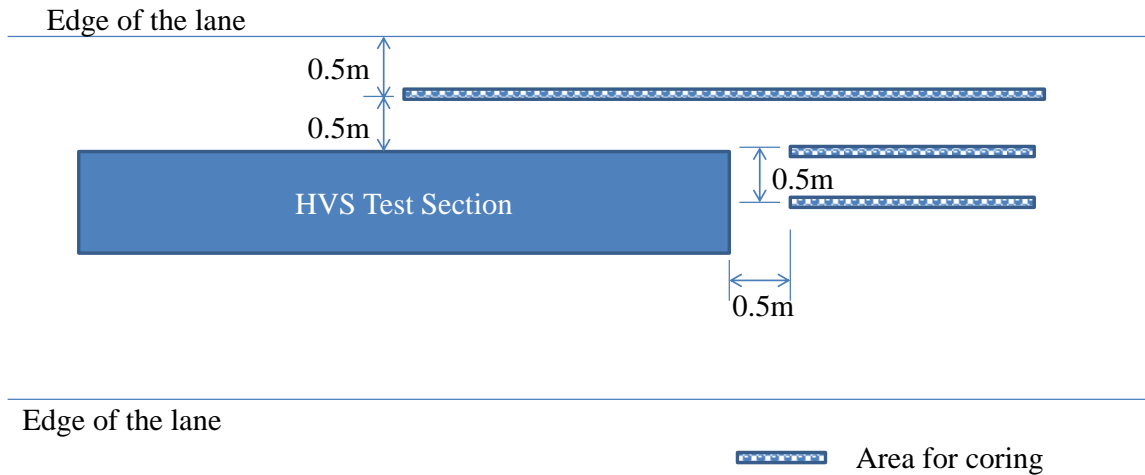
**Figure F-24. Schematic of coring layout (overhead view).**

## As-Built Layer Thicknesses

As-built layer thicknesses were determined using different methods depending on the layer type. HMA layer thicknesses were determined from cores taken near the test section, as described above, and from the cores taken while drilling the MDD boreholes. The as-built HMA layer thicknesses for the two test sections are listed in Table F-13.

**Table F-13. As-Built HMA Layer Thicknesses**

| Layer | Method | 670HC Average (in.) | 670HC Std. Dev.[1] (in.) | 671HC Average (in.) | 671HC Std. Dev. (in.) |
|-------|--------|---------------------|---------------------------|---------------------|------------------------|
| Bottom Lift | MDD hole | 2.4 | | 2.0 | |
| Bottom Lift | 6 in cores | 2.6 | 0.2 | 3.0 | 0.1 |
| Top Lift | MDD hole | N/A | | 2.6 | |
| Top Lift | 6 in cores | N/A | | 2.5 | 0.1 |

[1] Std. dev. = standard deviation

The recycled base and existing aggregate base thicknesses were determined from DCP measurements conducted for the nearby UCPRC test sections. For each DCP test, an 8 in (200 mm) diameter core was first drilled through the HMA layer. DCP testing was then conducted inside the core hole. The penetration curves for the two cells where Sections 670HC and 671HC were located are shown in Figure F-25 and Figure F-26, respectively. Layer interfaces are indicated by the changes in penetration rate.

According to Table F-12, there was only one clear change in penetration rate at approximately 20 in (500 mm) below the bottom of the HMA layer on Section 670HC. This indicates that the recycled base and old aggregate base layer had similar mechanical properties. Their combined as-built thicknesses were comparable to the 22.5 in (570 mm) design thickness. According to Table F-13, there were two clear changes in penetration rate for Section 671HC. The first was located approximately 10.2 in (260 mm) below

167

the bottom of the HMA layer, indicating the interface between the recycled base and the old aggregate base. The second was located between 20.5 in (520 mm) and 21.8 in (555 mm) below the bottom of the HMA layer, corresponding to the interface between the old aggregate base and the subgrade.
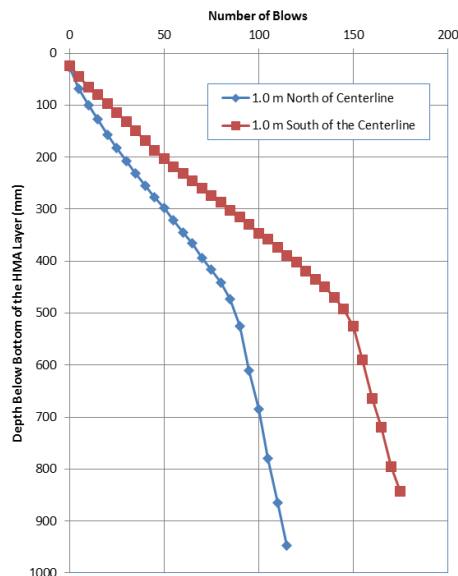


**Figure F-25. Unbound layer DCP penetration curves for Section 670HC.**
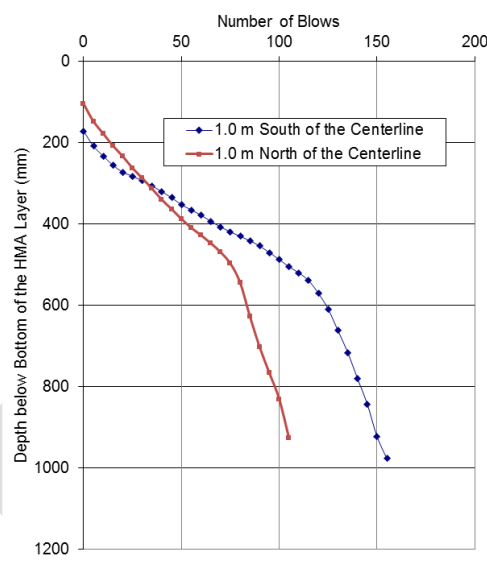
**Figure F-26. Unbound layer DCP penetration curves for Section 671HC.**

## DATA COLLECTION
The main objective of the APT study was to collect pavement response data during trafficking with different tires (single wide-base tire versus DTA) under various loading conditions, including varied tire pressures, pavement temperatures, wheel loads, and lateral offsets. The APT was conducted using an MK VI HVS manufactured by *Dynatest Consulting Inc*. Photographs of the HVS are shown in Figure F-27. The HVS is a linear loading machine with the following key features:

- Effective distance of travel of either 19.7 ft. (6 m) (as in this study) or 42.7 ft. (13 m) with an extension
- 26,000 bi-directional passes per day
- Half single axle load application
- Loading range of 5.6 to 22.5 kips (25 to 100 kN) using dual truck tires, and up to 45 kips (200 kN) using an aircraft tire
- Maximum speed of up to 12.4 mph (20 km/h) with a 42.7 ft. (13 m) travel distance
- Maximum of 2.9 ft. (0.9 m) transverse travel in increments of 1.0 to 3.0 in (25 to 75 mm)

| (a). Overall view of the HVS with temperature control chamber | (b). Interior view of the temperature control chamber while validating HVS half-axle load |

**Figure F-27. Heavy Vehicle Simulator (HVS).**

## Loading Program

The loading program for each HVS test section was designed to allow measurements of pavement responses under the different tires with the following loading combinations:

- A full factorial of pavement temperature, tire pressure, and half-axle load with the following levels:
  - Pavement temperatures: 68, 95, and 122°F
  - Tire pressures: 80, 100, 110, 125 psi for both DTA and the WBT, and 60/110, 80/110 psi for dual DTA with the two tires set to different tire pressures
  - Half-axle loads: 6, 8, 10, 14, 18 kips
- Distance between CLTA and centerline of the test section fixed at 0
- A smaller full factorial of tire pressure and lateral position of the centerline of the tire or tire assembly (CLTA) with the following levels:
  - Pavement temperature fixed at 122°F
  - Tire pressures: 80 and 125 psi
  - Half-axle load fixed at 10 kips
  - Distance between CLTA and centerline of the test section: 0, 7, and 12 in.

Once the above loading combinations were completed, a selected subset of loading combinations was repeated to evaluate changes in pavement condition caused by the testing. The selected subset included a full factorial of the following combinations:

- Pavement temperatures: 68, 95, and 122°F
- Tire pressures: 100 and 125 psi
- Half-axle load fixed at 10 kips

Unless specified otherwise, the CLTA was always aligned with the centerline of the HVS test section. The detailed planned testing sequence is shown in Table F-14. Also, it should be noted that the actual testing sequence had some slight variations from the planned sequence due to operational constraints. (Table F-15 lists the conversion values between the English and SI units for the quantities used in the loading program.) The actual loading sequence can be found in the "SectionHistory" table of the *MS Access* database delivered with this technical memorandum.

One hundred load repetitions were applied for each loading combination, and loading was applied in a channelized mode (i.e., no wander) in both directions.

**Table F-14. Planned HVS Loading Program**

| Sequence | Tire Type | Temperature (°F) | Tire Pressures (psi) | Half-Axle Load (kips) | Offset (inches) | Number of Cases |
|---|---|---|---|---|---|---|
| 1 | DTA | 68 | 80, 100, 110, 125, 60/110, 80/110 | 6, 8, 10, 14 | 0 | 24 |
| 2 | DTA | 95 | 80, 100, 110, 125, 60/110, 80/110 | 6, 8, 10, 14 | 0 | 24 |
| 3 | DTA | 122 | 80, 100, 110, 125, 60/110, 80/110 | 6, 8, 10, 14 | 0 | 24 |
| 4 | DTA | 122 | 80, 125 | 10 | 0, 7, 12 | 6 |
| 5 | NG-WBT | 68 | 80, 100, 110, 125 | 6, 8, 10, 14 | 0 | 16 |
| 6 | NG-WBT | 95 | 80, 100, 110, 125 | 6, 8, 10, 14 | 0 | 16 |
| 7 | NG-WBT | 122 | 80, 100, 110, 125 | 6, 8, 10, 14 | 0 | 16 |
| 8 | NG-WBT | 122 | 80, 125 | 10 | 0, 7, 12 | 6 |
| 9 | DTA | 68 | 80, 100, 110, 125, 60/110, 80/110 | 18 | 0 | 6 |
| 10 | DTA | 95 | 80, 100, 110, 125, 60/110, 80/110 | 18 | 0 | 6 |
| 11 | DTA | 122 | 80, 100, 110, 125, 60/110, 80/110 | 18 | 0 | 6 |
| 12 | NG-WBT | 68 | 80, 100, 110, 125 | 18 | 0 | 4 |
| 13 | NG-WBT | 95 | 80, 100, 110, 125 | 18 | 0 | 4 |
| 14 | NG-WBT | 122 | 80, 100, 110, 125 | 18 | 0 | 4 |
| 15 | NG-WBT | 122 | 100, 125 | 10 | 0 | 2 |
| 16 | NG-WBT | 95 | 100, 125 | 10 | 0 | 2 |
| 17 | NG-WBT | 68 | 100, 125 | 10 | 0 | 2 |
| 18 | DTA | 68 | 100, 125 | 10 | 0 | 2 |
| 19 | DTA | 95 | 100, 125 | 10 | 0 | 2 |
| 20 | DTA | 122 | 100, 125 | 10 | 0 | 2 |
| | | | | | **Total** | **174** |

**Table F-15. Conversion Table for the Quantities Used in the Loading Combinations**

| Quantity | English Value | English Unit | SI Value | SI Unit |
|---|---|---|---|---|
| Tire Pressure | 60 | psi | 419 | kPa |
| Tire Pressure | 80 | psi | 559 | kPa |
| Tire Pressure | 100 | psi | 698 | kPa |
| Tire Pressure | 110 | psi | 768 | kPa |
| Tire Pressure | 125 | psi | 873 | kPa |
| Temperature | 68 | °F | 20 | °C |
| Temperature | 95 | °F | 35 | °C |
| Temperature | 122 | °F | 50 | °C |
| Distance | 0 | inch | 0 | mm |
| Distance | 7 | inch | 178 | mm |
| Distance | 12 | inch | 305 | mm |
| Load | 6 | kips | 27 | kN |
| Load | 8 | kips | 36 | kN |

| Load | 10 | kips | 44 | kN |
|------|-----|------|-----|-----|
| Load | 14 | kips | 62 | kN |
| Load | 18 | kips | 80 | kN |

## Tire Assemblies

The make, brand, model, batch number, and overall tread width of the tires used in the tests are listed in Table F-16. The tires were supplied by Michelin. A schematic of the geometry for the two tire assemblies is shown in Figure F-28, and the tire footprints are illustrated in Figure F-29 and Figure F-30 for 9 kip half-axle load and 100 psi tire inflation pressure.

**Table F-16. Specifications for Tires Used in the Testing**

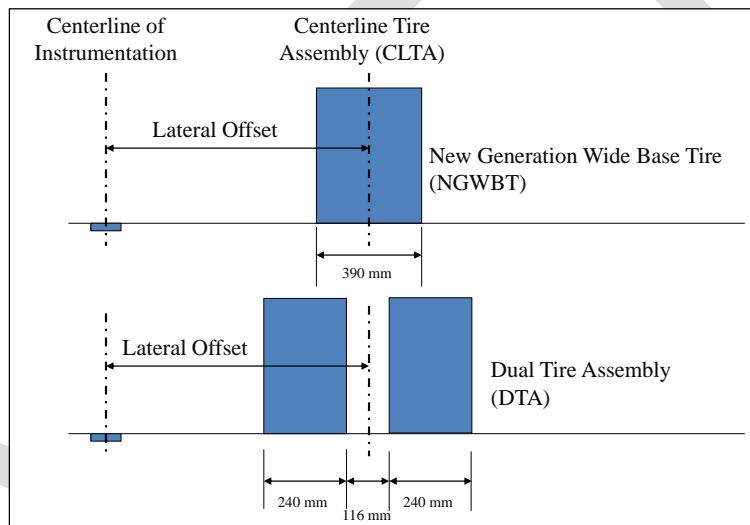| Assembly Type | Make | Brand | Model | Batch Number | Tread Width (mm) |
|---------------|------|-------|-------|--------------|------------------|
| DTA | Michelin | XDN2 M+S | 275/80 R22.5 | DOTM5EJN38X0612 | 240 |
| NG-WBT | Michelin | Xone XDN2 | 445/50R225 Radial | DOTB6DORF6X0412 | 390 |



**Figure F-28. Schematics of the tire assembly geometries.**



**Figure F-29. DTA footprint.**

171

**Figure F-30. New-generation wide-base tire footprint.**

## Data Collection Schedule

Data collected during the testing can be grouped into two types: static data and dynamic data. Static data are obtained from measurements that do not vary with wheel position, such as pavement temperature and surface profile. Dynamic data are obtained from measurements that vary with wheel position and include strain, pressure, and elastic deflection. Static data collection was triggered by schedule, while dynamic data collection was triggered by wheel movement. Dynamic data are essentially influence lines that describe how different pavement responses change with wheel position.

Pavement temperatures were recorded every five minutes and whenever dynamic data were collected. Surface profiles were measured at the beginning and end of testing and when the tire assembly was changed.

Dynamic data measured by the different sensors was collected using a shared sampling clock. All sensors were read simultaneously every time the wheel moved 0.3 in (7.4 mm). The wheel speeds were also recorded. A description of the design of the data acquisition system can be found in Reference (5). Dynamic data were collected for every HVS load repetition.

## Deflection Measurements

Deflection measurements were taken with a Dynatest falling weight deflectometer (FWD) along the centerline of each test section before and after testing. The drop locations are illustrated in Figure F-31 and cover both trafficked and untrafficked areas. Two FWD test sessions were conducted, the first in the early morning when the pavement was still cold and the second in midafternoon when the pavement was warmer.



HVS Test Section

FWD Drop Locations 33 @ 0.5m interval
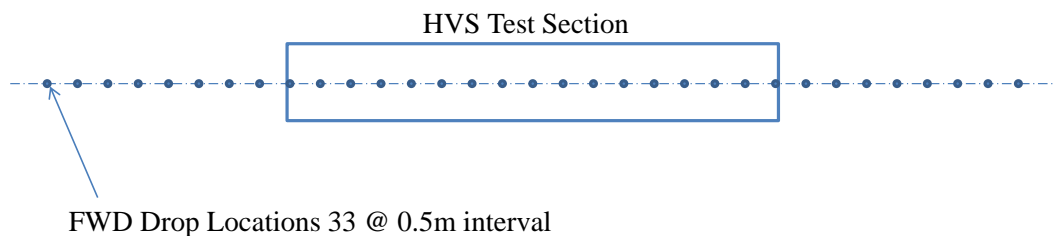
**Figure F-31. Schematic of FWD drop locations.**

# Appendix G:   Detailed Data Sample, Filtering, and Max/Min Selection

Some of the filtered and extracted data plots are provided in the figures below.
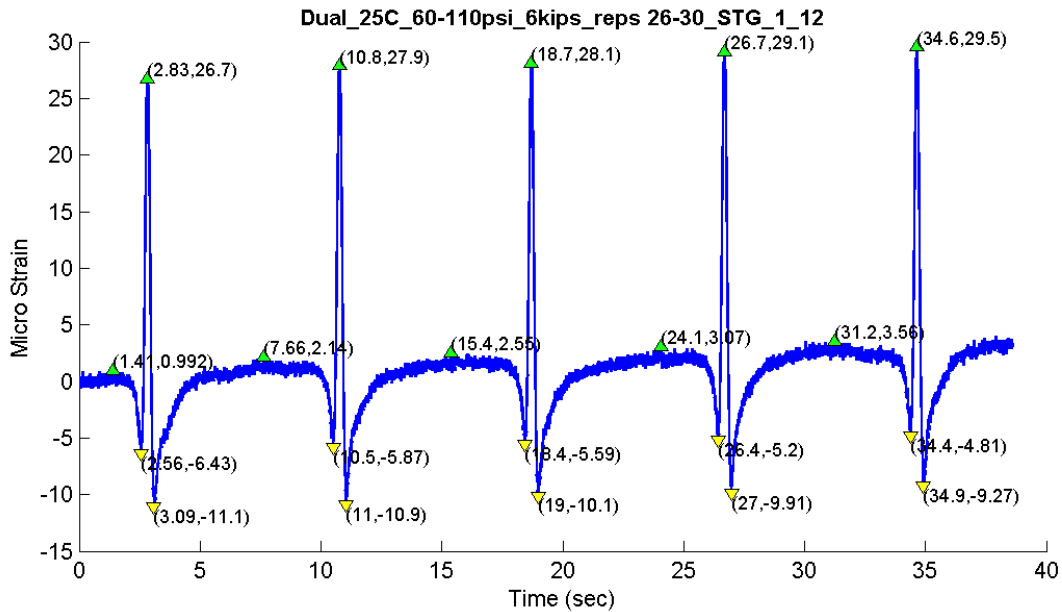


**Figure G-1. Florida, test pit section, surface transverse strain gauge 1_12 for dual-tire 25C, 60-110 psi tire pressure, 6 kips load.**
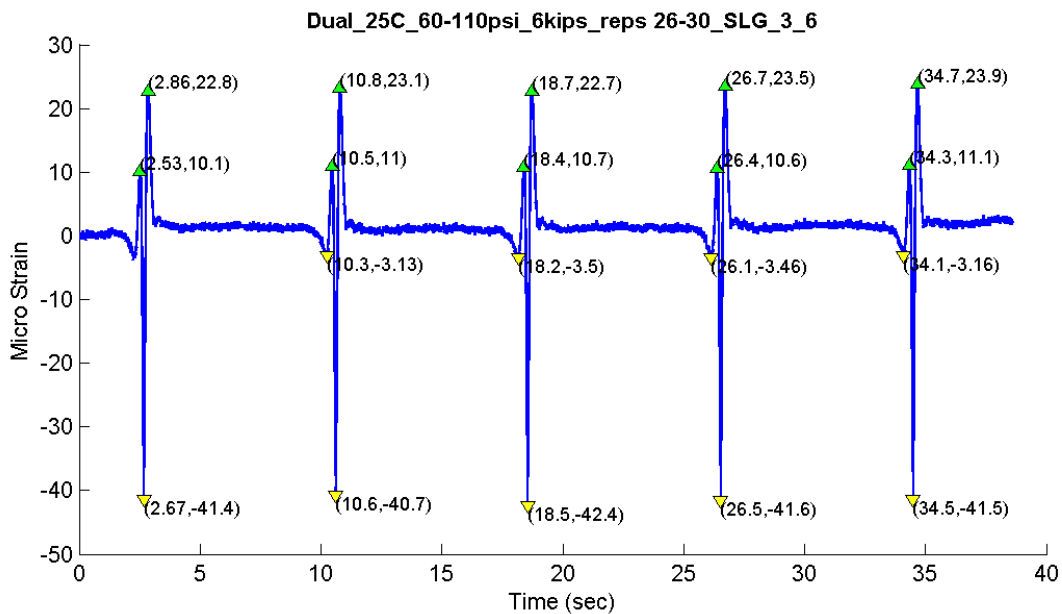


**Figure G-2. Florida, test pit section, surface longitudinal strain Gauge 3_6 for dual-tire 77 °F, 60-110 psi tire inflation pressure, 6 kips load.**
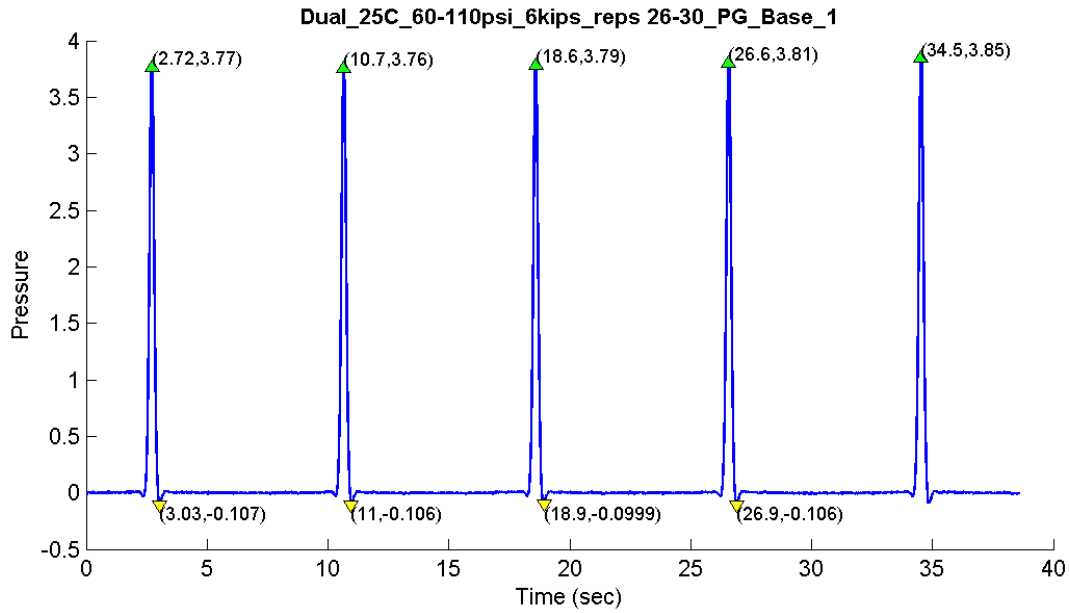
**Figure G-3. Florida, test pit section, pressure gauge at base sensor No. 1 for dual-tire 77 °F, 60-110 psi tire inflation pressure, 6 kips load.**
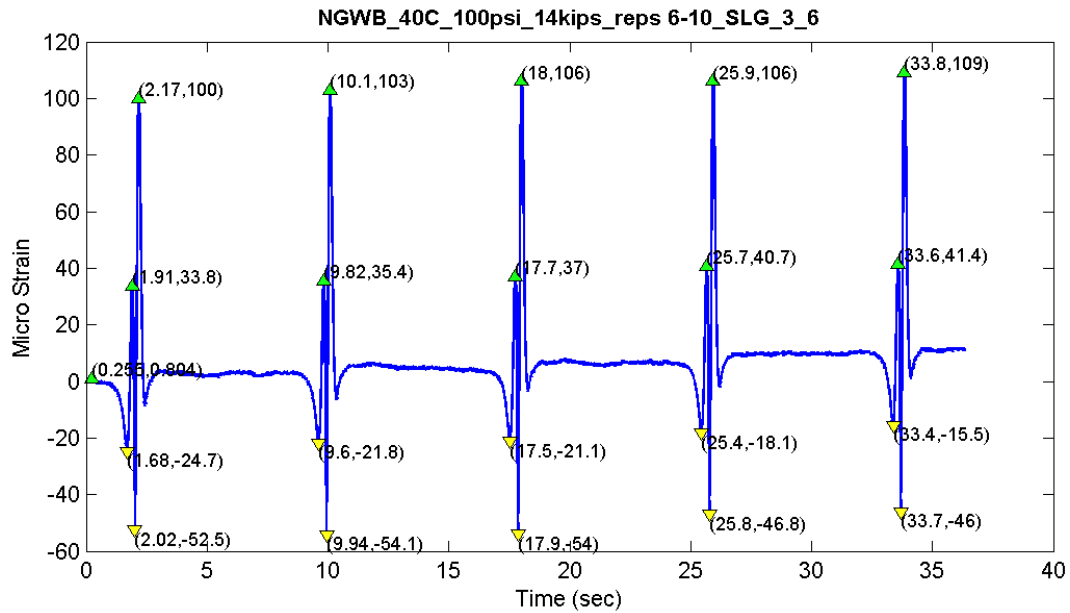


**Figure G-4. Florida, test pit section, surface longitudinal strain gauge sensor 3_6 for wide-base tire 104 °F, 100 Psi tire pressure, 14 kips load.**
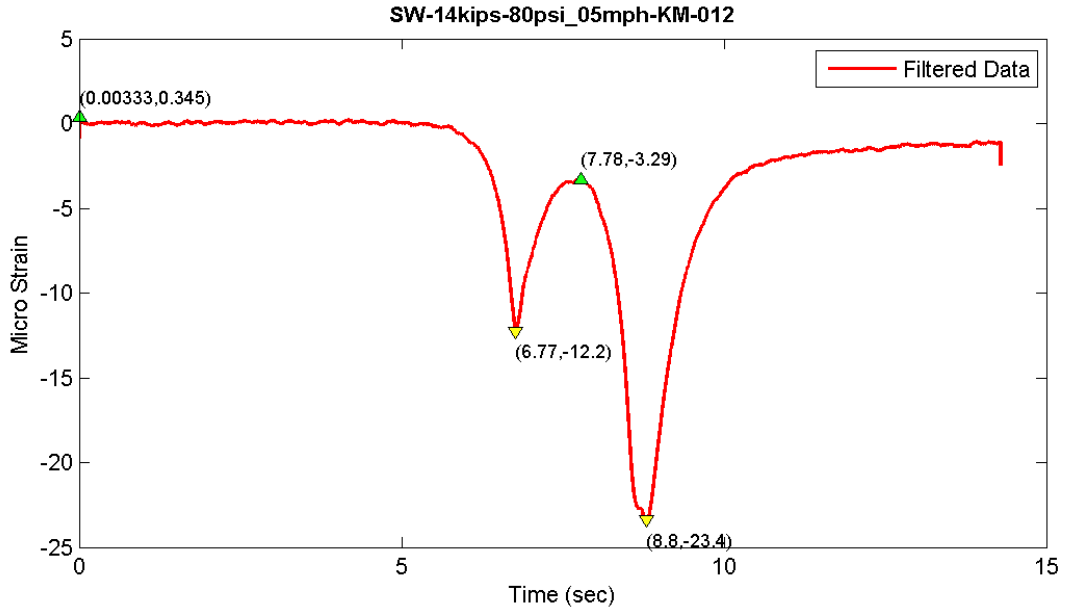
**Figure G-5. Ohio, driving section, strain gauge type KM sensor 12 for single wide-base tire run No. 26.**
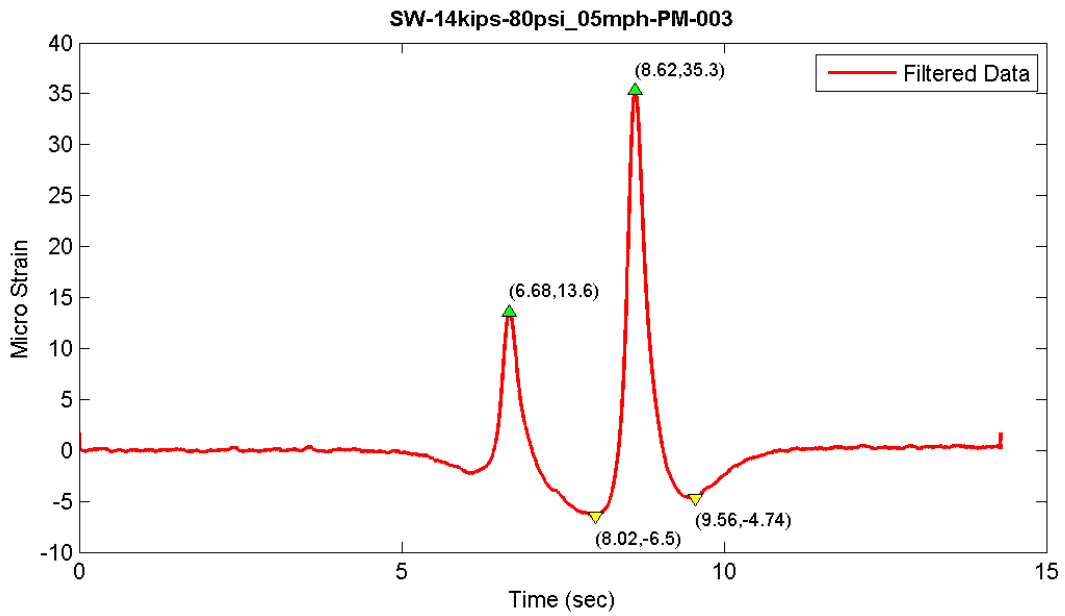


**Figure G-6. Ohio, driving section, strain gauge type Pm sensor 003 for single wide-base tire run No. 26.**

**Figure G-7. Ohio, driving section, linear displacement sensor 002 for single wide-base tire run No. 26.**



**Figure G-8. Ohio, driving section, shear strain gauge (Rosette) WFLM sensor 042 for single wide-base tire run No. 26.**

Sample Matalb Code used for data filtering and extraction process for Florida section is provided below:

```
%% Data Management: Filtering, Peaks/Valleys Extraction Code - Florida
%
% Data Upload
% Select the folder root and then wait while data are uploaded
% automatically. You can find the data files on workspace starting with a
% character 'v'.
% Depending on the number of files this may take several minutes!
clc
clear
mfoldpath = uigetdir('','Please select tes folder containing data (Test',...
    'Pit or Test Track).'); mfoldinfo = dir(mfoldpath);
maxresp.EG=[]; maxresp.SP=[]; avgresp.EG=[]; avgresp.SP=[]; pulse=[];
maxresp.allrep_SP= []; maxresp.allrep_EG= []; avgresp.allrep_SP = [];
avgresp.allrep_EG=[];maxresp.EG=[];maxresp.SP=[];avgresp.SP=[];avgresp.EG
=[];
%% Run the code over sensor readings (files)
for nn = 3:size(mfoldinfo,1)
    try  % catches any error
    %%
    foldpath = [mfoldpath,'\',mfoldinfo(nn).name];
    cd(foldpath);foldinfo= dir([foldpath,'\*.txt']);
    %   Use for deleting current folders
          % rmdir('Filtered','s'); rmdir('plots','s');
% Data Filtering-------------------------------------------
    % Add folder root where functions are located
 addpath(['C:\Users\Mojtaba\Documents\PhD Project\' ...
    'Wide-Base Project\WB Data\New data\Matlab Codes']);
 addpath(['C:\Users\Mojtaba\Documents\PhD Project\Wide-Base Project\' ...
    'WB Data\New data\Florida Data\Mojatab files']);
 % Build an new Folder for saving filtered data
 try
    rmdir('Filtered','s'); delete('peakdet.m'); % rmdir('Plots','s')
    delete('roundsd.m'); delete('Database.mat')
 end
 mkdir([foldpath,'\Filtered\']);
 froot=regexp(foldpath,'\','split');
 froot(end)
 v = genvarname(['dbase_',froot{end-1},'_',froot{end}]);
%% For each test case
 for i=1:size(foldinfo,1);
    % Build a new folder for saving plots - delete rows with NAN
    raw = importdata(foldinfo(i).name,',',6);
    raw.data = raw.data(~any(isnan(raw.data),2),:);
    fn = strrep(strtok(foldinfo(i).name,'.txt'),'-','_');
    dbase.(fn).filt=[]; dbase.(fn).filt(:,1:2)= raw.data(:,1:2);
    % mkdir([foldpath,'\Plots\',strtok(foldinfo(i).name,'.txt')]);
    % Use when want to delete a specific folder
    %   rmdir([foldpath,'\Plots\',strtok(foldinfo(i).name,'.txt')],'s');
 %% For Each sensor reading
 for j=3:size(raw.data,2)-5
    % Define Low-pass filter parameters for each sensor (trial and error)
    if (size(foldinfo,1)>7 && i<3)
        row = 3; Fp = 0.1; Fs=0.6;
    elseif (size(foldinfo,1)<7 && i>1)
```
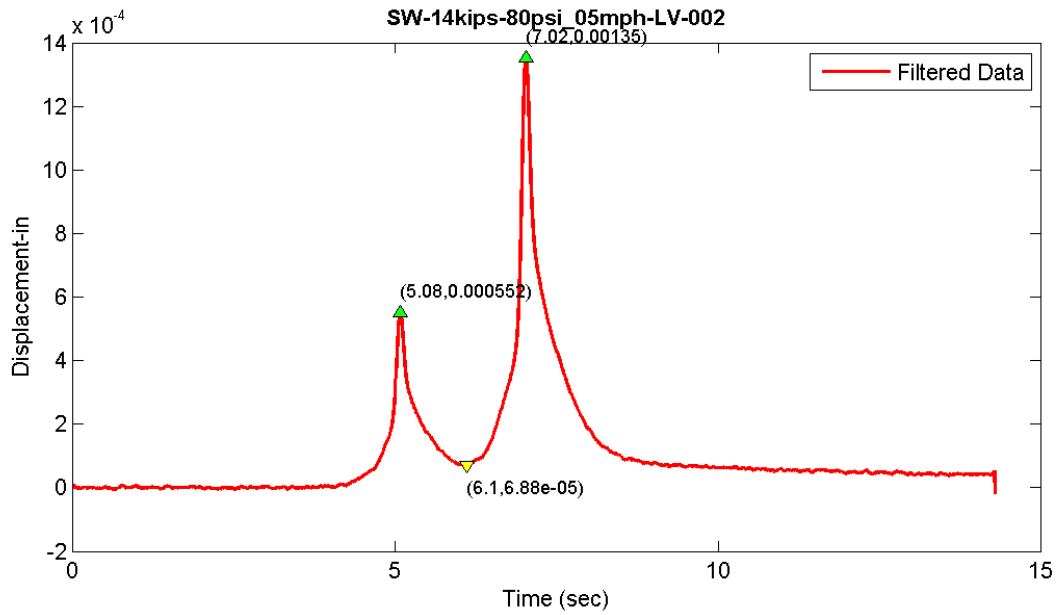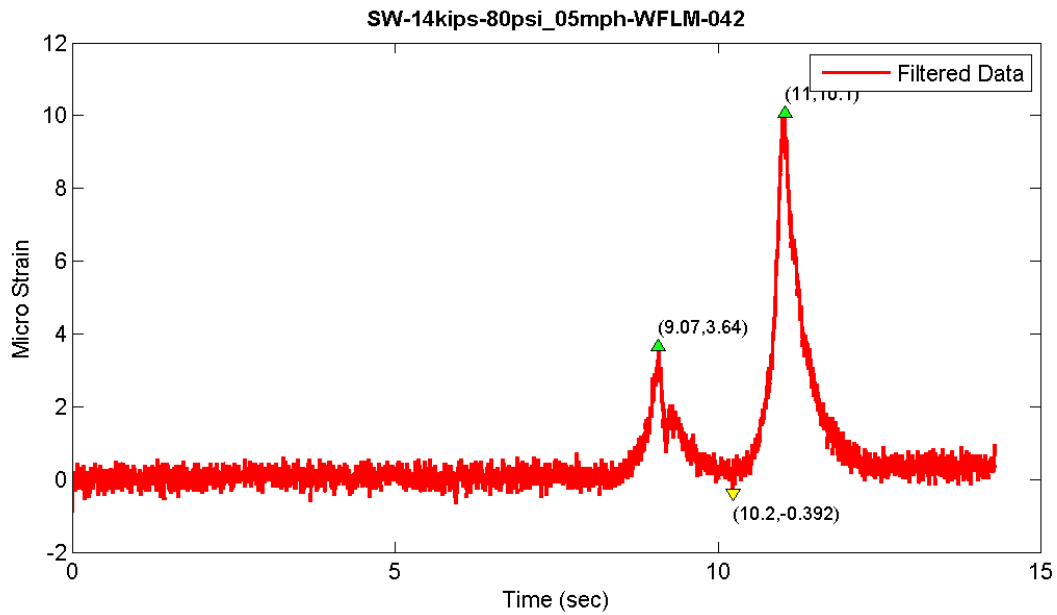
```matlab
            row = 2; Fp = 0.001;Fs=0.92;
        else
            row = 2; Fp = 0.1; Fs=0.92;
        end

  raw.smth(:,j) = low_filt(raw.data(:,j),Fp,Fs,size(raw.data(:,j),1));
        % Specific sensors need different treatments
        if (size(foldinfo,1)>7 && i<3)
            dev = avg_out(raw.smth(10:40,j),1,0);
        elseif (size(foldinfo,1)<7 && i>1)
            dev = avg_out(raw.smth(40:100,j),1,0);
        else
            dev = avg_out(raw.smth(40:100,j),1,0);
        end
         dbase.(fn).filt(:,j)= raw.smth(:,j)-dev;
% Find Initial Local Extrema
        maxf = max(dbase.(fn).filt,[],1); minf = min(dbase.(fn).filt,[],1);
        rangef =(maxf(1,j)-minf(1,j)); STD = std(dbase.(fn).filt(:,j));
        delta =abs(1.5*(1.0465 - 0.8066*STD + 0.1782*rangef)) ;
        if delta<=0; delta=0.1; end;
        [maxtab, mintab] = peakdet(dbase.(fn).filt(:,j),delta, dbase.(fn). ...
            filt(:,2));
% Adjust Local extrema
        cntr = 1;
  if size(foldinfo,1)< 6
     while (i==1 && (size(maxtab,1) < 20 || size (mintab,1) < 20)) || ...
            (i~=1 && (size(maxtab,1) < 5 || size (mintab,1) < 5))
            delta = delta/1.15;
            [maxtab, mintab] = peakdet(dbase.(fn).filt(:,j),delta, ...
                dbase.(fn).filt(:,2));
            cntr = cntr + 1;
            if cntr == 10; cntr = 1; break, end
     end
     while (i==1 && (size(maxtab,1) > 20 || size (mintab,1) > 20)) || ...
            (i~=1 && (size(maxtab,1) > 5 || size (mintab,1) > 5))
            delta = delta*1.125 ;
            [maxtab, mintab] = peakdet(dbase.(fn).filt(:,j),delta, dbase. ...
                (fn).filt(:,2));
            cntr = cntr+1;
            if cntr == 10; cntr = 1; break, end
     end
  end
   if size(foldinfo,1) > 6
     while (i==1 || i==2 && (size(maxtab,1) < 50 || size (mintab,1) < ...
            50)) || (i>2 && (size(maxtab,1) < 5 || size (mintab,1) < 5))
            delta = delta/1.1;
            [maxtab, mintab] = peakdet(dbase.(fn).filt(:,j),delta, ...
                dbase.(fn).filt(:,2));
            cntr = cntr + 1;
            if cntr == 20; cntr = 1; break, end
     end
     while (i==1 || i==2 && (size(maxtab,1) > 50 || size (mintab,1) > ...
            50)) || (i>2 && (size(maxtab,1) > 5 || size (mintab,1) > 5))
            delta = delta*1.05 ;
            [maxtab, mintab] = peakdet(dbase.(fn).filt(:,j),delta, ...
                dbase.(fn).filt(:,2));
            cntr = cntr+1;
```

```matlab
              if cntr == 20; cntr = 1; break, end
          end
       end
    % Save rut depth and local extrema and pulse duration
        %%%%%%%%%%%%%%%%%%%%%%%%%%%%%%%%%%%%%%%%%%%%%%%%%%%%%%
        % Note: rut depth is the difference before and after wheel
        % pass over the sensor.
        dbase.(fn).Rutting(j) = avg_out(dbase.(fn).filt(end-35:end,j),1,0);
        dbase.(fn).Extrema(j) = struct('max',maxtab,'min',mintab);
        % How many pressure cells exist? %for Test Pit 4, for Test Track 2
        p = 2;
        if (i > 2 || (size(foldinfo,1)<12 && i>1)) && (j > (size(raw.data,2)...
                -5) - p); % for most of runs is 27. Some runs do not have
STG_1_3 is 26
            [puls_dur puls_dur_avg] = pulse_duration(dbase.(fn).filt(:,2),...
                dbase.(fn).filt(:,j),0.01);
            dbase.(fn).Pulse_duration(1:size(puls_dur,1)-1,j-(size...
                (raw.data,2)-5 - p)) = cell2mat(puls_dur(2:end,2));
            dbase.Respsummrary.pulse(i,j-(size(raw.data,2)-5 - p-1))...
                = num2cell(puls_dur_avg);
        end


    %% Plot Original, filtered and local extrema points
        %%%%%%%%%%%%%%%%%%%%%%%%%%%%%%%%%%%%%%%%%%%%%%%%%%%%
        p = figure('visible','on');
        dev2 = avg_out(raw.data(1:35,j),1,0);
        plot(raw.data(:,2),raw.data(:,j)-dev2,'blue');
        hold on
        x = dbase.(fn).filt(:,2); y = dbase.(fn).filt(:,j);
        f = plot(x,y);set(f,'Color','red','LineWidth',1.5);xlabel('Time
(sec)');
        if j >= 27;
            ylabel('Pressure (kpa)');
        else
            ylabel('Micro Strain');
        end
        title(strcat(strtok(foldinfo(i).name,'.txt'),'_',
raw.textdata(6,j)),...
             'interpreter','none','FontWeight','bold');
        legend('Raw data (trnsfrd)','Filtered Data');
        whitebg = ([0.8 0.8 0.8]); set(gcf,'PaperPosition',[0 0 8 4])
        % Plot local extrema on the figure
     try
          plot(mintab(:,1), mintab(:,2),'kv','MarkerFaceColor',[1 1 .1]);
        for ii=1:size(mintab(:,1));
          text(mintab(ii,1),mintab(ii,2)-0.015*rangef,['(',num2str(roundsd ...
                (mintab(ii,1),3)), ',',...
          num2str(roundsd(mintab(ii,2),3)),')'],'FontSize',8) ;
        end
        for ii=1:size(maxtab(:,1));
          plot(maxtab(ii,1), maxtab(ii,2), 'k^','MarkerFaceColor',[.1 1 .1]);
          text(maxtab(ii,1),maxtab(ii,2)+0.015*rangef,['(',num2str(...
                roundsd(maxtab(ii,1),3)),',',...
           num2str(roundsd(maxtab(ii,2),3)),')'],'FontSize',8) ;
        end
     end
     hold off
```

```matlab
    %% % Save plot
    impath=[foldpath,'\Plots\',strtok(foldinfo(i).name,'.txt')];
    imname=[num2str(j),'-',char(strcat(raw.textdata(6,j)))];
    % Choose the plot format one the  png|jpg|bmp|gif
    saveas(p, fullfile(impath, imname), 'png');
clear memory
close(p)
%}
  %% Calculate max response and pulse duration
        config = regexp(strtok(foldinfo(i).name,'.txt'),'_','split');
          if ~isempty(dbase.(fn).Extrema(j).max) && ~isempty(dbase.(fn). ...
                Extrema(j).min)
            if i == 1 || (size(foldinfo,1)>12 && i==2)
            dbase.Respsummrary.maxresp.EG(i+1,j+5) = num2cell(max(max...
                (maxtab(:,2)),abs(min(mintab(:,2)))));
            dbase.Respsummrary.avgresp.EG(i+1,j+5) = num2cell(max...
                (avg_out(maxtab(:,2),1,1),abs(avg_out(mintab(:,2),1,-1))));
            dbase.Respsummrary.maxresp.EG(i+1,1:7) = [froot{end-1} config];
            dbase.Respsummrary.avgresp.EG(i+1,1:7) = [froot{end-1} config];
            else
            dbase.Respsummrary.maxresp.SP(i,j+5) = num2cell(max...
                (max(maxtab(:,2)),abs(min(mintab(:,2)))));
            dbase.Respsummrary.avgresp.SP(i,j+5) = num2cell(max...
                (avg_out(maxtab(:,2),1,1),abs(avg_out(mintab(:,2),1,-1))));
            dbase.Respsummrary.maxresp.SP(i,1:7) = [froot{end-1} config];
            dbase.Respsummrary.avgresp.SP(i,1:7) = [froot{end-1} config];
            end


          end
 end
%% Add test config for each row and save filtered data in Excel
if i == 1 || (size(foldinfo,1)>12 && i==2)
    dbase.Respsummrary.maxresp.EG(i+1,1:7) = [froot{end-1} config];
    dbase.Respsummrary.avgresp.EG(i+1,1:7) =  [froot{end-1} config];
    headerEG = [{'Section','Tire','Temp(C)','Pressure(psi)','Load(kip)'...
        ,'SensorType','Rep'}, raw.textdata(6,3:end)];
else
    dbase.Respsummrary.pulse(i,1) = config(end);
    dbase.Respsummrary.maxresp.SP(i,1:7) = [froot{end-1} config];
    dbase.Respsummrary.avgresp.SP(i,1:7) =  [froot{end-1} config];
    headerSP = [{'Section','Tire','Temp(C)','Pressure(psi)','Load(kip)'...
        ,'SensorType','Rep'}, raw.textdata(6,3:end)];
 end
impath=[foldpath,'\Filtered\'];
dbase.(fn).filt = [raw.textdata(6,:);num2cell(dbase.(fn).filt)];
xlswrite([impath,strtok(foldinfo(i).name,'.txt')],dbase.(fn).filt);
 end
 %%
 % For Test Pit 'PG_Asph_1','PG_Asph_2','PG_Base_1','PG_Base_2'
 % For Test Track 'PG_Asph_1','PG_Asph_2'
dbase.Respsummrary.pulse(1,:) = {'repetition','PG_Asph_1','PG_Asph_2'};
dbase.Respsummrary.maxresp.EG(1,:) = headerEG; dbase.Respsummrary. ...
    maxresp.SP(1,:) = headerSP;
dbase.Respsummrary.avgresp.EG(1,:) = headerEG; dbase.Respsummrary. ...
    avgresp.SP(1,:) = headerSP;
% Replace Empty cells with zero (not needed for avg)
dbase.Respsummrary.maxresp.SP(cellfun(@isempty,dbase.Respsummrary. ...
```

```matlab
        maxresp.SP)) = {0};
dbase.Respsummrary.maxresp.EG(cellfun(@isempty,dbase.Respsummrary. ...
        maxresp.EG)) = {0};
if nn == 3
        pulse = [headerSP(1:6),'PG_Asph_1','PG_Asph_2'];
        maxresp.allrep_EG = [headerEG(1:6),headerEG(8:end)];
        avgresp.allrep_EG = [headerEG(1:6),headerEG(8:end)];
        maxresp.allrep_SP = [headerSP(1:6),headerSP(8:end)];
        avgresp.allrep_SP = [headerSP(1:6),headerSP(8:end)];
        maxresp.SP = headerSP;    avgresp.SP = headerSP;
        maxresp.EG = headerEG;    avgresp.EG = headerEG;
end
for j = 2:size(dbase.Respsummrary.pulse,2)  % for Test Pit 2:5 for Test Track
2:3
        pulse_avg(1,j+5) = num2cell(avg_out(cell2mat(dbase.Respsummrary. ...
            pulse(2:end,j)),1,0));
end
pulse_avg(1,1:6) = dbase.Respsummrary.maxresp.SP(3,1:6);
max_allrep_SP(1,7:size(headerSP,2)-1) = num2cell(max(cell2mat(dbase. ...
        Respsummrary.maxresp.SP(2:end,8:end)),[],1));
max_allrep_SP(1,1:6) = dbase.Respsummrary.maxresp.SP(3,1:6);
max_allrep_EG(1,7:size(headerEG,2)-1) = num2cell(max(cell2mat(dbase. ...
        Respsummrary.maxresp.EG(2:end,8:end)),[],1));
max_allrep_EG(1,1:6) = dbase.Respsummrary.maxresp.EG(row,1:6);
for j=8:size(dbase.Respsummrary.avgresp.SP,2);
        avg_allrep_SP(1,j-1) = num2cell(avg_out(cell2mat(dbase.Respsummrary. ...
            avgresp.SP(2:end,j)),1,0));
end
for j=8:size(dbase.Respsummrary.avgresp.EG,2);
        avg_allrep_EG(1,j-1) = num2cell(avg_out(cell2mat(dbase.Respsummrary. ...
            avgresp.EG(2:end,j)),1,0));
end
avg_allrep_SP(1,1:6) = dbase.Respsummrary.avgresp.SP(3,1:6);
avg_allrep_EG(1,1:6) = dbase.Respsummrary.avgresp.EG(row,1:6);


pulse = vertcat(pulse,pulse_avg(1,:));
maxresp.allrep_SP = vertcat(maxresp.allrep_SP,max_allrep_SP(1,:));
avgresp.allrep_SP = vertcat(avgresp.allrep_SP,avg_allrep_SP(1,:));
maxresp.allrep_EG = vertcat(maxresp.allrep_EG,max_allrep_EG(1,:));
avgresp.allrep_EG = vertcat(avgresp.allrep_EG,avg_allrep_EG(1,:));
maxresp.SP = vertcat(maxresp.SP,dbase.Respsummrary.maxresp.SP(2:end,:));
avgresp.SP = vertcat(avgresp.SP,dbase.Respsummrary.avgresp.SP(2:end,:));
maxresp.EG = vertcat(maxresp.EG,dbase.Respsummrary.maxresp.EG(2:end,:));
avgresp.EG = vertcat(avgresp.EG,dbase.Respsummrary.avgresp.EG(2:end,:));
% Save database
save('Matlab_database', 'dbase')
%%%%%%%%%%%%%%%%%%%%%%%%%%%%%%%%%%
clear dbase froot maxf minf maxx minn x y
nn
end
end
%% Save final responses for the test case
savepath = uigetdir('','Please select a folder to save the results');
answer = inputdlg('Have you ever run the script before and saved the', ...
'results? y/n');
```

```matlab
if strcmp(answer,'n') == 1;

cell2csv([savepath,'\Pulse_Duration(sec).csv'],pulse,',');
cell2csv([savepath,'\MaxResponses_allrep_EG.csv'],maxresp.allrep_EG,',');
cell2csv([savepath,'\MaxResponses_allrep_SP.csv'],maxresp.allrep_SP,',');
cell2csv([savepath,'\AvgResponses_allrep_EG.csv'],avgresp.allrep_EG,',');
cell2csv([savepath,'\AvgResponses_allrep_SP.csv'],avgresp.allrep_SP,',');
cell2csv([savepath,'\MaxResponses_SP.csv'],maxresp.SP,',');
cell2csv([savepath,'\AvgResponses_SP.csv'],avgresp.SP,',');

else

cell2csv([savepath,'\Pulse_Duration(sec).csv'],pulse,',','a');
cell2csv([savepath,'\MaxResponses_allrep_EG.csv'],maxresp.allrep_EG,',','a');
cell2csv([savepath,'\MaxResponses_allrep_SP.csv'],maxresp.allrep_SP,',','a');
cell2csv([savepath,'\AvgResponses_allrep_EG.csv'],avgresp.allrep_EG,',','a');
cell2csv([savepath,'\AvgResponses_allrep_SP.csv'],avgresp.allrep_SP,',','a');
cell2csv([savepath,'\MaxResponses_SP.csv'],maxresp.SP,',','a');
cell2csv([savepath,'\AvgResponses_SP.csv'],avgresp.SP,',','a');

end

%------------------ END ----------------------------------------------
```

182

# Appendix H:    Database Management

**OVERVIEW OF SECTIONS AND DATABASES**

Different instrumented sections were built, and field and APT data were gathered. Databases from previous studies that considered wide-base tire were collected and added to the main database. The main database includes two sets: i) existing sections representing previous research, and ii) new sections, including sections built specifically for this project.

**Existing Sections**

The existing sections included in the database are:
- Ohio US-23 Hot Weather Test (1999)
- UC-Davis Rutting of Caltrans AC Mixes and Contact Stresses Database (2000)
- Florida Surface Strain Database (2010)
- UIUC Thin Pavement Sections (2000)
- Virginia-Tech Smart Road (2000-2002)

*Ohio US-23 Hot Weather Test (1999)*
The FHWA conducted controlled loading tests on U.S. Route 23 Test Road in hot weather conditions in Ohio. Testing was performed using four tire types in dual and wide-base configurations. Two pavement sections, 8 in and 4 in in thickness, were instrumented with strain gauge rosettes oriented vertically to measure strain traces induced from the passing wheel loads at three different speeds and tire inflation pressures (Xue and Weaver, 2011).

*UC-Davis Rutting of Caltrans AC Mixes and Contact Stresses Database (2000)*
Rutting of AC and asphalt-rubber hot-mix under different loads, tires, and temperatures was measured after APT at the Pavement Research Institute of Transportation Studies in Berkeley, California. The report presented the results of the APT on two overlay systems at elevated temperatures to investigate the effect of rutting in newly overlaid pavements. Two types of dual and two types of WBT were used in this study (Harvey and Paperscu, 2000).

*Florida Surface Strain Database (2010)*
The Florida Department of Transportation investigated pavement damage potential of four tire types, including a conventional dual-tire (11R22.5), a Super Single (425/65R22.5), and two wide-base single tires (445/50R22.5 and 455/55R22.5). Six test lanes were constructed considering both open- and dense-graded AC surface (Greene et al., 2010). The data include dense-graded sections. Surface strain and rutting profile were collected.

*UIUC Thin Pavement Sections (2000)*
To evaluate the effectiveness of geogrid on the performances of low-volume flexible pavements, nine low-volume flexible pavement sections were constructed at the Advanced Transportation Research Laboratory, University of Illinois at Urbana-Champaign. Three tire types, including dual, wide-base 425 and wide-base 455 were used in this study (Al-Qadi et al., 2008).

*Virginia-Tech Smart Road (2000-2002)*
The pavement research component of the Smart Road Project focused on the instrumentation, evaluation, and analysis of different flexible pavement sections. The flexible pavement sections of the Smart Road had an approximate total length of 1.4 km.  Twelve 100 m-long flexible pavement designs were included in this project. Different instrumentations and material characterization were used. A stand-alone software was designed as part of this research for database management purposes.

**New Sections**

The new sections specifically built for this project include the following:
- Delaware, Ohio
- UC-Davis
- Florida DOT

A unique test matrix was built and run for all test sections during the project as presented in Chapter 8.

**PRE-PROCESSING AND FILTERING**

Pre-processing data included removal of noise, smoothing, and extraction of peak points. Noise filtering and smoothing were done using the signal processing function (fdesign.lowpass/highpass) of Matlab. Smoothing is a process where important patterns in data are kept while unimportant data, such as noise, is left out. Depending on the wave form and noise characteristics, a low or high pass filter is used. Usually, a low-pass filter is needed to pass signals with a frequency lower than certain cutoff frequency and attenuate signals with frequencies higher than the cutoff frequency, thus resulting in a smooth wave.

A different Matlab code was written to extract the peak points and valleys. A sample Matlab Code is presented in Appendix G. A point is considered a maximum (or minimum) if it has the maximal (or minimal) value, and is preceded (to the left) by a value lower by a small amount of delta. Figure H-2 shows the filtering data extraction flowchart. Damaged or fully noisy data were removed from the analysis. An example of filtered and extracted peak points is presented in Figure H-2.

Other examples of the filtering and data extraction process are provided in Appendix G. Extracted information and filtered and raw data were stored in the database as *csv*. Interfaces were designed for each project to facilitate data access.

**ONLINE USER INTERFACE**
**Architecture**

A variety of open source technologies were used in the development of the tool:
- Java: open source object-oriented language predominantly used in server side development. Several features, such as portability, security, and ease of use, made it the first choice to write code for this tool
- MySQL: open source database
- Tomcat: application server to host web applications
- Apache: file hosting server
- JQuery: used to make web pages dynamic and interactive
- Spring: application container
- Hibernate: object relational mapping tool that helps avoid writing complex queries and treats everything as objects
- HTML: Standard Hypertext Mark-up Language for writing user interface (UI) code for browsers
- CSS: used for designing and styling the elements of web pages, such as text, tabs, menu items
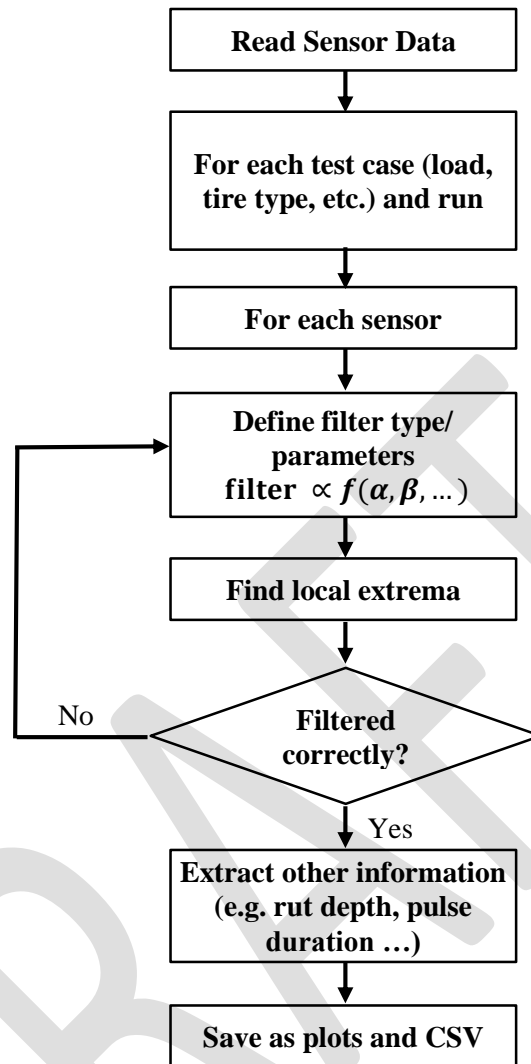- High charts: an external library used for plotting charts

**Figure H-1. Data filtering and local extrema extraction flowchart.**

A three-tier architecture model was adopted for data access. The UI does not interact directly with the database, but rather relays the command to a middle tier. The middle tier is responsible for performing business logic and directly interacts with the database. The three-tier model is very attractive because the middle tier maintains control over access and the updates that can be made to corporate data. Another advantage is that it simplifies the deployment of applications. Finally, in many cases, the three-tier architecture can provide performance advantages. Middle tier is now written in Java because of portability, speed, and security; the Java platform is fast becoming the standard platform for middle-tier development. Making use of Java's robustness, multithreading, and security features is considered a great advantage.
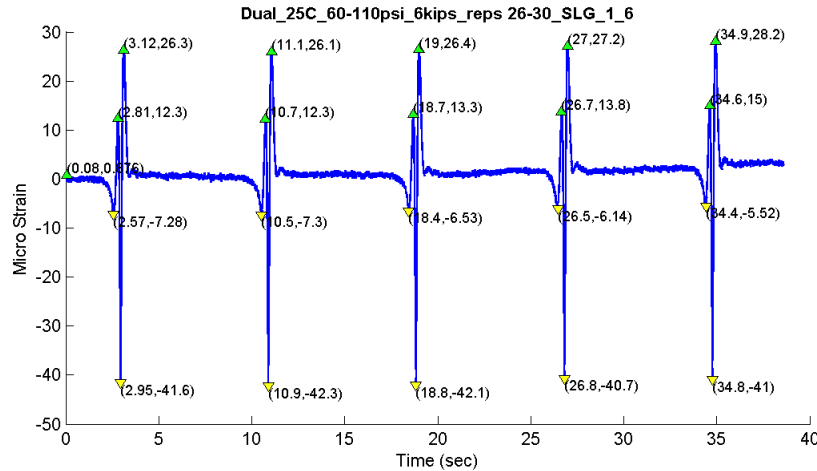
**Figure H-2. A sample filtered, peak points extracted case for Florida, test pit section.**

## Database and Management Systems

The data were stored in a structured manner maintaining relationships and dependencies. The results of various tests generated a lot of data in the form of csv, pdf, and jpeg. To visualize and access the data through a single console, RDBMS was used. An RDBMS provides a common storage location for all collected data. In addition, it enables the application of structured query language to retrieve data relevant to each requirement. RDBMS also facilitates visualization in the form of graphs and helps analyze data in a much better fashion.

RDBMS stands for Relational Database Management System, and its data are structured in database tables, fields, and records. Each RDBMS table consists of database table which in its turn consists of one or more database table fields. RDBMS stores data in a collection of tables that might be related by common fields (database table columns). RDBMS also provides relational operators to manipulate the data stored into database tables. Most RDBMS use structured query language (SQL) as database query language.

RDBMS is maintained because it ensures data safety. All changes made to an RDBMS, once committed, are immune to program crashes, and hence critical data are never lost. In addition, an RDBMS allows concurrent access to entities from various sources and therefore enables collaboration while ensuring all updates are automatic. An RDBMS also supports data integrity and scalability. SQL used in an RDBMS facilitates selective access to data as well as reporting.

An ER model is typically implemented as a database. In case of a relational database, the data are stored in tables, representing the entities. Some data fields in the tables point to indexes in other tables; these pointers represent the relationships. The three-schema approach uses three levels of ER models: conceptual data, logical data, and physical data; this methodology was implemented in development of the database.

MySQL client server database was also part of the database. In client server databases, each client initiates a connection using TCP/IP. Once the connection is established, a client can send a query to server process. The server process then looks into the disk to retrieve appropriate data. A database management system was used to store data efficiently. Earlier database users were programmers and code writers. However, the need to deal with the massive amount of data using easy language to interact with databases led to the development of SQL.

## Graph Features on Example Database

A project conducted in Delaware, Ohio, is used to show the capabilities of the database. This project is a field test run on the Ohio route US 23 (three sections in northbound, southbound, and ramp) using different load, tire inflation pressure and speed according to a test matrix. Response sensors include embedded strain gauges, pressure cells, MDD, and strain gauge rosettes at different depths. Data were collected for three sections: i) mainline section, driving lane, ii) ramp section, southbound, and iii) mainline section, passing lane. The database provides filtering of data based on several criteria, such as tire configuration, load, tire inflation pressure, load repetitions, and sensor type. Figure H-3 shows a snapshot of filters available in the database for data collected for the Ohio section. The data must be regularly categorized based on specific parameters; therefore, it was stored in an RDBMS.



**Figure H-3. Ohio section filters.**

For a thorough signal analysis of a particular sensor, plot functionality was provided. The plot filters data based on the parameters selected. Figure H-4 depicts a plot for the above filters. Time is plotted on the $x$-axis and strain on $y$-axis. Hovering the mouse over the graph provides the specific strain at that time. Zoom-in and zoom-out functionalities are also provided, using mouse drag. Figure H-5 shows the zoom-in action, and Figure H-6 provides a snapshot of the zoom-in version of the graph in Figure H-4.
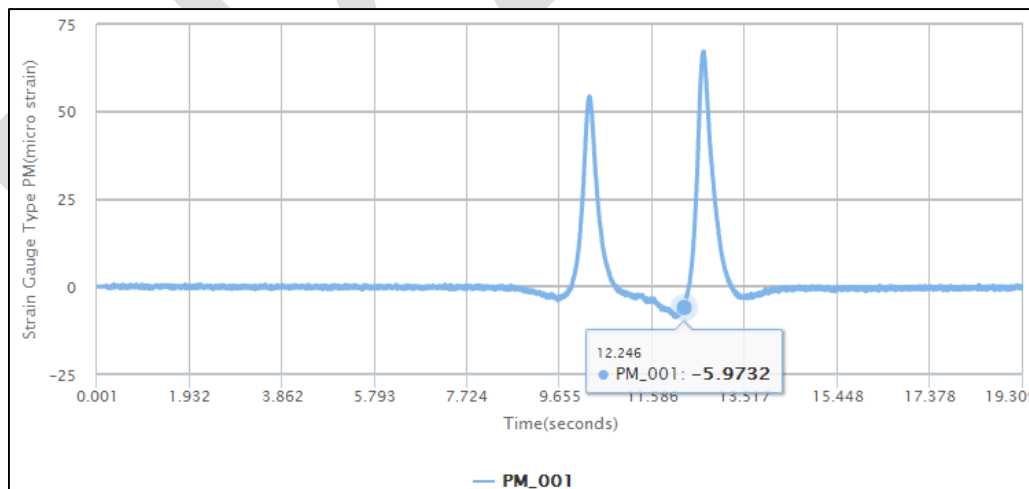


**Figure H-4. Snapshot of the plotted sensor reading for specified filters.**
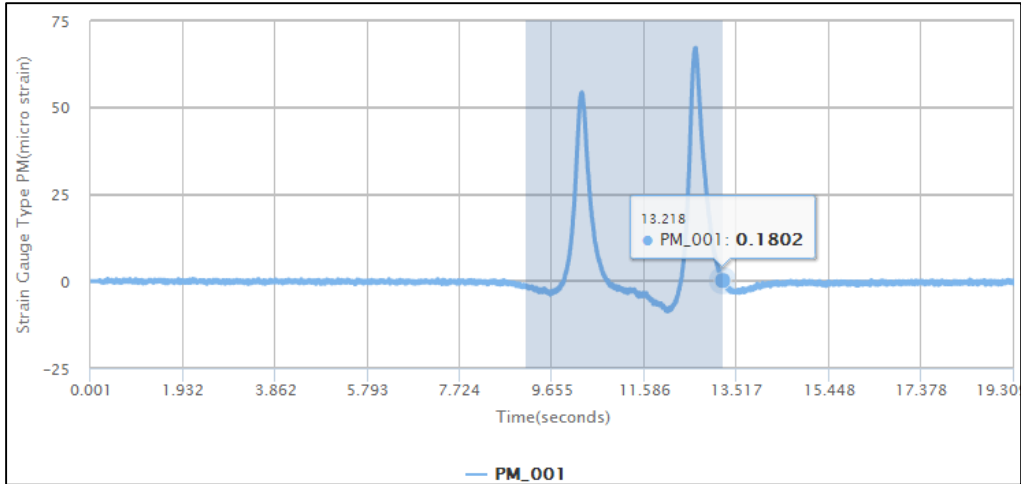
**Figure H-5. Zoomed-in example feature of the interface.**
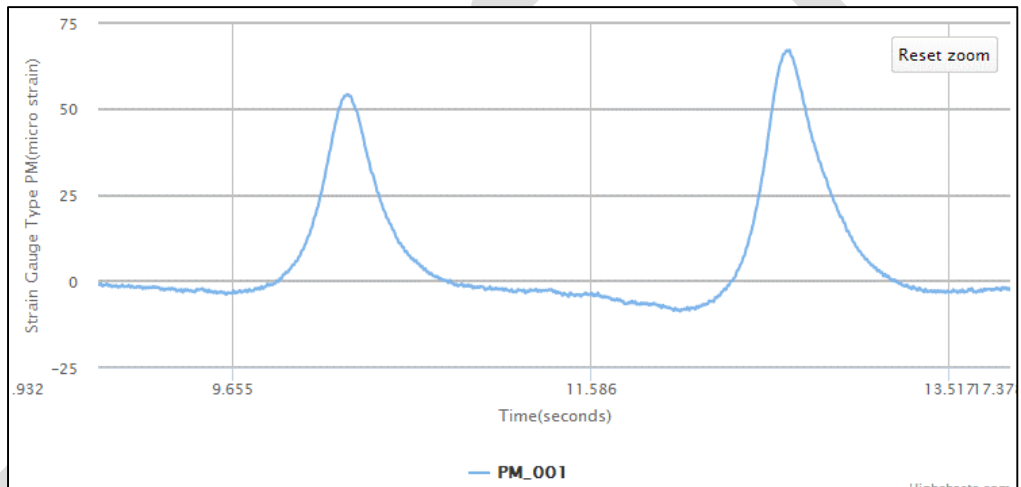

**Figure H-6. Zoomed-in shot of the sensor in previous example.**

As presented in Figure H-6, the zoom-out functionality is also provided. Clicking *Reset zoom* button will zoom out the graph, as shown in Figure H-5. To enable further analysis of sensor values, downloading a copy of the graph as a *jpeg*, *svg* or *png* was also facilitated. This can be accessed using the top right button. Figure H-7 explains the download functionality in greater detail.

The database also allows for the extraction of summary data on various criteria, as shown in Figure H-3. Summary data can be extracted simultaneously for multiple sensor values. Further, *Download All* feature allows the user to download all the summary data, regardless of the cases for the selected sensor values. For all other sections, similar filters and plotting features are provided. This will facilitate data visualization for users. Also, the download options allow access to the filtered data for further analysis. Moreover, raw data are provided in the original format for the users interested in checking raw data.
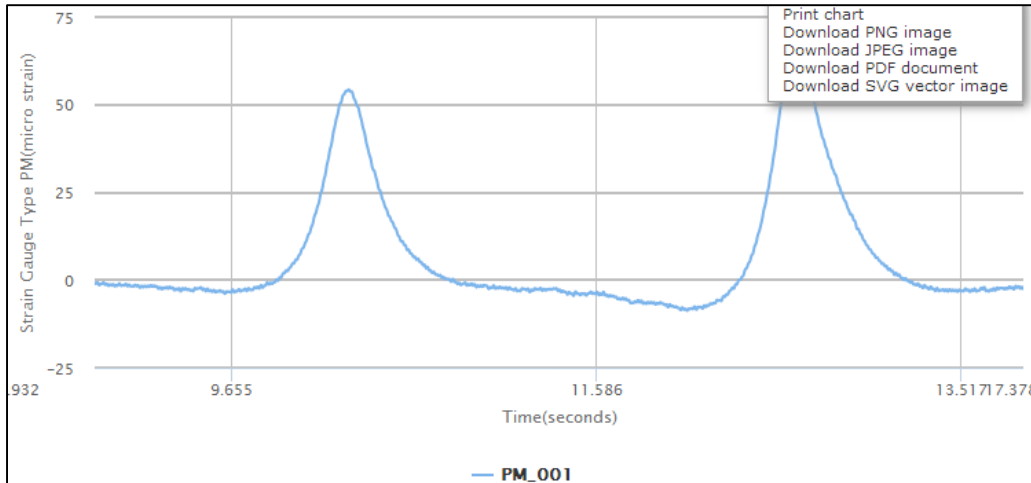
**Figure H-7. Download functionality of the interface.**

## OVERVIEW OF SOURCE CODE AND FUNCTIONALITIES

It is recommended to import the project in an IDE like Eclipse. The eclipse project file is provided. The user needs to import it as a Maven Project. The following description will provide certain snippets as to how to implement some of the core functionalities.

### Source Code Structure

The package structure is divided into three parts: controller, data access objects and model classes. The controllers are basically the entry point for a *GET* and a *POST* call. Most of the business logic is written in controllers. Data access objects are responsible for inserting, querying, and deleting an object from the database. Finally, Model Classes are POJO that maps to a particular row in MySQL database.
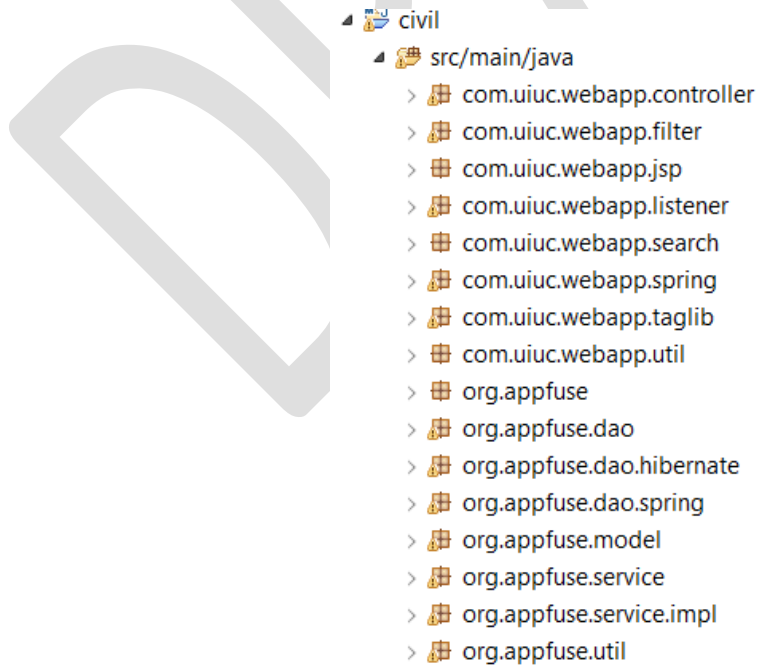

**Figure H-8. Source code structure.**

189

The steps to perform a *GET* request are presented in Figure H-9.

```java
package com.uiuc.webapp.controller;

import java.io.File;

@Controller
@RequestMapping("/davis")
public class DavisController {
    @Autowired
    private IUCDavisDao davisDao;
    @Autowired
    private IDavisSummaryDao davisSummaryDao;

    @Autowired
    private PropertyPlaceholderConfigurer propertyConfigurer;
    private static final String PATH = "C:\\work\\civil_enginering\\UCDavis\\Archive
    @Autowired
    private PropertyLoaderService loaderService;

    public DavisController() {
    }

    @RequestMapping(method = RequestMethod.GET)
    public void displayCharts() {

    }

    @RequestMapping(value = "/sensorTypes", method = RequestMethod.GET)
    @ResponseBody
    List<String> getSensorType() {
        List<String> davis = davisDao.getSensorType();
        return davis;
    }

    @RequestMapping(value = "/sensorNames/{sensorType}", method = RequestMethod.GET)
```

**Figure H-9. Explaining GET request.**

In the figure, *@Controller* and *@RequestMapping* signifies a spring controller and the URL path assigned to this controller, respectively. When *http://localhost:8080/davis* is typed, method named *display charts()* will be executed. Nothing is performed in that method; no logic will be performed and davis.jsp will be opened. If *http://localhost:8080/davis/sensorTypes* is typed, the method name *getSensorType()* is called. *DavisDAO* implementation has a method *getSensorType()*, which will return all sensor types available for Davis. Inside *DavisDAO* implementation, an interface instead of implementation was introduced.

```java
package org.appfuse.dao;

import java.util.List;

public interface IUCDavisDao extends GenericDao<UCDavis, Long> {

    List<String> getSensorType();

    List<String> getTestIds();

    List<String> getTirePressure(String testId, String sensor);

    List<String> getLoad(String testId, String sensor);

    List<String> getWheelType(String sensor, String testId, String pressure,
            String load);

    List<String> getTrafficking(String sensor, String testId, String pressure,
            String load);

    List<String> getRepetition(String sensor, String testId, String pressure,
            String load, String wheelType, String trafficking);

    List<String> getFileName(String sensor, String testId, String pressure,
            String load, String wheelType, String trafficking, String cycle);

    List<String> getDate();

    List<String> getTemp(String date);
}
```

**Figure H-10. Davis section DAO Interface.**

```java
@Repository
public class UCDavisDaoImpl extends GenericDaoHibernate<UCDavis, Long>
        implements IUCDavisDao {

    public UCDavisDaoImpl() {
        super(UCDavis.class);
        // TODO Auto-generated constructor stub
    }

    @SuppressWarnings("unchecked")
    public List<String> getSensorType() {
        return this.getHibernateTemplate().executeFind(
                new HibernateCallback<List<String>>() {

                    public List<String> doInHibernate(Session session)
                            throws HibernateException, SQLException {
                        List<String> query = session.createSQLQuery(
                                "SELECT DISTINCT(sensor) FROM UCDavis").list();

                        return query;
                    }
                });
    }

    @SuppressWarnings("unchecked")
    public List<String> getTestIds() {
        return this.getHibernateTemplate().executeFind(
                new HibernateCallback<List<String>>() {

                    public List<String> doInHibernate(Session session)
                            throws HibernateException, SQLException {
                        List<String> query = session.createSQLQuery(
                                "SELECT DISTINCT(testId) FROM UCDavis").list();

                        return query;
                    }
                });
    }
```

**Figure H-11. Davis section DAO Implementation.**

191

```
@Entity
@Table
public class UCDavis implements Serializable {

    /**
     *
     */
    private static final long serialVersionUID = 4610218925220349783L;
    private String tirePressure;
    private String loadKip;
    private String testId;
    private String cycles;
    private String sensorType;
    private String sensor;
    private String trafficking;
    private String wheelType;
    private String filePath;
    private String dateTime;
    private Long id;

    @Id
    @GeneratedValue(strategy = GenerationType.AUTO)
    public Long getId() {
        return id;
    }

    public void setId(Long id) {
        this.id = id;
    }

    public String getTirePressure() {
        return tirePressure;
    }
}
```

**Figure H-12. Davis section POJO.**

**Plotting Charts**

A third-party library called High *Charts.js* was used to plot charts in real time. To plot line graphs is straightforward, provided all the APIs of high charts are known. For instance, to access the Florida new data page, *http://localhost:8080/florida* is typed. After selecting and plotting a case, a JavaScript function defined in *florida.jsp* is called (Figure H-7). This function sends all selected parameters to *Florida Controller* and decides which data to return. *FloridaController* requests *Florida DAO* to fetch the values satisfying the given case. *Florida Controller* converts the value to *JSON* and passes it to *florida.jsp*. After calling *AJAX*, the high charts *api* is called with the given data and a chart is displayed.



**Figure H-13. Florida sensor filter.**

192

```javascript
function plot() {
    var url = "/florida/sensor/" + $(track).val() + "/" + $(tireType).val()
            + "/" + $(temp).val() + "/" + $(pressure).val() + "/"
            + $(code).val() + "/" + $(repetition).val() + "/"
            + $(sensor).val() + "/" + $(sensorValues).val() + "/";
    var time;
    var value;
    $
            .blockUI({
                message : '<h1>We are processing your request. Please be patient....</h1>'
            });

    $.ajax({
        url : url,
        type : "GET",
        success : function(smartphone) {

            for ( var key in smartphone) {
                time = key;
                value = smartphone[key];
            }
            var v = $(sensorValues).val();
            if (v.indexOf("SL") != -1) {
                v += "(micro strain)";
            }
            var k = tickPoint(10, eval(time).length);
            $('#container').highcharts({
                chart : {
                    borderWidth : 1,
                    zoomType : 'x'
```

**Figure H-14. Plot Javascript function.**

## File Hosting

The IP address and port number of Apache HTTP server are provided in a file called *configuration.properties*. When executing, *DconfigFile= <path of the configuration file>* needs to be passed. The content of configuration file is:

> *file.hosting.server=98.253.59.23*
> *file.hosting.port=80*

These values are used by the controller to pass to UI layer. The Controller layer can be seen in Figure H-15.

```java
@RequestMapping(value = "/download/{testId}/{sensor}/{pressure}/{load}/{wheelType}/{trafficking}/{cycle}/{date}", method = RequestMethod.GET)
@ResponseBody
public FileSystemResource download(@PathVariable String testId,
        @PathVariable String sensor, @PathVariable String pressure,
        @PathVariable String load, @PathVariable String wheelType,
        @PathVariable String trafficking, @PathVariable String cycle,
        @PathVariable String date) {
    List<String> list = null;
    if (sensor.equalsIgnoreCase("TEMP")) {
        list = davisDao.getTemp(date);
    } else {
        list = davisDao.getFileName(sensor, testId, pressure, load,
                wheelType, trafficking, cycle);
    }
    String path = PATH + list.get(0);
    return new FileSystemResource(new File(path));
}

@ModelAttribute("address")
public String getAddress() {
    String server = (String) loaderService.properties
            .get("file.hosting.server");
    String port = (String) loaderService.properties
            .get("file.hosting.port");
    return server + ":" + port;
}
```

**Figure H-15. Controller Layer.**

The address consists of two parts: base address and relative address. The base address represents the server address and relative address is the actual file address on the specified server. The *getAddress()* method forms an address of *Apache HTTP* server and sets it in the model attribute called address. On the UI, this base address is retrieved and appended to a particular file address. To render base address a tree structure view an external library called *JStree* was used.

```html
<div id="tabs-1">

    <div id="jstree">
        <!-- in this example the tree is populated from inline HTML -->
        <ul>
            <li>Loading History
                <ul>
                    <li><a
                        href="http://${address}\Interface-Meeting\WB Data Folder\Docs\UC Davis Data\Profile Data\504RF-WideBase_LoadingHistory_06-20-2011.csv">504RF*</a>
                    <li><a
                        href="http://${address}\Interface-Meeting\WB Data Folder\Docs\UC Davis Data\Profile Data\505RF-LoadingHistory_06-17-2011.csv">505RF</a></li>
                    <li><a
                        href="http://${address}\Interface-Meeting\WB Data Folder\Docs\UC Davis Data\Profile Data\506RF-LoadingHistory_06-20-2011.csv">506RF</a></li>
                    <li><a
                        href="http://${address}\Interface-Meeting\WB Data Folder\Docs\UC Davis Data\Profile Data\507RF-LoadingHistory_06-20-2011.csv">507RF</a></li>
                    <li><a
                        href="http://${address}\Interface-Meeting\WB Data Folder\Docs\UC Davis Data\Profile Data\508RF-LoadingHistory_06-20-2011.csv">508RF</a></li>
                    <li><a
                        href="http://${address}\Interface-Meeting\WB Data Folder\Docs\UC Davis Data\Profile Data\509RF-LoadingHistory_06-20-2011.csv">509RF</a></li>
                    <li><a
                        href="http://${address}\Interface-Meeting\WB Data Folder\Docs\UC Davis Data\Profile Data\510RF-LoadingHistory_06-20-2011.csv">510RF</a></li>
                    <li><a
                        href="http://${address}\Interface-Meeting\WB Data Folder\Docs\UC Davis Data\Profile Data\511RF-LoadingHistory_06-20-2011.csv">511RF</a></li>
                    <li><a
                        href="http://${address}\Interface-Meeting\WB Data Folder\Docs\UC Davis Data\Profile Data\512RF-LoadingHistory_06-20-2011.csv">512RF</a></li>
                    <li><a
                        href="http://${address}\Interface-Meeting\WB Data Folder\Docs\UC Davis Data\Profile Data\513RF-LoadingHistory_06-20-2011.csv">513RF</a></li>

                </ul>
            </li>
        </ul>
    </div>
```

**Figure H-16. HTML snippet for specifying downloadable file.**

```javascript
$(function() {
    $("#jstree").jstree().bind("select_node.jstree", function(e, data) {
        var href = data.node.a_attr.href;
        document.location.href = href;

        //  $("#the_div").load(href);
    });
    $("#labTest").jstree().bind("select_node.jstree", function(e, data) {
        var href = data.node.a_attr.href;
        document.location.href = href;

        //  $("#the_div").load(href);
    });
    $("#tirePressure").jstree().bind("select_node.jstree",
            function(e, data) {
                var href = data.node.a_attr.href;
                document.location.href = href;

                //  $("#the_div").load(href);
            });

});
```

**Figure H-17. Javascript snippet for tree type structure.**

**Database Schema**

Figure H-18 describes the names of the tables in the database, and Figure H-19 shows the relationship between them.

| Name | Engine | Version | Row Format | Rows | Avg Row Length | Data Length | Max Data Length | Index Length | Data Free | Auto Incre... | Create Time | U |
|---|---|---|---|---|---|---|---|---|---|---|---|---|
| app_user | InnoDB | 10 | Compact | 2 | 8192 | 16384 | 0 | 32768 | 0 | 1 | 2013-11-02 16:1... | |
| davissummary | InnoDB | 10 | Compact | 66123 | 278 | 18399232 | 0 | 0 | 4194304 | 72715 | 2013-12-14 12:0... | |
| florida_reading | InnoDB | 10 | Compact | 13150668 | 38 | 504365056 | 0 | 1473085440 | 4194304 | 0 | 2014-01-19 13:1... | |
| floridasp | InnoDB | 10 | Compact | 5172553 | 704 | 3643260928 | 0 | 0 | 7340032 | 5443363 | 2014-01-06 05:1... | |
| floridaspreadingtesttrack | InnoDB | 10 | Compact | 12802235 | 516 | 6616514560 | 0 | 0 | 5242880 | 14576515 | 2014-01-19 13:4... | |
| floridaspsummary | InnoDB | 10 | Compact | 3879 | 409 | 1589248 | 0 | 0 | 4194304 | 4269 | 2014-01-20 13:4... | |
| floridasptesttrack | InnoDB | 10 | Compact | 1472 | 89 | 131072 | 0 | 0 | 0 | 1630 | 2014-01-19 19:4... | |
| load_ps | InnoDB | 10 | Compact | 0 | 0 | 16384 | 0 | 81920 | 0 | 0 | 2013-11-02 16:1... | |
| loads | InnoDB | 10 | Compact | 0 | 0 | 16384 | 0 | 0 | 0 | 1 | 2013-11-02 16:1... | |
| ohioreading | InnoDB | 10 | Compact | 12060568 | 631 | 7614758912 | 0 | 0 | 5242880 | 12969183 | 2013-11-02 18:0... | |
| ohiosummary | InnoDB | 10 | Compact | 1790 | 887 | 1589248 | 0 | 0 | 4194304 | 2021 | 2013-11-10 06:2... | |
| pressurespeed | InnoDB | 10 | Compact | 0 | 0 | 16384 | 0 | 0 | 0 | 1 | 2013-11-02 16:1... | |
| psi_rep | InnoDB | 10 | Compact | 0 | 0 | 16384 | 0 | 81920 | 0 | 0 | 2013-11-02 16:1... | |
| reading | InnoDB | 10 | Compact | 0 | 0 | 16384 | 0 | 0 | 0 | 1 | 2013-11-02 16:1... | |
| rep_sensor | InnoDB | 10 | Compact | 0 | 0 | 16384 | 0 | 81920 | 0 | 0 | 2013-11-02 16:1... | |
| repetition | InnoDB | 10 | Compact | 0 | 0 | 16384 | 0 | 0 | 0 | 1 | 2013-11-02 16:1... | |
| role | InnoDB | 10 | Compact | 2 | 8192 | 16384 | 0 | 0 | 0 | 1 | 2013-11-02 16:1... | |
| section | InnoDB | 10 | Compact | 0 | 0 | 16384 | 0 | 0 | 0 | 1 | 2013-11-02 16:1... | |
| section_tire_types | InnoDB | 10 | Compact | 0 | 0 | 16384 | 0 | 81920 | 0 | 0 | 2013-11-02 16:1... | |
| sensor_reading | InnoDB | 10 | Compact | 0 | 0 | 16384 | 0 | 81920 | 0 | 0 | 2013-11-02 16:1... | |
| sensorreading | InnoDB | 10 | Compact | 0 | 0 | 16384 | 0 | 0 | 0 | 1 | 2013-11-02 16:1... | |
| state | InnoDB | 10 | Compact | 0 | 0 | 16384 | 0 | 0 | 0 | 1 | 2013-11-02 16:1... | |
| state_reading | InnoDB | 10 | Compact | 12339193 | 38 | 472907776 | 0 | 1381695488 | 7340032 | 0 | 2013-11-02 18:0... | |
| state_section | InnoDB | 10 | Compact | 0 | 0 | 16384 | 0 | 81920 | 0 | 0 | 2013-11-02 16:1... | |
| stateentity | InnoDB | 10 | Compact | 1194 | 96 | 114688 | 0 | 0 | 0 | 1292 | 2013-11-02 18:0... | |
| tire_type_load | InnoDB | 10 | Compact | 0 | 0 | 16384 | 0 | 81920 | 0 | 0 | 2013-11-02 16:1... | |
| tiretype | InnoDB | 10 | Compact | 0 | 0 | 16384 | 0 | 0 | 0 | 1 | 2013-11-02 16:1... | |
| ucdavis | InnoDB | 10 | Compact | 6190 | 256 | 1589248 | 0 | 0 | 4194304 | 6721 | 2013-11-25 20:3... | |
| user_role | InnoDB | 10 | Compact | 2 | 8192 | 16384 | 0 | 65536 | 0 | 0 | 2013-11-02 16:1... | |

**Figure H-18. All tables.**

195

**Figure H-19. ER diagram.**